

Supporting information for:

Reactivities of Cyclonickellated Complexes with Hydroxylamines:
Formation of a κ^O , κ^N -Aminoxide Derivative and Adducts Featuring κ^O -
Hydroxylamine and κ^N -Imine

*Rajib K. Sarker, Loïc P. Mangin, and Davit Zargarian**

Département de chimie, Université de Montréal, Montréal (Québec), Canada H3C 3J7

zargarian.davit@umontreal.ca

**RECEIVED DATE (to be automatically inserted after your manuscript is accepted if required according to
the journal that you are submitting your paper to)**

TABLE OF CONTENTS:

1	General information and considerations	S3
2	Procedures for the synthesis of new ligand and Ni complexes	S3
3	NMR Spectra of new compounds	S10
	Ligand 3-NMe ₂ -C ₆ H ₄ OP(<i>i</i> -Pr) ₂ (Figures S1-S9)	S10
	Complex 4' (Figures S10-S16)	S15
	Complexes 5a , 5b , 5c (Figures S17-S43)	S19
	Complexes 6a , 6b , 6c (Figures S44-S71)	S34
	Complexes 7a , 7b , 7c , 7d (Figures S72-S107)	S49
	Complexes 8a , 8b (Figures S108-S125)	S69
4	³¹ P NMR spectra of some crude reaction mixtures	S79
5	Procedure and ³¹ P NMR spectra of the time profile experiments	S85
6	PXRD spectra of selected complexes	S89
7	Crystallographic data tables	S94
	Table S1 (Complex 4')	S94
	Table S2 (Complexes 5a-5c)	S95
	Table S3 (Complexes 6b , 6c)	S96
	Table S4 (Complexes 7b-7d)	S97
	Table S5 (Complexes 8a , 8b)	S98
	Additional Thermal ellipsoid plots	S99
	Figures S154 (4') & S155 (5a) & S156 (5b)	S99
	Figures S157 (5c) & S158 (6a) & S159 (6b)	S100
	Figures S160 (6c) & 161 (7b) & 162 (7c)	S101
	Figure S163 (7d) & S164 (8a) & S165 (8b)	S101
	Table S6 (Bond distances)	S103
	Table S7 (Bond angles)	S103
8	Regarding the unusually downfield signals in the ¹ H NMR spectra of 6c and 7c	S104
9	DFT Computational studies	S105
10	References	S111

1. General experimental considerations

All manipulations were carried out under a nitrogen atmosphere using standard Schlenk techniques and an inert-atmosphere box. Solvents were dried by passage over a column of activated alumina, collected under nitrogen, and stored over 3 Å molecular sieves inside transfer/storage flasks equipped with high vacuum valves (Straus flasks). Et₃N was dried over CaH₂. The Ni^{II} precursor [(*i*-PrCN)NiBr₂]_n used throughout this study was prepared as reported previously.¹ The dimeric precursors **1-3** were prepared using a published procedure.² Other reagents were purchased from Sigma-Aldrich or FisherSci and used without further purification.

The NMR spectra were recorded at 400 MHz (¹H), 125.72 MHz (¹³C), and 202.4 MHz (³¹P). Chemical shift values are reported in ppm (δ) and referenced internally to the residual solvent signals (¹H and ¹³C: 1.94 and 118.26 ppm for CD₃CN; 7.26 and 77.16 for CDCl₃; 7.16 and 128.06 for C₆D₆) or externally (³¹P: H₃PO₄ in D₂O, δ = 0). The minimal precision of the NMR spectra was found to be 0.3 Hz for ¹H, 0.7 Hz for ¹³C and 2 Hz for ³¹P.

Single crystals of all the structurally characterized complexes were grown from Et₂O solutions cooled to -35 °C. The crystallographic data for all structures were collected on either a Bruker Microsource (Cu radiation) or a Bruker Venture Metaljet (Ga radiation) via the Bruker APEX II or APEX III³ software packages. Cell refinement and data reduction were performed using SAINT.⁴ An empirical absorption correction, based on multiple measurements of equivalent reflections, was applied using the program SADABS or TWINABS.⁵ The space group was confirmed by the XPREP⁶ routine in APEX. The structures were solved in OLEX⁷ using the SHELX⁸ suite and refined by full-matrix least squares with SHEXL.⁹ All non-hydrogen atoms were refined with anisotropic displacement parameters, whereas hydrogen atoms were set in calculated positions and refined via the riding model, with thermal parameters being 1.5 times that of the carbon bearing the H in question. All Thermal ellipsoid plots were drawn using OLEX.

2. Procedures for the synthesis of the new phosphinite ligand and the Ni complexes

3-NMe₂-C₆H₄OP(*i*-Pr)₂. A 100 mL Schlenk flask was charged with Et₃N (1.252 mL, 8.975 mmol, 1.2 equiv) and 3-NMe₂-C₆H₄OH (1.026 mL, 7.479 mmol, 1 equiv) dissolved in 35 mL THF. Dropwise addition of ClP(*i*-Pr)₂ (1.190 mL, 7.479 mmol, 1 equiv) to this solution led to salt precipitation. The resulting mixture was stirred under inert atmosphere for 2 h at room temperature, followed by solvent evaporation and extraction of the residues with 3 × 25 mL Et₂O. Evaporation of the extracts afforded the target ligand as a dark oil (1.689 g, 6.667 mmol, 89 %). ¹H NMR (400 MHz, 20 °C, C₆D₆): δ 1.03 (dd, 6H, CH(CH₃), ³J_{HH} = 7.2, ³J_{HP} = 15.7), 1.20 (dd, 6H, CH(CH₃), ³J_{HH} = 7.0, ³J_{HP} = 10.4), 1.82 (dsept, 2H, CH(CH₃)₂, ³J_{HH} = 7.1, ²J_{HP} = 2.7), 2.52 (s, 6H, N(CH₃), 6.30 (m, 1H, C_{Ar}-H, ³J_{HH} = 8.3, ⁴J_{HP} = 2.5, ⁴J_{HH} = 0.5), 6.76 (psq, 1H, C_{Ar}-H, ⁴J_{HH} = 2.3), 6.87 (psdtd, 1H, C_{4Ar}-H, ³J_{HH} = 8.1, ³J = 2.3, ³J = 0.8), 7.15 (t, 1H, C_{Ar}-H, ³J_{HH} = 8.1). ¹³C{¹H} NMR (125.72 MHz, 20 °C, C₆D₆): δ 17.26 (d, ²J_{PC} = 8.7, CH₃), 17.99 (d, ²J_{PC} = 20.7, CH₃), 28.65 (d, ²J_{PC} = 18.4, CH), 40.21 (s, NCH₃), 103.48 (d, ²J_{PC} = 10.3, C_{Ar}), 106.85 (d, ²J_{PC} = 0.8, C_{Ar}), 107.15 (d, ²J_{PC} = 12.0, C_{Ar}), 130.03 (s, C_{Ar}), 152.38 (s, C_{Ar}), 161.01 (d, ²J_{PC} = 8.8, C_{1Ar}). ³¹P{¹H} NMR (202.4 MHz, 20 °C, CDCl₃): 143.87 (s, 1P).

{κ^P,κ^C-(*i*-Pr)₂PO-(5-NMe₂-C₆H₃)}Ni(μ-Br)₂ (4'). A 100 mL Schlenk flask was charged with a solution of the ligand 3-NMe₂-C₆H₄OP(*i*-Pr)₂ (984 mg, 3.882 mmol, 1.00 equiv) in 40 mL MeCN, {(*i*-PrCN)NiBr₂]_n (1.340 g, 4.658 mmol, 1.2 equiv), and Et₃N (471 mg, 4.658 mmol, 1.2 equiv). The mixture was stirred at room temperature overnight. Evaporation of the solvent, followed by extraction with toluene (3 × 20 mL)

and evaporation of the volatiles gave a viscous material. This was dissolved in minimum amount of Et₂O and then hexane was added to precipitate the desired dimer. Cannula filtration of the mixture and subsequent evaporation of the filtrate gave a solid residue (0.937 mg). NMR analysis of this solid showed that it contained both the desired dimer, **4**, and the new complex **4'**, the product of reprotonation at the aryl-Ni moiety. The ³¹P{¹H} NMR (C₆D₆) spectrum showed a singlet at 196.7 assigned to **4** and two doublets at ca. 150 (d, 1P, *J*_{PP} = 323.0), 182 (d, 1P, *J*_{PP} = 323.1) assigned to **4'**. Based on the weight of the solid residue obtained from the reaction and the integration values of these signals, we estimate yields of 38% for **4** and 20% for **4'**. Several attempts at purification of this mixture by recrystallization resulted in the isolation of a small crop of crystals for complex **4'**, but we did not succeed in isolating pure samples of the desired dimer **4**. For this reason, the crude mixture generated from the reaction of {(*i*-PrCN)NiBr₂}_n with the ligand was used for reactivity studies with hydroxy amines. The NMR spectra of [{κ^P,κ^C-(*i*-Pr)₂PO-(5-NMe₂-C₆H₃)}{κ^P-(*i*-Pr)₂PO-(5-NMe₂-C₆H₄)}NiBr] (**4'**) are provided here. ¹H NMR (400 MHz, 20 °C, CDCl₃): δ 1.38 (dd, 12H, CHCH₃, ³*J*_{HH} = 7.2, ³*J*_{HP} = 13.4), 1.46-1.54 (m, 12H), 2.59 (sext, 2H, CH(CH₃)(CH₃), ³*J*_{HP} = 7.1, ³*J*_{HH} = 2.1), 2.78 (s, 6H, NCH₃), 2.79 (s, 6H, NCH₃), 2.80 (m, 2H, CH(CH₃)(CH₃)), 5.95 (dd, 1H, *o*-C₆H₅, ³*J*_{HH} = 8.7, ⁵*J*_{HH} = 2.4), 6.15 (d, 1H, *o*-C₆H₅, ⁵*J*_{HH} = 2.8), 6.30 (dd, 1H, ³*J*_{HH} = 8.2, ⁵*J*_{HH} = 2.1), 6.78 (dt, 1H, *p*- or *m*-C₆H₅), 6.86 (ps q, 1H, C₆H₅), 7.01(t, 1H, *p*-C₆H₅, ³*J*_{HH} = 8.1), 7.17 (dd, 1H, *o*-C₆H₅, ³*J*_{HH} = 8.7, ⁵*J*_{HH} = 0.7), 7.36 (s, 1H). ¹³C{¹H} NMR (125.72 MHz, 20 °C, CDCl₃): δ 17.28 (s, CH₃), 18.02 (s, CH₃), 19.01(d, CH₃, *J*_{CP} = 3.7), 20.47 (d, CH₃, *J*_{CP} = 4.7), 28.58 (d, PCH, *J*_{CP} = 2.7), 28.82 (d, PCH, *J*_{CP} = 2.7), 29.76 (d, PCH, *J*_{CP} = 3.1), 29.93 (d, PCH, *J*_{CP} = 3.1), 40.63(d, *J*_{CP} = 12.7), 95.72 (d, *J*_{CP} = 14.1), 105.23 (d, C_{Ar}, *J*_{CP} = 6.4), 106.36, 107.08, 108.73 (d, C_{Ar}, *J*_{CP} = 5.2) 128.49, 129.26, 142.80 (d, *J*_{CP} = 12.3, C_{Ar}), 150.38, 151.59, 155.80 (d, *J*_{CP} = 5.2, C_{Ar}), 169.38, 169.56. ³¹P{¹H} NMR (202.4 MHz, 20 °C, CDCl₃): 150.27 (d, 1P, *J*_{PP} = 323.0), 182.46 (d, 1P, *J*_{PP} = 323.1).

[{κ^P,κ^C-(*i*-Pr)₂PO-C₆H₄}{NH₂OBn}Ni(Cl/Br)] (**5a-Cl** and **5a-Br**; Bn= CH₂Ph). A 50 mL Schlenk flask containing 10 mL MeCN was charged with O-benzylhydroxylamine hydrochloride (76 mg, 0.476 mmol, 4 equiv) and Et₃N (48 mg, 0.476 mmol, 4 equiv). The resulting mixture was stirred for 45 min under inert atmosphere and at room temperature. To this mixture was added the dimer [{κ^P,κ^C-(*i*-Pr)₂PO-C₆H₄}Ni(μ-Br)]₂ (**1**, 83 mg, 0.119 mmol, 1 equiv) and the stirring was continued overnight under the same condition. Removal of volatiles under vacuum left a sticky, brown residue, which was treated with ca. 1 mL of Et₂O, filtered and the filtrate kept at -35 °C overnight. Brown crystals were separated and washed with cold hexane. (Yield: 37 mg, 0.086 mmol 35 %). ¹H NMR (400 MHz, 20 °C, CDCl₃): δ 1.36 (dd, 6H, CHCH₃, ³*J*_{HH} = 7.0, ³*J*_{HP} = 14.7), 1.52 (dd, 6H, CHCH₃, ³*J*_{HH} = 7.2, ³*J*_{HP} = 17.7), 2.36 (psoct, 2H, CHCH₃, ³*J*_{HH} ≈ ³*J*_{HP} = 7.1), 5.35 (br s, 2H, OCH₂), 6.06 (br s, 2H, NH₂), 6.68 (d, 1H, C3/6-*H*, ³*J*_{HH} = 7.8), 6.73 (t, 1H, C4/5-*H*, ³*J*_{HH} = 7.3), 7.02 (t, 1H, C4/5-*H*, ³*J*_{HH} = 7.4), 7.10 (d, 1H, C3/6-*H*, ³*J*_{HH} = 7.6). ¹³C{¹H} NMR (125.72 MHz, 20 °C, CDCl₃): δ 17.00 (s, CH₃), 18.14 (d, ²*J*_{PC} = 3.7, CH₃), 28.14 (s, P-CH), 28.40 (s, P-CH), 78.74 (s, CH₂), 110.70 (d, ²*J*_{PC} = 13, 1C, C2), 121.21 (d, *J*_{PC} = 2.05, 1C, C4/5), 127.20 (s, 1C, C4/5), 128.94 (s, 2C, C_{Ar}), 129.21 (s, 1C, C_{Ar}), 129.45 (s, 2C, C_{Ar}), 134.63 (s, 1C, C_{Ar}), 136.25 (br, 1C, C3/6), 167.91 (d, *J*_{PC} = 11.5, 1C, C1_{Ar}). The spectrum does not display the anticipated signals for two quaternary aromatic carbons. ³¹P{¹H} NMR (202.4 MHz, 20 °C, CDCl₃): 195.19 (**5a-Cl**, 87%), 198.25 (**5a-Br**, 13%).

[{κ^P,κ^C-(*i*-Pr)₂PO-C₆H₄}{κ^N-Et₂NOH}NiBr] (**5b**). A 50 mL Schlenk flask containing 5 mL of CH₂Cl₂ was charged with the parent dimer [{κ^P,κ^C-(*i*-Pr)₂PO-C₆H₄}Ni(μ-Br)]₂ (**1**, 100 mg, 0.134 mmol, 1.00 equiv) and Et₂NOH (0.024 mg, 0.268 mmol, 2.00 equiv). The solution was stirred overnight at room temperature and under inert atmosphere. Removal of volatiles under vacuum left a sticky, brown residue, which was treated with ca. 1 mL of Et₂O, filtered and the filtrate kept at -35 °C overnight. Brown crystals were separated and

washed with cold hexane. (Yield: 0.049 mg, 41 %). ^1H NMR (400 MHz, 20 °C, C_6D_6): δ 1.05 (t, 6H, NCH_2CH_3 , $^3J_{\text{HH}} = 7.2$), 1.24 (dd, 6H, CHCH_3 , $^3J_{\text{HH}} = 7.0$, $^3J_{\text{HP}} = 14.2$), 1.55 (dd, 6H, CHCH_3 , $^3J_{\text{HH}} = 7.2$, $^3J_{\text{HP}} = 17.0$), 2.15-2.27 (m, 4H, overlap of NCH_2 and PCH), 2.31-2.41 (m, 2H, NCH_2), 6.89 (dd, 1H, $\text{C}3/6_{\text{Ar}}\text{-H}$, $^3J_{\text{HH}} = 7.7$, $^4J_{\text{HH}} = 1.4$), 6.99 (tdd, 1H, $\text{C}4/5_{\text{Ar}}\text{-H}$, $^3J_{\text{HH}} = 7.5$, $^4J_{\text{HH}} = 1.7$, $^5J_{\text{HP}} = 1.3$), 7.08 (tdd, 1H, $\text{C}4/5_{\text{Ar}}\text{-H}$, $^3J_{\text{HH}} = 7.4$, $^4J_{\text{HH}} = 2.0$, $^6J_{\text{HP}} = 1.6$), 7.85 (dt, 1H, $\text{C}3/6_{\text{Ar}}\text{-H}$, $^3J_{\text{HH}} = 7.7$, $^4J_{\text{HP}} \approx ^4J_{\text{HH}} = 1.8$), 9.02 (s, 1H, OH). $^{13}\text{C}\{^1\text{H}\}$ NMR (125.72 MHz, 20 °C, C_6D_6): δ 9.24 (s, NCH_2CH_3), 17.12 (d, $^2J_{\text{PC}} = 1.6$, PCHCH_3), 18.63 (d, $^2J_{\text{PC}} = 3.9$, PCHCH_3), 28.80 (d, $J_{\text{PC}} = 26.3$, PCH), 53.99 (s, NCH_2), 110.01 (d, $J_{\text{PC}} = 13.09$), 120.39 (d, $J = 2.3$), 126.71 (s), 134.01 (d, $J = 36.3$), 135.02 (d, $J = 3.9$), 167.60 (d, $^2J_{\text{PC}} = 13.3$, $\text{C}1$). $^{31}\text{P}\{^1\text{H}\}$ NMR (202.4 MHz, 20 °C, C_6D_6): 201.52 (s, 1P).

[[PhOP(*i*-Pr) $_2$] $\{\kappa^{\text{O}},\kappa^{\text{N}}$ -ON(Bn) $_2$ }]NiBr] (5c). A 50 mL Schlenk flask containing 5 mL of CH_2Cl_2 was charged with the parent dimer [$\{\kappa^{\text{P}},\kappa^{\text{C}}\text{-(i-Pr)}_2\text{PO-C}_6\text{H}_4\}$ Ni(μ -Br)] $_2$ (**1**, 100 mg, 0.144 mmol, 1.00 equiv) and *N,N*-dibenzylhydroxylamine (61 mg, 0.287 mmol, 2.00 equiv). The solution was stirred overnight at room temperature and under inert atmosphere. Removal of volatiles under vacuum left a sticky, red residue, which was treated with ca. 1 mL of Et_2O , filtered and the filtrate kept at -35 °C overnight. Dark red crystals were separated and washed with cold hexane. (Yield: 77 mg, 0.138 mmol 55 %). ^1H NMR (400 MHz, 20 °C, C_6D_6): δ 1.02 (dd, 6H, CHCH_3 , $^3J_{\text{HH}} = 7.1$, $^3J_{\text{HP}} = 14.6$), 1.19 (dd, 6H, CHCH_3 , $^3J_{\text{HH}} = 17.1$, $^3J_{\text{HP}} = 7.1$), 2.00 (psoct, 2H, PCH , $^3J_{\text{HH}} = 7.1$), 3.43 (dd, 2H, NCH_2 , $^2J_{\text{HH}} = 13.2$, $^4J_{\text{HP}} = 6.3$), 4.07 (dd, 2H, NCH_2 , $^2J_{\text{HH}} = 13.0$, $^4J_{\text{HP}} = 1.9$), 6.90 (t, 1H, $p\text{-C}_{\text{Ar}}\text{H}$, $^3J_{\text{HH}} = 7.3$), 7.20-7.10 (m, 8H, $\text{C}_{\text{Ar}}\text{-H}$), 7.42 (d, 2H, $o\text{-C}_{\text{Ar}}\text{H}$, $^3J_{\text{HH}} = 8.4$), 7.47 (d, 4H, $o\text{-C}_{\text{Ar}}\text{H}$, $^3J_{\text{HH}} = 7.0$). $^{13}\text{C}\{^1\text{H}\}$ NMR (125.72 MHz, 20 °C, C_6D_6): δ 16.78 (s, 2C, CH_3), 17.62 (d, 2C, $^2J_{\text{PC}} = 5.5$, CH_3), 28.79 (s, C, PCH), 29.02 (s, C, PCH), 63.40 (s, 2C, NCH_2), 121.21 (d, 2C, $J = 4.9$, C_{Ar}), 123.67 (s, 1C, C_{Ar}), 128.54 (s, 4C, C_{Ar}), 128.68 (s, 2C, C_{Ar}), 129.52 (s, 2C, C_{Ar}), 132.41 (s, 4C, C_{Ar}), 132.92 (s, 2C, C_{Ar}), 156.34 (d, $^2J_{\text{PC}} = 3.7$, $\text{C}1$). $^{31}\text{P}\{^1\text{H}\}$ NMR (202.4 MHz, 20 °C, C_6D_6): δ 173.31 (s, 1P).

[[$\{\kappa^{\text{P}},\kappa^{\text{C}}\text{-(i-Pr)}_2\text{PO-(5-Cl-C}_6\text{H}_3\text{)}\}$ $\{\kappa^{\text{N}}\text{-NH}_2\text{OBn}\}$]Ni(Cl/Br)] (6a-Cl and 6a-Br). A 50 mL Schlenk flask containing 10 mL of CH_2Cl_2 was charged with *O*-benzylhydroxylamine hydrochloride (100 mg, 0.143 mmol, 1.0 equiv) and Et_3N (58 mg, 0.572 mmol, 4 equiv). The resulting mixture was stirred for 45 min under inert atmosphere at room temperature. To this mixture was added the dimer [$\{\kappa^{\text{P}},\kappa^{\text{C}}\text{-(i-Pr)}_2\text{PO-(5-Cl-C}_6\text{H}_3\text{)}\}$ Ni(μ -Br)] $_2$ (**2**, 91 mg, 0.119 mmol, 1 equiv) and was stirred overnight under same condition. Removal of volatiles under vacuum left a sticky, yellow residue, which was treated with ca. 1 mL of Et_2O , filtered and the filtrate kept at -35 °C overnight. Needle shaped yellow crystals were separated and washed with cold hexane. (Yield: 66 mg, 0.137 mmol, 49 %). ^1H and ^{13}C NMR data are provided for the bromo derivative only. ^1H NMR (400 MHz, 20 °C, C_6D_6): δ 1.12 (dd, 6H, CHCH_3 , $^3J_{\text{HH}} = 6.9$, $^3J_{\text{HP}} = 14.8$), 1.43 (dd, 6H, CHCH_3 , $^3J_{\text{HH}} = 7.1$, $^3J_{\text{HP}} = 17.8$), 2.17 (sept, 2H, $\text{CH}(\text{CH}_3)(\text{CH}_3)$, $^3J_{\text{HH}} = 7.0$), 4.94 (s, 2H, OCH_2), 5.19 (s, 2H, NH_2), 6.86 (d, 1H, $\text{C}3\text{-H}$, $^3J_{\text{HH}} = 7.7$), 6.9 (br s, 2H, $\text{C}_{\text{Ar}}\text{-H}$), 7.07-7.02 (m, 3H, $p\text{-}$ and $m\text{-C}_6\text{H}_5$), 7.12 (d, 1H, $o\text{-C}_6\text{H}_5$, $^3J_{\text{HH}} = 7.3$). $^{13}\text{C}\{^1\text{H}\}$ NMR (125.72 MHz, 20 °C, C_6D_6): δ 16.77 (s, CH_3), 17.99 (s, CH_3), 18.37 (s, CH_3), 28.22 (s, PCH), 28.47 (s, PCH), 78.38, 111.43 (d, $J_{\text{CP}} = 13.4$, C_{Ar}), 121.30 28.23 (s, C_{Ar}), 128.59 (s, C_{Ar}), 128.86 (s, C_{Ar}), 129.05 (s, C_{Ar}), 129.44 (s, C_{Ar}), 132.73 (s, C_{Ar}), 135.01 (s, C_{Ar}), 137.45 (s, C_{Ar}), 137.78 (br s, C_{Ar}). $^{31}\text{P}\{^1\text{H}\}$ NMR (202.4 MHz, 20 °C, C_6D_6): 195.59 (**6a-Cl**, 57%), 198.97 (**6a-Br**, 43%).

[[$\{\kappa^{\text{P}},\kappa^{\text{C}}\text{-(i-Pr)}_2\text{PO-(5-Cl-C}_6\text{H}_3\text{)}\}$ $\{\kappa^{\text{N}}\text{-(CH}_3\text{CH}_2\text{-)}(\text{CH}_3\text{CH=)}\text{N}\}$]Ni(Br)] (6b). A 50 mL Schlenk flask containing 10 mL MeCN was charged with the dimer [$\{\kappa^{\text{P}},\kappa^{\text{C}}\text{-(i-Pr)}_2\text{PO-(5-Cl-C}_6\text{H}_3\text{)}\}$ Ni(μ -Br)] $_2$ (**2**, 153 mg, 0.20 mmol, 1.00 equiv) and Et_2NOH (36 mg, 0.40 mmol, 2.00 equiv). The solution was stirred

overnight at room temperature and under inert atmosphere. Removal of volatiles under vacuum left a sticky, brown residue, which was treated with ca. 1 mL of Et₂O, filtered and the filtrate kept at -35 °C overnight. Brown crystals were separated and washed with cold hexane. (Yield: 49 mg, 0.11 mmol, 27 %). ¹H NMR (400 MHz, 20 °C, C₆D₆): δ 1.12 (dd, 3H, ³J_{HH} = 7.0, ³J_{HP} = 14, CHCH₃), 1.19 (dd, 3H, ³J_{HH} = 7.0, ³J_{HP} = 14, CHCH₃), 1.40 (t, 3H, ³J_{HH} = 7.4, NCH₂CH₃), 1.47 (dd, 3H, CHCH₃, ³J_{HH} = 7.2, ³J_{HP} = 17.0), 1.51 (dd, 3H, CHCH₃, ³J_{HH} = 7.2, ³J_{HP} = 17.0), 2.19 (d, 3H, NCHCH₃, ³J_{HH} = 5.1), 2.28 (psoct, 2H, CHCH₃, ³J_{HH} = 7.1), 3.14 (sext, 1H, NCH₂, ³J_{HH} = 6.9), 3.75 (sextd, 1H, NCH₂, ³J_{HH} = 7.5, ⁴J_{HP} = 1.5), 6.18 (dd, 1H, C3-H, ³J_{HH} = 8.1, ⁴J_{HP} = 0.7), 6.49-6.55 (m, 1H, NCH), 6.80 (ddd, 1H, C4-H, ³J_{HH} = 8.2, ⁴J_{HH} = 2.0, ⁶J_{HP} = 0.9), 6.92 (d, 1H, C6-H, ⁴J_{HH} = 2.1). ¹³C{¹H} NMR (125.72 MHz, 20 °C, C₆D₆): δ 15.72 (s, 1C, NCH₂CH₃), 16.80 (d, 1C, ²J_{PC} = 2.4, PCHCH₃), 17.00 (d, 1C, ²J_{PC} = 1.8, PCHCH₃), 18.56 (d, 1C, ²J_{PC} = 1.4, PCHCH₃), 18.60 (d, 1C, ²J_{PC} = 1.5, PCHCH₃), 23.47 (s, 1C, NCHCH₃), 28.62 (d, 1C, ¹J_{PC} = 12.4, PCH), 28.89 (d, 1C, ¹J_{PC} = 11.7, PCH), 56.43 (s, 1C, NCH₂), 111.45 (d, 1C, ²J_{PC} = 13.2, C₂), 121.00 (d, ¹J_{PC} = 2.2, C_{Ar}), 127.55 (s, C_{Ar}), 138.07 (d, 1C, ¹J_{PC} = 2.6, C_{Ar}), 166.34 (s, 1C, NCH). ³¹P{¹H} NMR (202.4 MHz, 20 °C, C₆D₆): δ 195.50 (s, 1P).

[{κ^P,κ^C-(i-Pr)₂PO-(5-Cl-C₆H₃)}{κ^N-(PhCH₂)-(PhCH=N)Ni(Br)}] (6c). A 50 mL Schlenk flask containing 10 mL MeCN was charged with dimer [^{κ^P,κ^C-(i-Pr)₂PO-(5-Cl-C₆H₃)}Ni(μ-Br)]₂ (153 mg, 0.20 mmol, 1.00 equiv) and Bn₂NOH (85 mg, 0.40 mmol, 2.00 equiv). The solution was stirred overnight at room temperature and under inert atmosphere. Removal of volatiles under vacuum left a sticky, yellow residue, which was treated with ca. 1 mL of Et₂O, filtered and the filtrate kept at -35 °C overnight. Yellow crystals were separated and washed with cold hexane. (Yield: 133 mg, 0.27 mmol, 57 %). ¹H NMR (400 MHz, 20 °C, C₆D₆): δ 1.20 (dd, 3H, ³J_{HH} = 7.0, ³J_{HP} = 14.4, CHCH₃), 1.24 (dd, 3H, ³J_{HH} = 7.0, ³J_{HP} = 15.2, CHCH₃), 1.50 (dd, 3H, CHCH₃, ³J_{HH} = 7.2, ³J_{HP} = 17.0), 1.62 (dd, 3H, CHCH₃, ³J_{HH} = 7.2, ³J_{HP} = 17.5), 2.24 (psoct, 1H, CHCH₃, ³J_{HH} = ³J_{HP} = 7.0), 2.45 (psoct, 1H, CHCH₃, ³J_{HH} = ³J_{HP} = 7.0), 5.30 (dd, 1H, NCH₂, ²J_{HH} = 15.6, ⁴J_{HP} = 1.5), 5.75 (d, 1H, NCH₂, ²J_{HH} = 15.7), 6.37 (dd, 1H, C3-H, ³J_{HH} = 8.2, ⁴J_{HP} = 0.8), 6.60 (ddd, 1H, C4-H, ³J_{HH} = 8.2, ⁴J_{HH} = 2.1, ⁶J_{HP} = 0.9), 6.61 (d, 1H, C6-H, ⁴J_{HH} = 2.1), 7.10-7.1 (m, 6H, (*p*- and *m*-Ph)₂), 7.21-7.24 (m, 2H, Ph), 7.80 (d, 1H, NCH, ⁴J_{HP} = 8.7), 8.82 (d, 2H, CH-ortho-Ph, ³J_{HH} = 7.1). ¹³C{¹H} NMR (125.72 MHz, 20 °C, C₆D₆): δ 16.79 (d, 1C, ²J_{CP} = 2.5, PCHCH₃), 17.12 (s, 1C, PCHCH₃), 18.42 (d, 1C, ²J_{CP} = 3.3, PCHCH₃), 18.94 (d, 1C, ²J_{CP} = 3.0, PCHCH₃), 28.55 (d, 1C, ¹J_{CP} = 20.6, PCH), 28.82 (d, 1C, ¹J_{CP} = 23.2, PCH), 63.46 (s, 1C, NCH₂), 111.42 (d, 1C, ²J_{PC} = 13.2, C₂), 121.44 (d, 1C, ¹J_{PC} = 2.0, C_{Ar}), 128.43 (s, 2C, Ph), 128.69 (s, 1C, Ph), 129.18 (s, 2C, Ph), 131.27 (s, 2C, Ph), 131.75 (s, 2C, Ph), 131.8 (s, 1C, Ph), 132.11 (s, 1C, Ph), 132.21 (s, 1C, C_{Ar} or Ph), 133.81 (d, 1C, ¹J_{PC} = 1.5, C_{Ar}), 134.73 (s, 1C, C_{Ar} or Ph), 137.75 (d, 1C, ¹J_{PC} = 2.5, C_{Ar}), 166.52 (s, 1C, NCH), 168.03 (d, ²J_{CP} = 14.1, 1C, C₁). ³¹P{¹H} NMR (202.4 MHz, 20 °C, C₆D₆): δ 196.32 (s, 1P).}

[{κ^P,κ^C-(i-Pr)₂PO-(5-OMe-C₆H₃)}{κ^N-NH₂OBN}Ni(Cl/Br)] (7a-Cl and 7a-Br): A 50 mL Schlenk flask containing 10 mL CH₂Cl₂ was charged with O-benzylhydroxylamine hydrochloride (55 mg, 0.344 mmol, 2.5 equiv) and Et₃N (35 mg, 0.344 mmol, 2.5 equiv). The resulting mixture was stirred for 45 min under inert atmosphere at room temperature. To this mixture was added the dimer [^{κ^P,κ^C-(i-Pr)₂PO-(5-OMe-C₆H₃)}Ni(μ-Br)]₂ (104 mg, 0.138 mmol, 1.0 equiv) and was stirred overnight under same condition. Removal of volatiles under vacuum left a sticky, brown residue, which was treated with ca. 1 mL of Et₂O, filtered and the filtrate kept at -35 °C overnight. Very fine brown crystals were separated and washed with cold hexane. (Yield: 52 mg, 0.11 mmol, 40%). ¹H and ¹³C NMR data are provided for the chloro derivative}

only. ^1H NMR (400 MHz, 20 °C, C_6D_6): δ 1.22 (dd, 6H, CHCH_3 , $^3J_{\text{HH}} = 7.0$, $^3J_{\text{HP}} = 14.5$), 1.52 (dd, 6H, CHCH_3 , $^3J_{\text{HH}} = 7.2$, $^3J_{\text{HP}} = 17.6$), 2.20-2.23 (m, 2H, CHCH_3), 3.35 (s, 3H, OCH_3), 5.16 (br s, 2H, OCH_2), 5.46 (br s, 2H, NH_2), 6.56 (dd, 1H, C3-H , $^3J_{\text{HH}} = 7.8$, $^4J_{\text{HP}} = 1.9$), 6.62 (br s, 1H, C6-H), 7.01-7.09 (m, 4H, $\text{C}_{\text{Ar}}\text{-H}$), 7.22 (d, 2H, $\text{O-C}_{\text{Ar}}\text{-H}$, $^3J_{\text{HH}} = 7.8$). $^{13}\text{C}\{^1\text{H}\}$ NMR (125.72 MHz, 20 °C, C_6D_6): δ 16.89 (s, CH_3), 18.12 (d, $^2J_{\text{PC}} = 2.7$, CH_3), 28.17 (s, P-CH), 28.43 (s, P-CH), 54.81 (s, OCH_3), 78.38 (s, CH_2), 97.84 (d, $^2J_{\text{PC}} = 14.2$, 1C, C6), 107.72 (d, $J_{\text{PC}} = 2.05$, 1C, C3), 128.59 (s, 1C, C_{Ar}), 128.79 (s, 2C, C_{Ar}), 128.88 (s, 1C, C_{Ar}), 129.51 (s, 2C, C_{Ar}), 135.40 (s, 1C, C_{Ar}), 160.74 (s, 1C, C_{Ar}). $^{31}\text{P}\{^1\text{H}\}$ NMR (202.4 MHz, 20 °C, C_6D_6): δ 193.59 (**7a-Cl**, 70%), 197.12 59 (**7a-Br**, 30%).

[$\{\kappa^{\text{P}},\kappa^{\text{C}}\text{-}(i\text{-Pr})_2\text{PO-(5-OMe-C}_6\text{H}_3)\}\{\kappa^{\text{N}}\text{-(CH}_3\text{CH}_2\text{)-(CH}_3\text{CH=)N}\}\text{Ni(Br)}$] (7b**).** A 50 mL Schlenk flask containing 10 mL MeCN was charged with the dimer [$\{\kappa^{\text{P}},\kappa^{\text{C}}\text{-}(i\text{-Pr})_2\text{PO-(5-OMe-C}_6\text{H}_3)\}\text{Ni}(\mu\text{-Br})$] $_2$ (**3**, 204 mg, 0.269 mmol, 1.00 equiv) and Et_2NOH (48 mg, 0.54 mmol, 2.00 equiv). The solution was stirred overnight at room temperature and under inert atmosphere. Removal of volatiles under vacuum left a sticky, brown residue, which was treated with ca. 1 mL of Et_2O , filtered and the filtrate kept at -35 °C overnight. Brown crystals were separated and washed with cold hexane. (Yield: 124 mg, 50 %). ^1H NMR (400 MHz, 20 °C, C_6D_6): δ 1.23 (dd, 3H, CHCH_3 , $^3J_{\text{HH}} = 7.0$, $^3J_{\text{HP}} = 14.6$), 1.29 (dd, 3H, CHCH_3 , $^3J_{\text{HH}} = 7.0$, $^3J_{\text{HP}} = 14.6$), 1.49 (t, 3H, CH_2CH_3 , $^3J_{\text{HH}} = 7.4$), 1.56 (dd, 3H, CHCH_3 , $^3J_{\text{HH}} = 7.2$, $^3J_{\text{HP}} = 15.4$), 1.60 (dd, 3H, CHCH_3 , $^3J_{\text{HH}} = 7.2$, $^3J_{\text{HP}} = 15.4$), 2.31 (d, 3H, NCHCH_3 , $^3J_{\text{HH}} = 4.9$), 2.33-2.43 (m, 2H, PCHCH_3), 3.23-3.30 (m, 1H, NCH_2), 3.35 (s, 3H, OCH_3), 3.80-3.90 (m, 1H, NCH_2), 6.28 (dd, 1H, $\text{C3}_{\text{Ar}}\text{-H}$, $^3J_{\text{HH}} = 8.4$, $^4J_{\text{HP}} = 0.8$), 6.5 (ddd, 1H, $\text{C4}_{\text{Ar}}\text{-H}$, $^3J_{\text{HH}} = 8.4$, $^3J_{\text{HP}} = 2.6$, $^3J_{\text{HH}} = 0.9$), 6.61 (d, 1H, $\text{C6}_{\text{Ar}}\text{-H}$, $^4J_{\text{HP}} = 2.2 \approx ^4J_{\text{HH}} = 2.2$), 6.63-6.67 (m, 1H, NCH). $^{13}\text{C}\{^1\text{H}\}$ NMR (125.72 MHz, 20 °C, C_6D_6): δ 15.83 (s, 1C, NCH_2CH_3), 16.95 (d, 1C, $^2J_{\text{PC}} = 1.8$, PCHCH_3), 17.14 (d, 1C, $^2J_{\text{PC}} = 1.2$, PCHCH_3), 18.71 (d, 1C, $^2J_{\text{PC}} = 1.5$, PCHCH_3), 18.74 (d, 1C, $^2J_{\text{PC}} = 1.8$, PCHCH_3), 23.61 (s, 1C, NCHCH_3), 28.56 (d, 1C, $^1J_{\text{PC}} = 12.7$, PCH), 28.83 (d, 1C, $^1J_{\text{PC}} = 12.0$, PCH), 54.80 (s, 1C, OCH_3), 56.56 (s, 1C, NCH_2), 97.55 (d, 1C, $^3J_{\text{PC}} = 13.9$, C6), 107.68 (d, 1C, $^4J_{\text{PC}} = 2.0$, C4), 122.79 (d, 1C, $J_{\text{PC}} = 33.6$, C_{Ar}), 137.47 (d, 1C, $^3J_{\text{PC}} = 2.7$, C3_{Ar}), 160.33 (s, 1C, C_{Ar}), 165.95 (s, 1C, NCH), 168.55 (d, 1C, $J_{\text{PC}} = 14.9$, C1). $^{31}\text{P}\{^1\text{H}\}$ NMR (202.4 MHz, 20 °C, C_6D_6): δ 193.84 (s, 1P).

[$\{\kappa^{\text{P}},\kappa^{\text{C}}\text{-}(i\text{-Pr})_2\text{PO-(5-OMe-C}_6\text{H}_3)\}\{\kappa^{\text{N}}\text{-(PhCH}_2\text{)-(PhCH=)N}\}\text{Ni(Br)}$] (7c**).** A 50 mL Schlenk flask containing 10 mL MeCN was charged with the dimer [$\{\kappa^{\text{P}},\kappa^{\text{C}}\text{-}(i\text{-Pr})_2\text{PO-(5-OMe-C}_6\text{H}_3)\}\text{Ni}(\mu\text{-Br})$] $_2$ (**3**, 200 mg, 0.265 mmol, 1.00 equiv) and Bn_2NOH (113 mg, 0.529 mmol, 2.00 equiv). The solution was stirred overnight at room temperature and under inert atmosphere. Removal of volatiles under vacuum left a sticky, yellow residue, which was treated with ca. 1 mL of Et_2O , filtered and the filtrate kept at -35 °C overnight. Yellow crystals were separated and washed with cold hexane. (Yield: 144 mg, 0.25 mmol, 46 %). ^1H NMR (400 MHz, 20 °C, C_6D_6): δ 1.30 (dd, 3H, CHCH_3 , $^3J_{\text{HH}} = 7.0$, $^3J_{\text{HP}} = 14.3$), 1.34 (dd, 3H, CHCH_3 , $^3J_{\text{HH}} = 7.0$, $^3J_{\text{HP}} = 14.9$), 1.58 (dd, 3H, CHCH_3 , $^3J_{\text{HH}} = 7.2$, $^3J_{\text{HP}} = 16.9$), 1.71 (dd, 3H, CHCH_3 , $^3J_{\text{HH}} = 7.2$, $^3J_{\text{HP}} = 17.3$), 2.34 (psoct, 1H, PCH , $^3J_{\text{HH}} = 7.2$), 2.53 (oct, 1H, PCH , $^3J_{\text{HH}} = 6.9$), 3.27 (s, 3H, OCH_3), 5.41 (d, 1H, NCH_2 , $^2J_{\text{HH}} = 15.8$), 5.93 (d, 1H, NCH_2 , $^2J_{\text{HH}} = 15.8$), 6.30 (dd, 1H, $\text{C3}_{\text{Ar}}\text{-H}$, $^3J_{\text{HH}} = 8.4$, $^4J_{\text{HP}} = 2.0$), 6.48 (d, 1H, $\text{C4}_{\text{Ar}}\text{-H}$, $^3J_{\text{HH}} = 8.4$), 6.61 (d, 1H, $\text{C6}_{\text{Ar}}\text{-H}$, $^4J_{\text{HP}} = 2.5 \approx ^4J_{\text{HH}} = 2.5$), 7.10-7.13 (m, 6H, (p - and m -Ph) $_2$), 7.28 (d, 2H, o -Ph, $J_{\text{HH}} = 8.0$), 7.86 (d, 1H, NCH , $^4J_{\text{HP}} = 8.6$), 8.93 (d, 2H, o -Ph, $^3J_{\text{HH}} = 8.1$). $^{13}\text{C}\{^1\text{H}\}$ NMR (125.72 MHz, 20 °C, C_6D_6): δ 16.92 (d, 1C, $^2J_{\text{CP}} = 2.5$, PCHCH_3), 17.24 (s, 1C, PCHCH_3), 18.55 (d, 1C, $^2J_{\text{CP}} = 3.5$, PCHCH_3), 19.07 (d, 1C, $^2J_{\text{CP}} = 3.2$, PCHCH_3), 28.50 (d, 1C, $J_{\text{CP}} = 17.2$, PCH), 28.77 (d, 1C, $J_{\text{CP}} = 19.8$, PCH), 54.72 (s, 1C, OCH_3), 63.37 (s, 1C, NCH_2), 96.81 (d, 1C, $^3J_{\text{PC}} = 13.8$, C6), 107.87 (d, 1C, $^3J_{\text{PC}} = 1.2$, C3), 122.77 (d, 1C, $J_{\text{PC}} = 33.2$, C_{Ar}), 128.39 (s, 2C, Ph), 128.59 (s, 1C, Ph), 129.17 (s, 2C, Ph), 131.36 (s, 2C, Ph), 131.88 (s, 2C, C_{Ar}), 131.93 (s, 1C, C_{Ar}), 137.05 (d, 1C, $J_{\text{PC}} = 2.7$, C4_{Ar}), 160.31 (s, 1C,

C_{Ar}), 166.12 (s, 1C, NCH), 168.38 (d, 1C, $J_{PC} = 14.4$, C_{Ar}). $^{31}P\{^1H\}$ NMR (202.4 MHz, 20 °C, C_6D_6): δ 194.94 (s, 1P).

$\{[\kappa^P, \kappa^C-(i-Pr)_2PO-(5-OMe-C_6H_4)\{\kappa^N-Et_2NH\}NiBr] (7d)$. A 50 mL Schlenk flask containing 10 mL toluene was charged with the dimer $[\{\kappa^P, \kappa^C-(i-Pr)_2PO-(OMe-C_6H_3)Ni(\mu-Br)\}_2]$ (**1**, 100 mg, 0.132 mmol, 1 equiv) and Et_2NH (0.019 mg, 0.264 mmol, 2 equiv). The solution was stirred overnight at room temperature and under inert atmosphere. Removal of volatiles under vacuum left a sticky, brown residue, which was treated with ca. 1 mL of Et_2O , filtered and the filtrate kept at -35 °C overnight. Brown crystals were separated and washed with cold hexane. (Yield: 53 mg, 44 %). 1H NMR (400 MHz, 20 °C, C_6D_6): δ 1.22 (dd, 6H, $CHCH_3$, $^3J_{HP} = 14.5$, $^3J_{HH} = 7.0$), 1.43(t, 6H, CH_2CH_3 , $^3J_{HH} = 6.7$), 1.54 (dd, 6H, $CHCH_3$, $^3J_{HP} = 17.0$, $^3J_{HH} = 7.2$), 2.13 (br s, 3H, overlap of NCH_2 and NH), 2.34 (psoct, 2H, PCH), 3.22 (br s, CH_2), 3.36 (s, OCH_3), 6.38 (d, 1H, $C3_{Ar}-H$, $^3J_{HH} = 7.7$), 6.55 (d, 1H, $C4_{Ar}-H$, $^3J_{HH} = 8.0$), 6.60 (d, 1H, $C6_{Ar}-H$, $^3J_{HH} = 2.5$). $^{13}C\{^1H\}$ NMR (125.72 MHz, 20 °C, C_6D_6): δ 15.30 (s, 2C, NCH_2CH_3), 17.07 (d, 2C, $^2J_{PC} = 1.7$, $PCHCH_3$), 18.78 (d, 2C, $^2J_{PC} = 3.2$, $PCHCH_3$), 28.85 (s, 1C, PCH), 29.12 (s, 1C, PCH), 46.57 (d, 2C, $^2J_{PC} = 1.4$, NCH_2), 54.75 (s, 1C, OCH_3), 97.80 (d, 1C, $^3J_{PC} = 13.6$, $C6$), 107.52 (d, 1C, $^4J_{PC} = 2.1$, $C4$), 122.21 (d, 1C, $^2J_{PC} = 34.5$, $C2/1$), 134.60 (d, 1C, $^2J_{PC} = 3.1$, $C3$), 160.26 (d, 1C, $^2J_{PC} = 1.0$, C_{Ar}), 168.55 (d, 1C, $^2J_{PC} = 14.9$, $C1$). $^{31}P\{^1H\}$ NMR (202.4 MHz, 20 °C, C_6D_6): 192.64 (s, 1P).

$\{[\kappa^P, \kappa^C-(i-Pr)_2PO-(5-NMe_2-C_6H_3)\{\kappa^N-H_2NOBn\}Ni(Cl/Br)] (8a-Cl$ and **8a-Br). A 50 mL Schlenk flask containing 25 mL MeCN was charged with a solution of the proligand 3- $NMe_2-C_6H_4OP(i-Pr)_2$ (157 mg, 0.619 mmol, 1.00 equiv), $\{(i-PrCN)NiBr_2\}_n$ (214 mg, 0.744 mmol, 1.2 equiv), and Et_3N (75 mg, 0.744 mmol, 2 equiv). The mixture was stirred at room temperature overnight. In a separate 8 mL vial, *O*-benzylhydroxylamine hydrochloride (198 mg, 1.239 mmol, 2 equiv) and Et_3N (125 mg, 1.239 mmol, 2 equiv) were dissolved in 5 mL of MeCN, stirred for 45 min and then added to the 50 mL flask. The resulting mixture was again stirred overnight at room temperature. Removal of volatiles under vacuum left a sticky, brown residue, which was treated with ca. 2 mL of Et_2O , filtered and the filtrate kept at -35 °C overnight. Brown crystals were separated and washed with cold hexane. (Yield: 164 mg, 0.349 mmol, 55 %). 1H and ^{13}C NMR data are provided for the chloro derivative only. 1H NMR (400 MHz, 20 °C, C_6D_6): δ 1.27 (dd, 6H, $CHCH_3$, $^3J_{HH} = 6.1$, $^3J_{HP} = 14.1$), 1.56 (dd, 6H, $CHCH_3$, $^3J_{HH} = 6.5$, $^3J_{HP} = 17.2$), 2.27 (br s, 2H, PCH), 2.55 (s, 6H, $N(CH_3)_2$), 5.25 (br s, 2H, OCH_2), 5.47 (br s, 2H, NH_2), 6.35 (broad s, 1H, $C3_{Ar}-H$), 6.45 (s, 1H, $C4_{Ar}-H$), 7.01-7.09 (m, 4H, p, m- $C_{Ar}-H$), 7.28 (d, 2H, o- $C_{Ar}-H$). $^{13}C\{^1H\}$ NMR (125.72 MHz, 20 °C, C_6D_6): δ 15.96 (d, $^2J_{CP} = 1.2$, CH_3), 17.20 (d, $^2J_{CP} = 2.7$, CH_3), 27.17 (s, P-CH), 27.43 (s, P-CH), 39.40 (s, N- CH_3), 77.38 (s, O- CH_2), 95.81 (s, 1C, $C4$), 106.09 (s, 1C, $C3$), 127.59 (s, 1C, C_{Ar}), 127.74 (s, 2C, C_{Ar}), 128.52 (s, 2C, C_{Ar}), 134.74 (s, 1C, C_{Ar}), 135.70 (s, 1C, C_{Ar}), 135.74 (s, 1C, C_{Ar}), 150.56 (s, 1C, C_{Ar}). $^{31}P\{^1H\}$ NMR (202.4 MHz, 20 °C, C_6D_6): 192.78 59 (**8a-Cl**, 77%), 196.11 59 (**8a-Br**, 23%).**

$\{[\kappa^P, \kappa^C-(i-Pr)_2PO-(5-NMe_2-C_6H_3)\{\kappa^N-(CH_3CH_2)-(CH_3CH=N)\}Ni(Br)] (8b)$. A 100 mL Schlenk flask containing 25 mL MeCN was charged with the proligand 3- $NMe_2-C_6H_4OP$ (375 mg, 1.48 mmol, 1.00 equiv), the nickel precursor $\{(i-PrCN)NiBr_2\}_n$ (511 mg, 1.78 mmol, 1.20 equiv), and Et_3N (248.30 μ L, 1.78 mmol, 1.20 equiv). The resulting mixture was stirred at room temperature overnight followed by reduction of volume to 5 mL under vacuum. Next, excess Et_2O was added to the mixture and placed in the fridge for 45 min to precipitate the impurities. After 45 min the solution was filtered through cotton. To the filtrate was added Et_2NOH (149.0 μ L, 1.48 mmol, 1.00 equiv) and stirred overnight at room temperature maintaining inert atmosphere. Removal of the volatiles under vacuum left a sticky, brown residue, which was treated with ca. 2 mL of Et_2O , filtered and the filtrate kept at -35 °C overnight. Brown crystals were

separated and washed with cold hexane. (Yield: 128 mg, 0.10 mmol, 18 %). ^1H NMR (400 MHz, 20 °C, C_6D_6): δ 1.27 (dd, 3H, CHCH_3 , $^3J_{\text{HH}} = 6.9$, $^3J_{\text{HP}} = 14.5$), 1.33 (dd, 3H, CHCH_3 , $^3J_{\text{HH}} = 6.9$, $^3J_{\text{HP}} = 14.7$), 1.53 (t, 3H, NCH_2CH_3 , $^3J_{\text{HH}} = 7.3$), 1.60 (dd, 3H, CHCH_3 , $^3J_{\text{HH}} = 7.3$, $^3J_{\text{HP}} = 15.8$), 1.64 (dd, 3H, CHCH_3 , $^3J_{\text{HH}} = 7.2$, $^3J_{\text{HP}} = 15.6$), 2.38 (d, 3H, NCHCH_3 , $^3J_{\text{HH}} = 4.5$), 2.41-2.49 (m, 2H, PCH), 2.55 (s, 6H, $\text{N}(\text{CH}_3)_2$), 3.34 (pssext, 1H, NCH_2 , $^3J_{\text{HH}} = 6.6$), 3.91 (pssext, 1H, NCH_2 , $^3J_{\text{HH}} = 7.0$), 6.26 (d, 1H, $\text{C}4_{\text{Ar}}\text{-H}$, $^3J_{\text{HH}} = 7.6$), 6.33 (d, 1H, $\text{C}3_{\text{Ar}}\text{-H}$, $^3J_{\text{HH}} = 8.3$), 6.45 (d, 1H, $\text{C}6_{\text{Ar}}\text{-H}$, $^4J_{\text{HH}} = 2.5 \approx ^4J_{\text{HP}} = 2.5$), 6.71 (br s, 1H, NCH). $^{13}\text{C}\{^1\text{H}\}$ NMR (125.72 MHz, 20 °C, C_6D_6): δ 15.90 (s, 1C, NCH_2CH_3), 17.03 (d, 1C, $^2J_{\text{PC}} = 2.0$, PCH CH_3), 17.22 (d, 1C, $^2J_{\text{PC}} = 1.1$, PCH CH_3), 18.81 (d, 1C, $^2J_{\text{PC}} = 3.6$, PCH CH_3), 23.66 (s, 1C, PCH CH_3), 28.55 (d, 1C, $^1J_{\text{PC}} = 12.5$, PCH), 28.81 (d, 1C, $^1J_{\text{PC}} = 11.6$, PCH), 40.53 (s, 2C, NCH_3), 56.67 (s, 1C, NCHCH_3), 65.91 (s, 1C, NCH_2), 96.92 (d, 1C, $^5J_{\text{PC}} = 14$, C_{Ar}), 106.82 (d, 1C, $^4J_{\text{PC}} = 2.0$, C_{Ar}), 118.39 (d, 1C, $J_{\text{PC}} = 34.8$, C_{Ar}), 137.50 (d, 1C, $J_{\text{PC}} = 2.6$, C_{Ar}), 151.21 (s, 1C, C_{Ar}), 165.66 (s, 1C, NCH), 169.16 (d, 1C, $J_{\text{PC}} = 15.0$, C1). $^{31}\text{P}\{^1\text{H}\}$ NMR (202.4 MHz, 20 °C, C_6D_6): δ 192.89 (s, 1P).

3. NMR spectra of new compounds

Ligand **3-NMe₂-C₆H₄OP(*i*-Pr)₂**

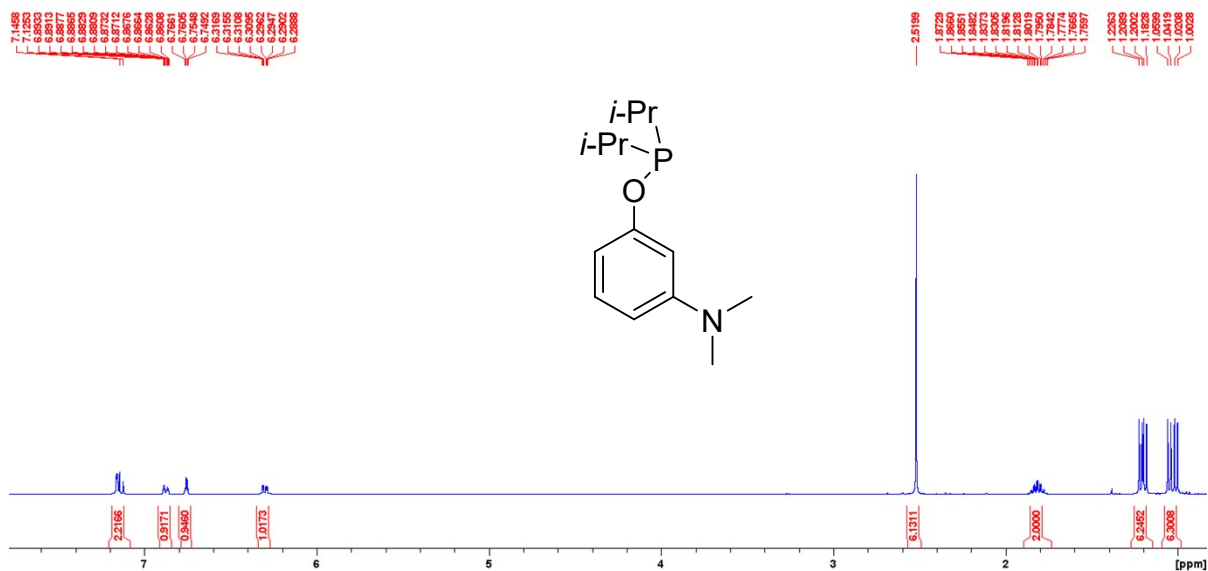


Figure S1. Full ¹H NMR spectrum of **3-NMe₂-C₆H₄OP(*i*-Pr)₂** in C₆D₆.

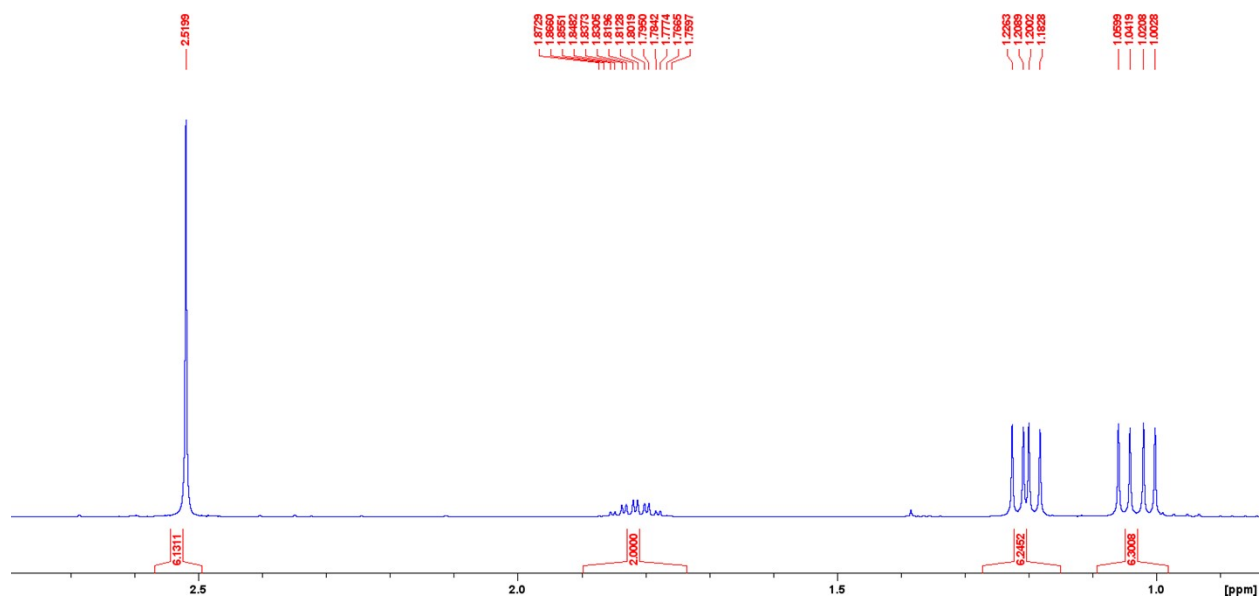


Figure S2. The aliphatic region of the ¹H NMR spectrum of **3-NMe₂-C₆H₄OP(*i*-Pr)₂** in C₆D₆.

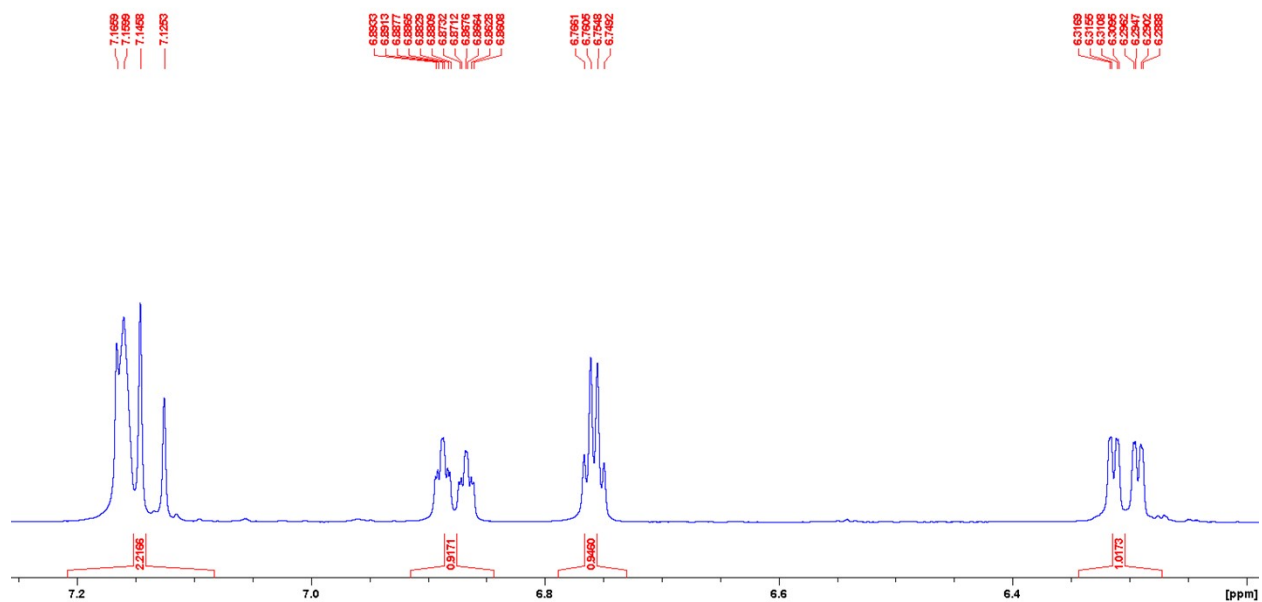


Figure S3. The aromatic region of the ^1H NMR spectrum of $3\text{-NMe}_2\text{-C}_6\text{H}_4\text{OP}(i\text{-Pr})_2$ in C_6D_6 .

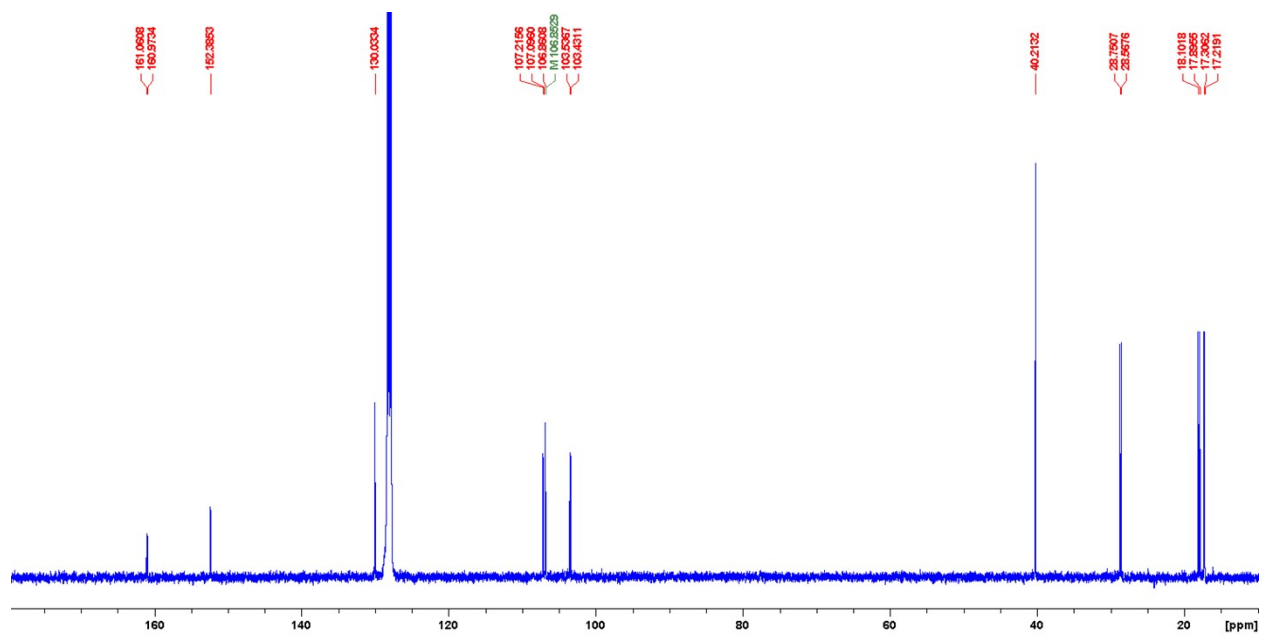


Figure S4. Full $^{13}\text{C}\{^1\text{H}\}$ NMR spectrum of $3\text{-NMe}_2\text{-C}_6\text{H}_4\text{OP}(i\text{-Pr})_2$ in C_6D_6 .

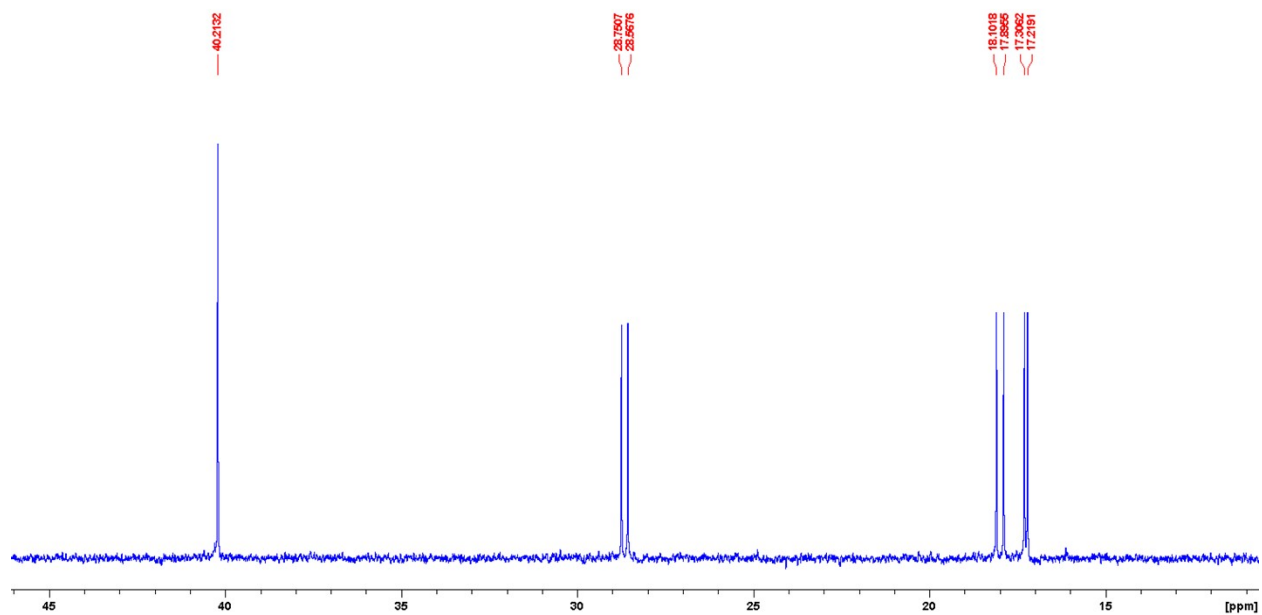


Figure S5. The aliphatic region of the $^{13}\text{C}\{^1\text{H}\}$ NMR spectrum of **3-NMe₂-C₆H₄OP(*i*-Pr)₂** in C₆D₆.

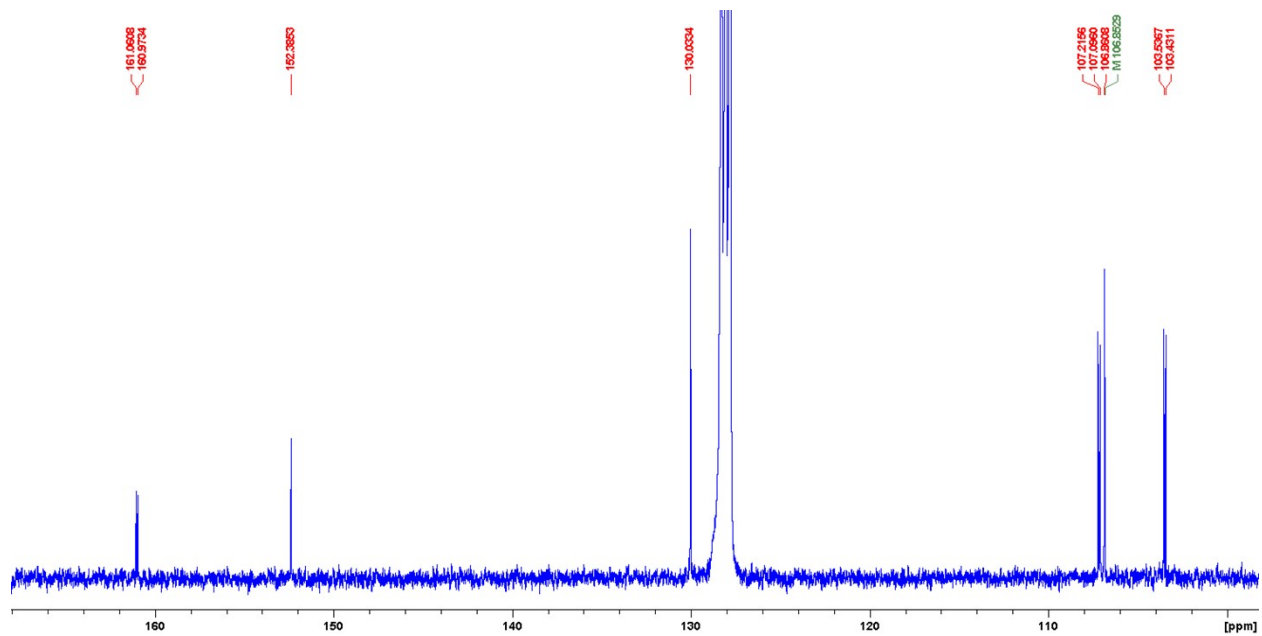


Figure S6. The aromatic region of the $^{13}\text{C}\{^1\text{H}\}$ NMR spectrum of **3-NMe₂-C₆H₄OP(*i*-Pr)₂** in C₆D₆.

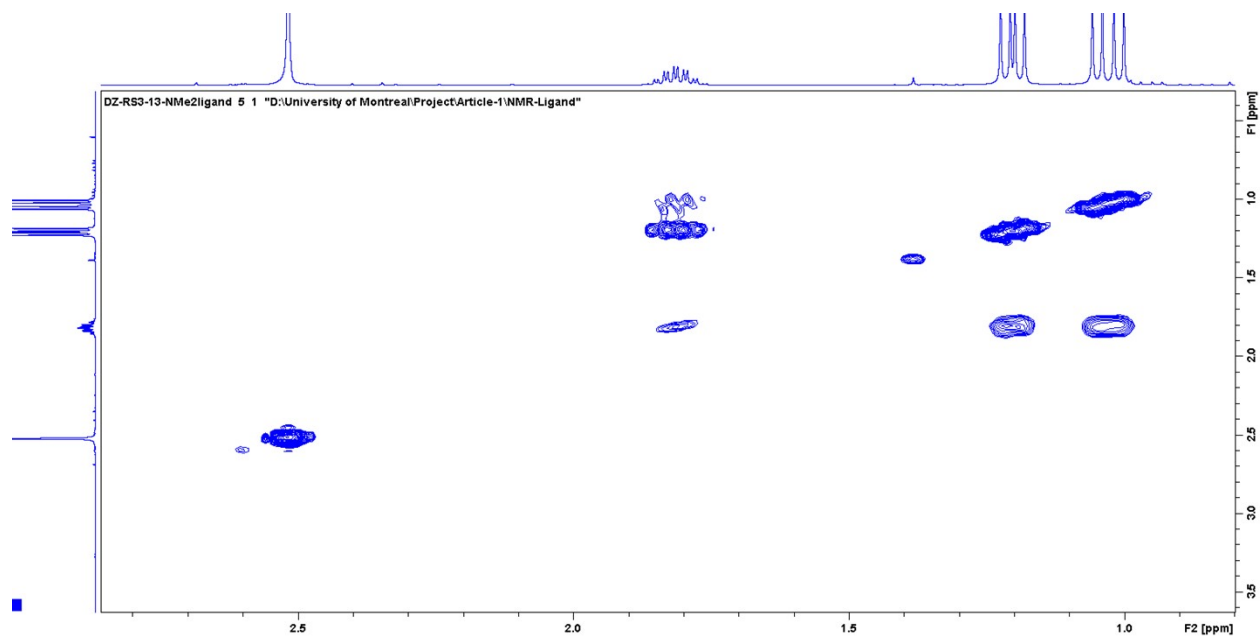


Figure S7. The aliphatic region of the COSY NMR spectrum of $3\text{-NMe}_2\text{-C}_6\text{H}_4\text{OP}(i\text{-Pr})_2$ in C_6D_6 .

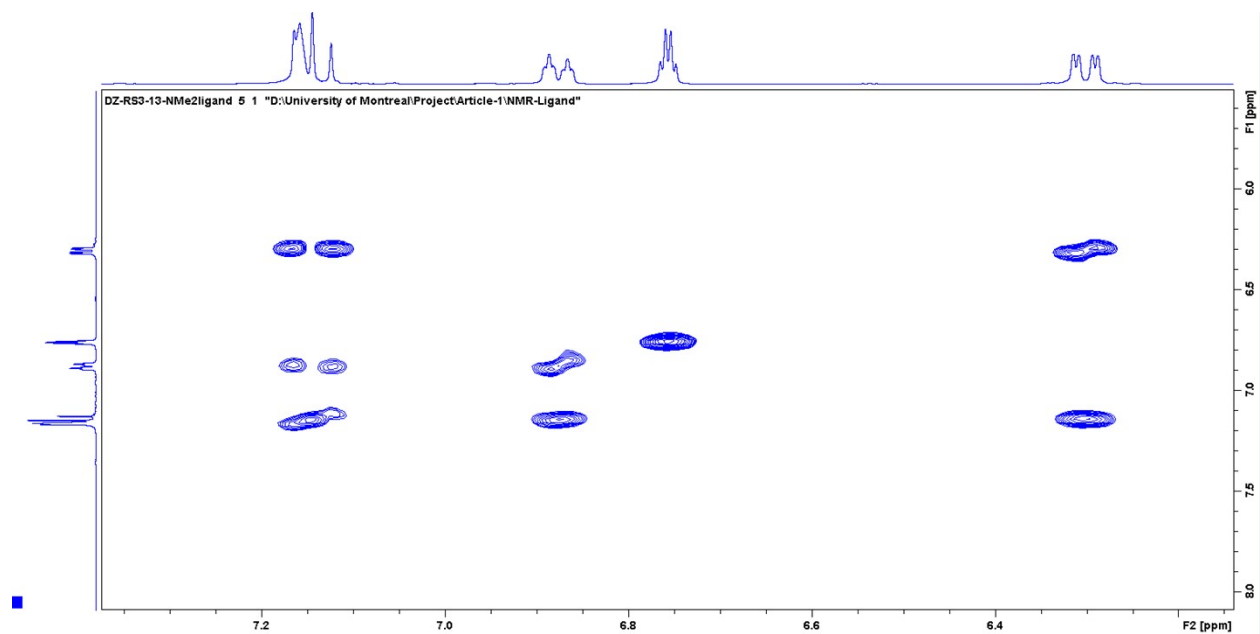


Figure S8. The aromatic region of the COSY NMR spectrum of $3\text{-NMe}_2\text{-C}_6\text{H}_4\text{OP}(i\text{-Pr})_2$ in C_6D_6 .

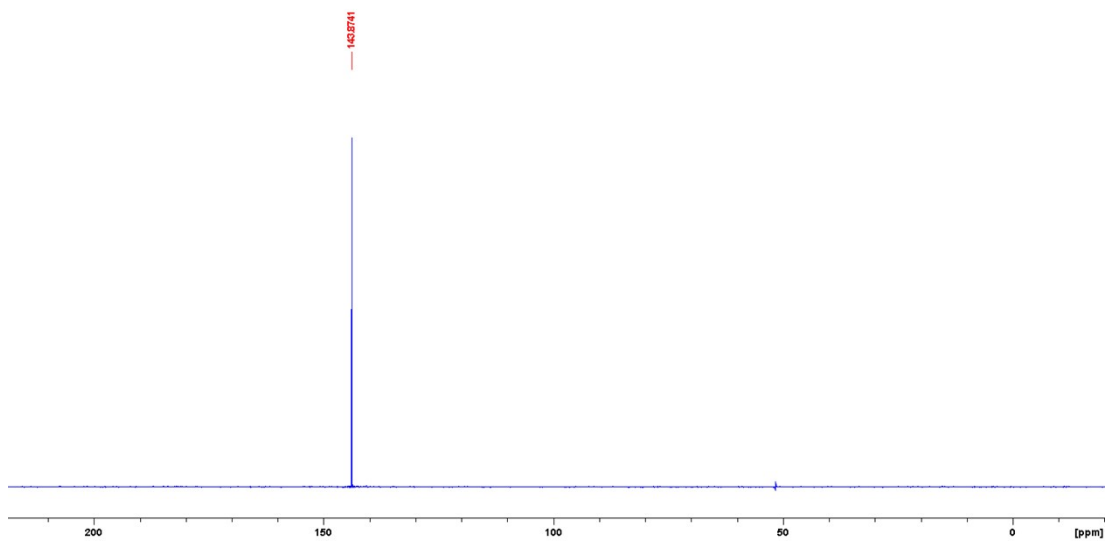


Figure S9. $^{31}\text{P}\{^1\text{H}\}$ NMR spectrum of $3\text{-NMe}_2\text{-C}_6\text{H}_4\text{OP}(i\text{-Pr})_2$ in C_6D_6 .

NMR spectra of Complex 4':

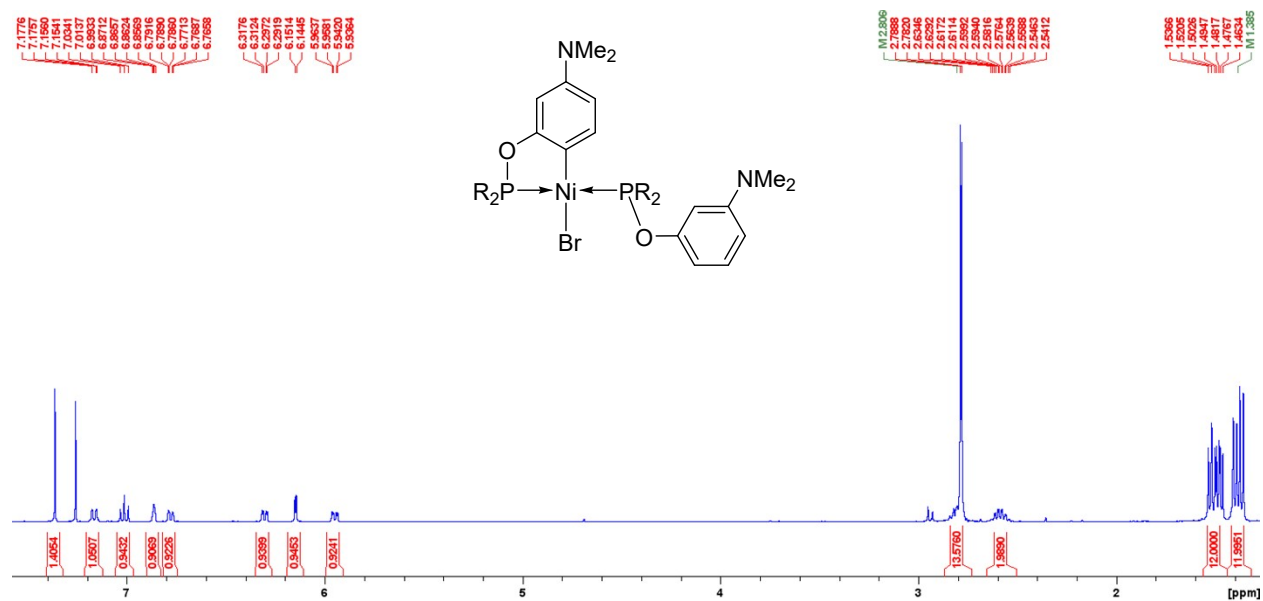


Figure S10. Full ^1H NMR spectrum of 4' in CDCl_3

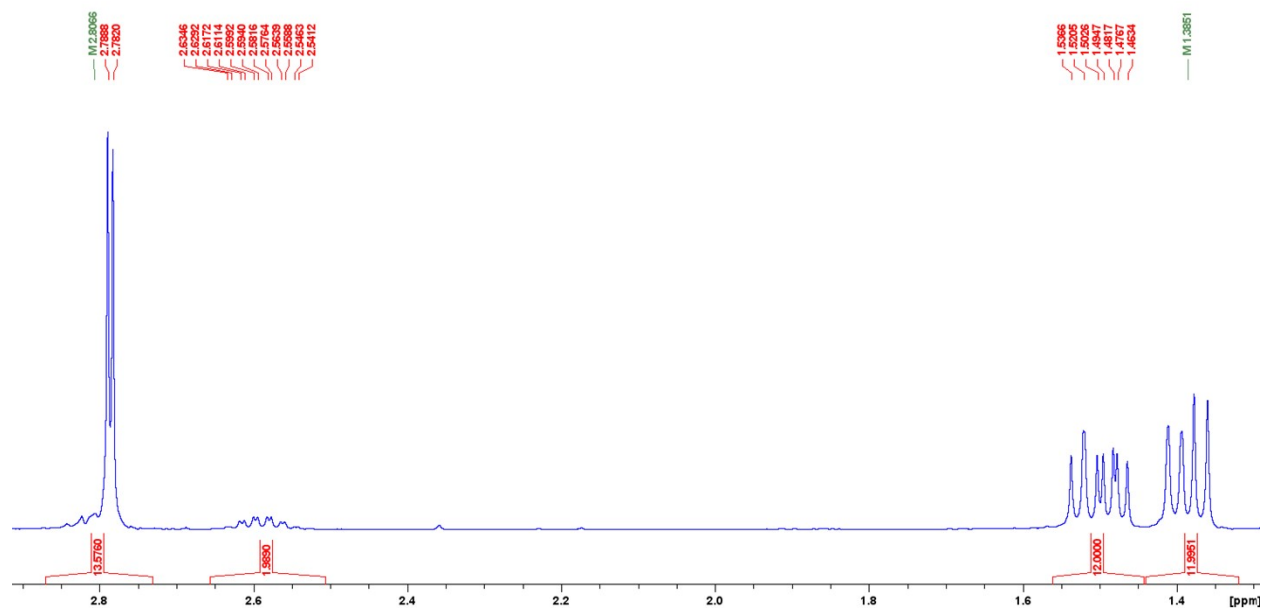


Figure S11. The aliphatic region of the ^1H NMR spectrum of 4' in CDCl_3 .

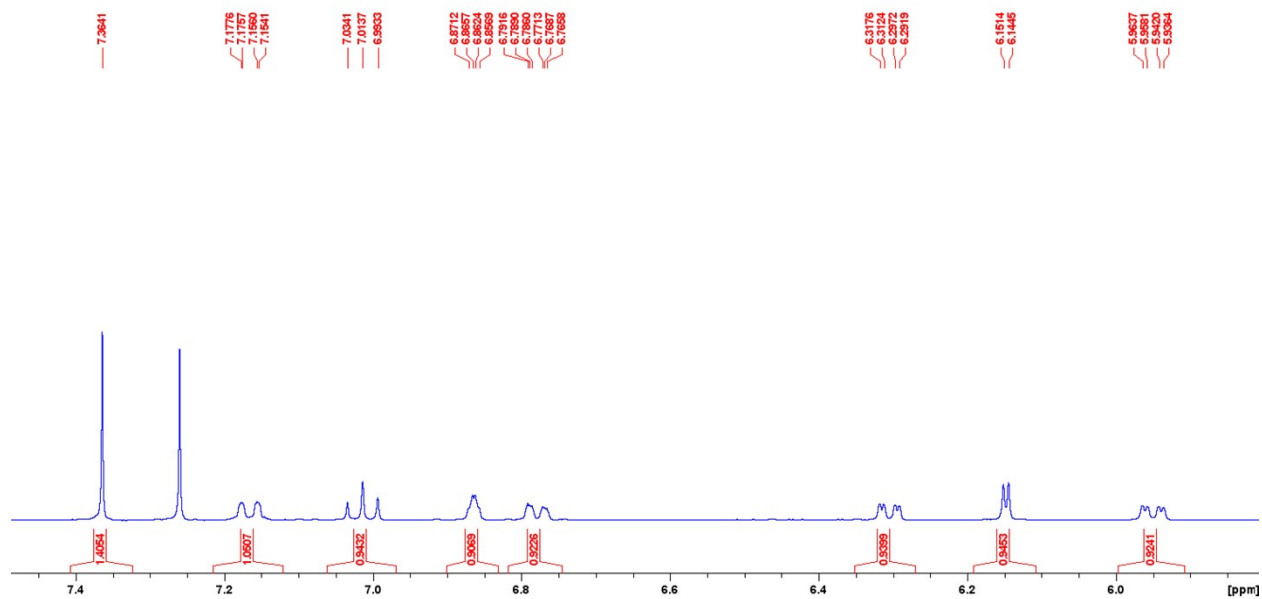


Figure S12. The aromatic region of the ^1H NMR spectrum of **4'** in CDCl_3 .

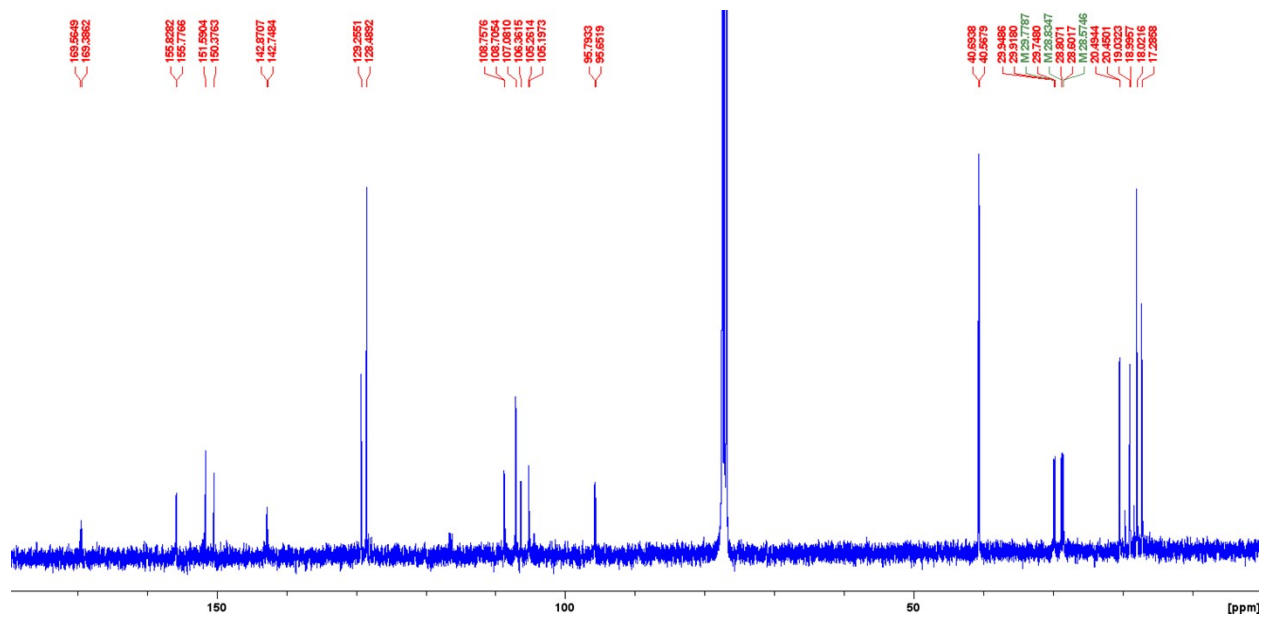


Figure S13. Full $^{13}\text{C}\{^1\text{H}\}$ NMR spectrum of **4'** in CDCl_3 .

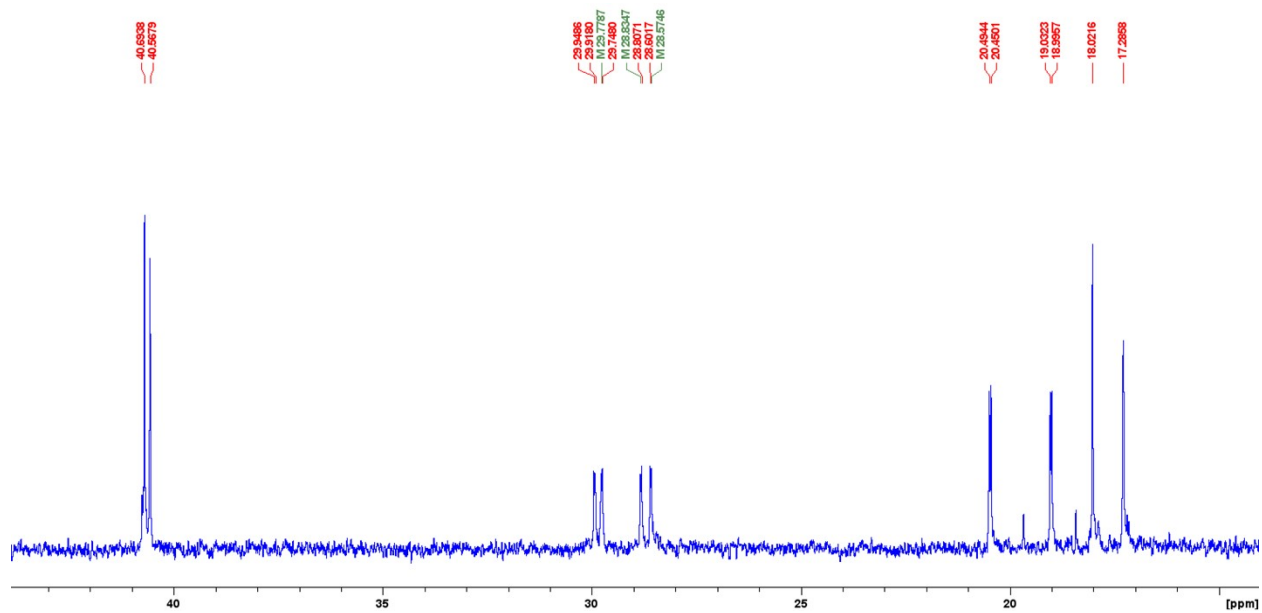


Figure S14. The aliphatic region of the $^{13}\text{C}\{^1\text{H}\}$ NMR spectrum of **4'** in CDCl_3 .

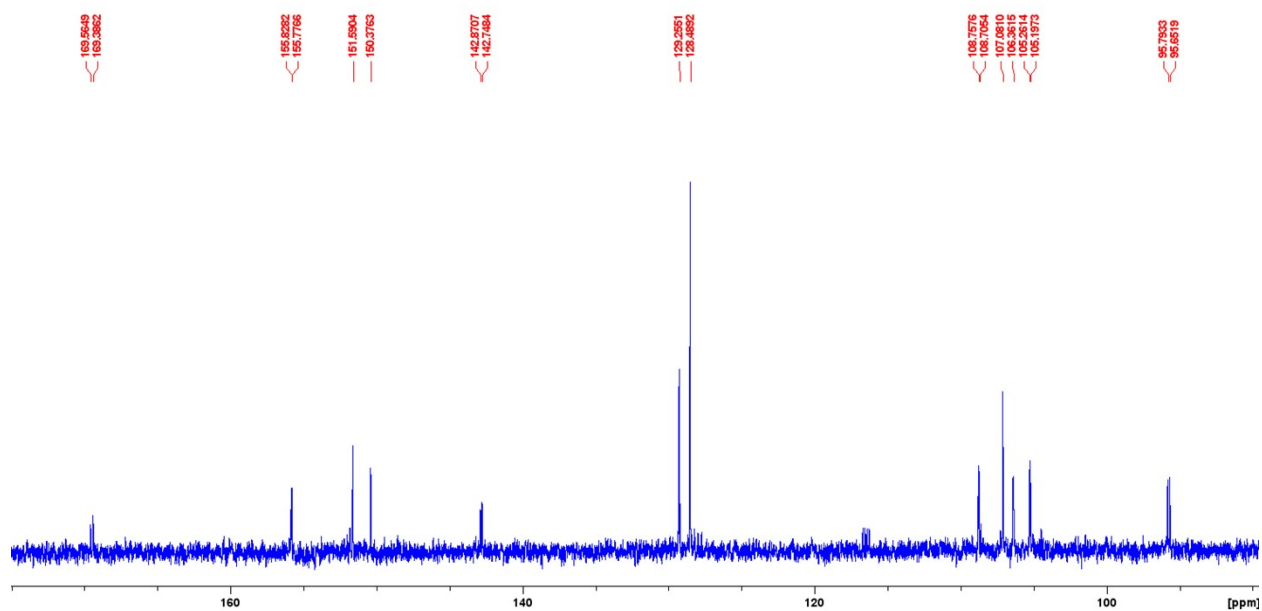


Figure S15. The aromatic region of the $^{13}\text{C}\{^1\text{H}\}$ NMR spectrum of **4'** in CDCl_3 .

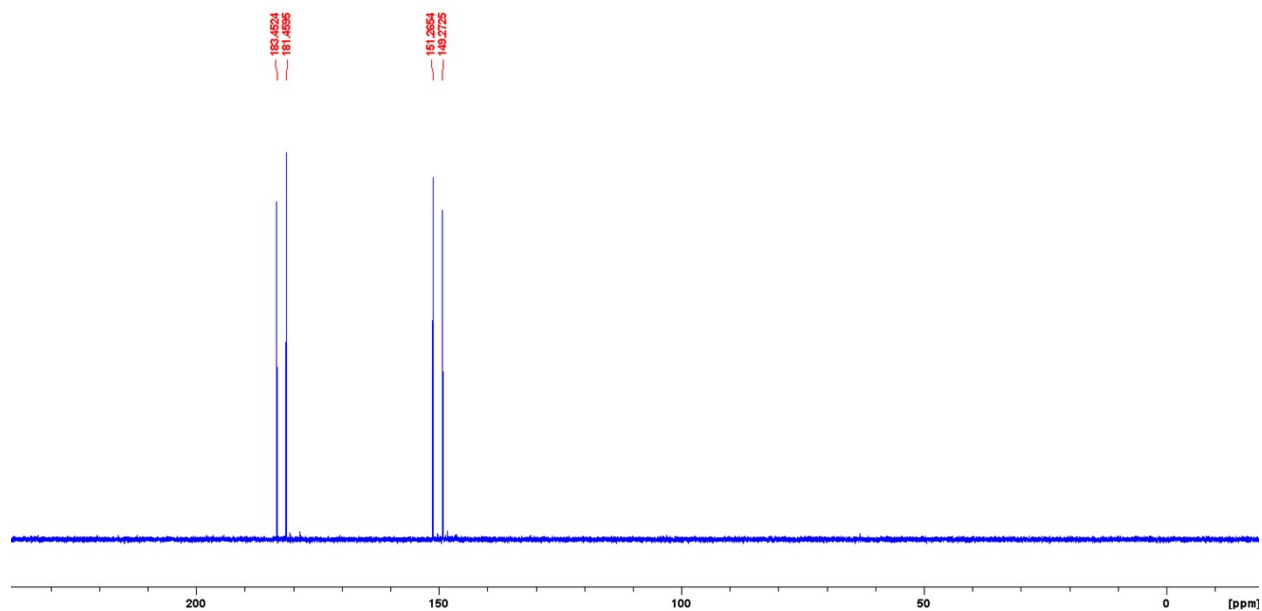


Figure S16. Full ^{31}P NMR spectrum of **4'** in CDCl_3 .

NMR spectra of complex **5a**

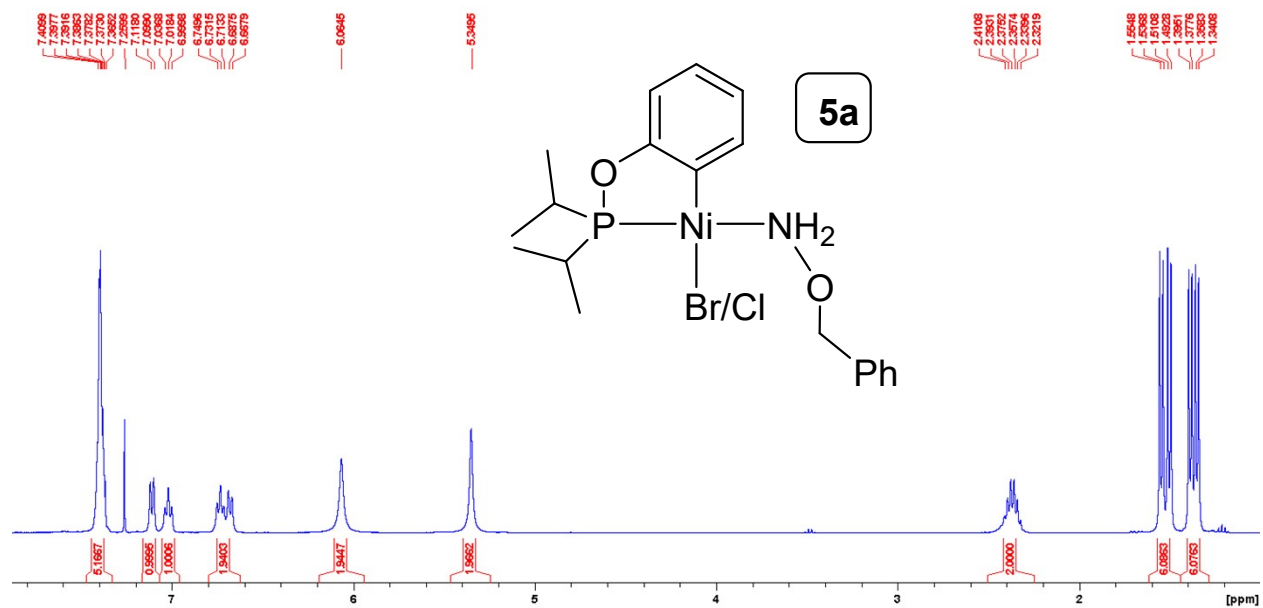


Figure S17. Full ^1H NMR spectrum of **5a** in CDCl_3 .

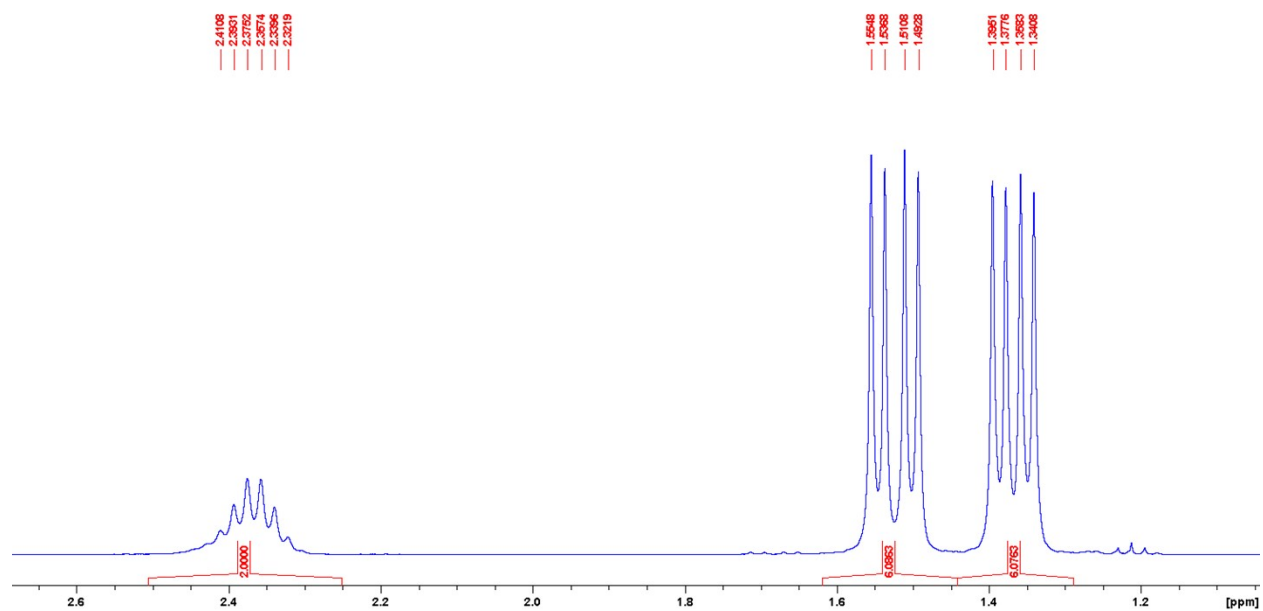


Figure S18. The aliphatic region of the ^1H NMR spectrum of **5a** in CDCl_3 .

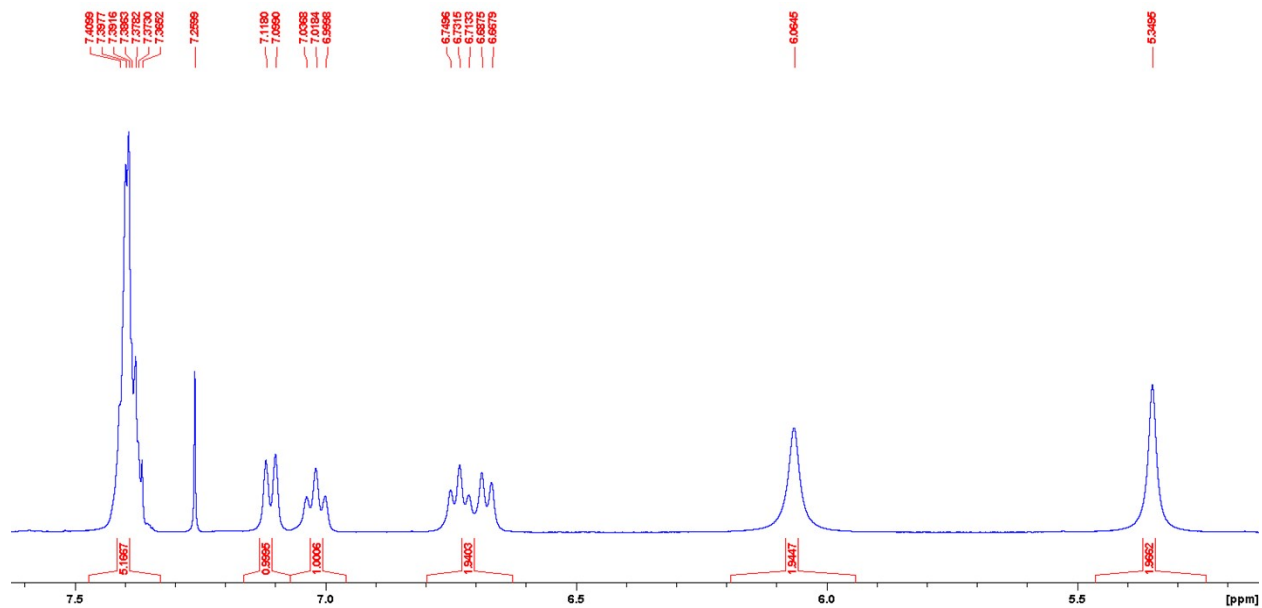


Figure S19. The aromatic region of the ^1H NMR spectrum of **5a** in CDCl_3 .

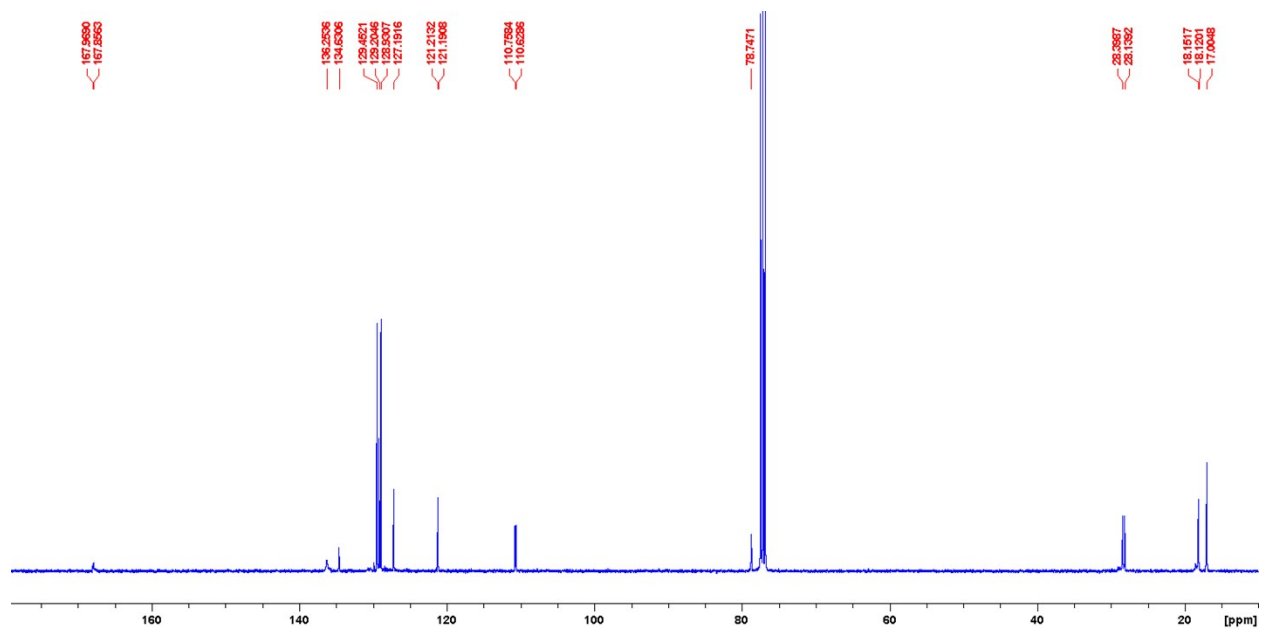


Figure S20. Full $^{13}\text{C}\{^1\text{H}\}$ NMR spectrum of **5a** in CDCl_3 .

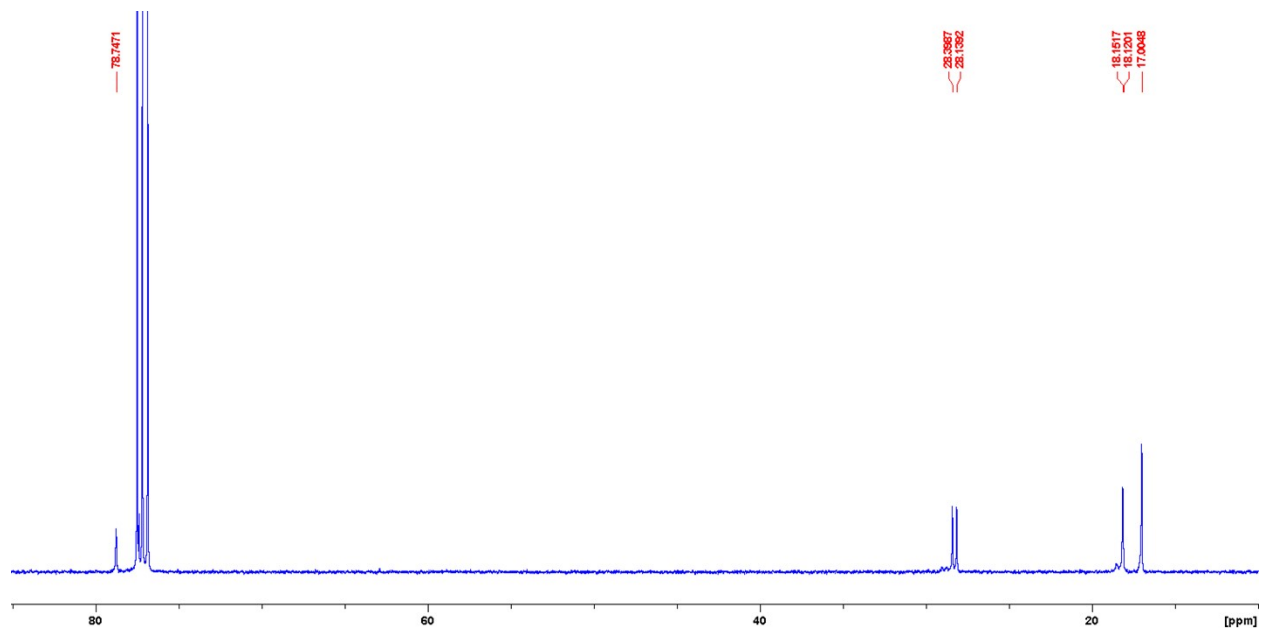


Figure S21. The aliphatic region of the $^{13}\text{C}\{^1\text{H}\}$ NMR spectrum of **5a** in CDCl_3 .

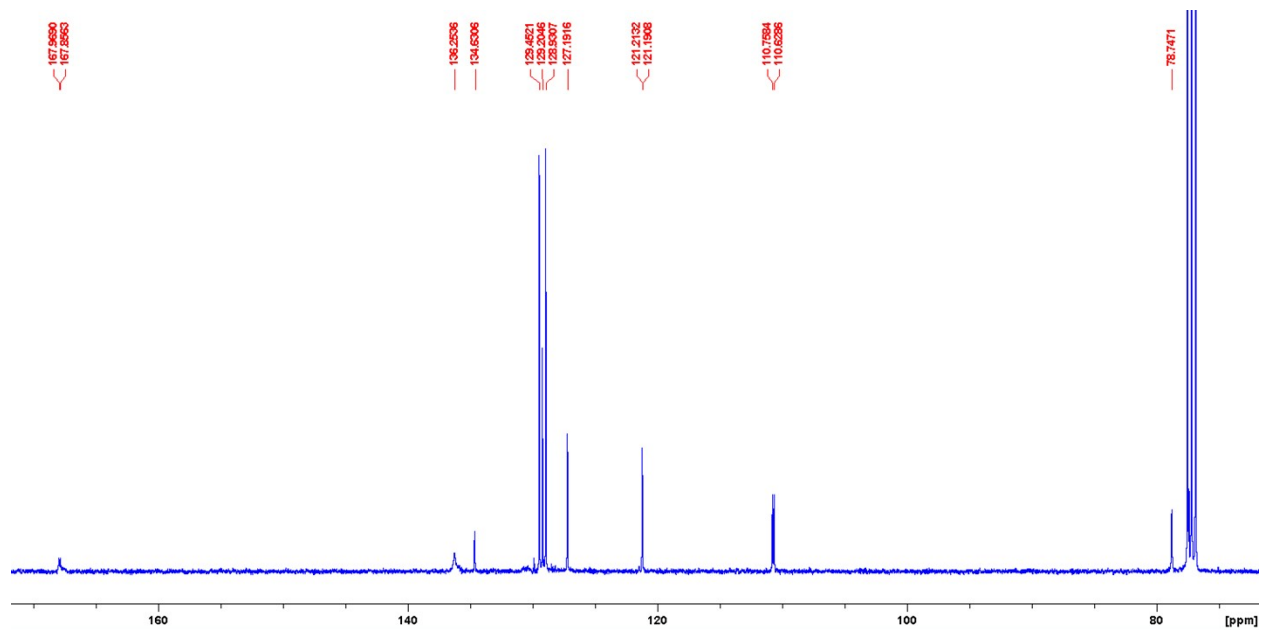


Figure S22. The aromatic region of the $^{13}\text{C}\{^1\text{H}\}$ NMR spectrum of **5a** in CDCl_3 .

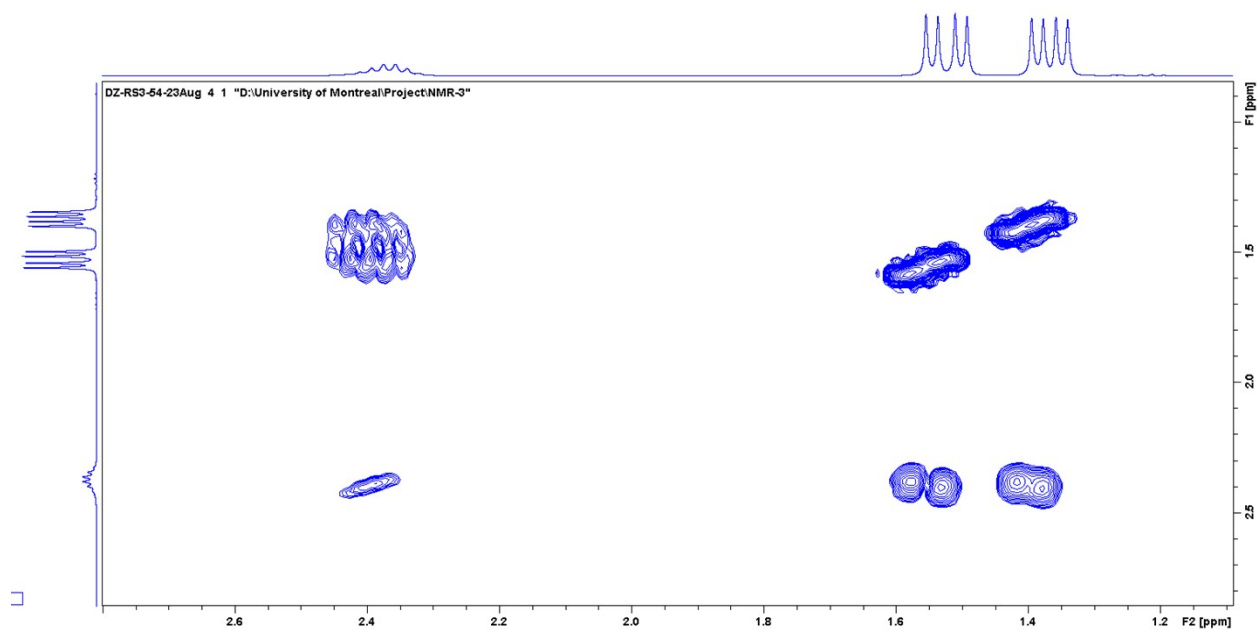


Figure S23. The aliphatic region of the COSY NMR spectrum of **5a** in CDCl_3 .

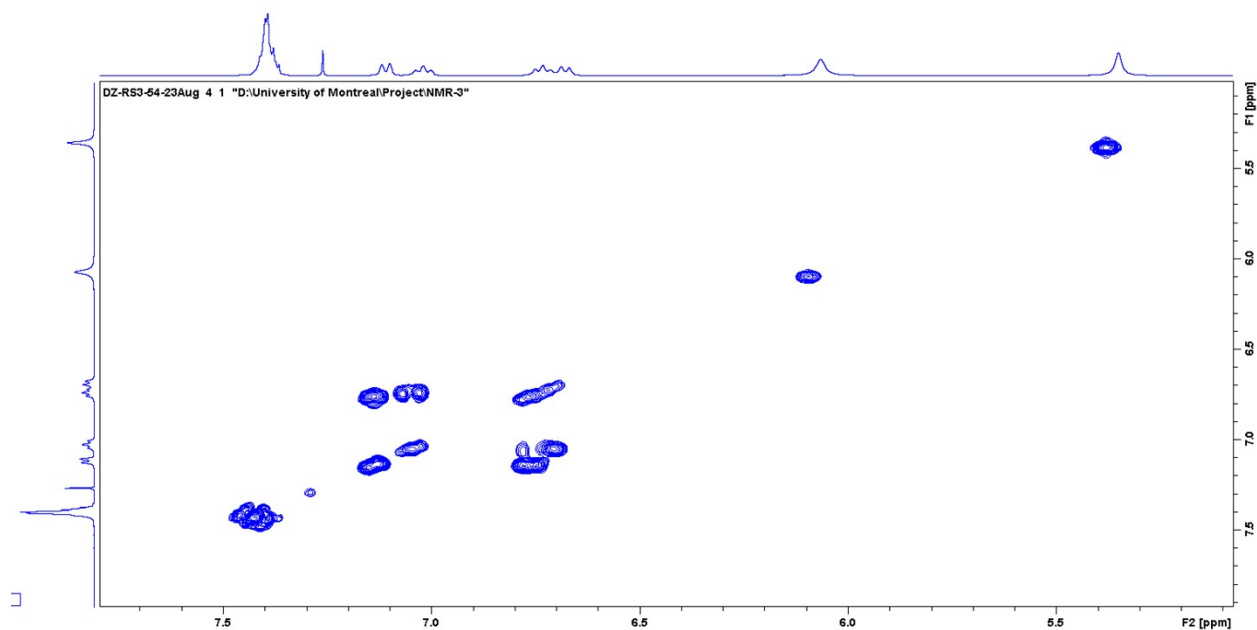


Figure S24. The aromatic region of the COSY NMR spectrum of **5a** in CDCl_3 .

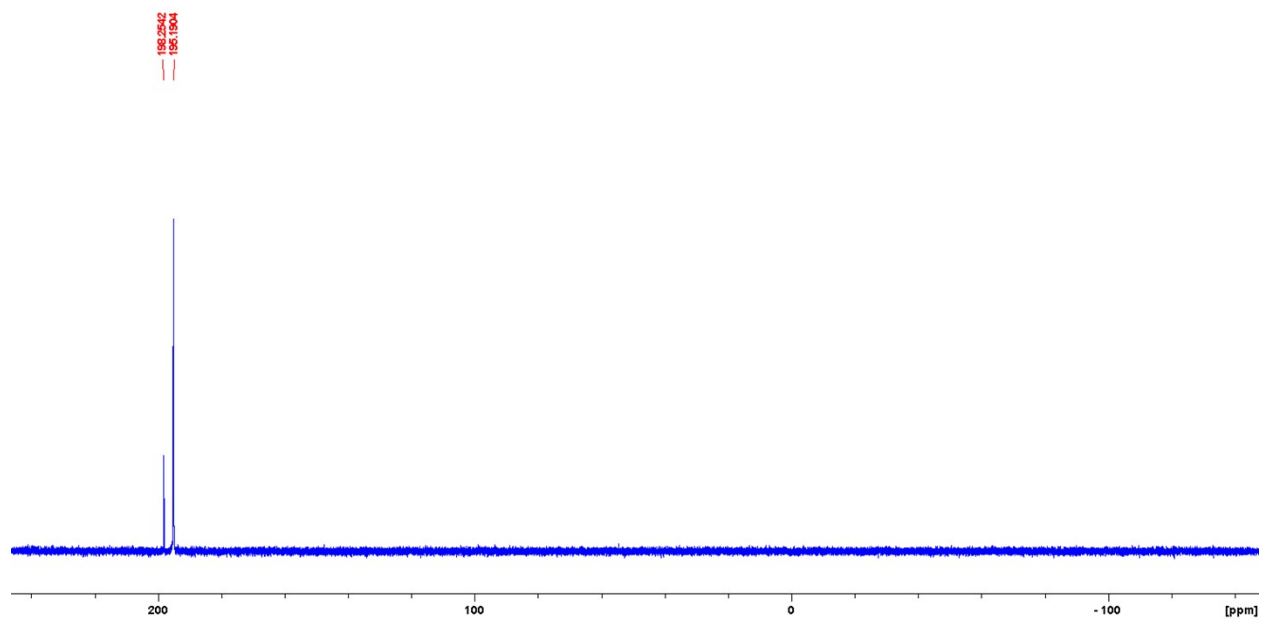


Figure S25. $^{31}\text{P}\{^1\text{H}\}$ NMR spectrum of **5a** in CDCl_3 .

NMR spectra of complex **5b**

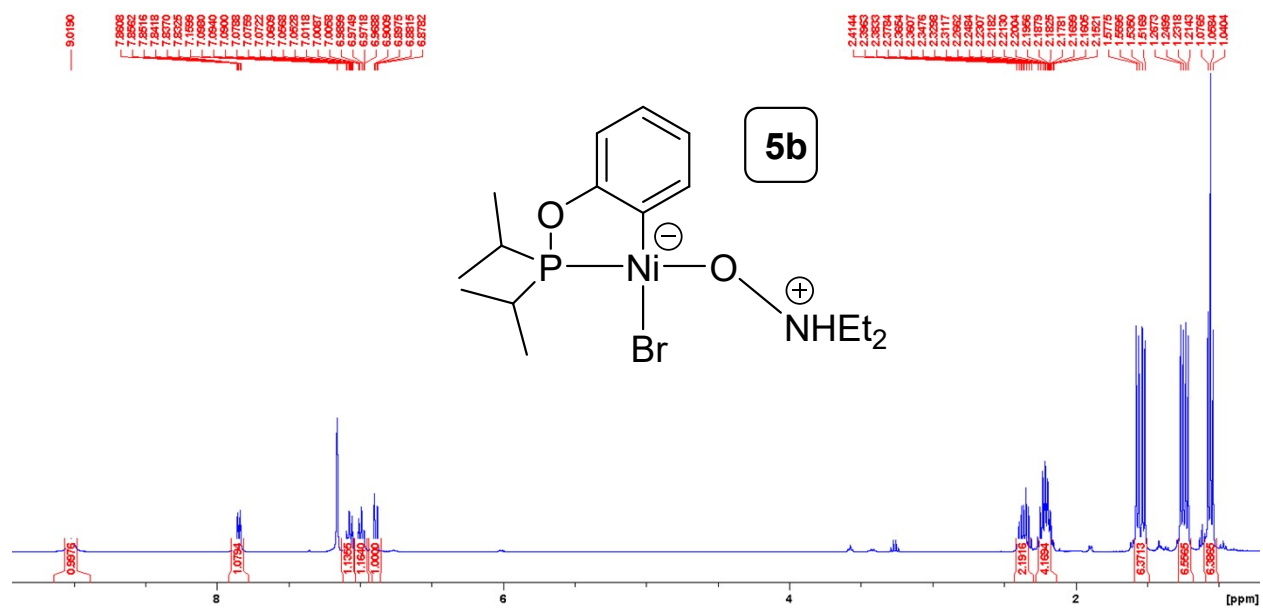


Figure S26. Full ¹H NMR spectrum of **5b** in C₆D₆.

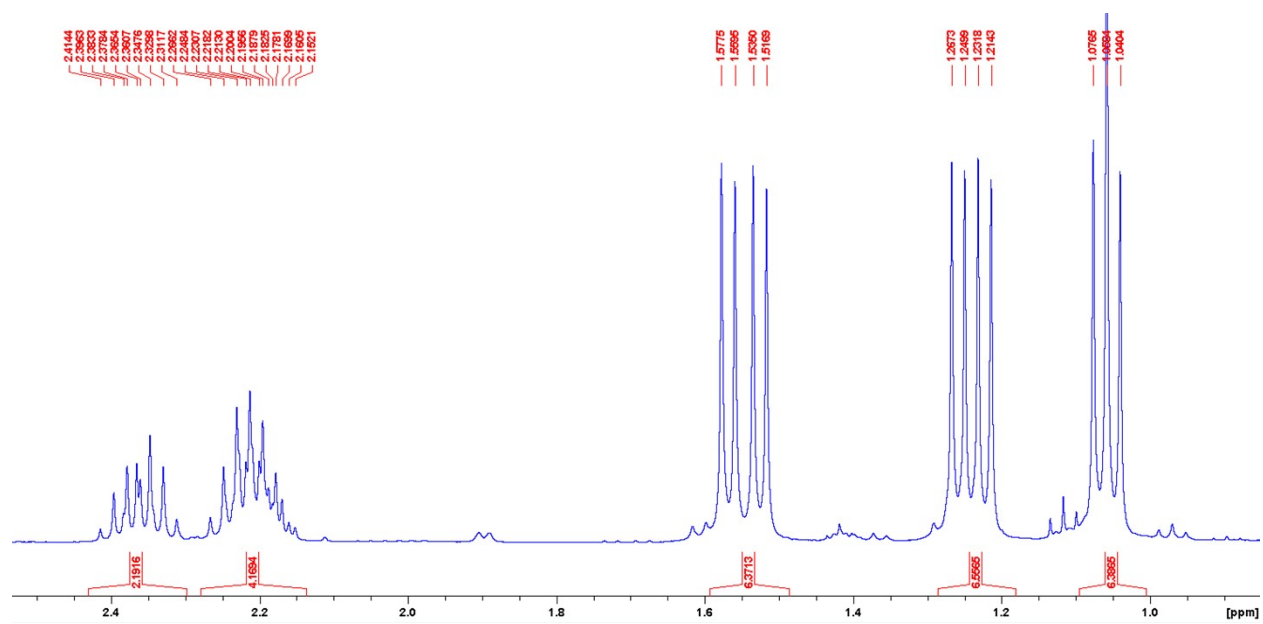


Figure S27. The aliphatic region of the ¹H NMR spectrum of **5b** in C₆D₆.

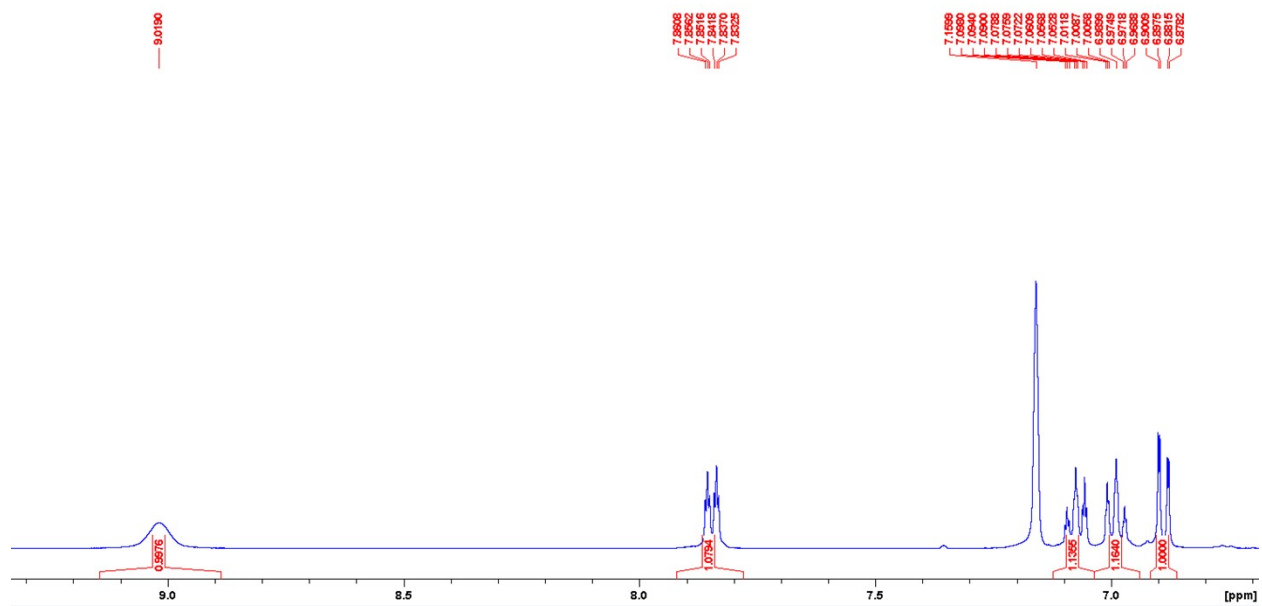


Figure S28. The aromatic region of the ^1H NMR spectrum of **5b** in C_6D_6 .

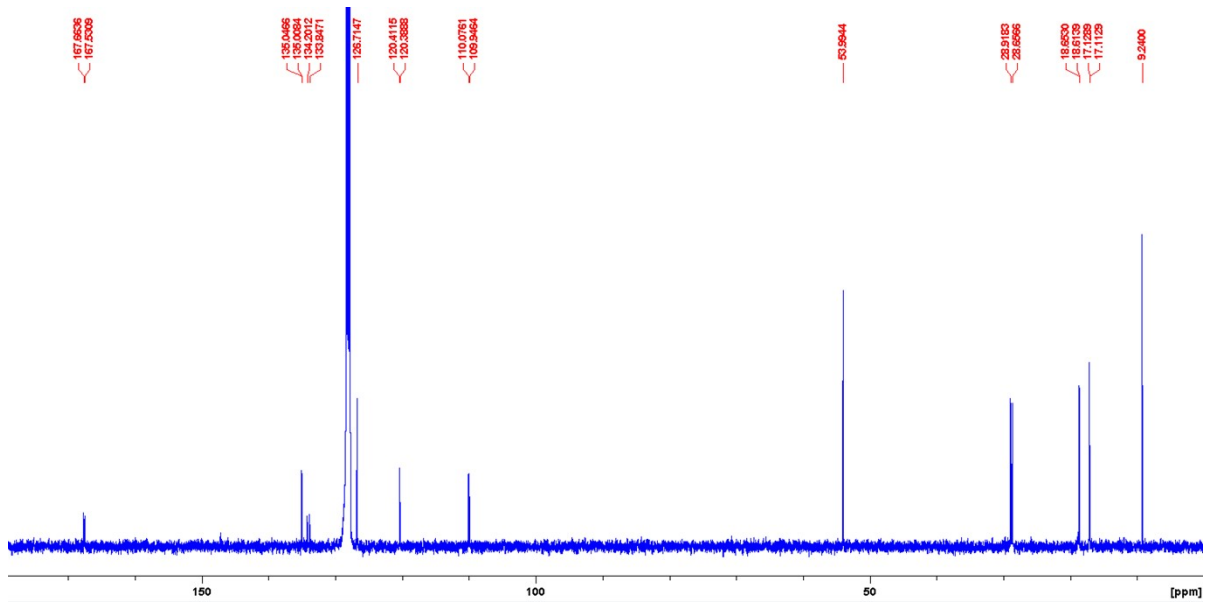


Figure S29. Full ^{13}C NMR spectrum of **5b** in C_6D_6 .

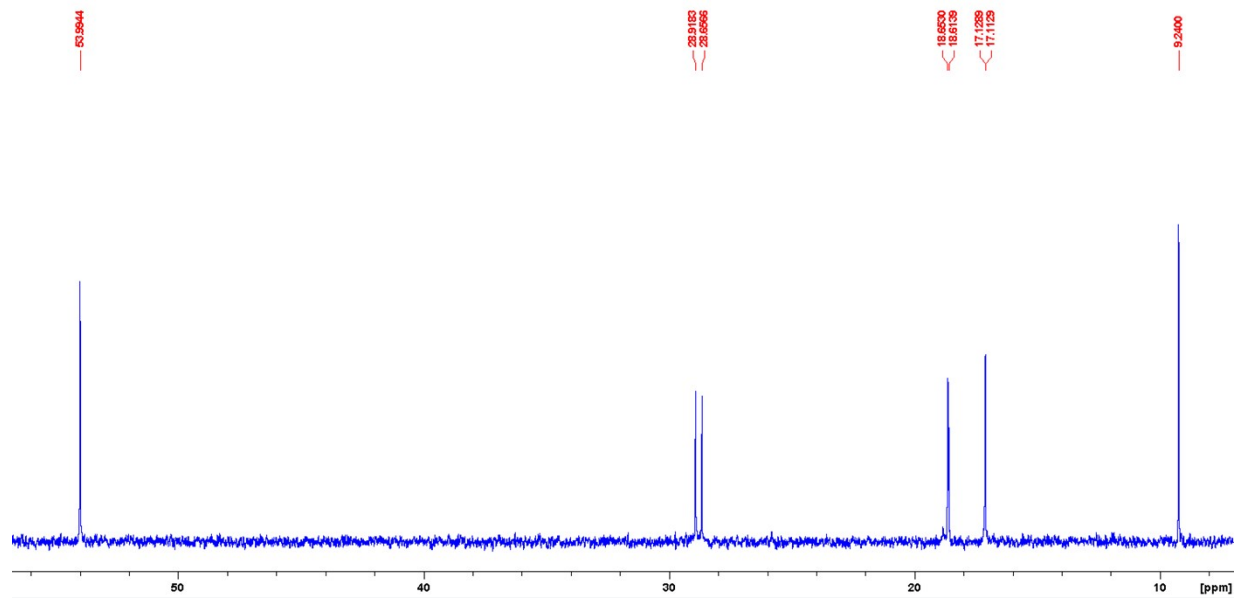


Figure S30. The aliphatic region of the ^{13}C NMR spectrum of **5b** in C_6D_6 .

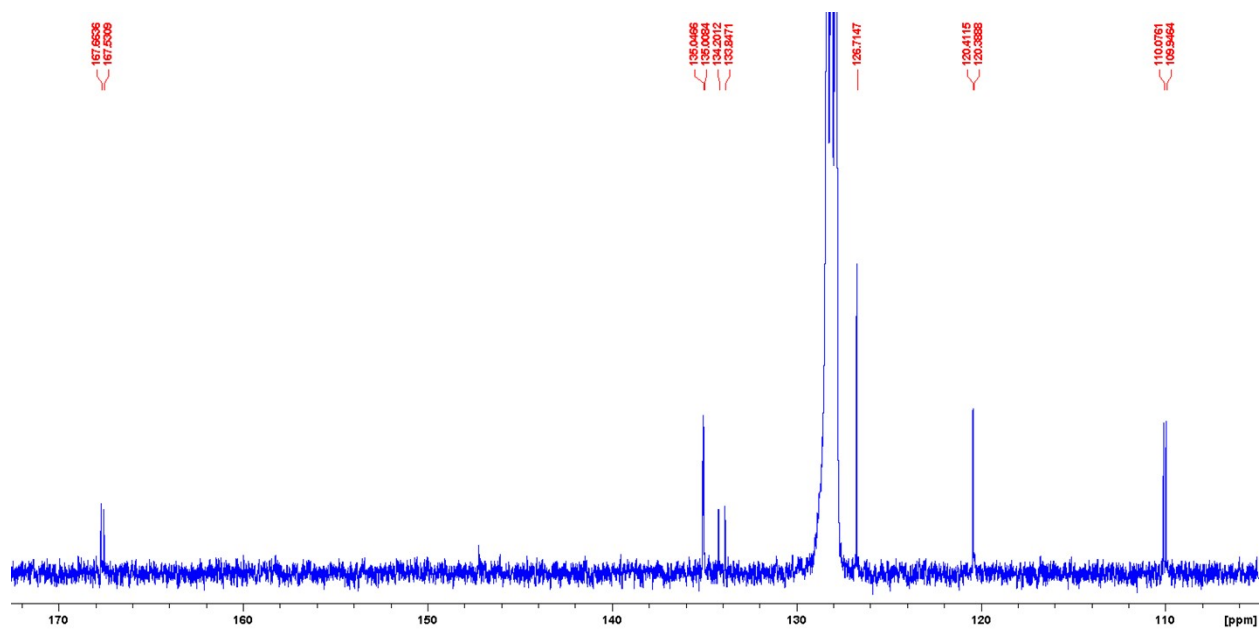


Figure S31. The aromatic region of the ^{13}C NMR spectrum of **5b** in C_6D_6 .

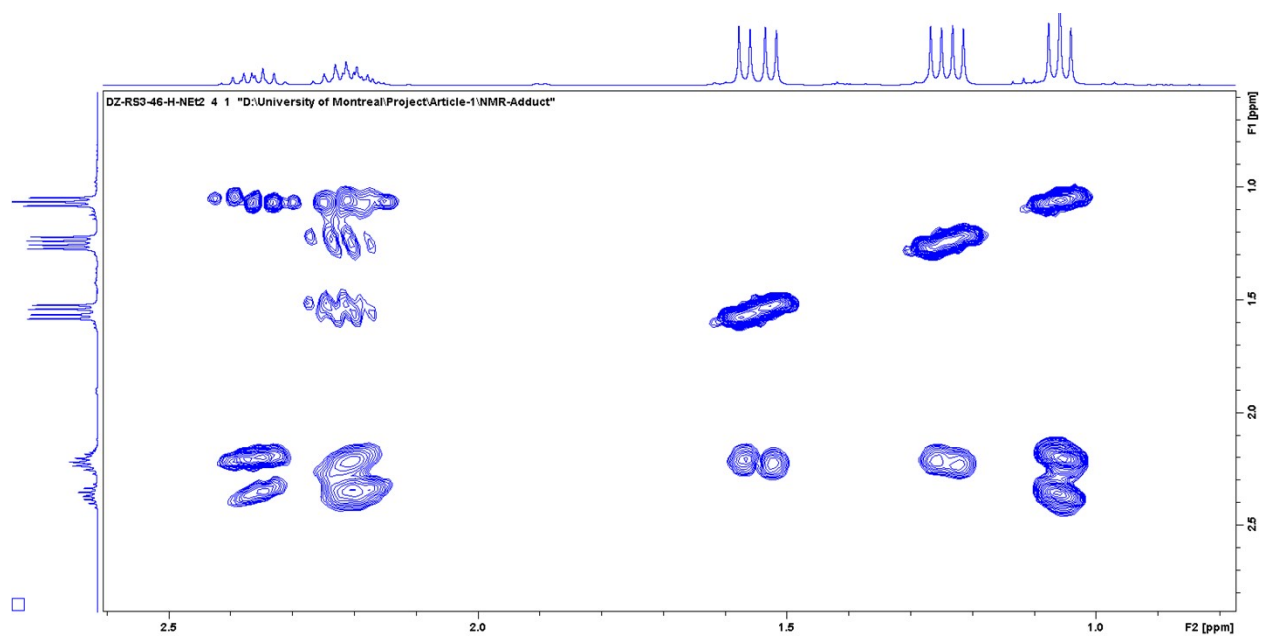


Figure S32. The aliphatic region of the COSY NMR spectrum of **5b** in C₆D₆.

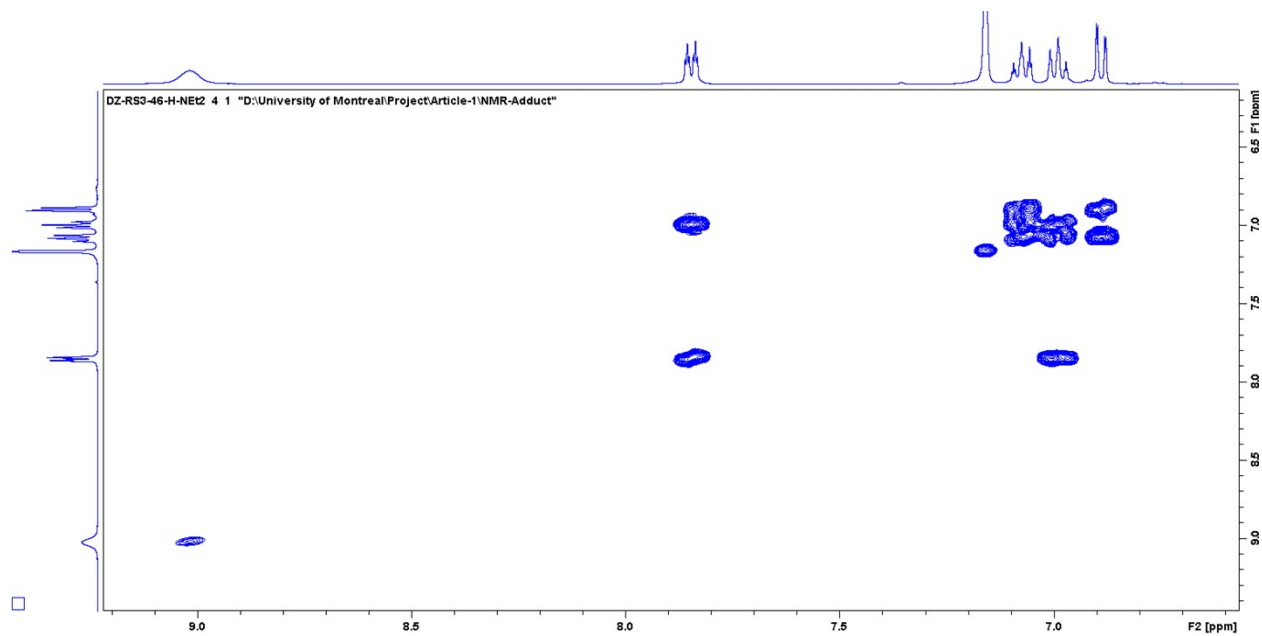


Figure S33. The aromatic region of the COSY NMR spectrum of **5b** in C₆D₆.

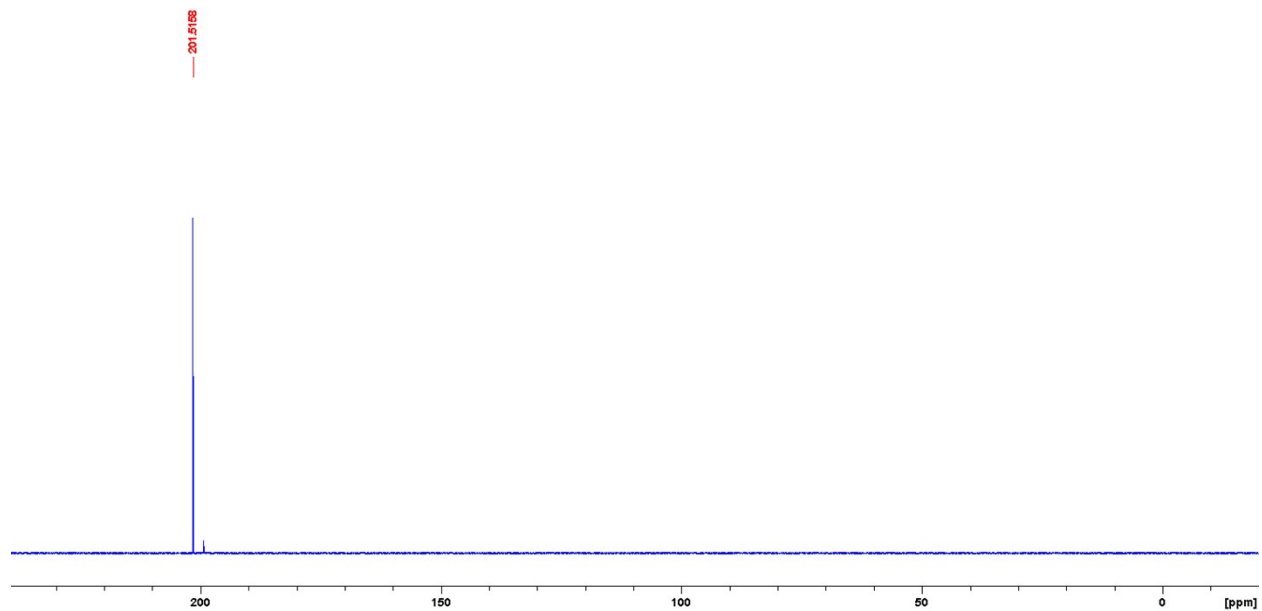


Figure S34. Full $^{31}\text{P}\{^1\text{H}\}$ NMR spectrum of **5b** in C_6D_6 .

NMR spectra of complex **5c**

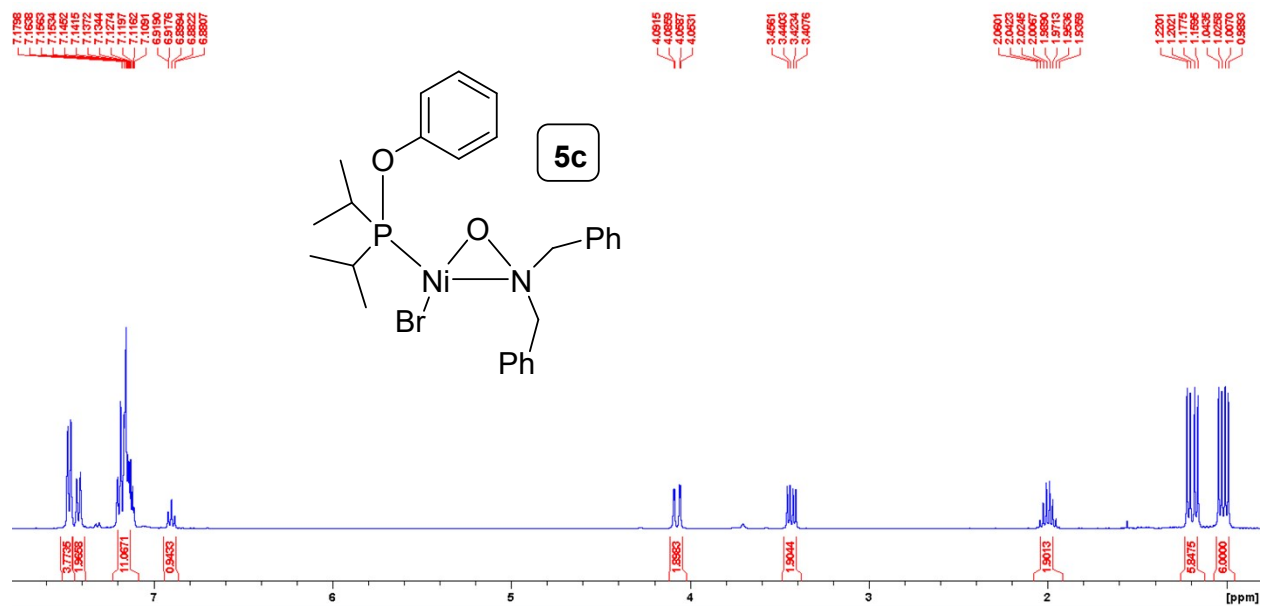


Figure S35. Full ^1H NMR spectrum of **5c** in C_6D_6 .

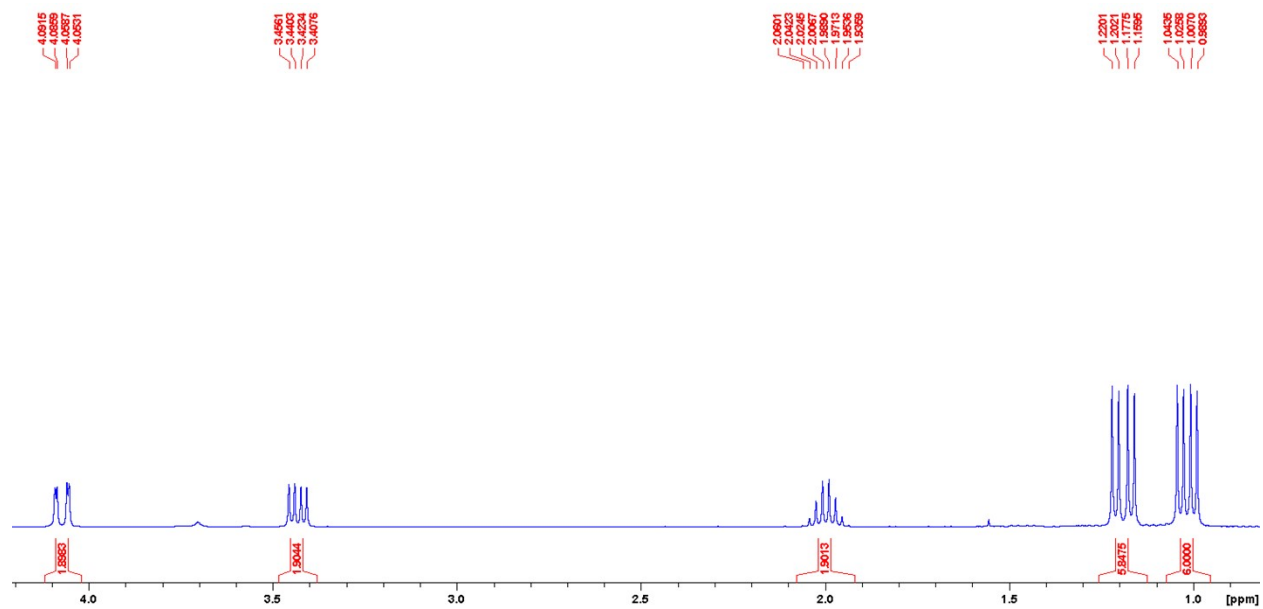


Figure S36. The aliphatic region of the ^1H NMR spectrum of **5c** in C_6D_6 .

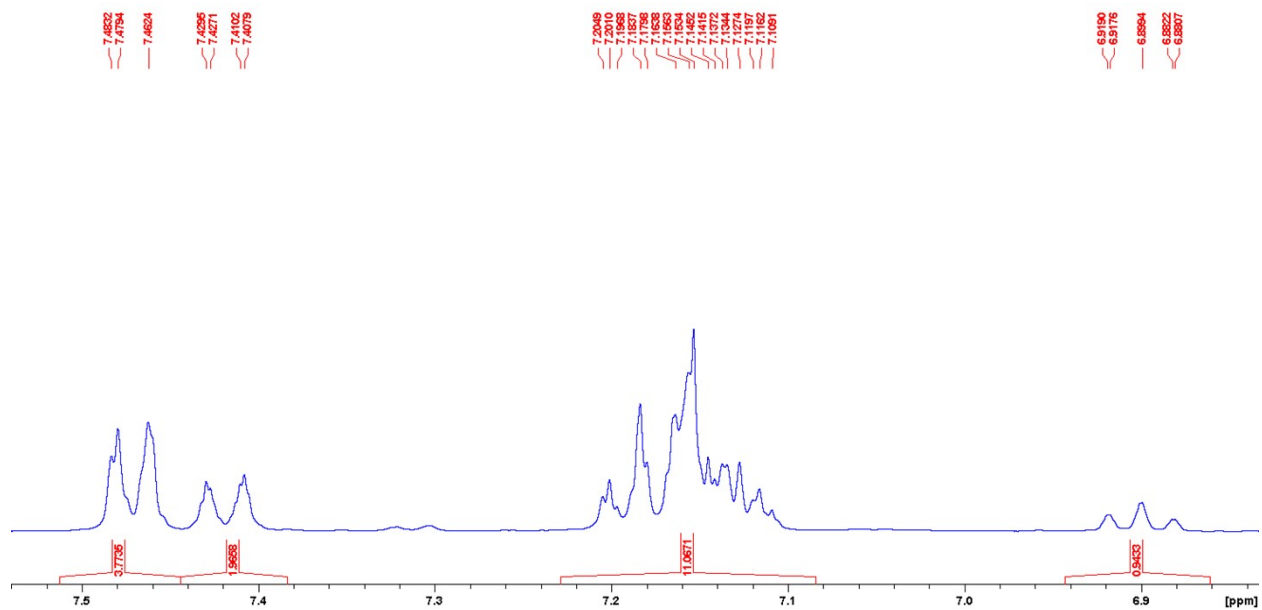


Figure S37. The aromatic region of the ^1H NMR spectrum of **5c** in C_6D_6 .

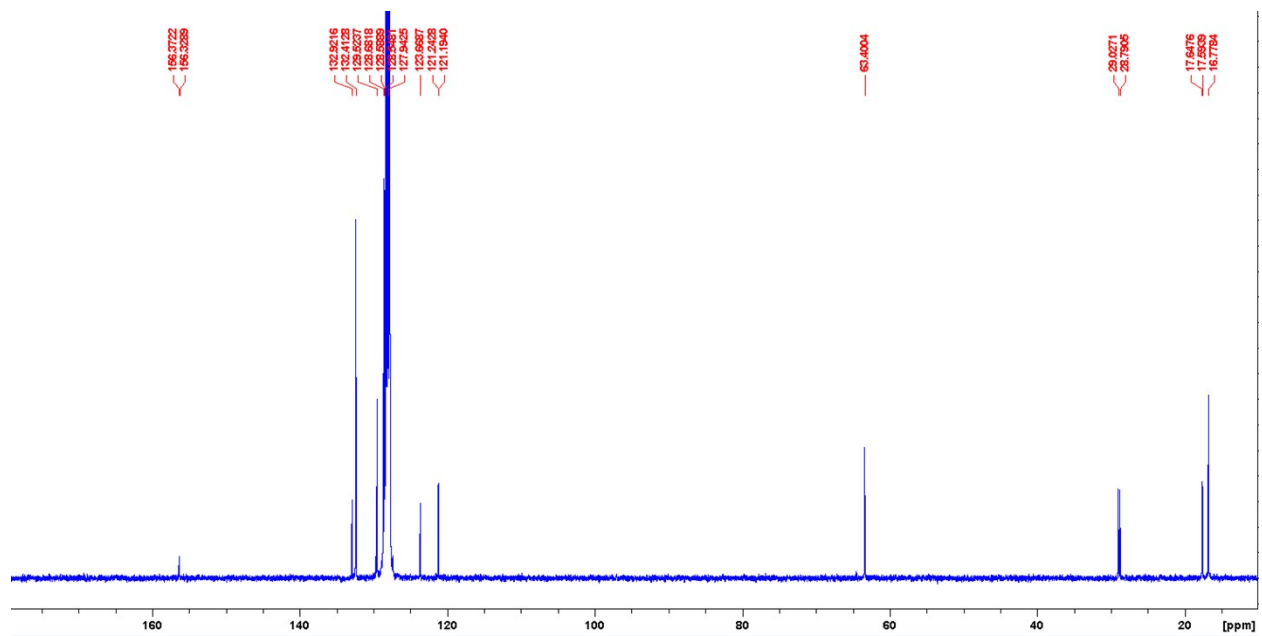


Figure S38. Full ^{13}C NMR spectrum of **5c** in C_6D_6 .

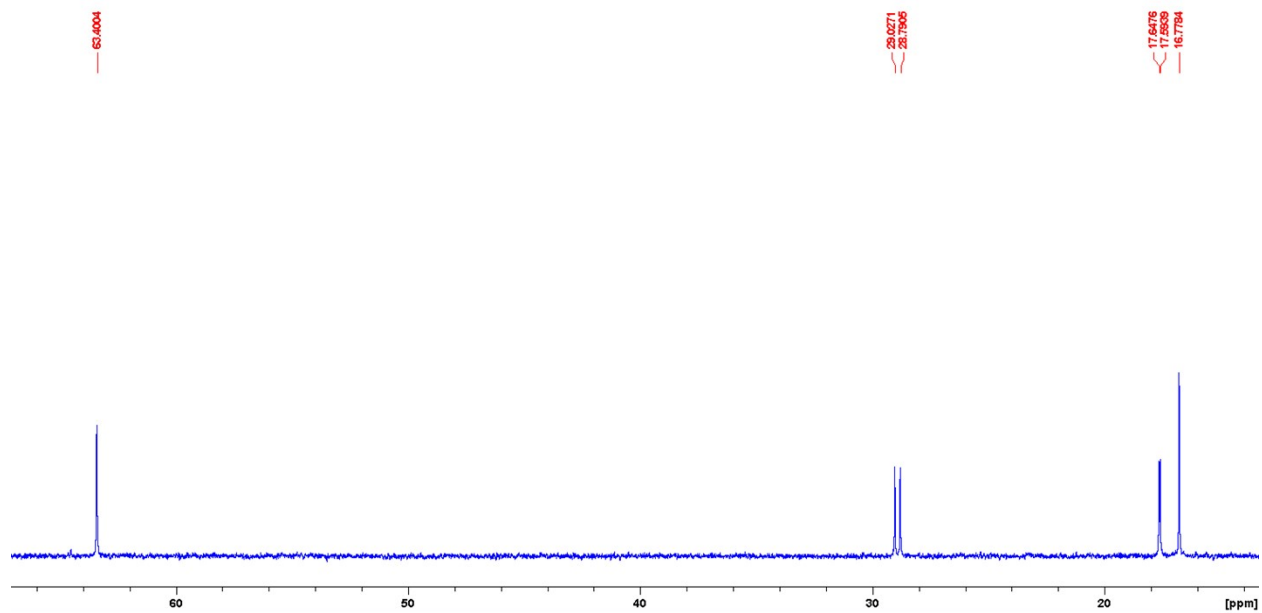


Figure S39. The aliphatic region of the ^{13}C NMR spectrum of **5c** in C_6D_6 .

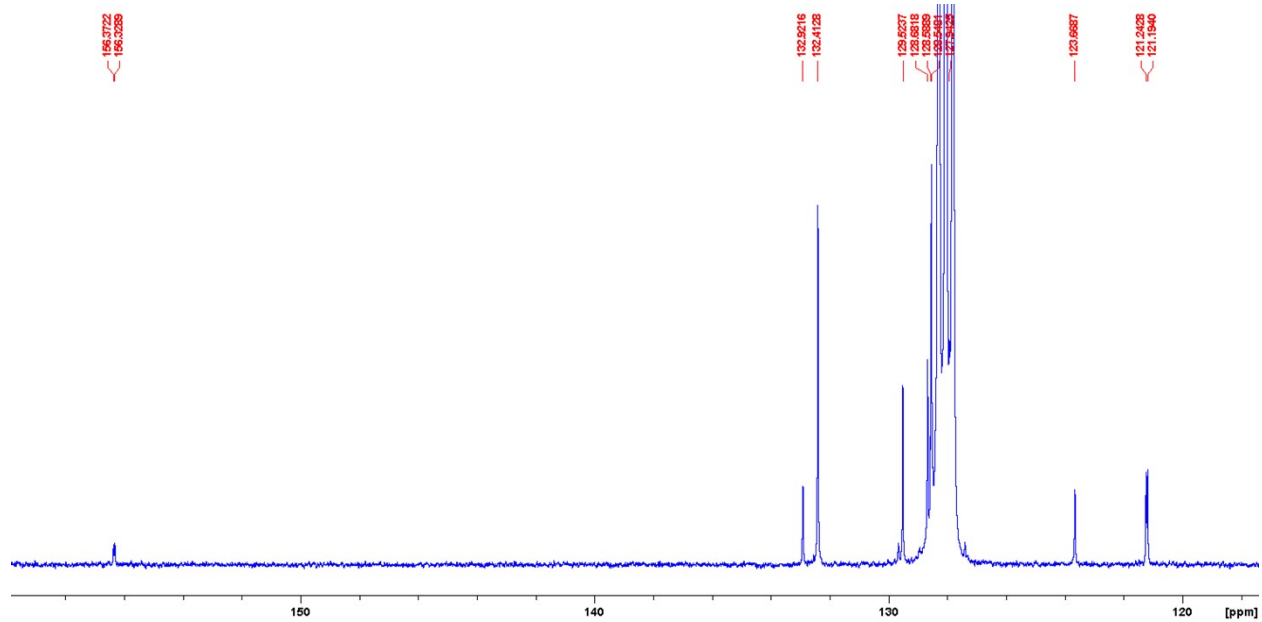


Figure S40. The aromatic region of the ^{13}C NMR spectrum of **5c** in C_6D_6 .

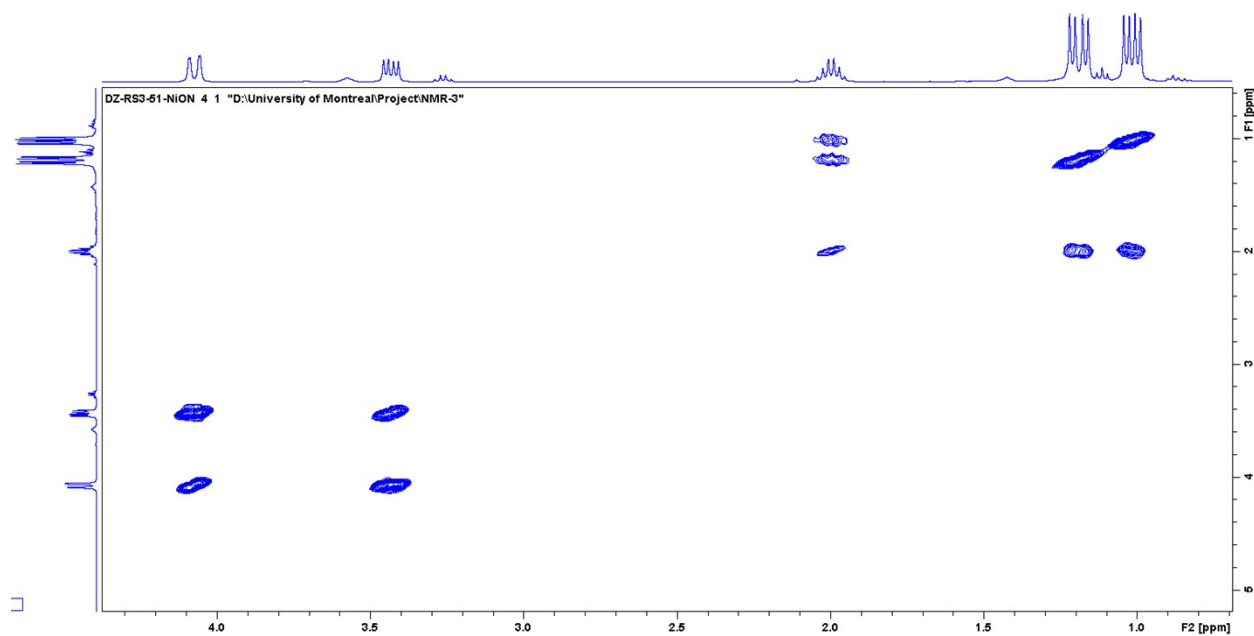


Figure S41. The aliphatic region of the COSY NMR spectrum of **5c** in C₆D₆.

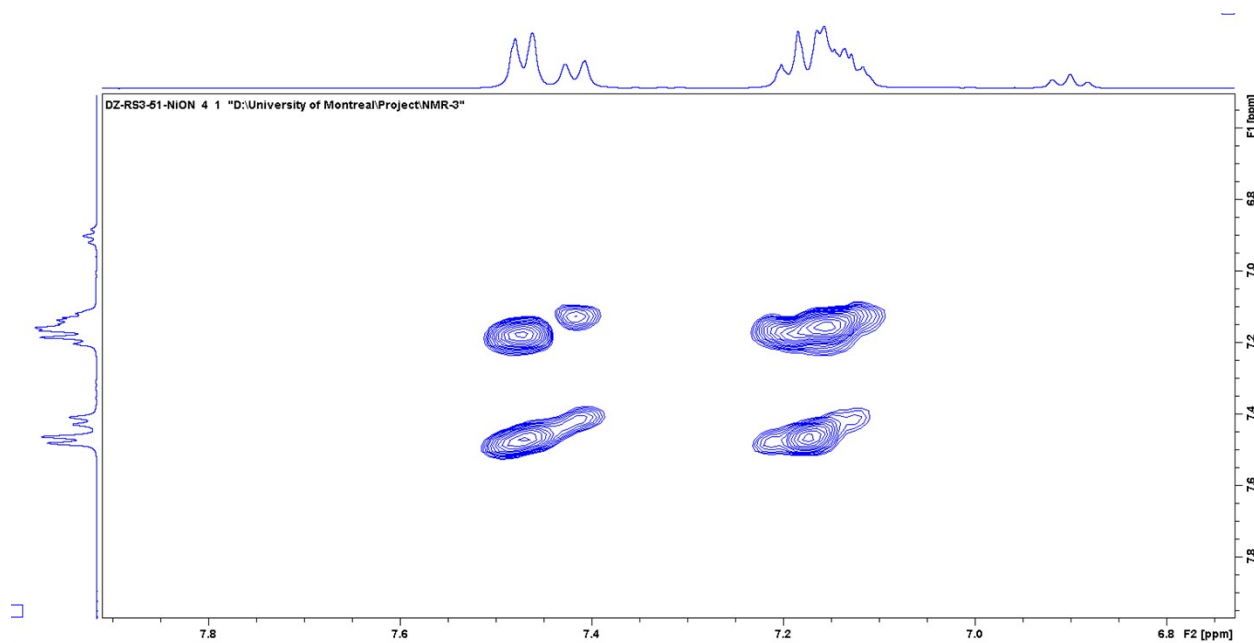


Figure S42. The aromatic region of the COSY NMR spectrum of **5c** in C₆D₆.

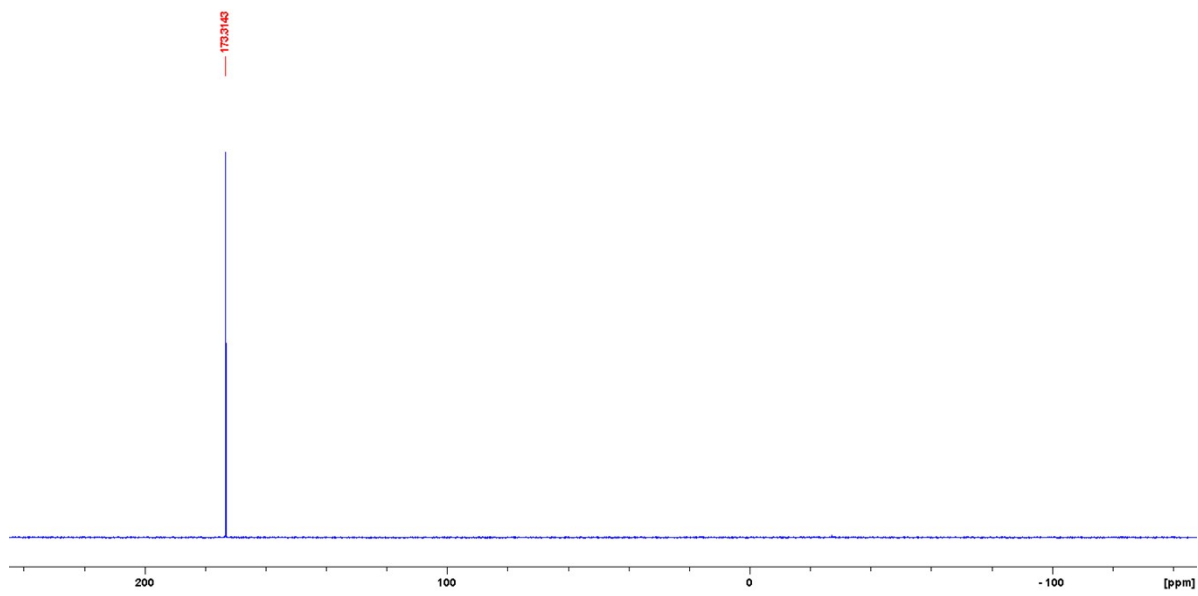


Figure S43. Full $^{31}\text{P}\{^1\text{H}\}$ NMR spectrum of **5c** in C_6D_6 .

NMR spectra of complex **6a**

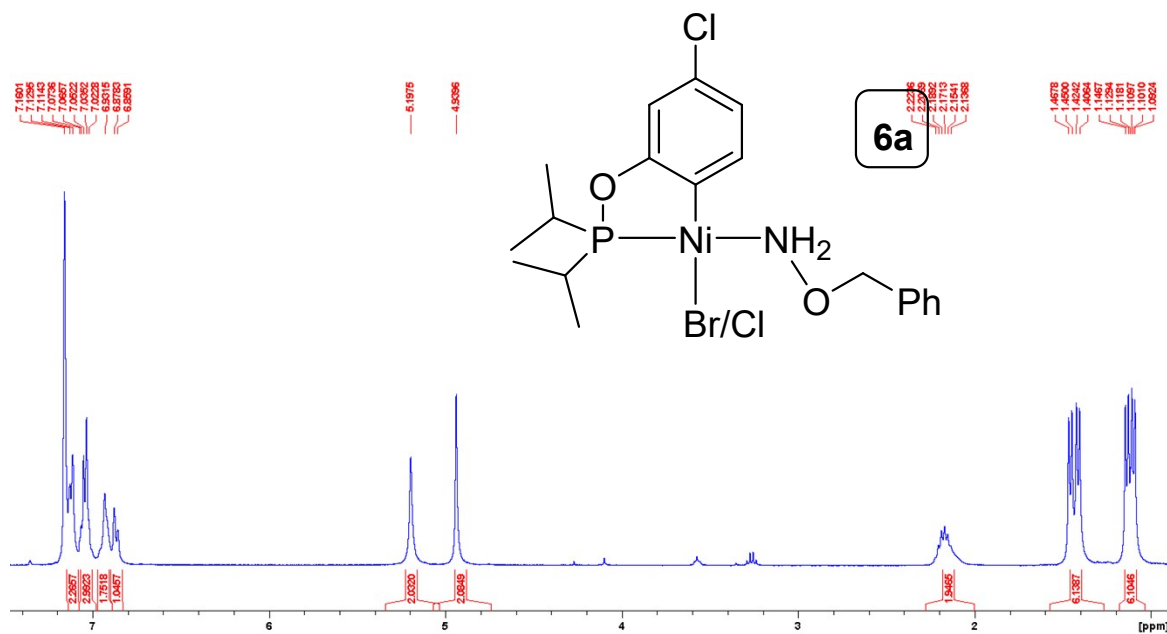


Figure S44. Full ^1H NMR spectrum of **6a** in C_6D_6 .

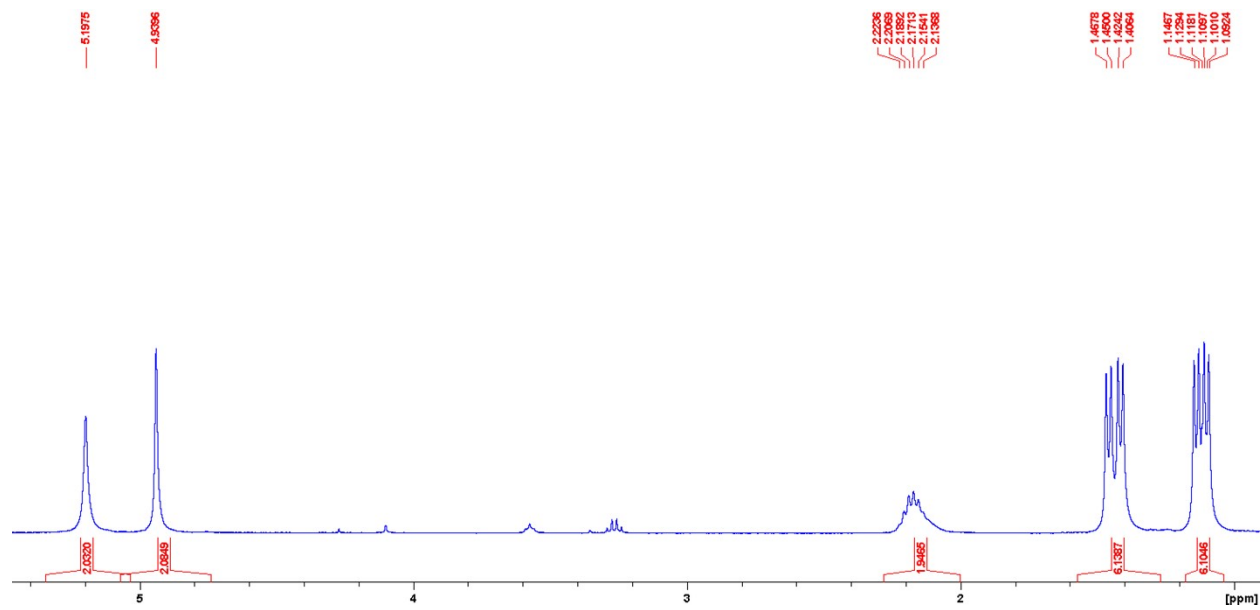


Figure S45. The aliphatic region of the ^1H NMR spectrum of **6a** in C_6D_6 .

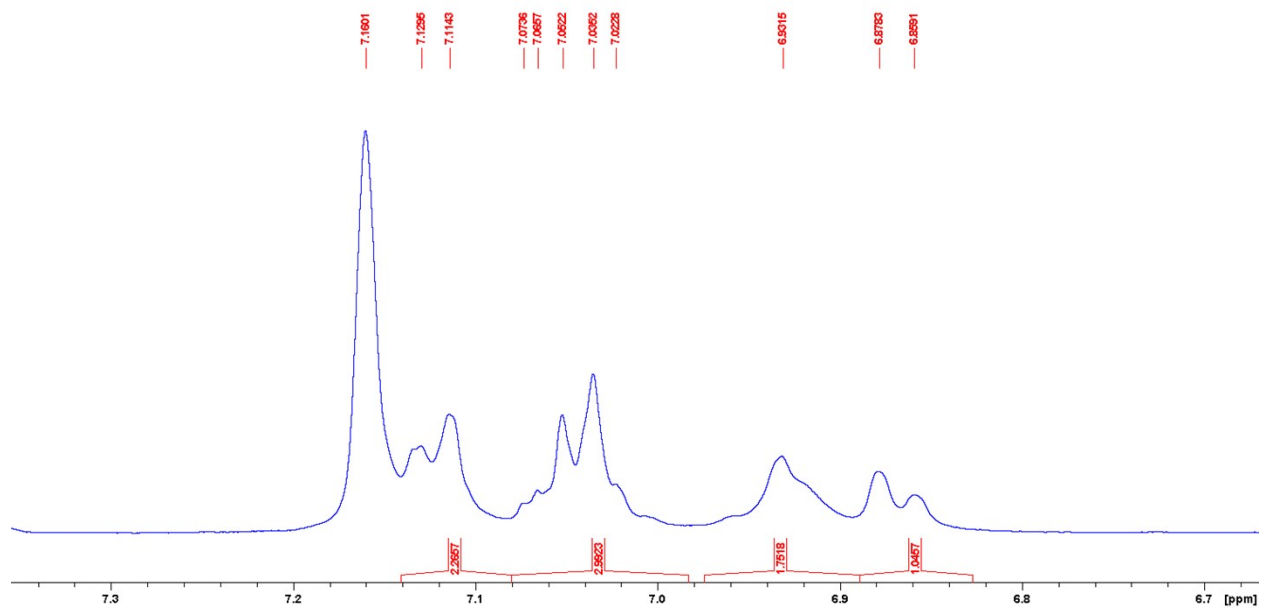


Figure S46. The aromatic region of the ^1H NMR spectrum of **6a** in C_6D_6 .

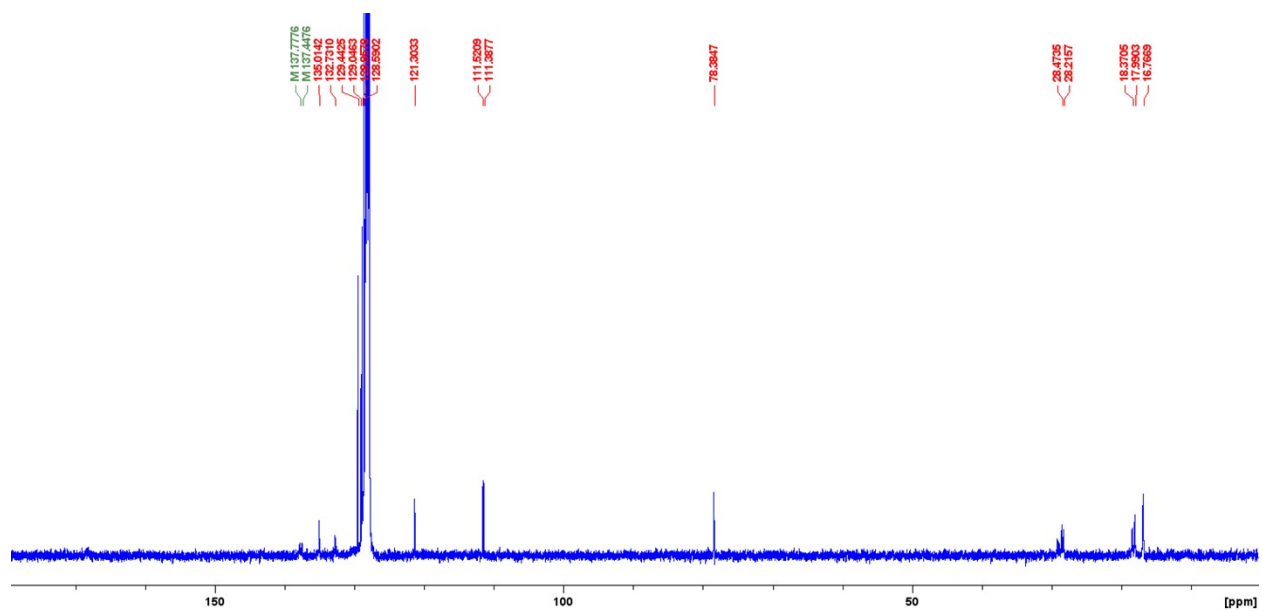


Figure S47. Full ^{13}C NMR spectrum of **6a** in C_6D_6 .

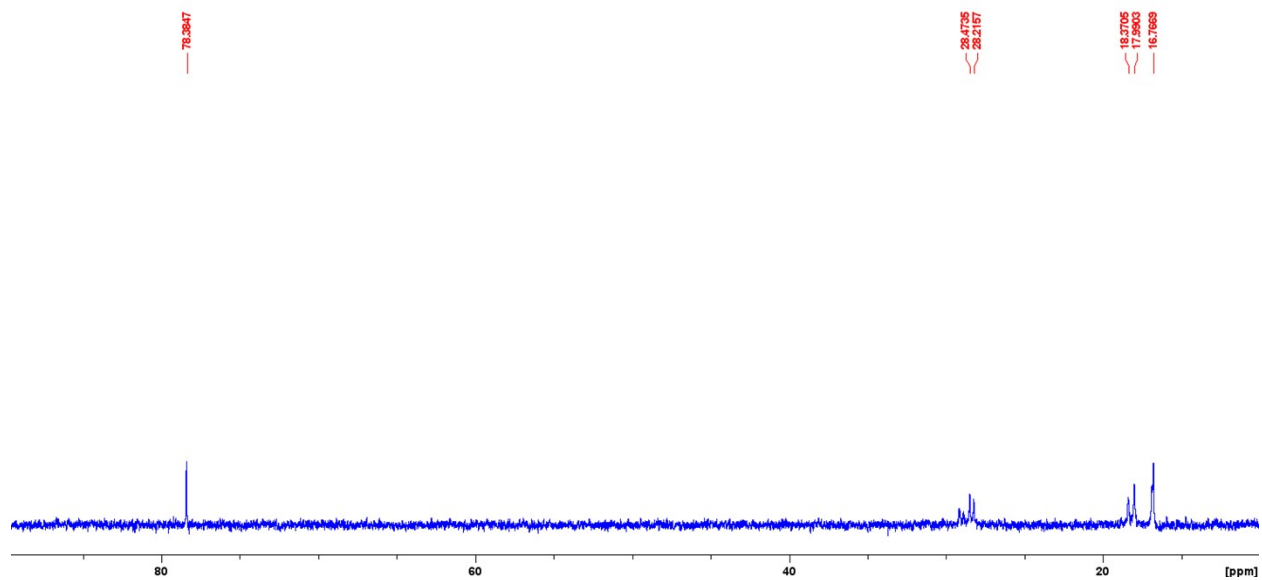


Figure S48. The aliphatic region of the ^{13}C NMR spectrum of **6a** in C_6D_6 .

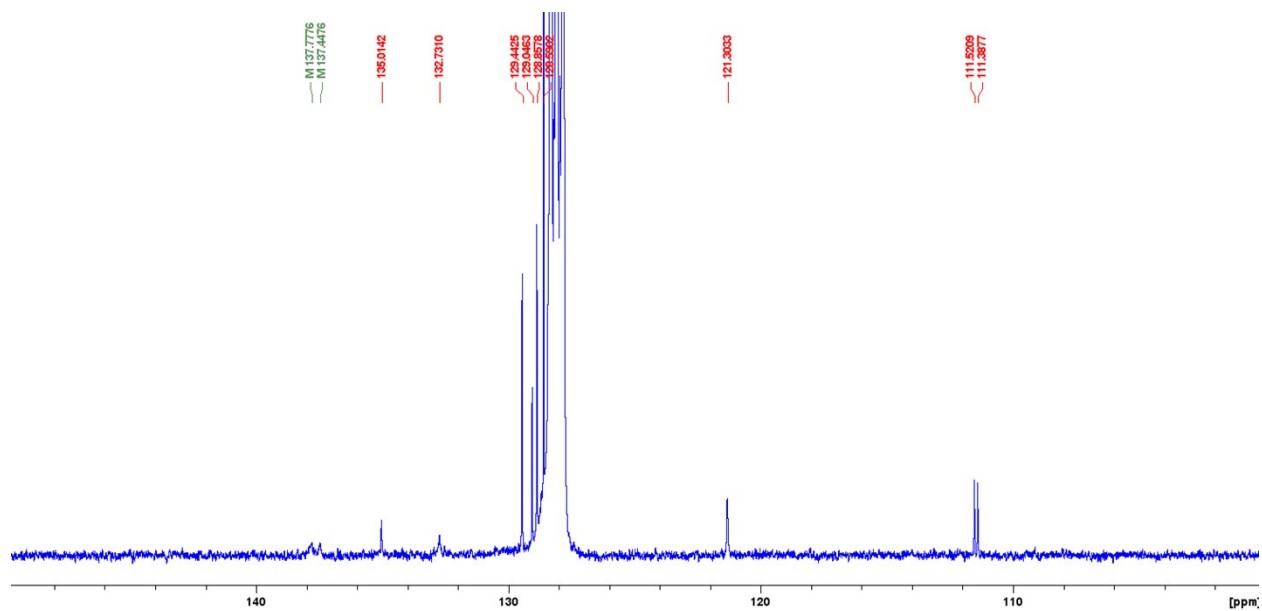


Figure S49. The aromatic region of the ^{13}C NMR spectrum of **6a** in C_6D_6 .

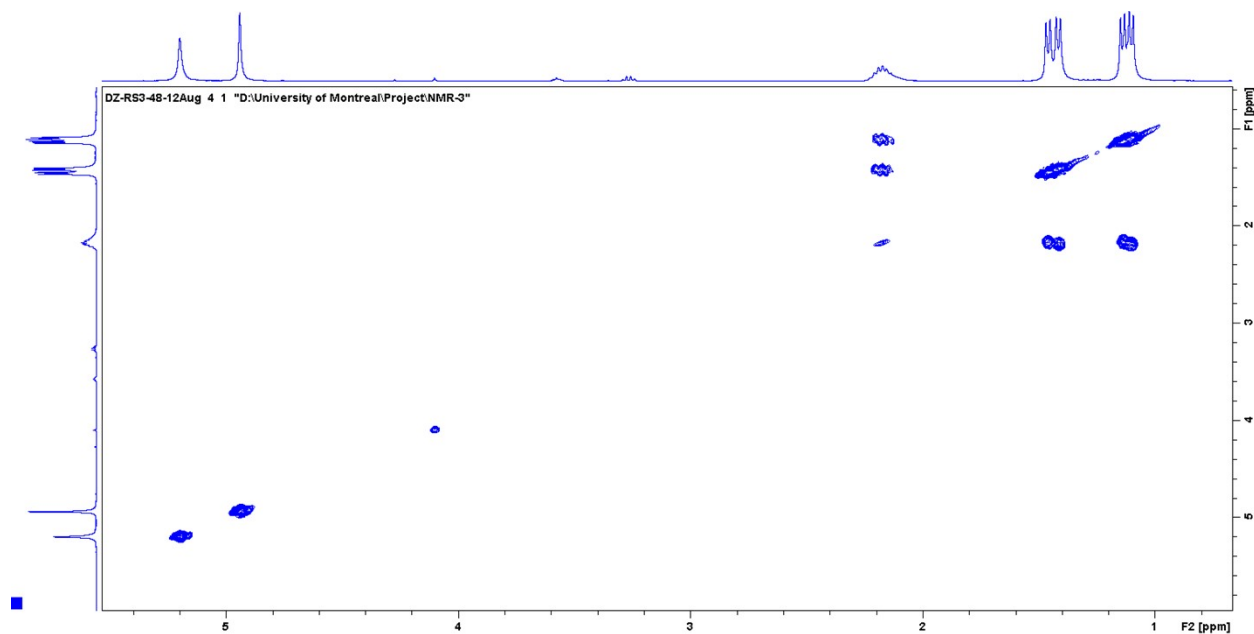


Figure S50. The aliphatic region of the COSY NMR spectrum of **6a** in C₆D₆.

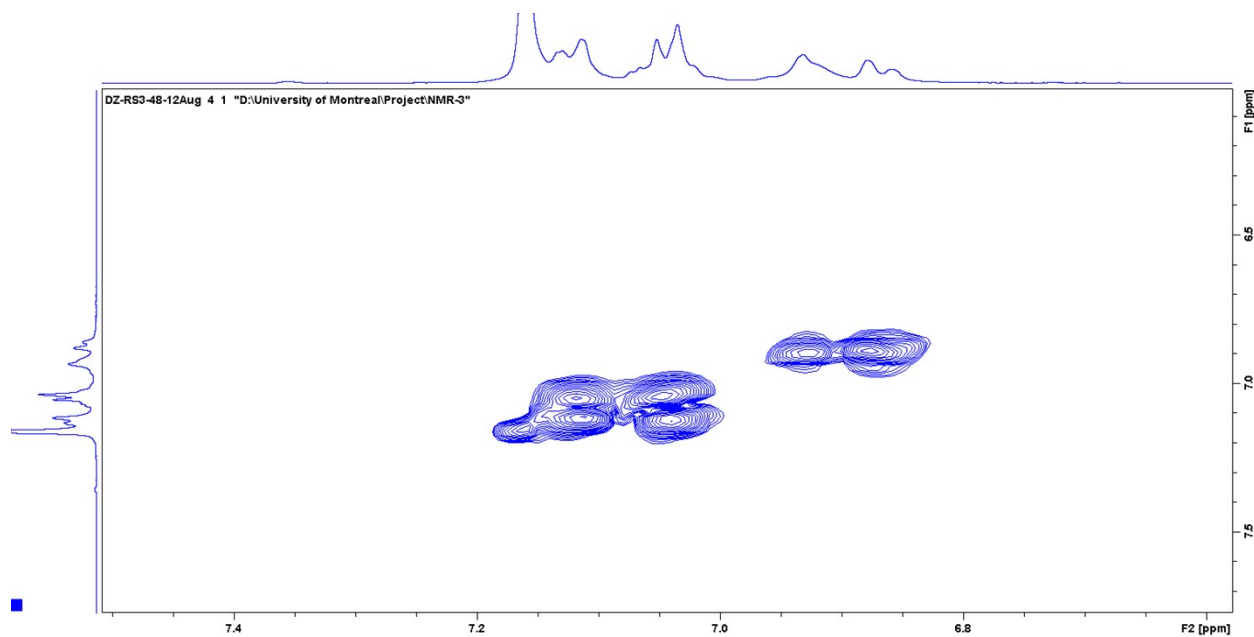


Figure S51. The aromatic region of the COSY NMR spectrum of **6a** in C₆D₆.

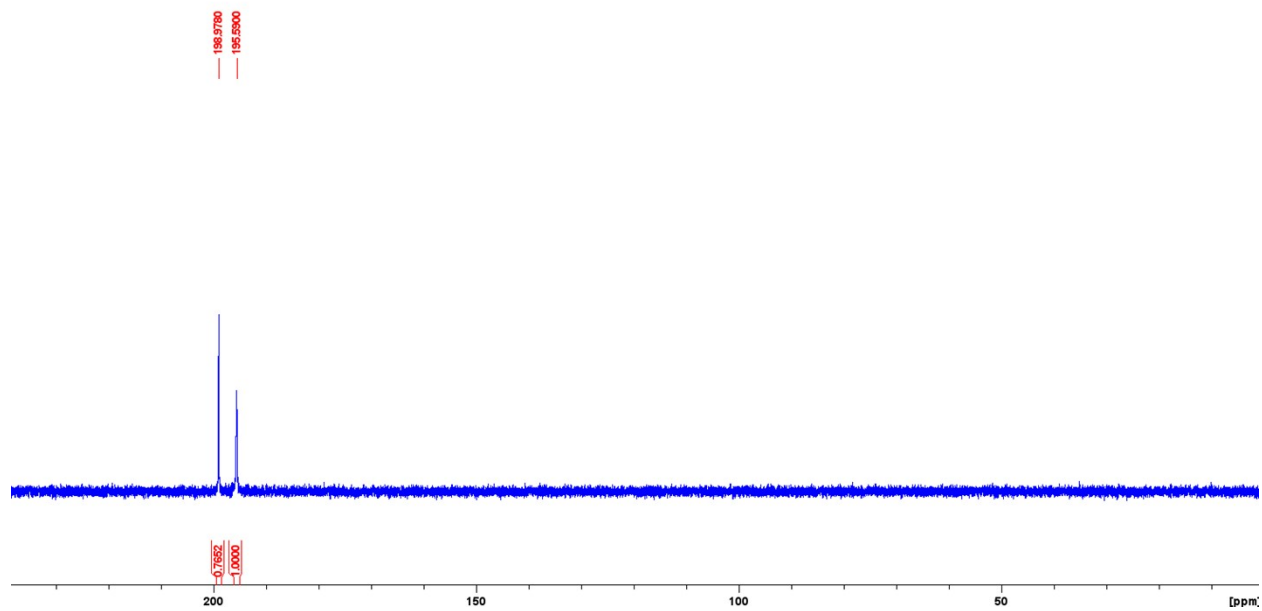


Figure S52. $^{31}\text{P}\{^1\text{H}\}$ NMR spectrum of **6a** in C_6D_6 .

NMR spectra of complex **6b**

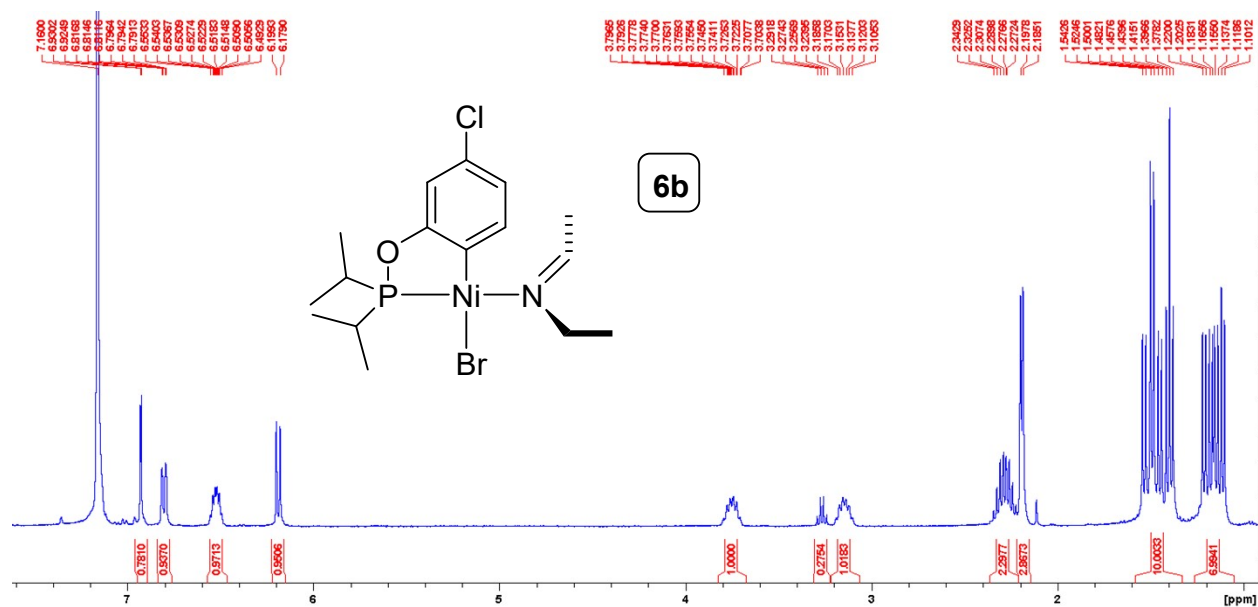


Figure S53. Full ^1H NMR spectrum of **6b** in C_6D_6 .

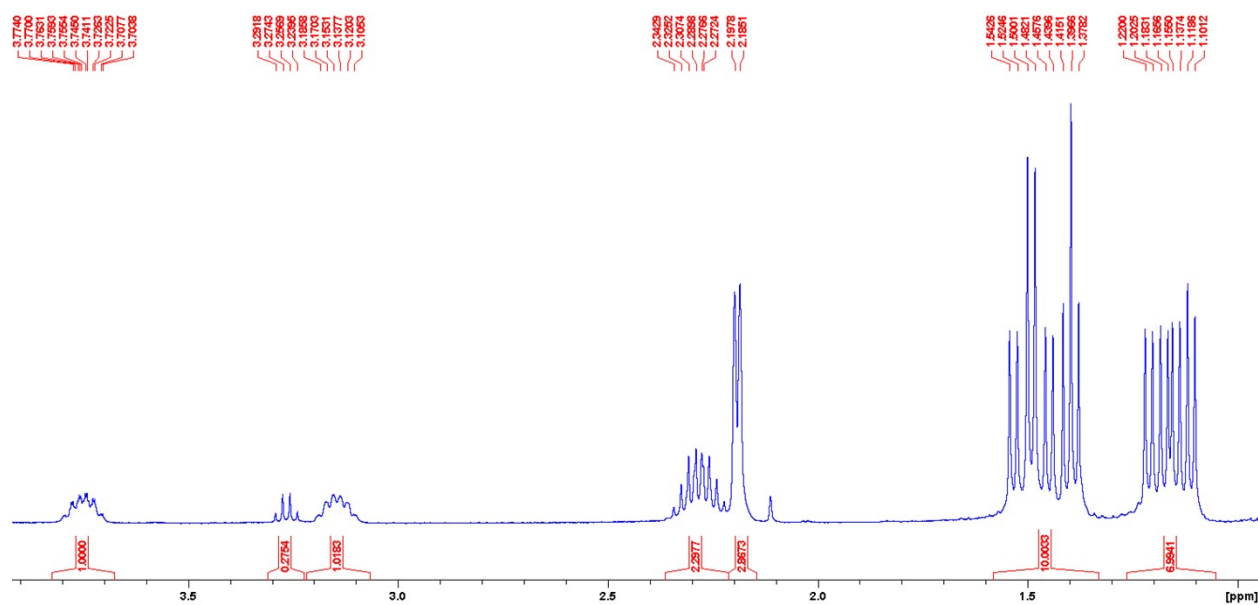


Figure S54. The aliphatic region of the ^1H NMR spectrum of **6b** in C_6D_6 .

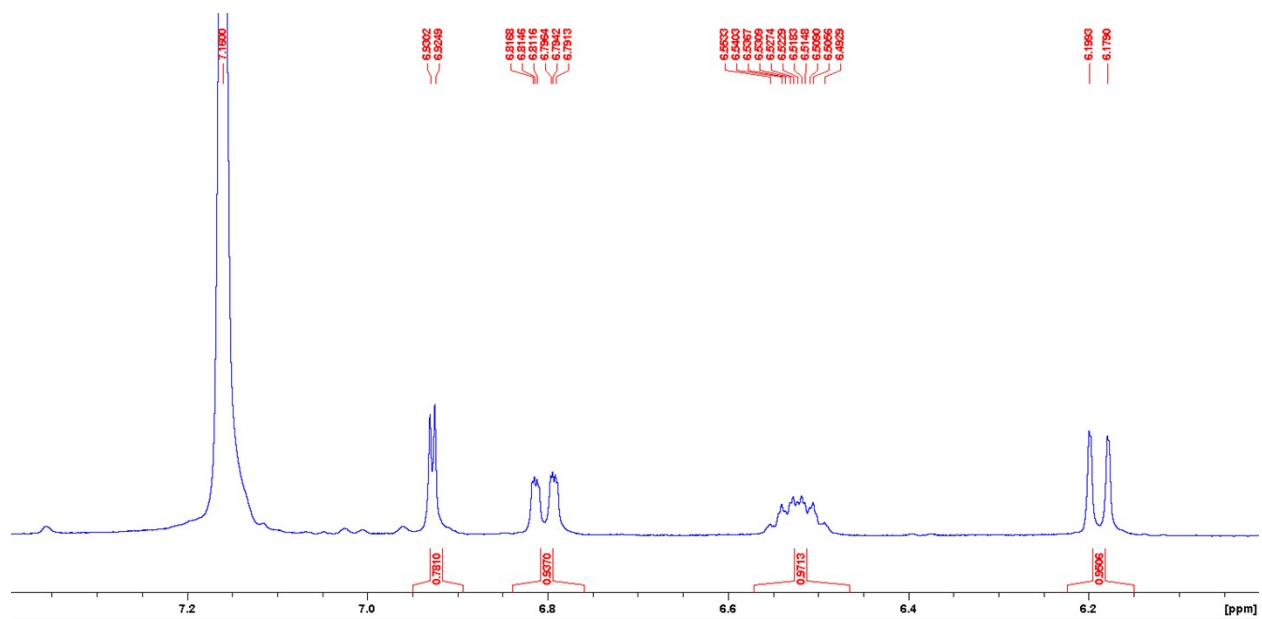


Figure S55. The aromatic region of the ^1H NMR spectrum of **6b** in C_6D_6 .

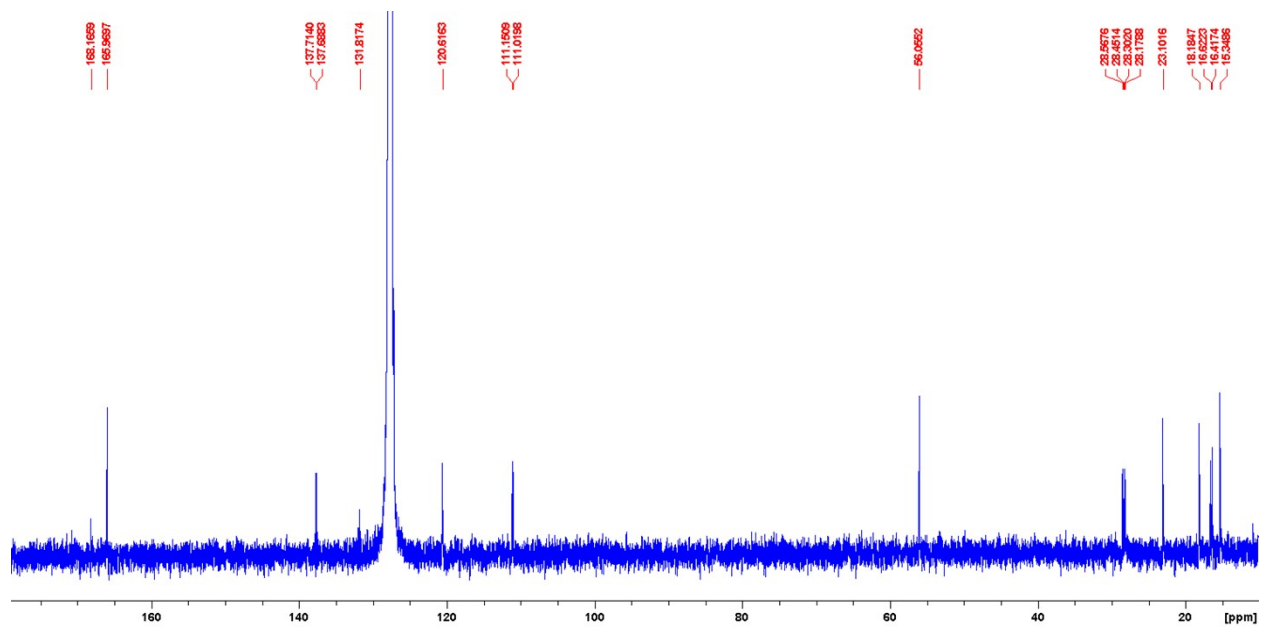


Figure S56. Full ^{13}C NMR spectrum of **6b** in C_6D_6 .

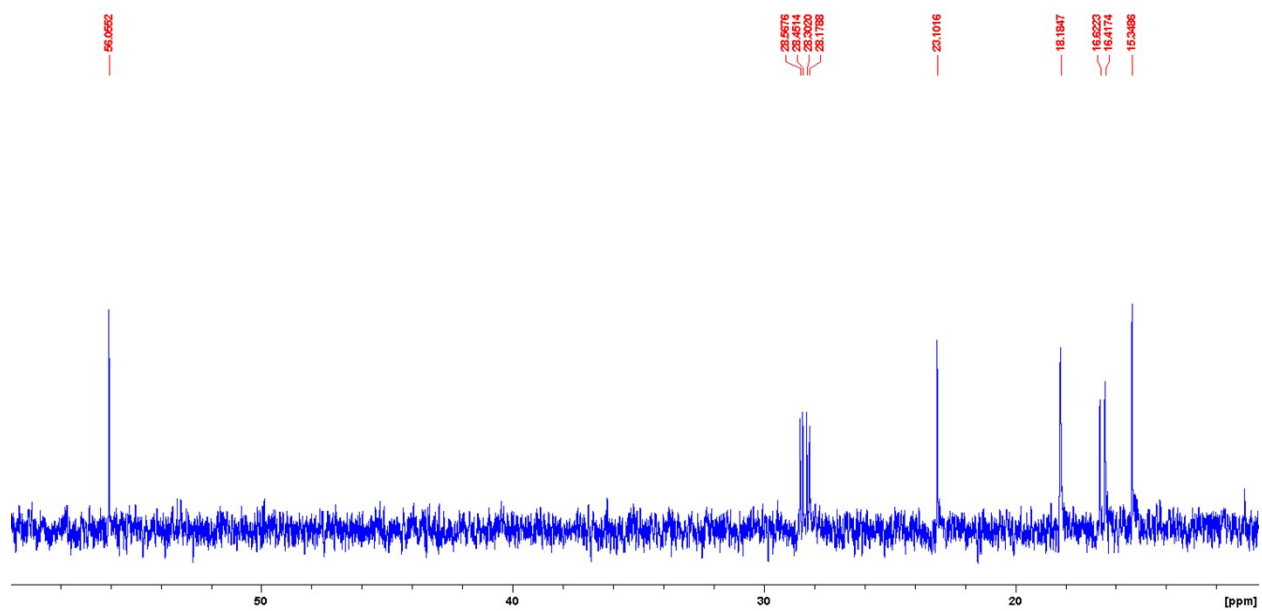


Figure S57. The aliphatic region of the ^{13}C NMR spectrum of **6b** in C_6D_6 .

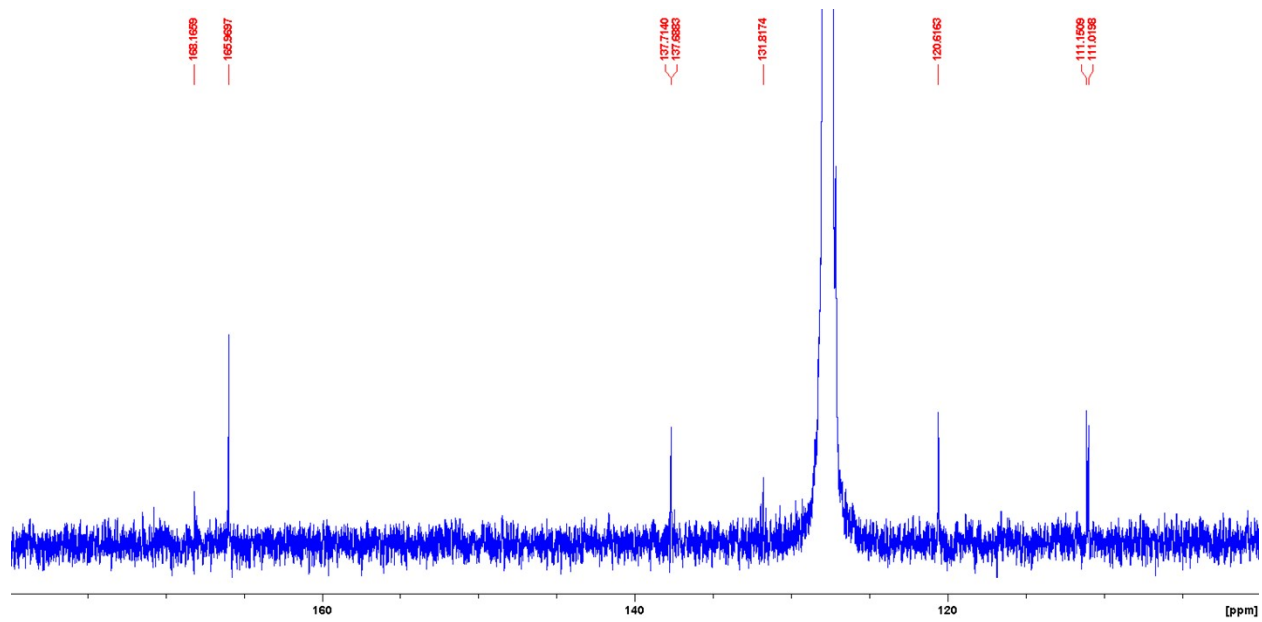


Figure S58. The aromatic region of the ^{13}C NMR spectrum of **6b** in C_6D_6 .

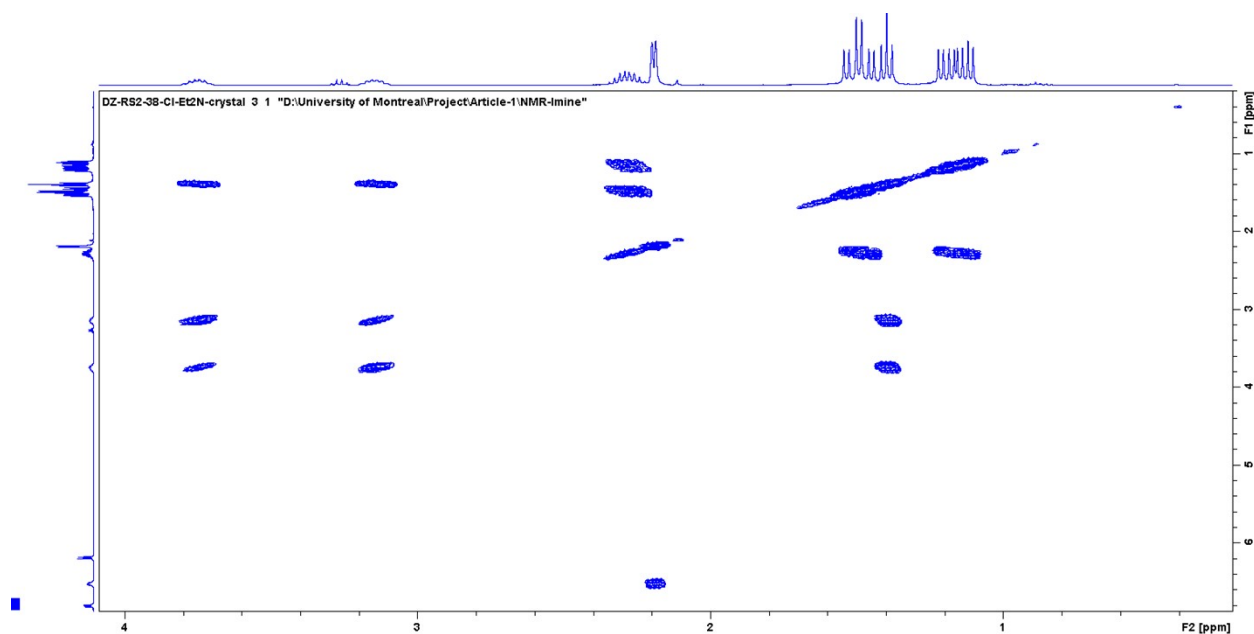


Figure S59. The aliphatic region of the COSY NMR spectrum of **6b** in C_6D_6 .

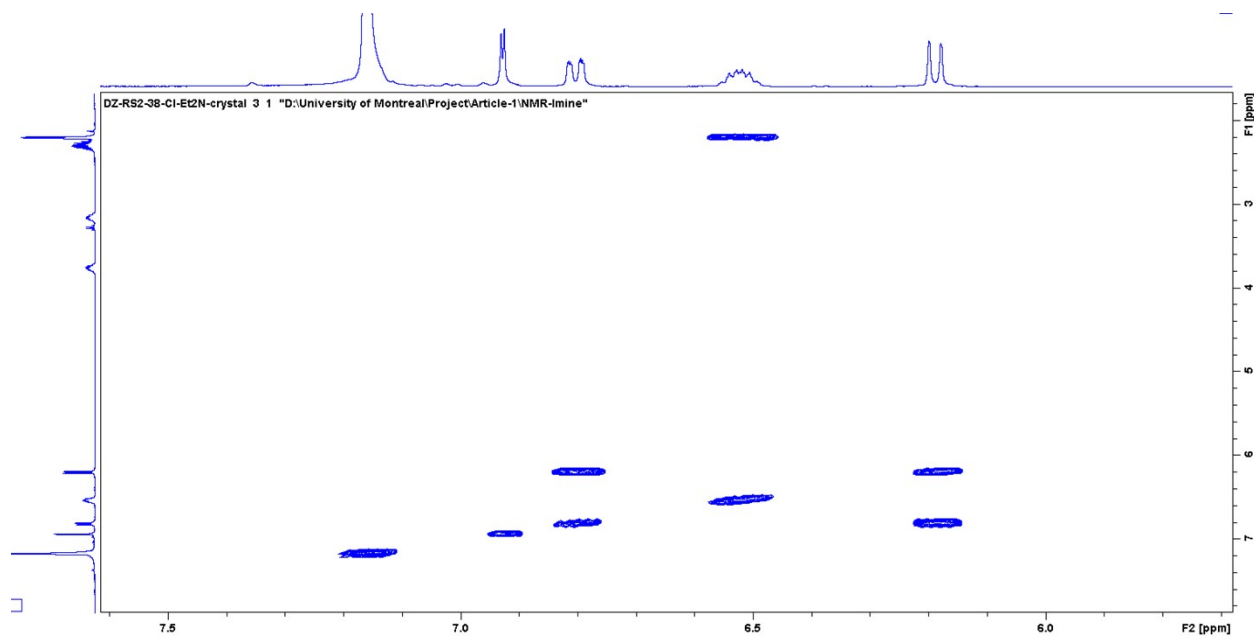


Figure S60. The aromatic region of the COSY NMR spectrum of **6b** in C_6D_6 .

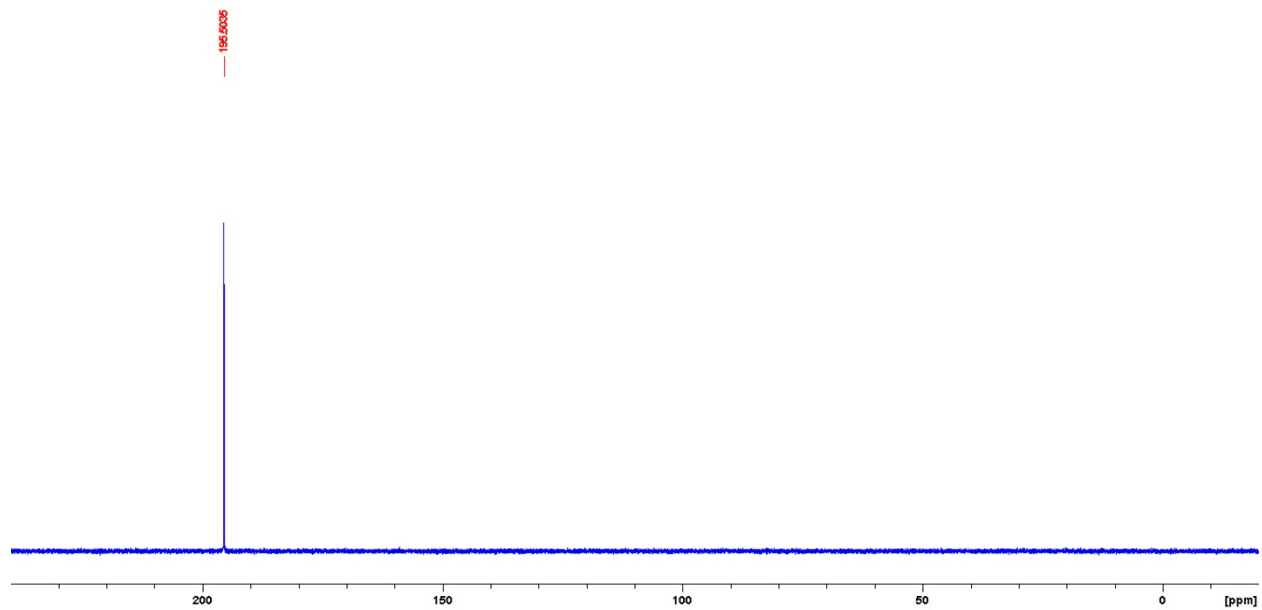


Figure S61. Full $^{31}\text{P}\{^1\text{H}\}$ NMR spectrum of **6b** in C_6D_6 .

NMR spectra of complex **6c**

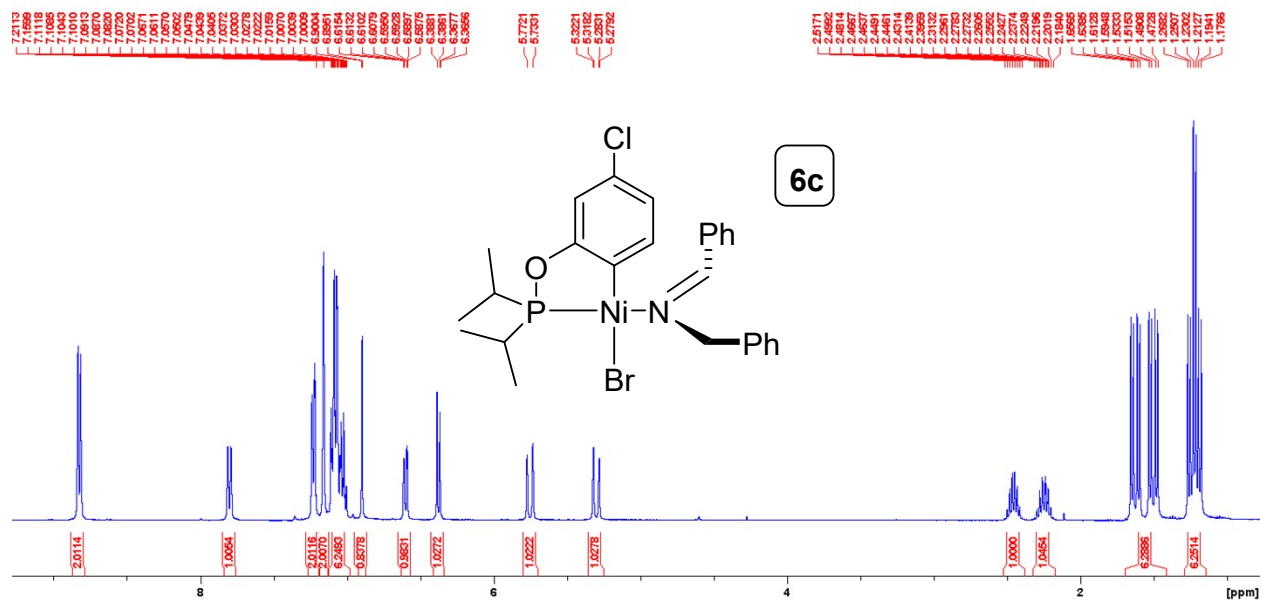


Figure S62. Full ^1H NMR spectrum of **6c** in C_6D_6 .

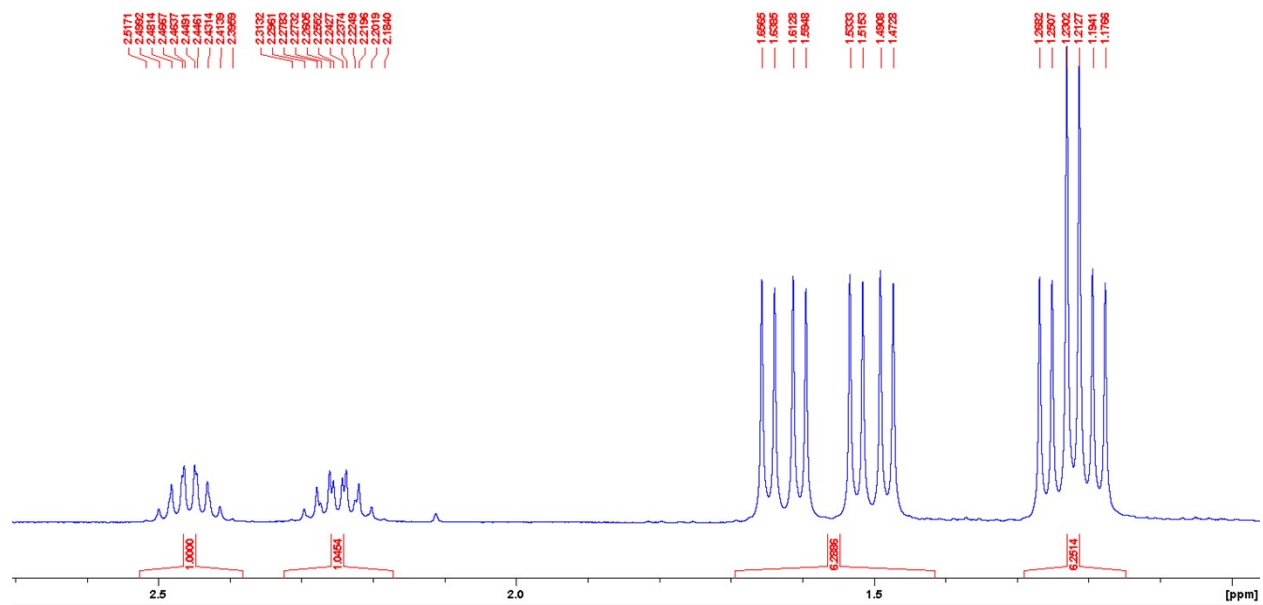


Figure S63. The aliphatic region of the ^1H NMR spectrum of **6c** in C_6D_6 .

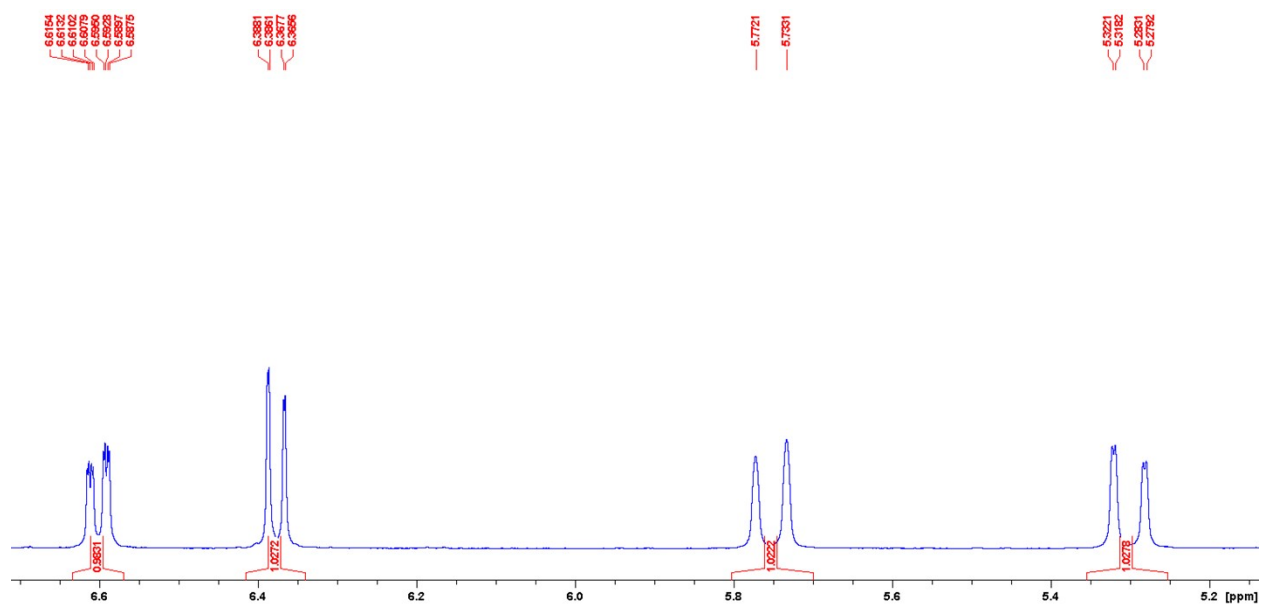


Figure S64. The olefinic region of the ^1H NMR spectrum of **6c** in C_6D_6 .

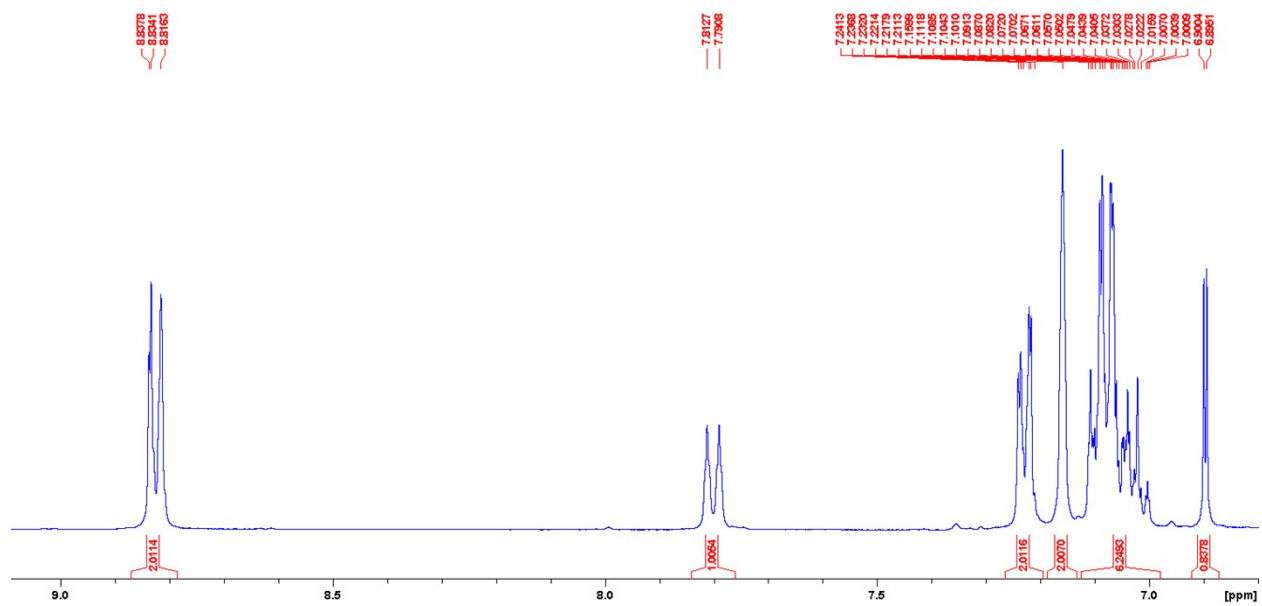


Figure S65. The aromatic region of the ^1H NMR spectrum of **6c** in C_6D_6 .

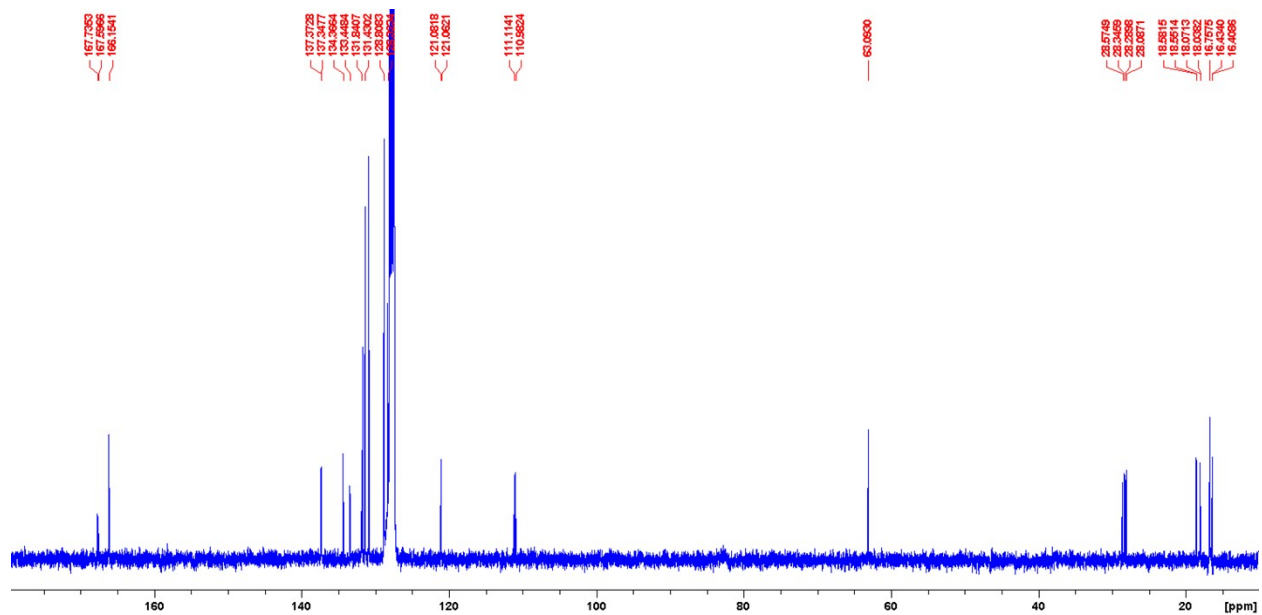


Figure S66. Full ^{13}C NMR spectrum of **6c** in C_6D_6 .

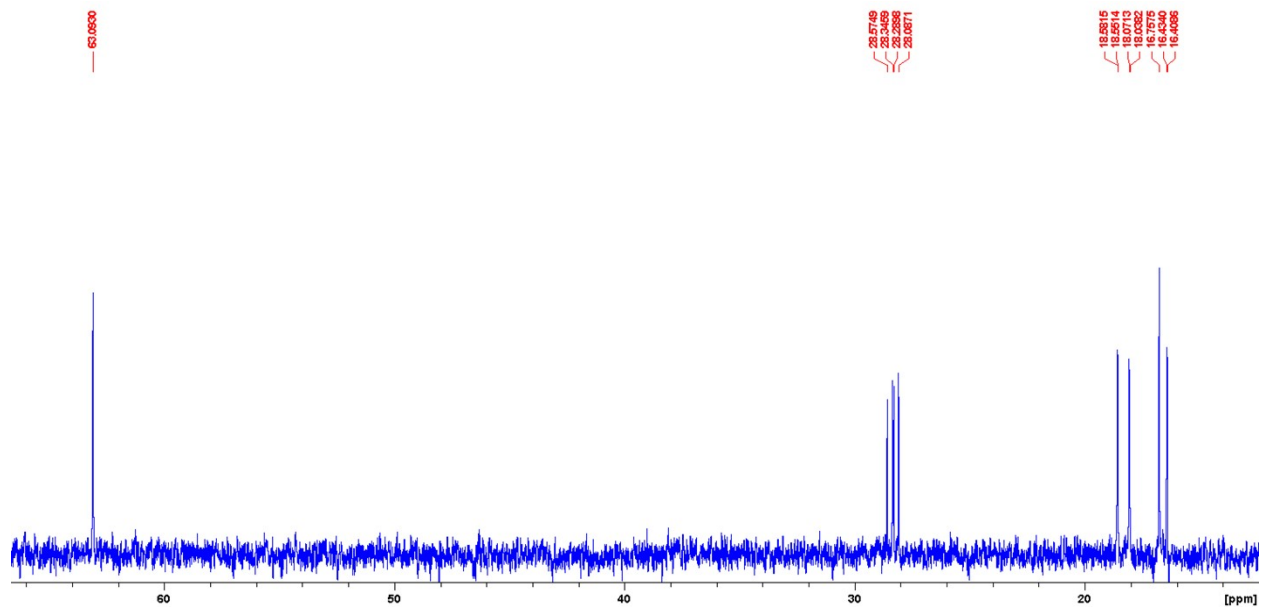


Figure S67. The aliphatic region of the ^{13}C NMR spectrum of **6c** in C_6D_6 .

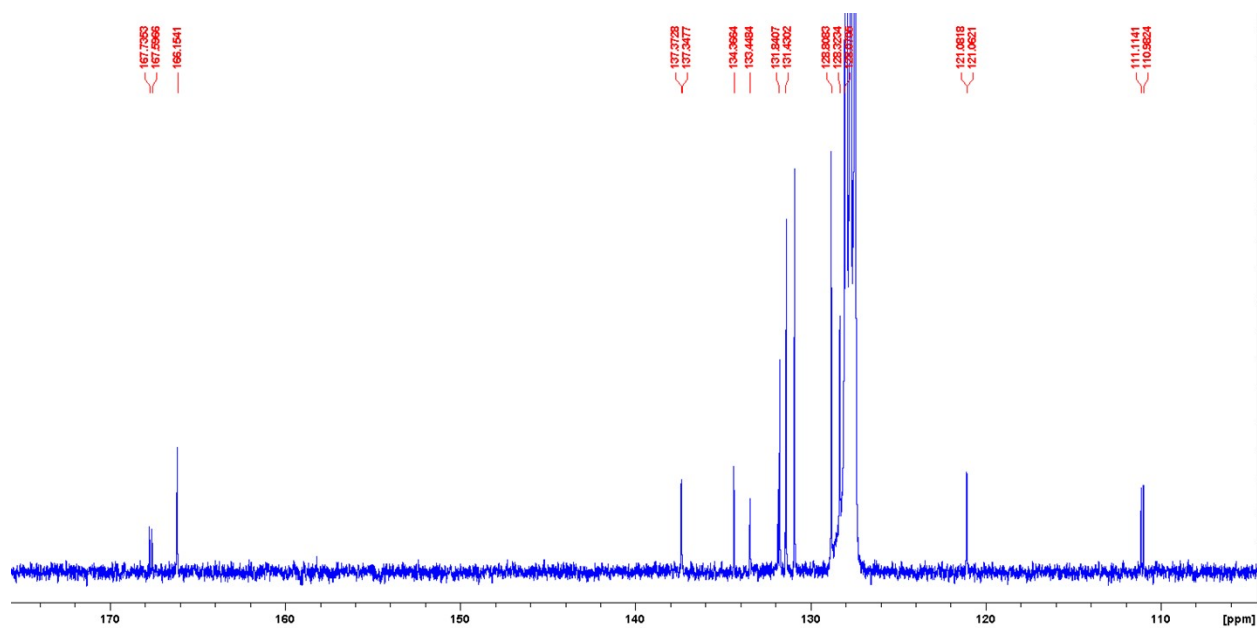


Figure S68. The aromatic region of the ^{13}C NMR spectrum of **6c** in C_6D_6 .

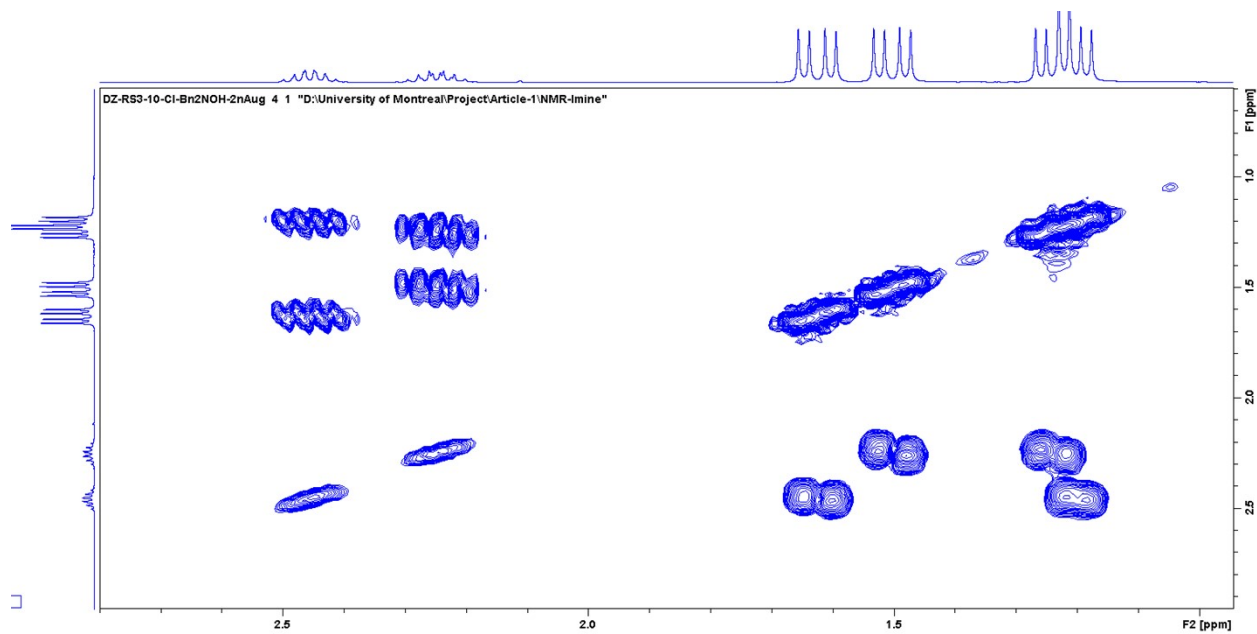


Figure S69. The aliphatic region of the COSY NMR spectrum of **6c** in C_6D_6 .

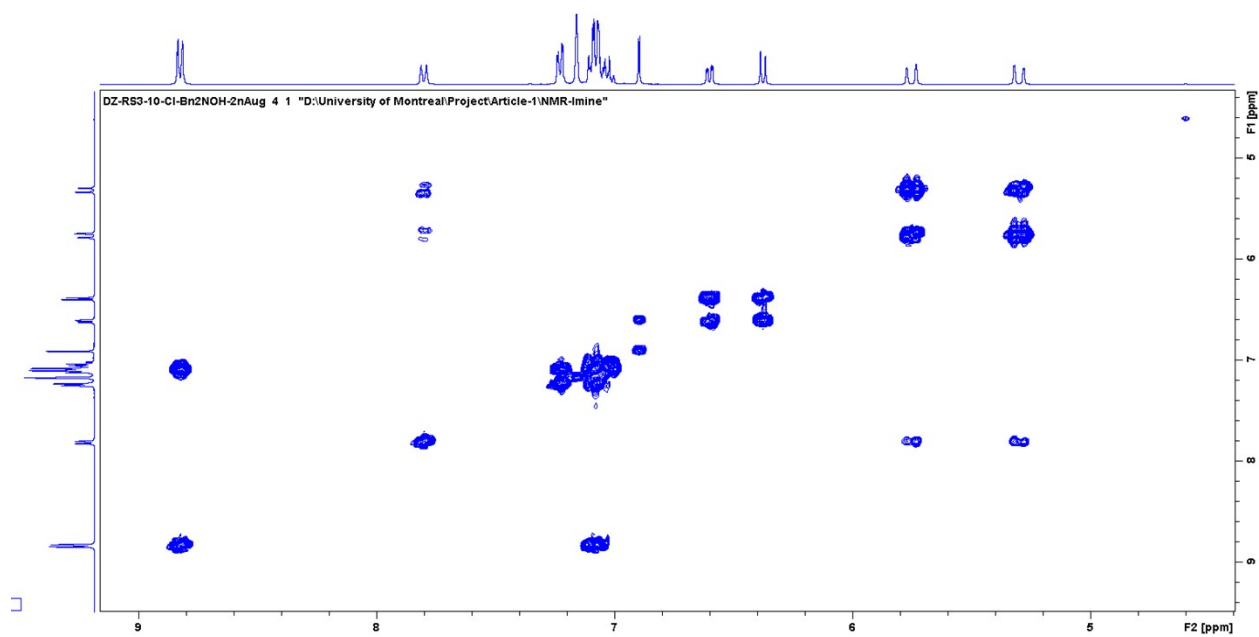


Figure S70. The aromatic region of the COSY NMR spectrum of **6c** in C_6D_6 .

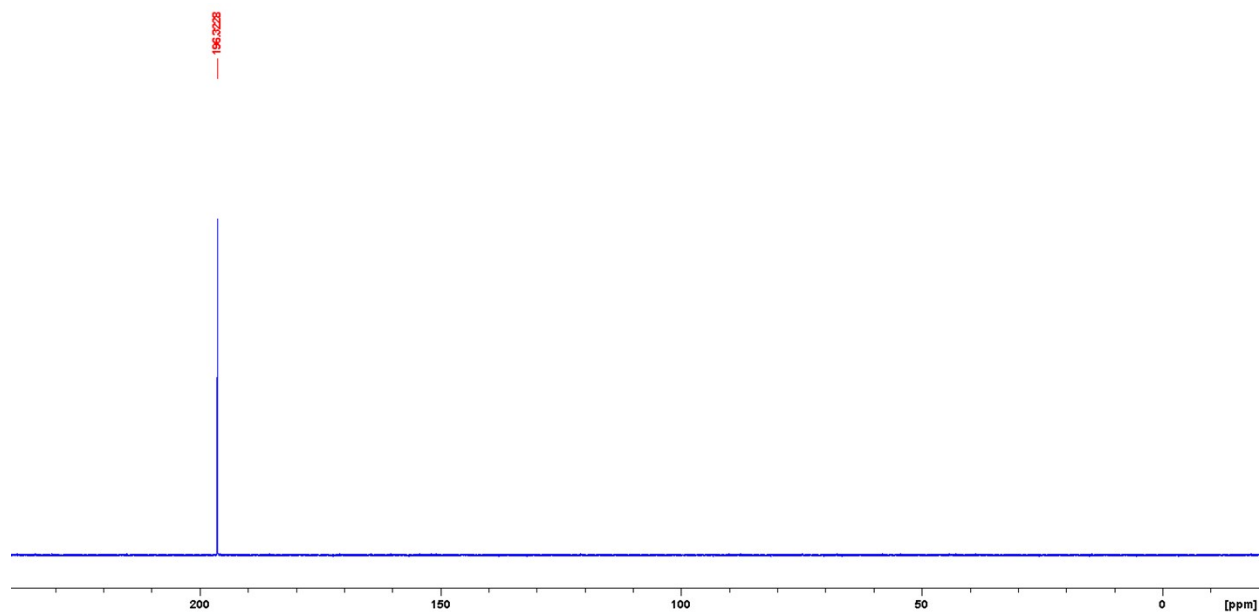


Figure S71. $^{31}P\{^1H\}$ NMR spectrum of **6c** in C_6D_6 .

NMR spectra of complex **7a**

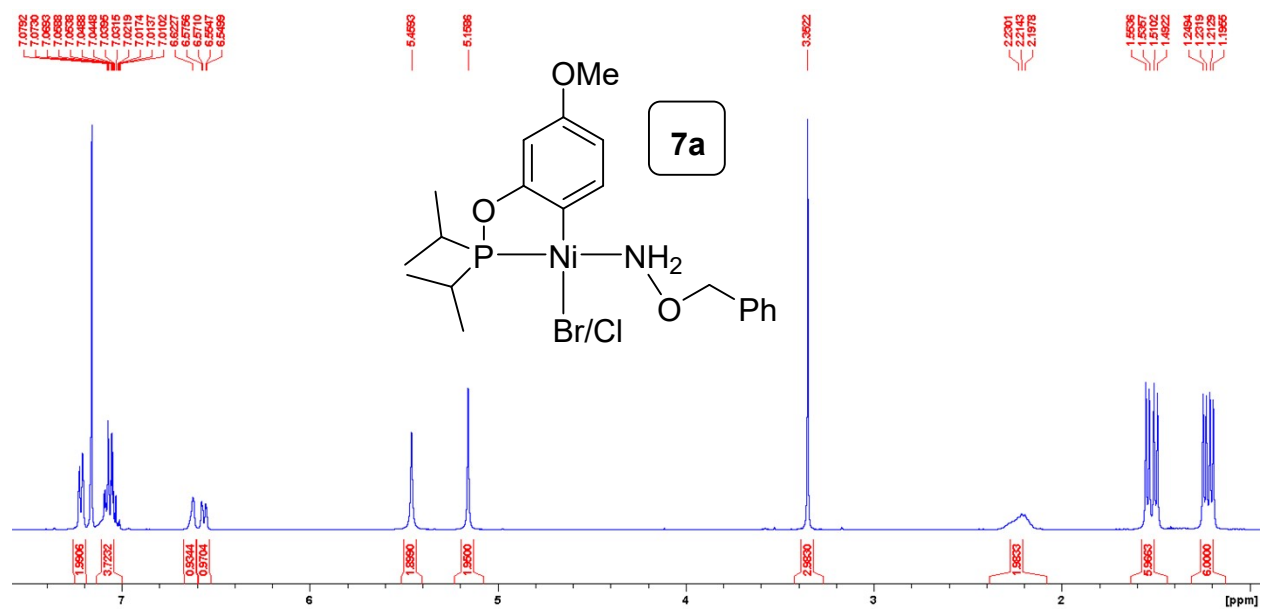


Figure S72. Full ¹H NMR spectrum of **7a** in C₆D₆.

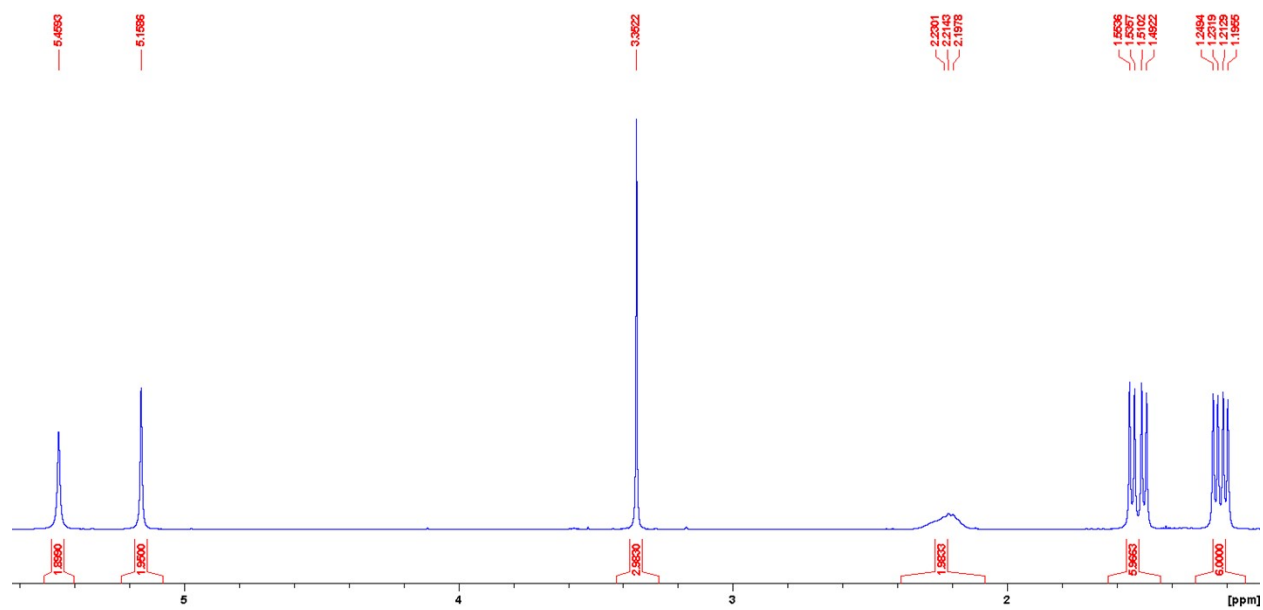


Figure S73. The aliphatic region of the ¹H NMR spectrum of **7a** in C₆D₆.

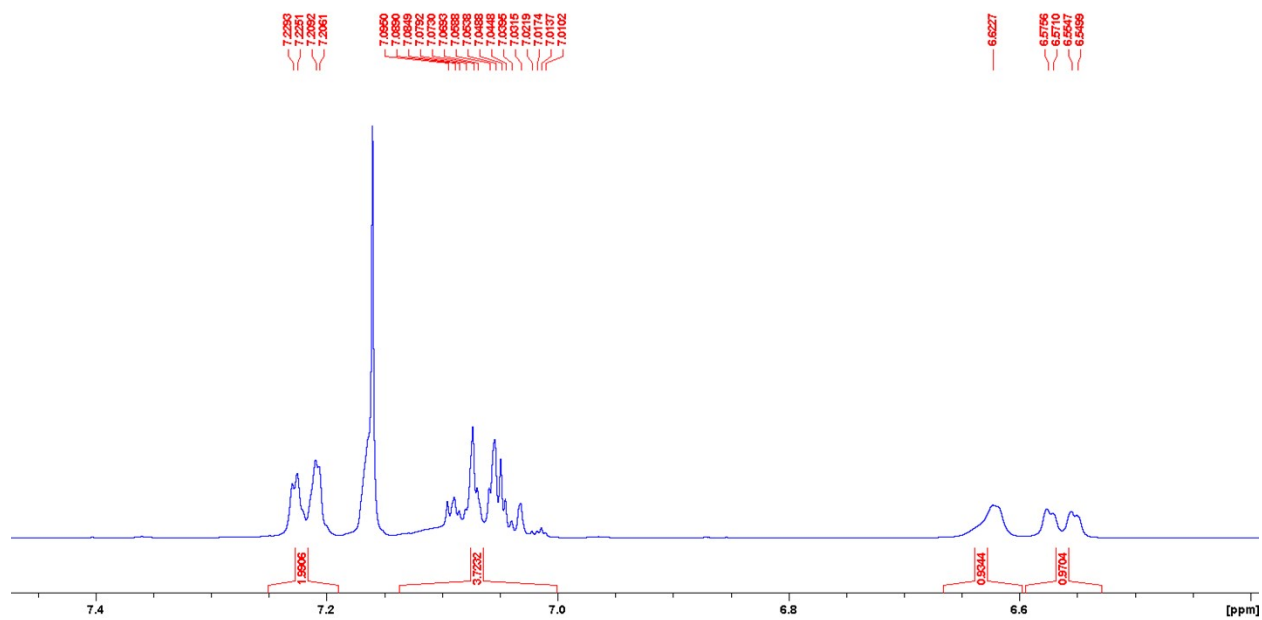


Figure S74. The aromatic region of the ^1H NMR spectrum of **7a** in C_6D_6 .

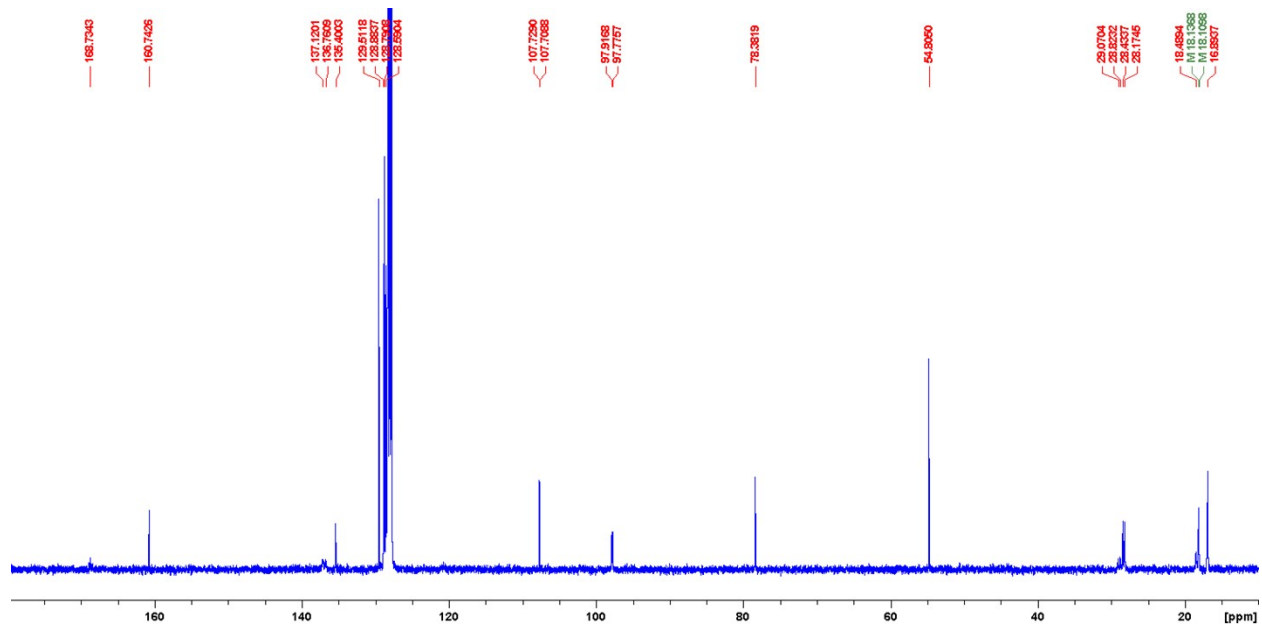


Figure S75. Full ^{13}C NMR spectrum of **7a** in C_6D_6 .

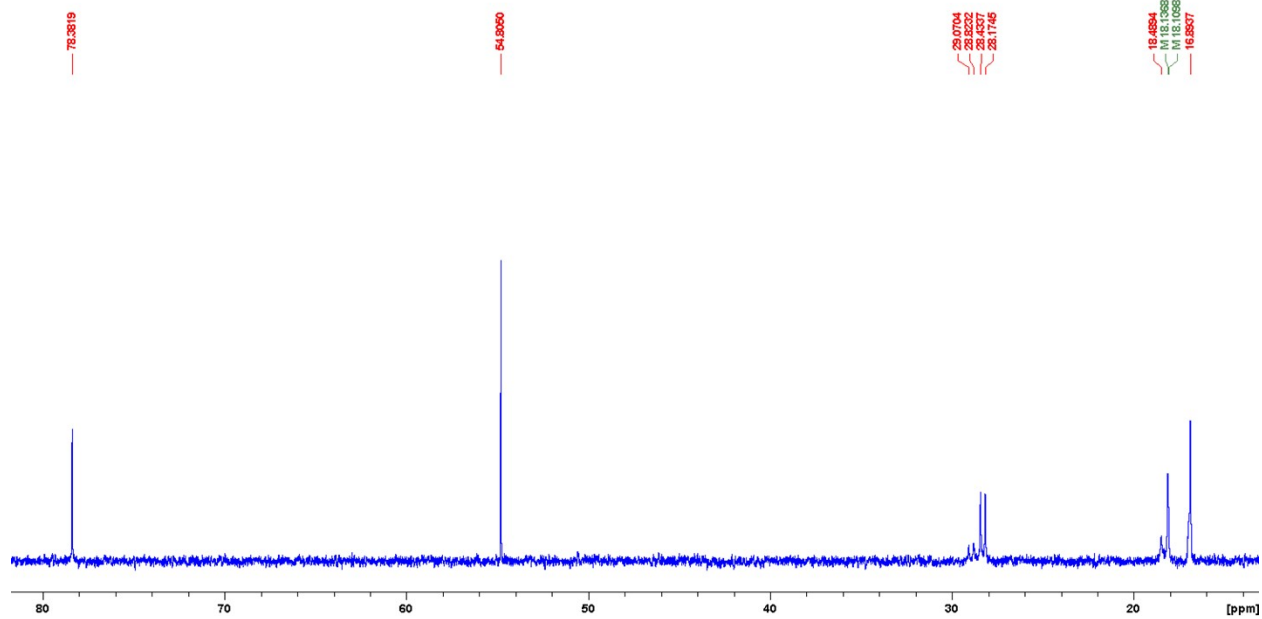


Figure S76. The aliphatic region of the ^{13}C NMR spectrum of **7a** in C_6D_6 .

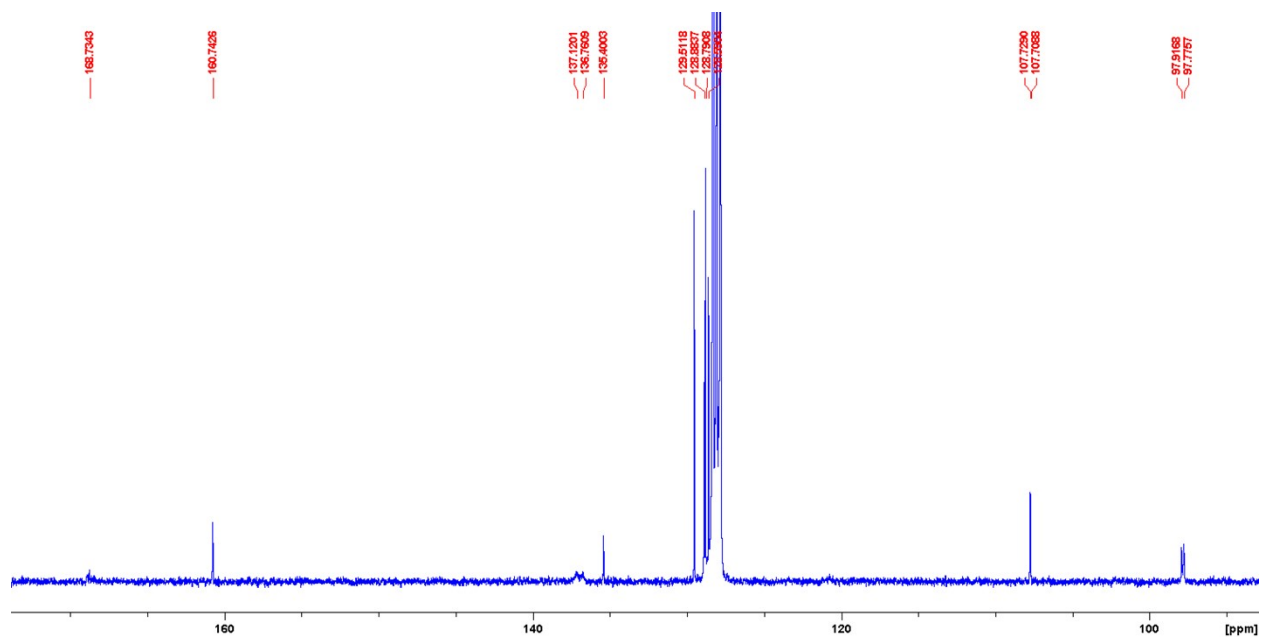


Figure S77. The aromatic region of the ^{13}C NMR spectrum of **7a** in C_6D_6 .

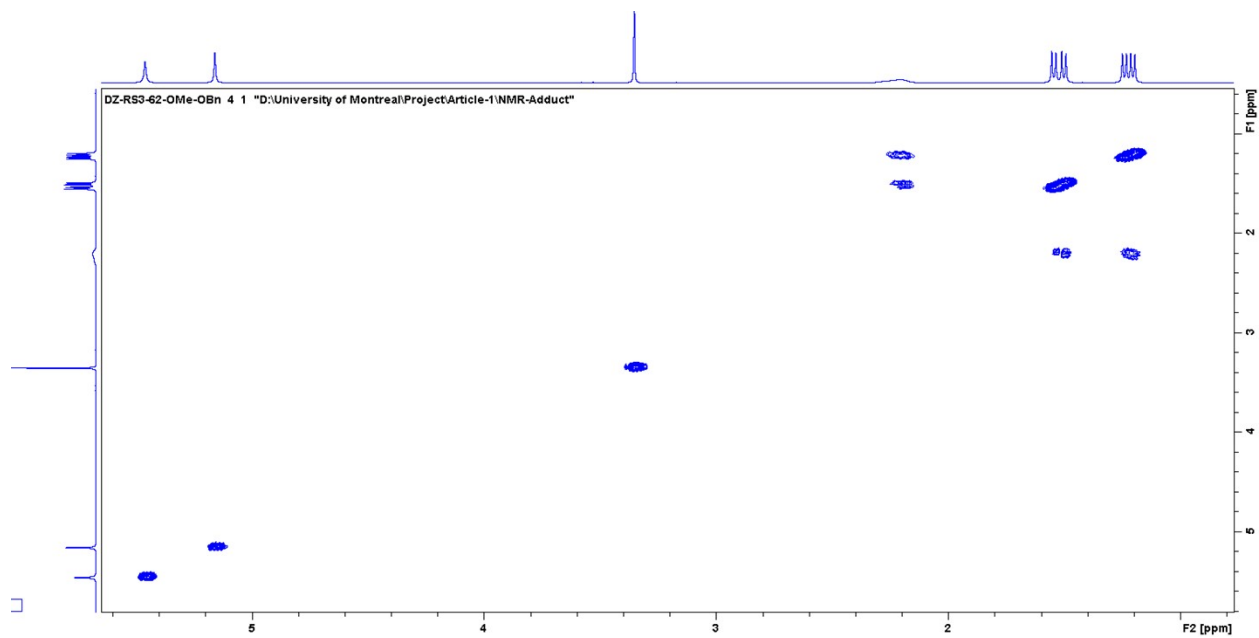


Figure S78. The aliphatic region of the COSY NMR spectrum of **7a** in C₆D₆.

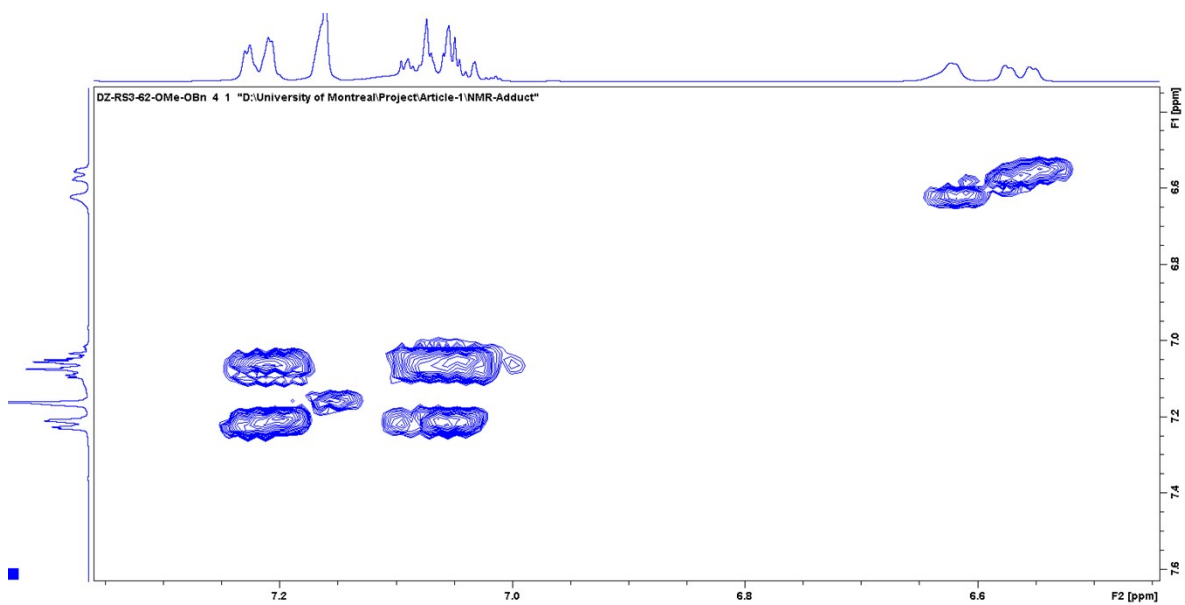


Figure S79. The aromatic region of the COSY NMR spectrum of **7a** in C₆D₆.

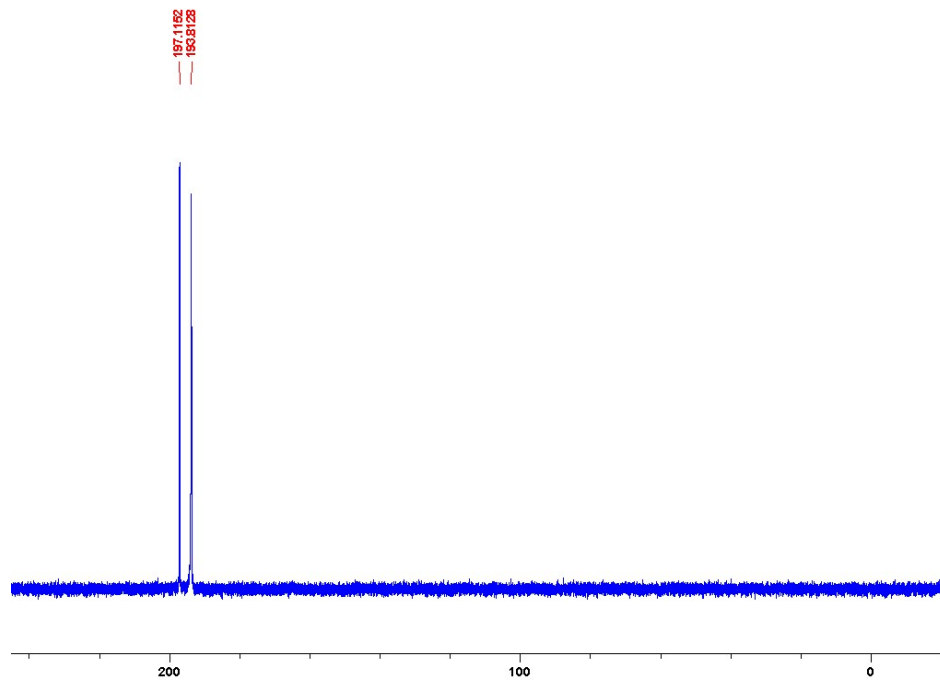


Figure S80. $^{31}\text{P}\{^1\text{H}\}$ NMR spectrum of **7a** in C_6D_6 .

NMR spectra of complex 7b

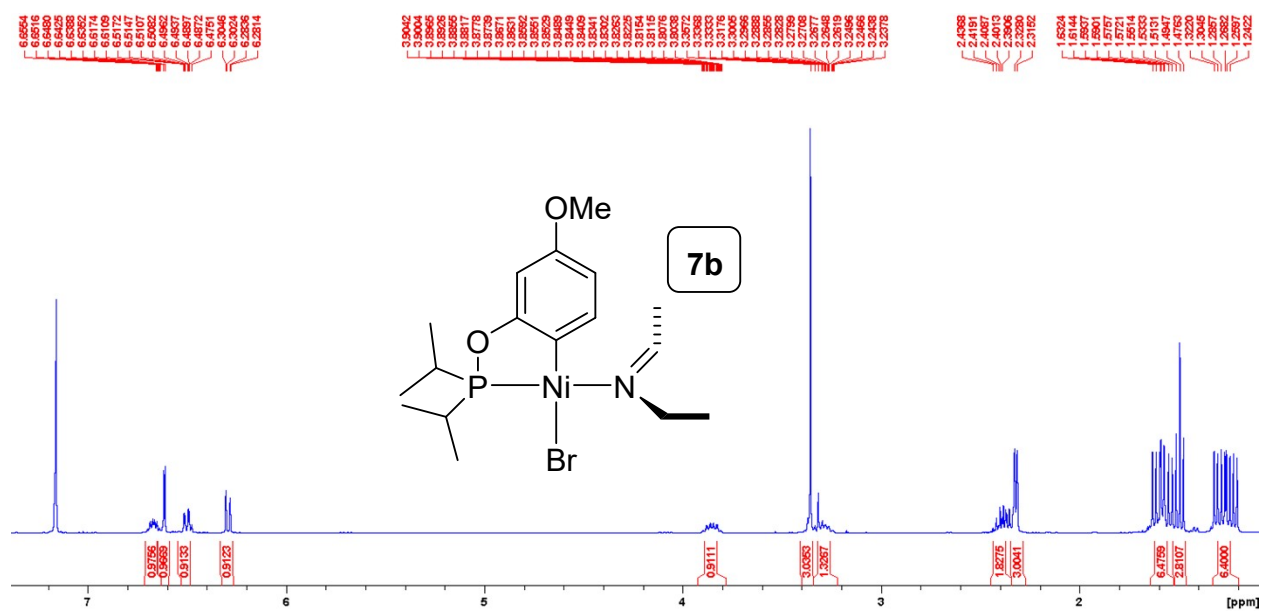


Figure S81. Full ¹H NMR spectrum of 7b in C₆D₆.

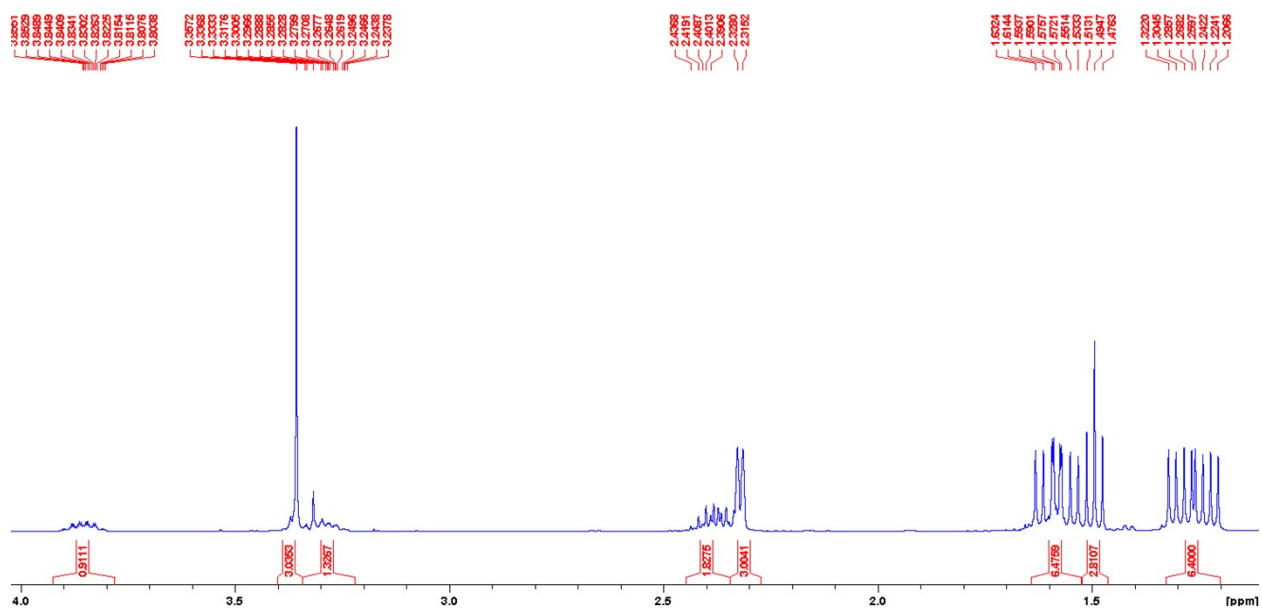


Figure S82. The aliphatic region of the ¹H NMR spectrum of 7b in C₆D₆.

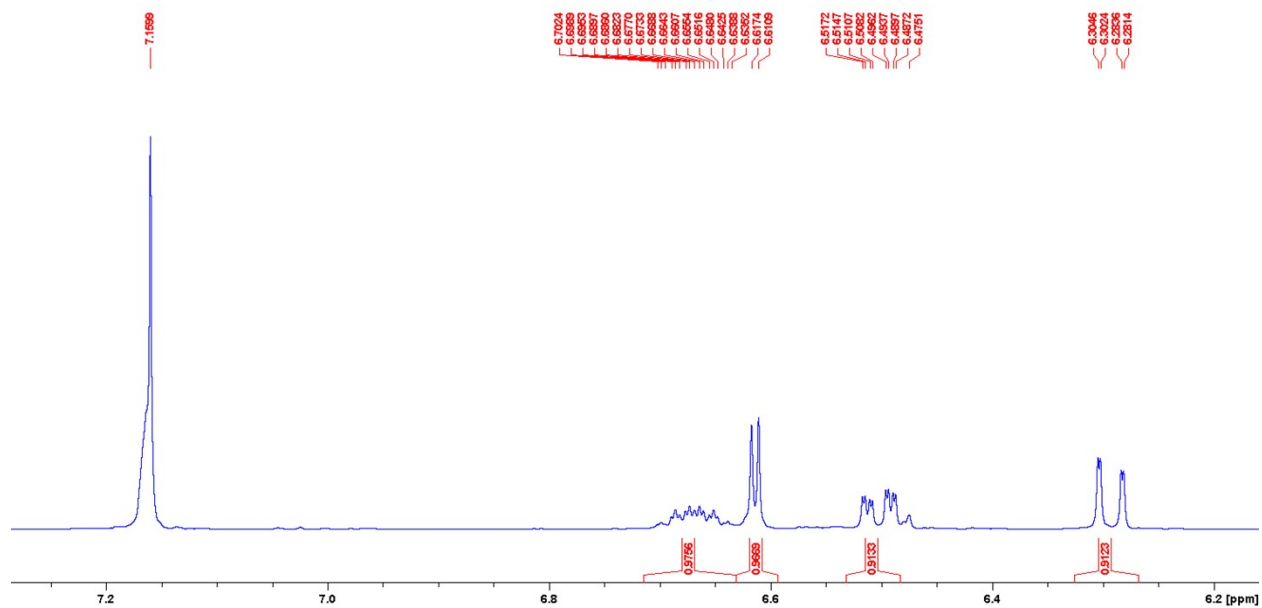


Figure S83. The aromatic region of the ^1H NMR spectrum of **7b** in C_6D_6 .

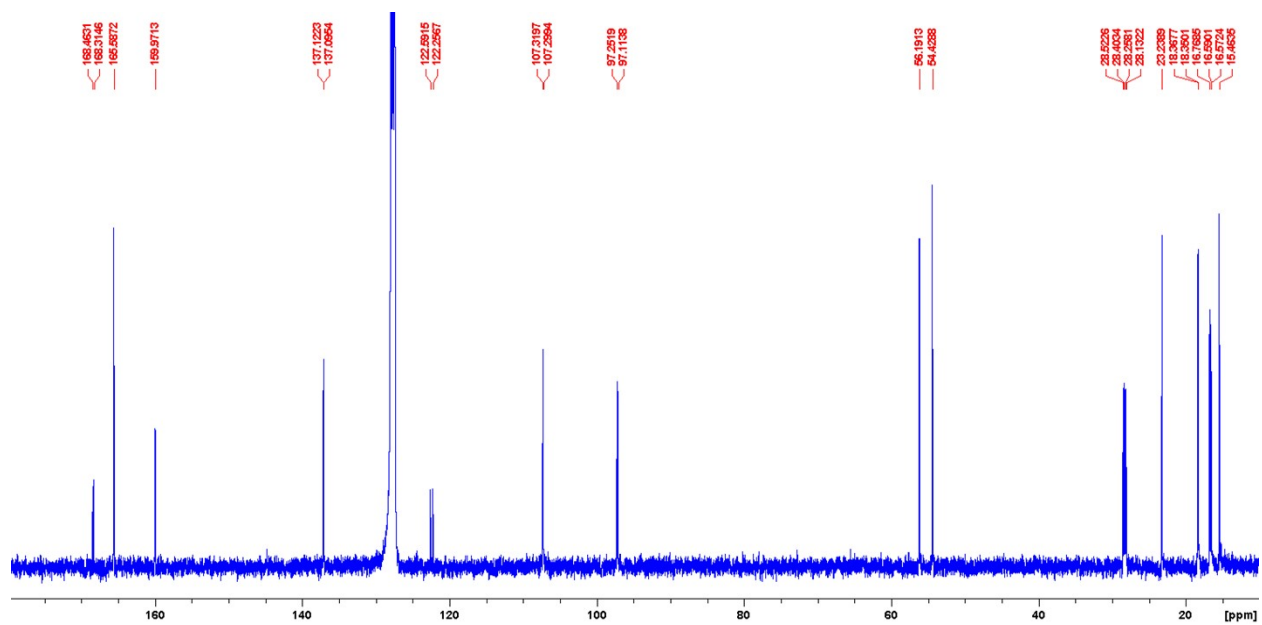


Figure S84. Full ^{13}C NMR spectrum of **7b** in C_6D_6 .

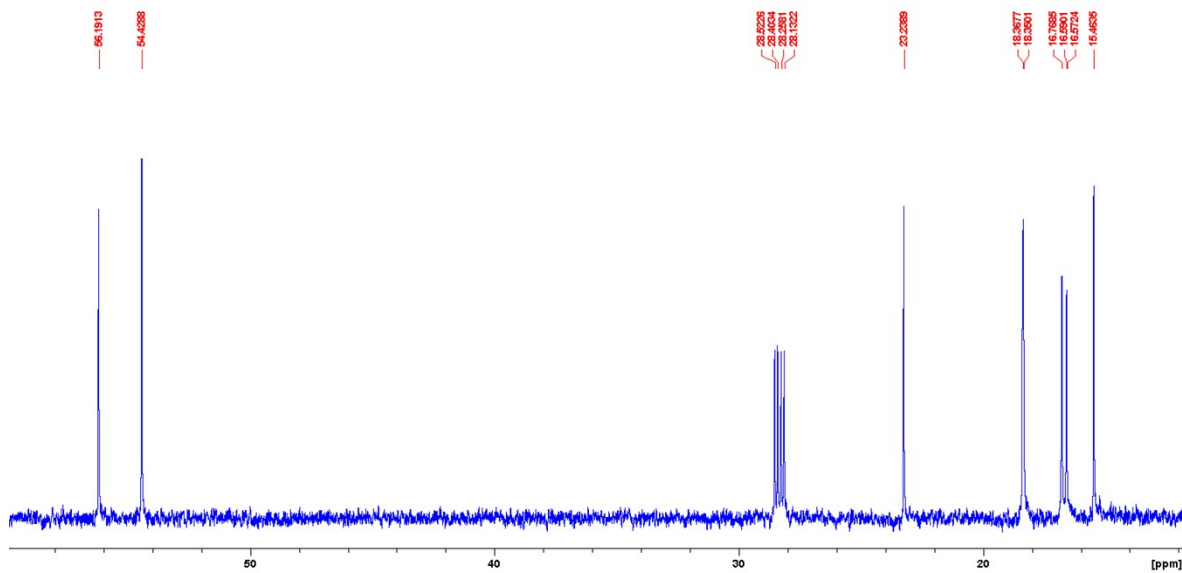


Figure S85. The aliphatic region of the ^{13}C NMR spectrum of **7b** in C_6D_6 .

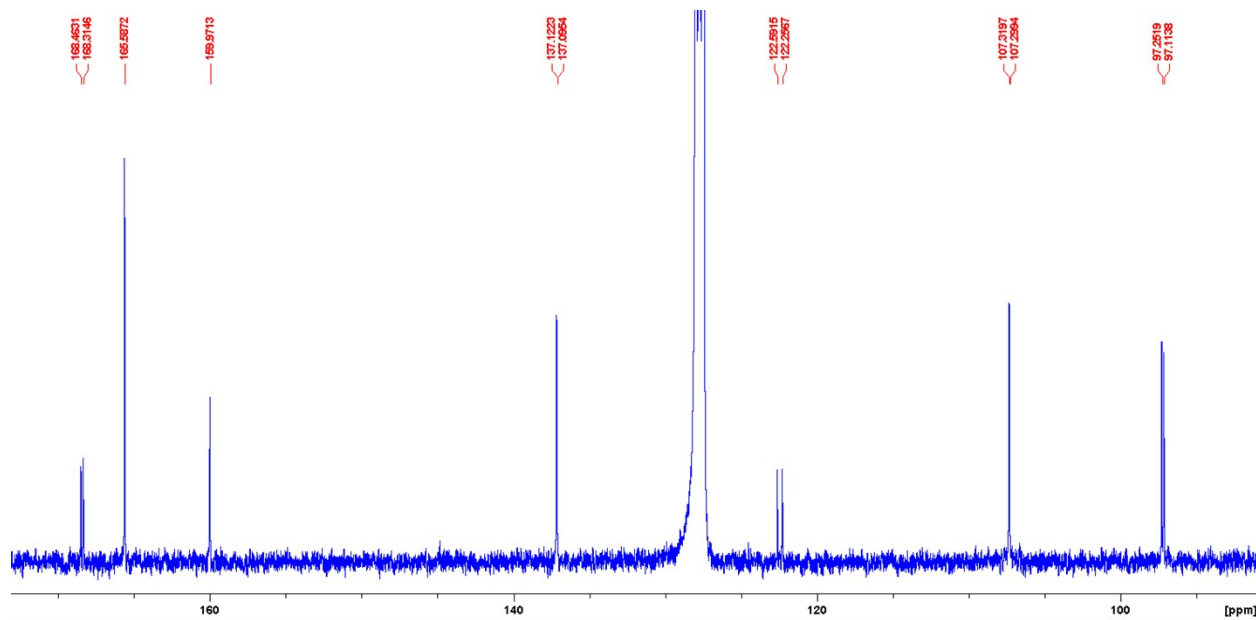


Figure S86. The aromatic region of the ^{13}C NMR spectrum of **7b** in C_6D_6 .

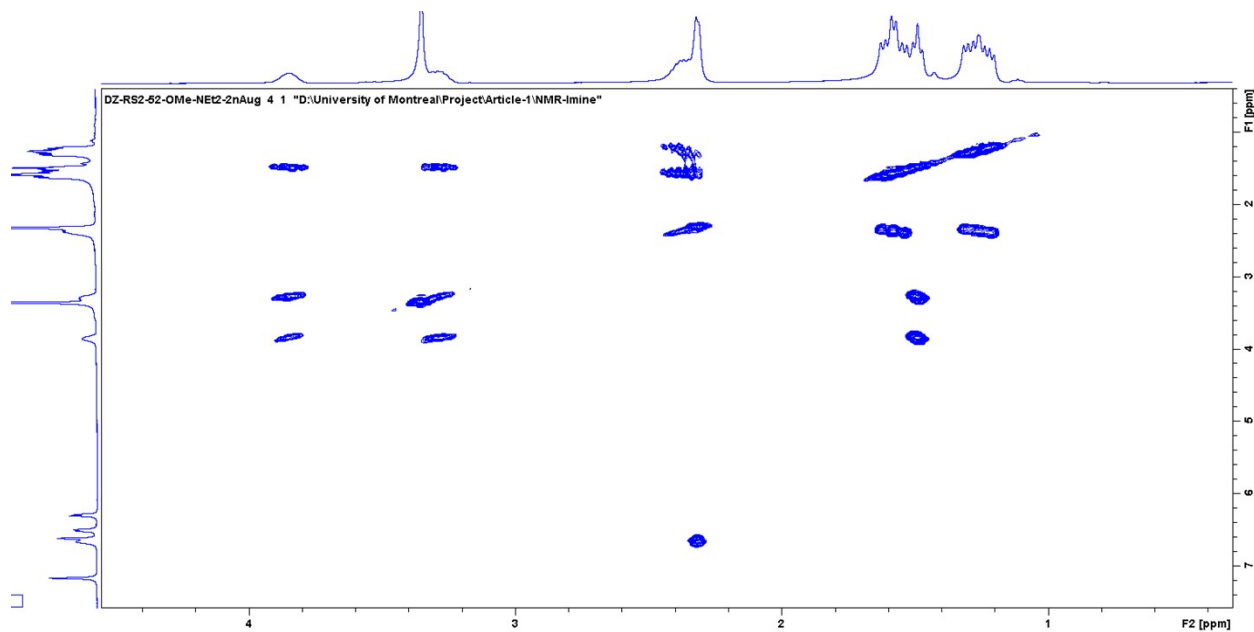


Figure S87. The aliphatic region of the COSY NMR spectrum of **7b** in C_6D_6 .

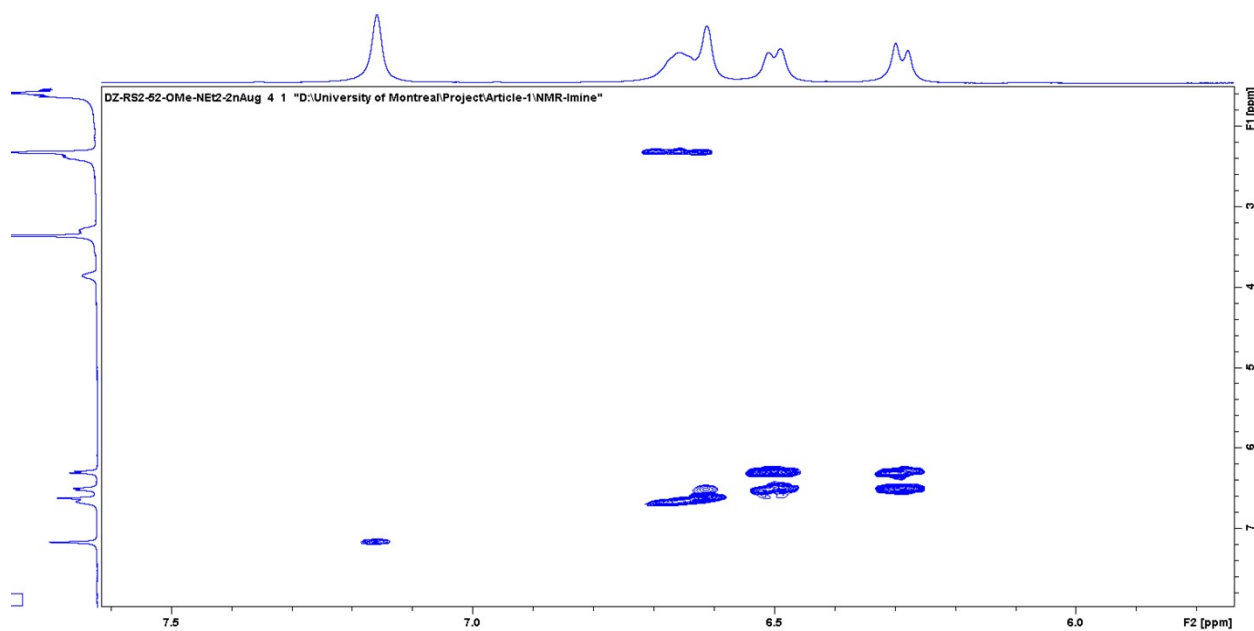


Figure S88. The aromatic region of the COSY NMR spectrum of **7b** in C_6D_6 .

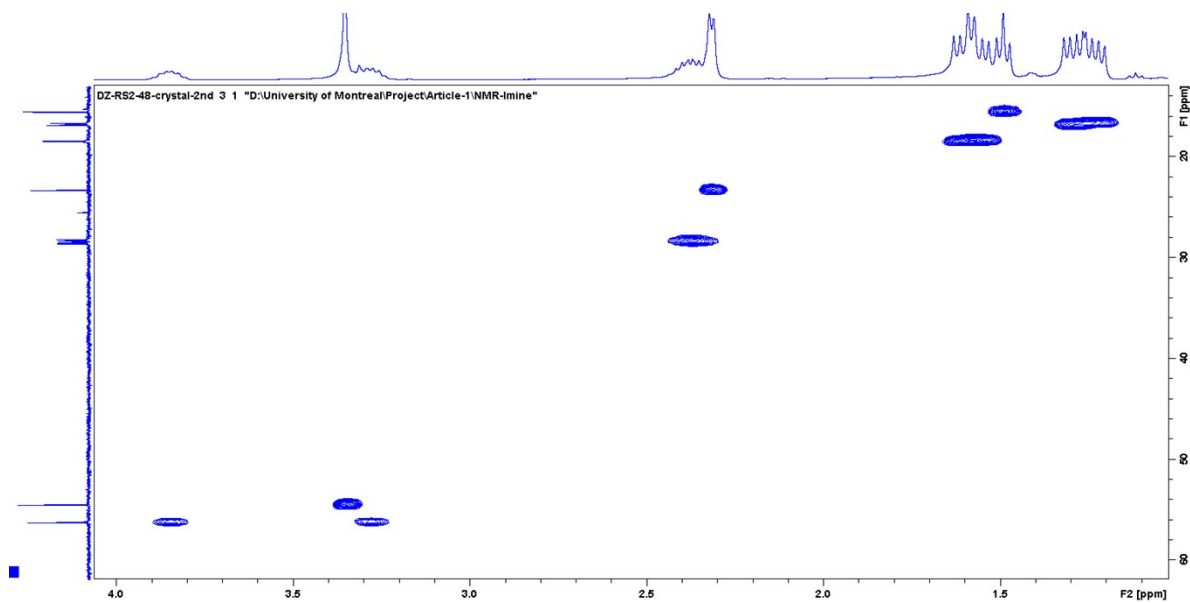


Figure S89. The aliphatic region of the HSQC NMR spectrum of **7b** in C_6D_6 .

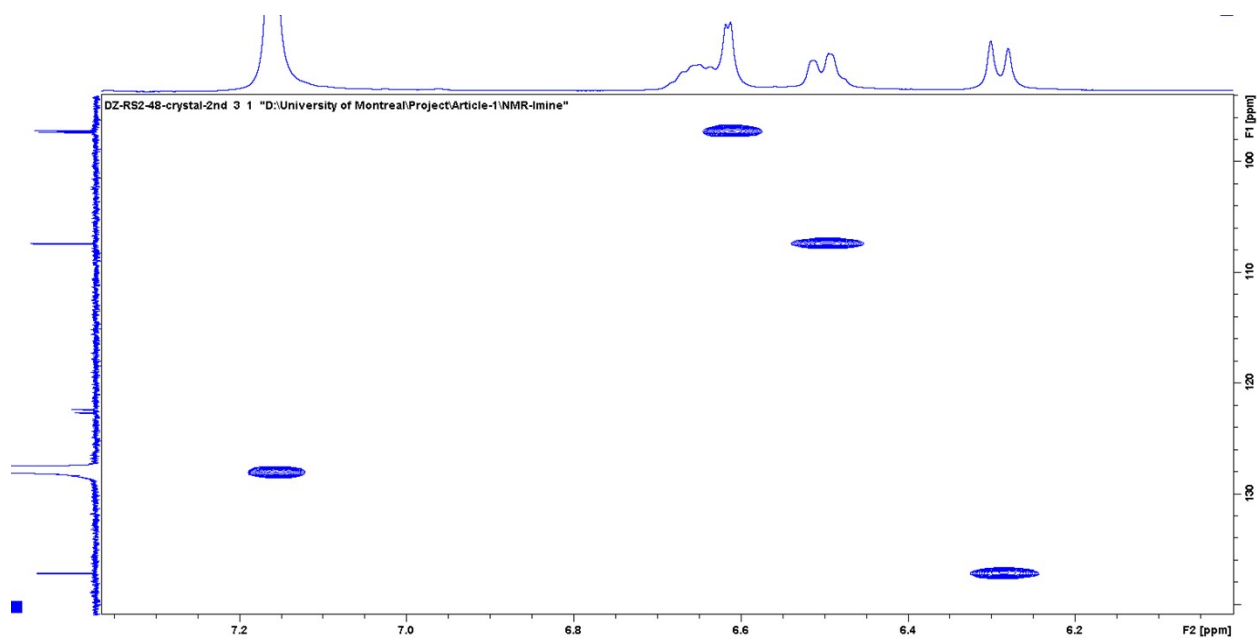


Figure S90. The aromatic region of the HSQC NMR spectrum of **7b** in C_6D_6 .

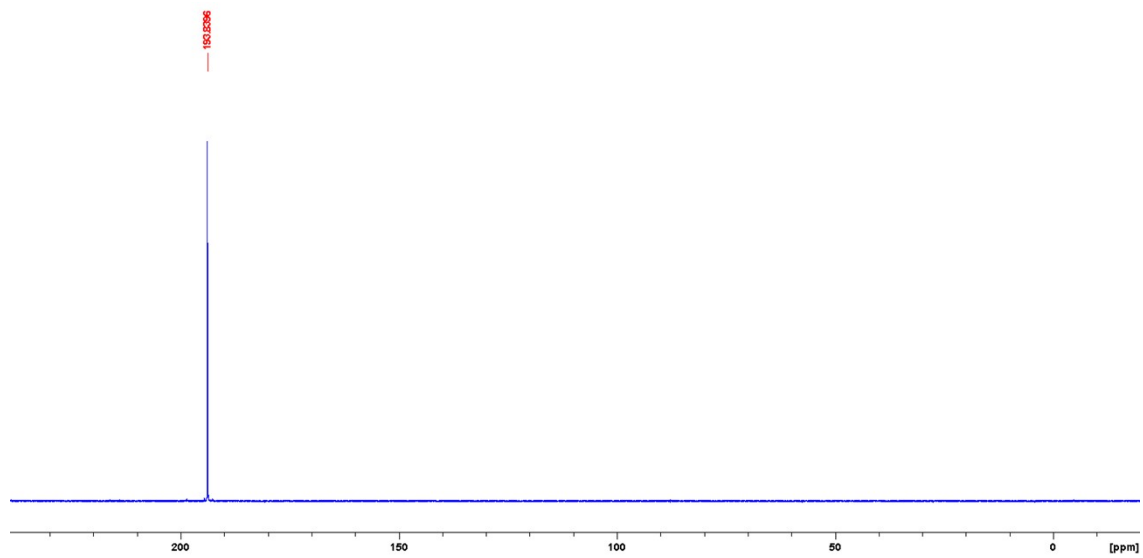


Figure S91. $^{31}\text{P}\{^1\text{H}\}$ NMR spectrum of **7b** in C_6D_6 .

NMR spectra of complex **7c**

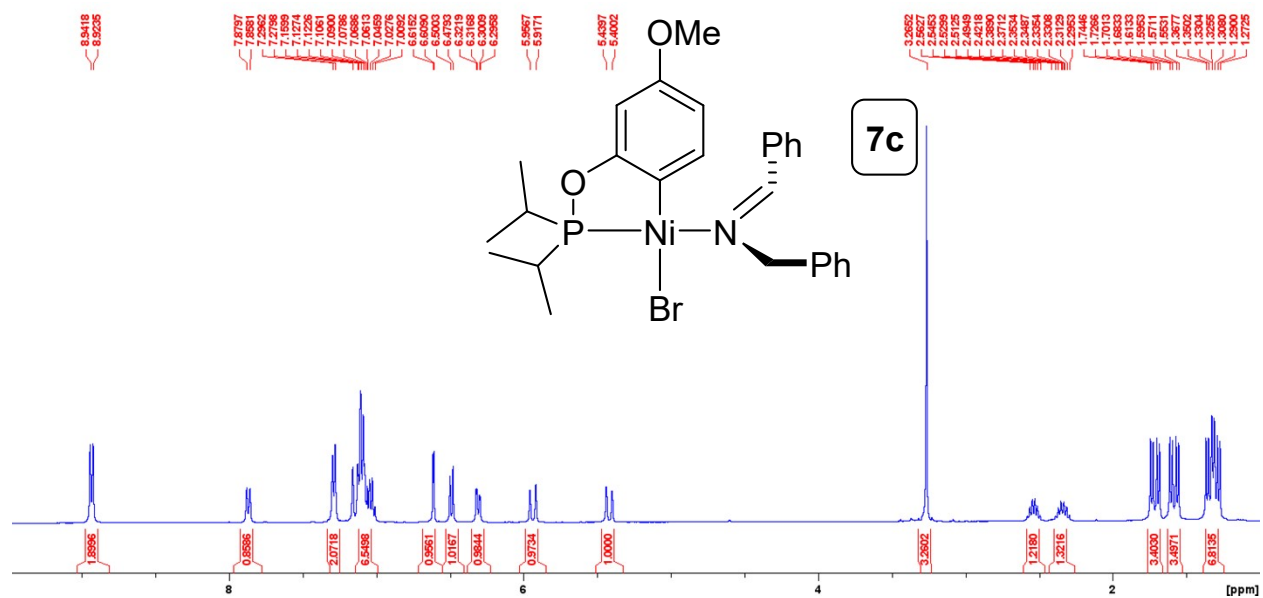


Figure S92. Full ^1H NMR spectrum of **7c** in C_6D_6 .

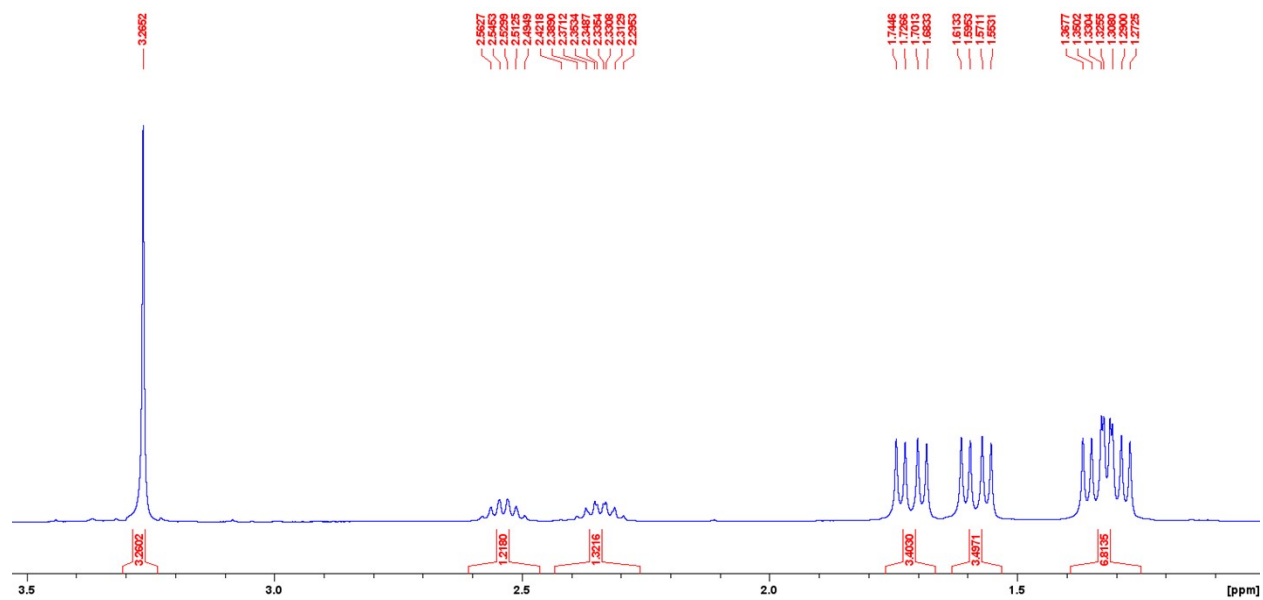


Figure S93. The aliphatic region of the ^1H NMR spectrum of **7c** in C_6D_6 .

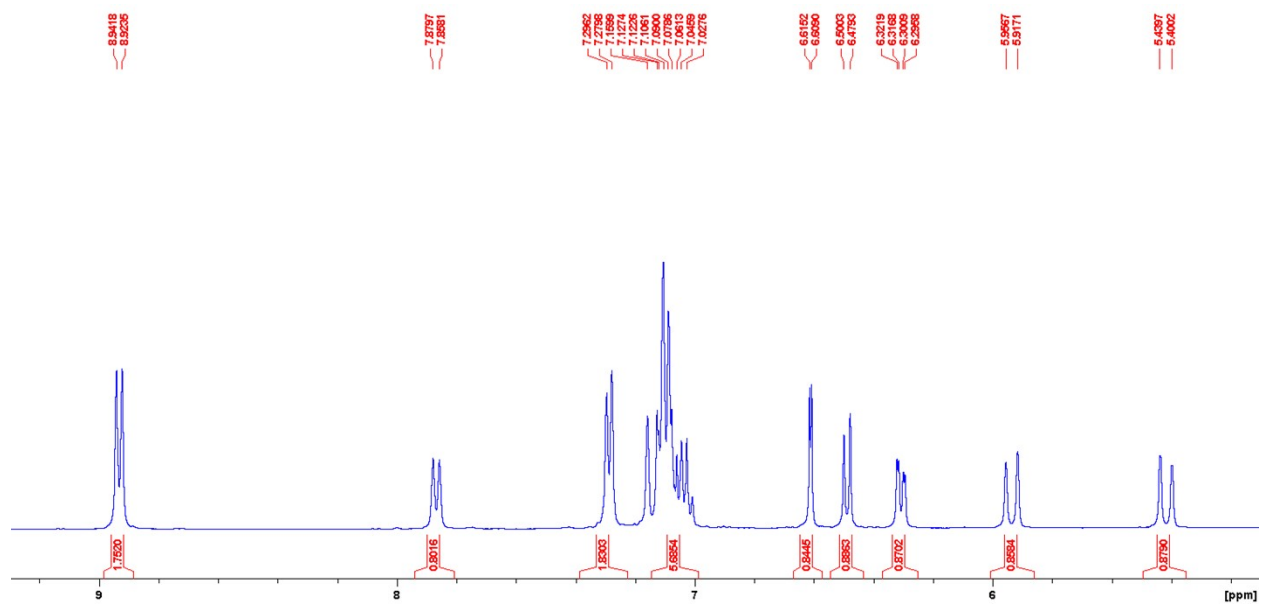


Figure S94. The aromatic region of the ^1H NMR spectrum of **7c** in C_6D_6 .

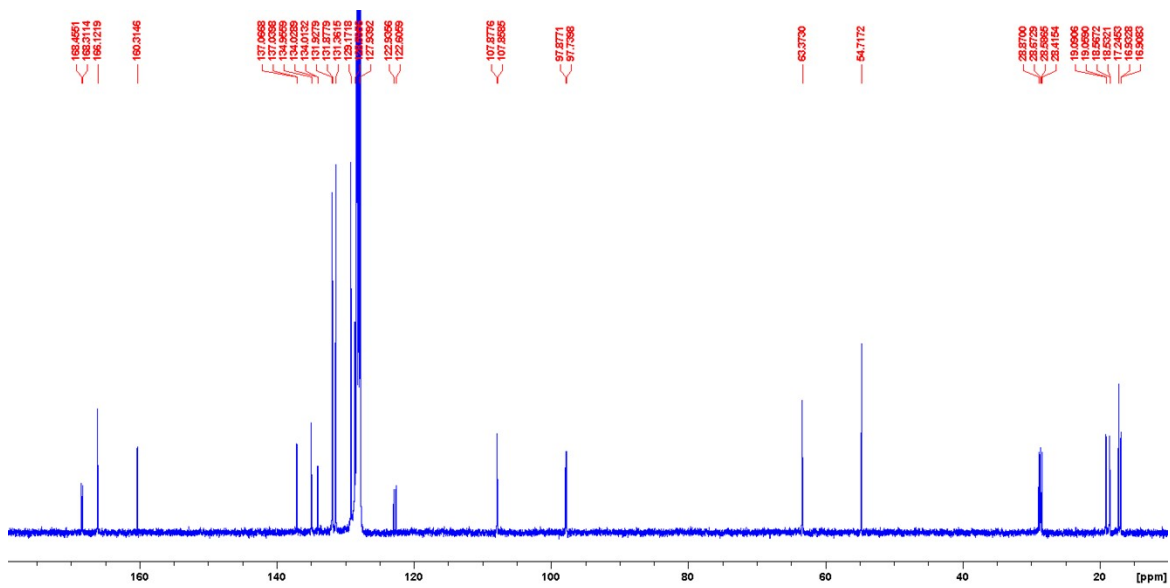


Figure S95. Full ^{13}C NMR spectrum of **7c** in C_6D_6 .

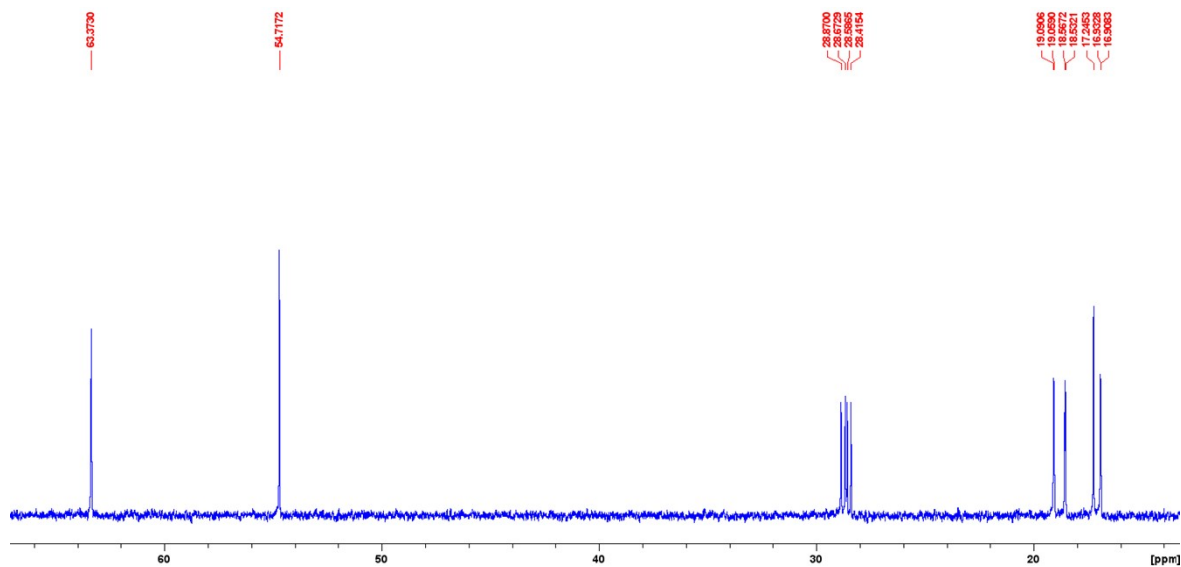


Figure S96. The aliphatic region of the ^{13}C NMR spectrum of **7c** in C_6D_6 .

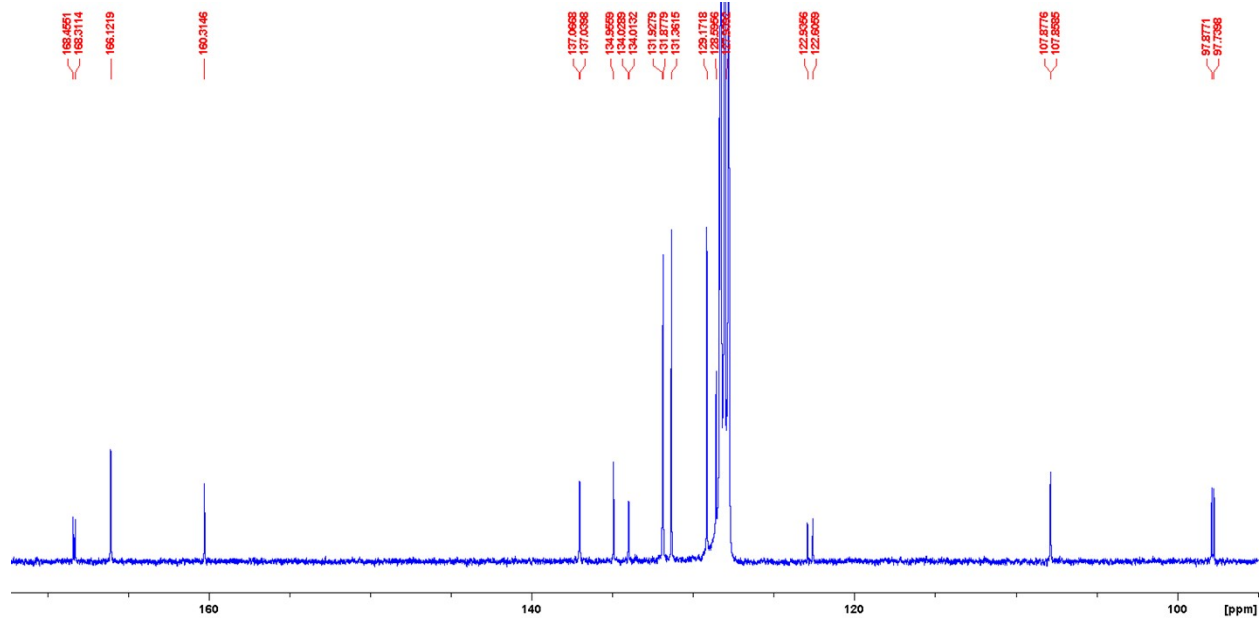


Figure S97. The aromatic region of the ^{13}C NMR spectrum of **7c** in C_6D_6 .

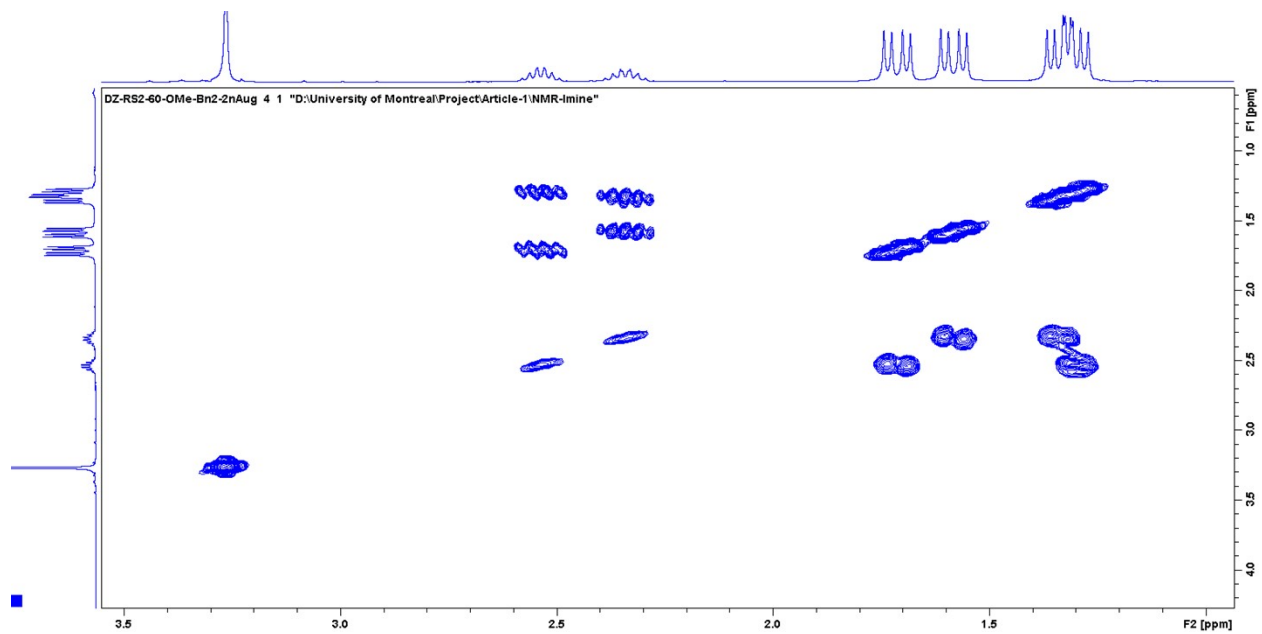


Figure S98. The aliphatic region of the COSY NMR spectrum of **7c** in C_6D_6 .

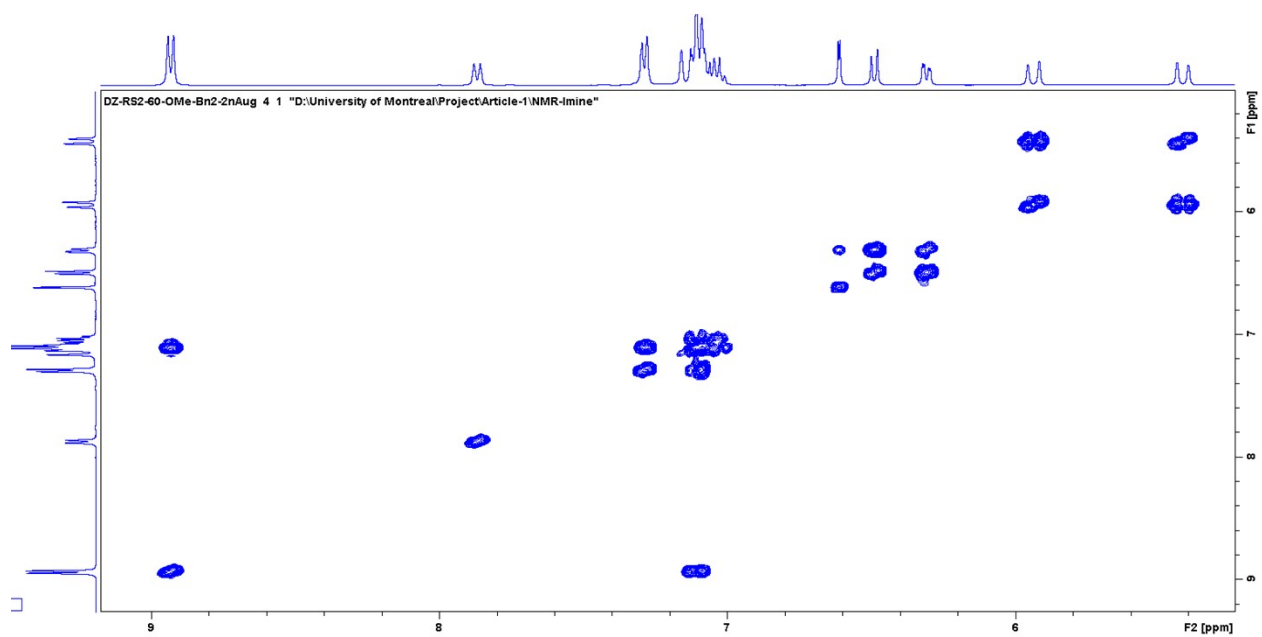


Figure S99. The aromatic region of the COSY NMR spectrum of **7c** in C_6D_6 .

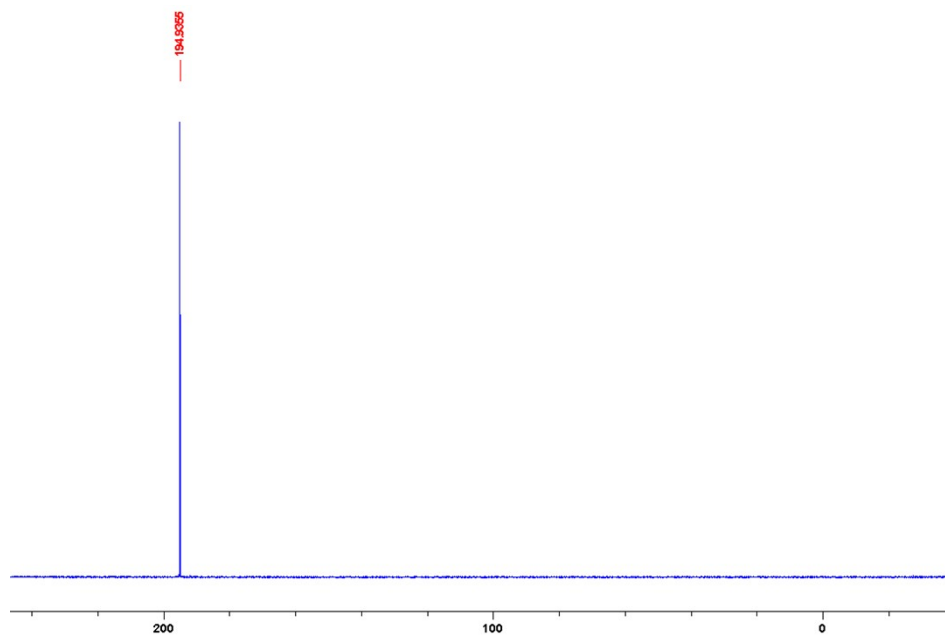


Figure S100. $^{31}\text{P}\{^1\text{H}\}$ NMR spectrum of **7c** in C_6D_6 .

NMR spectra of complex **7d**

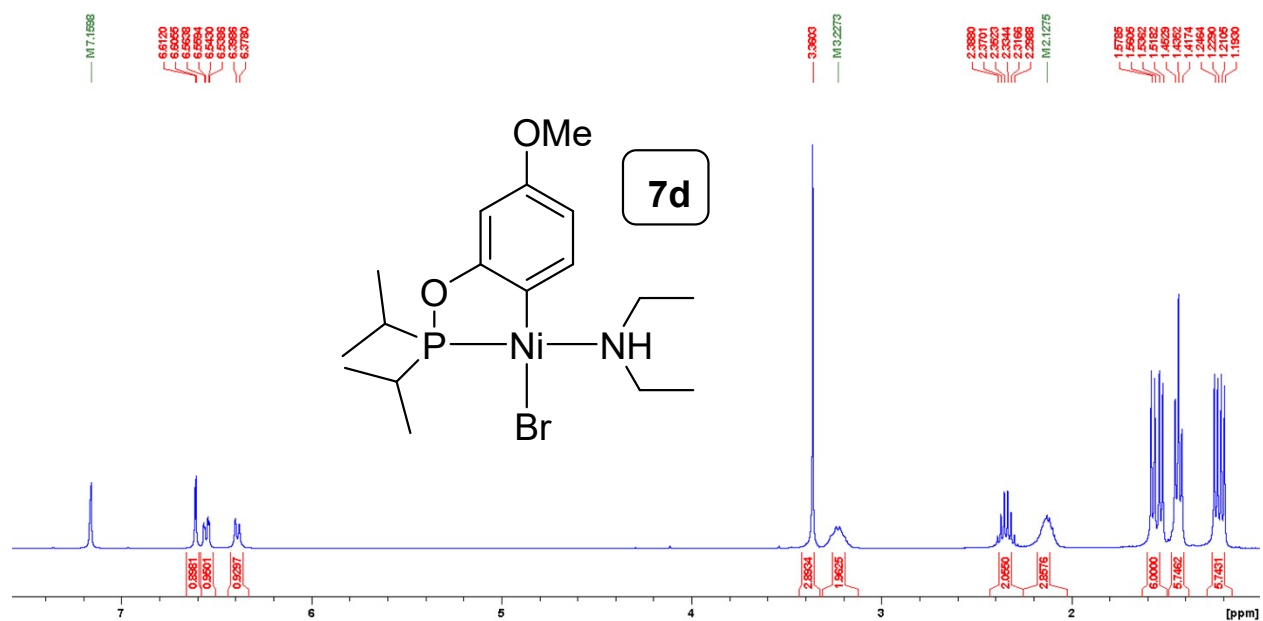


Figure 101. Full ^1H NMR spectrum of **7d** in C_6D_6 .

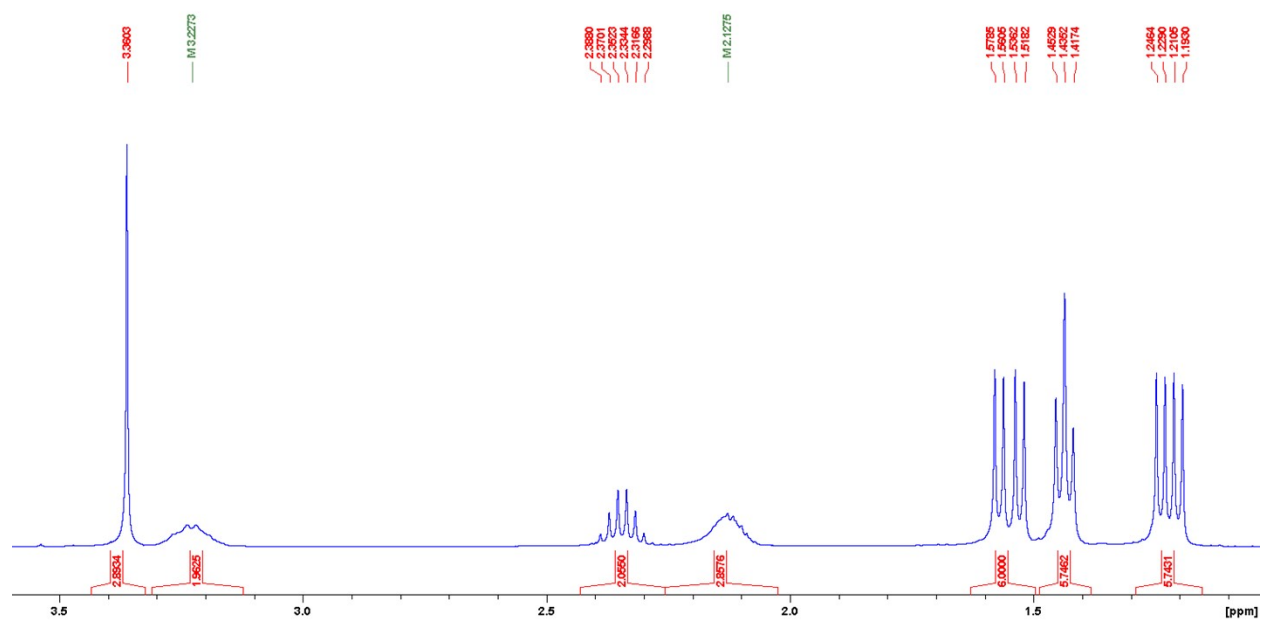


Figure S102. The aliphatic region of the ^1H NMR spectrum of **7d** in C_6D_6 .

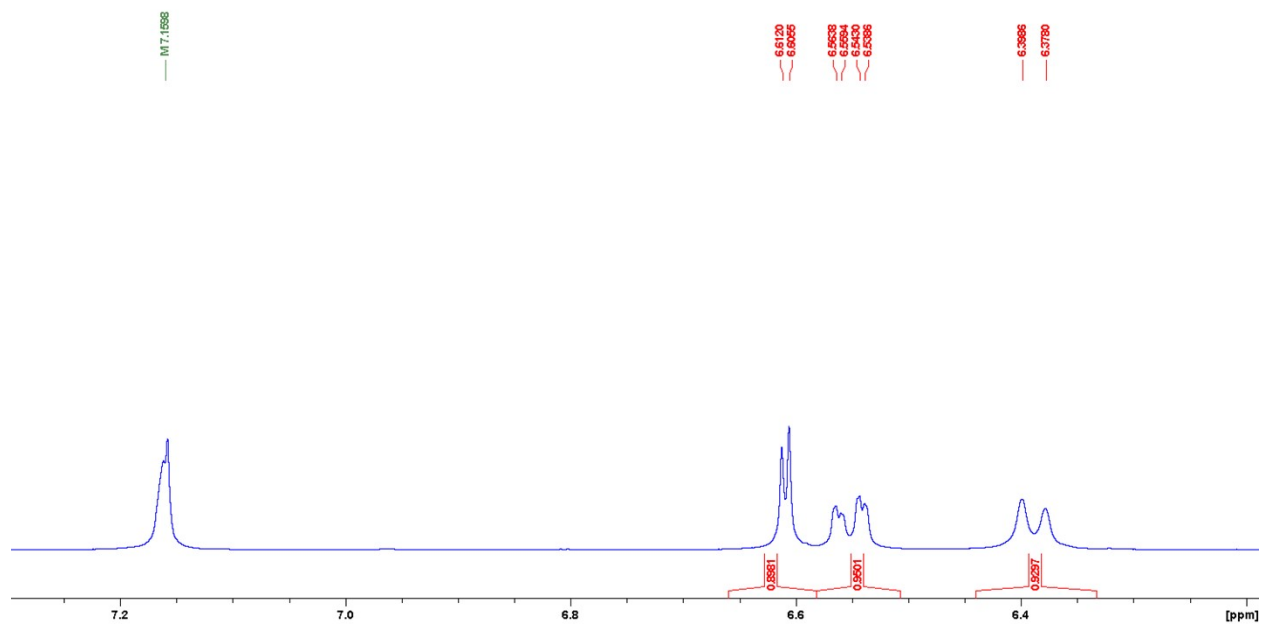


Figure S103. The aromatic region of the ^1H NMR spectrum of **7d** in C_6D_6 .

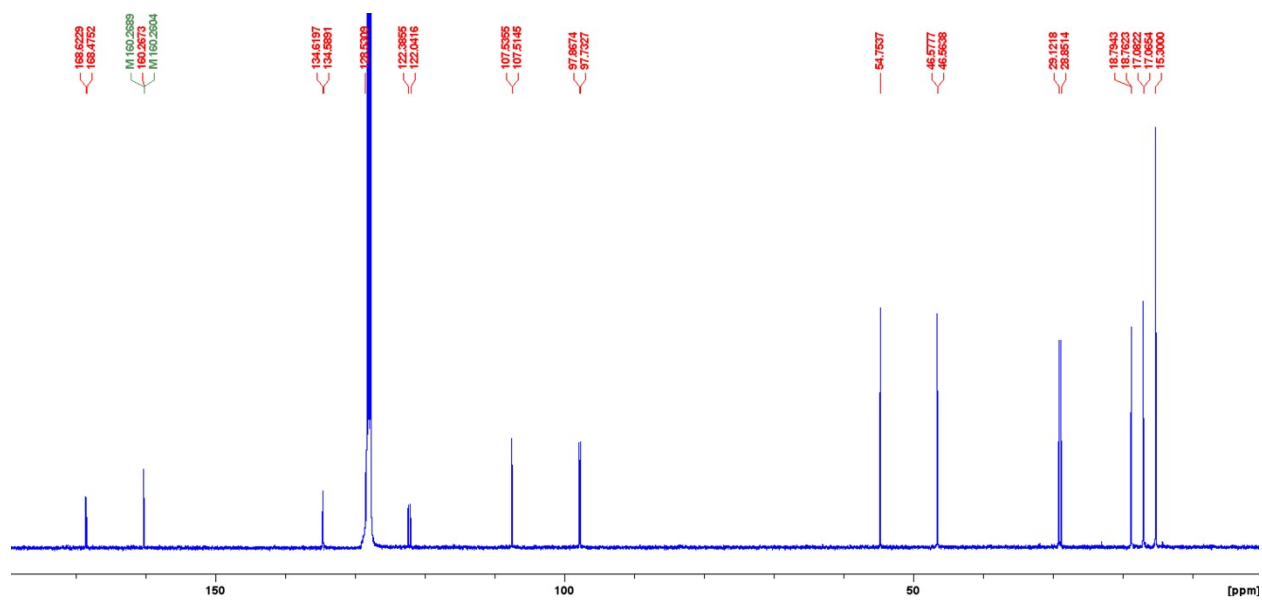


Figure S104. Full ^{13}C NMR spectrum of **7d** in C_6D_6 .

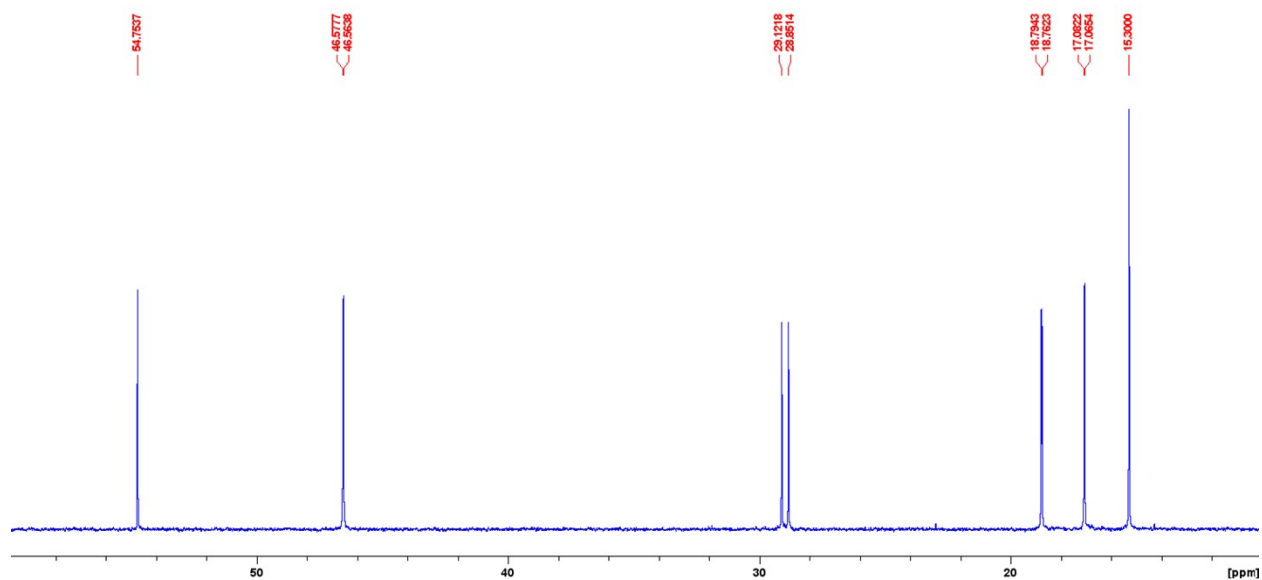


Figure S105. The aliphatic region of the ^{13}C NMR spectrum of **7d** in C_6D_6 .

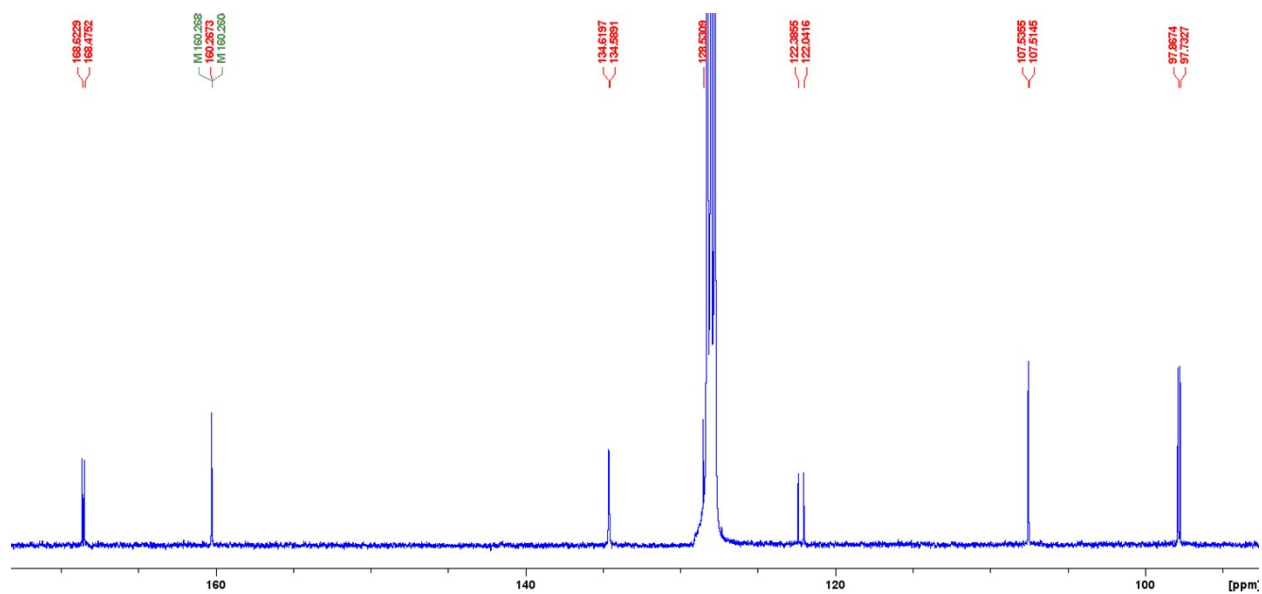


Figure S106. The aromatic region of the ^{13}C NMR spectrum of **7d** in C_6D_6 .

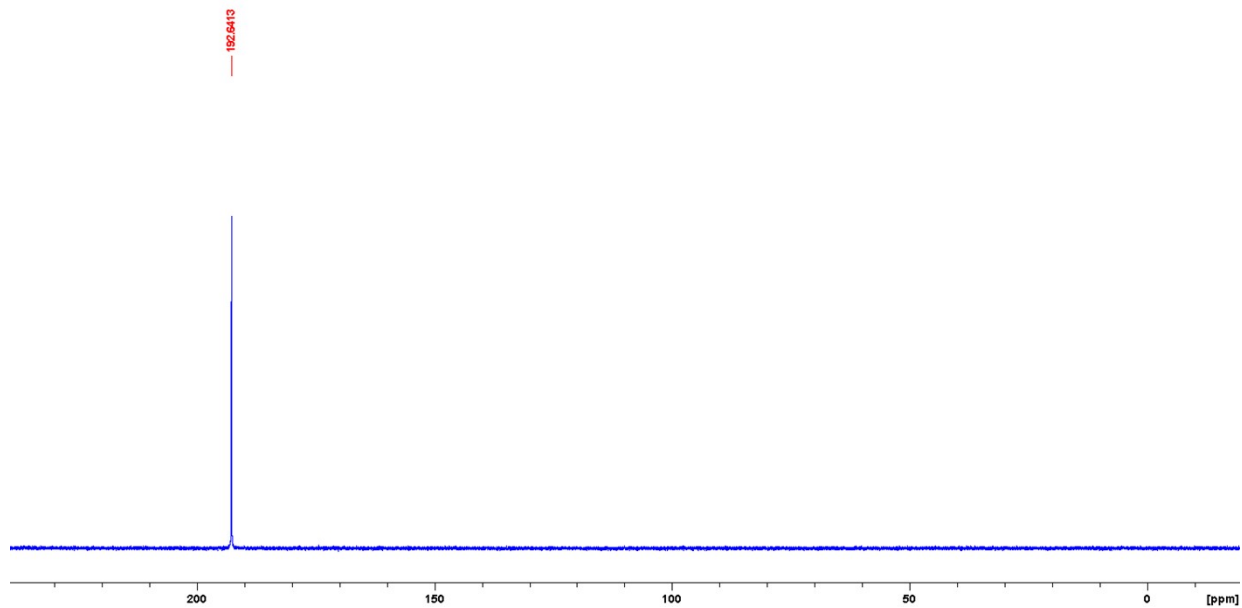


Figure S107. $^{31}\text{P}\{^1\text{H}\}$ NMR spectrum of **7d** in C_6D_6 .

NMR spectra of complexes **8a**

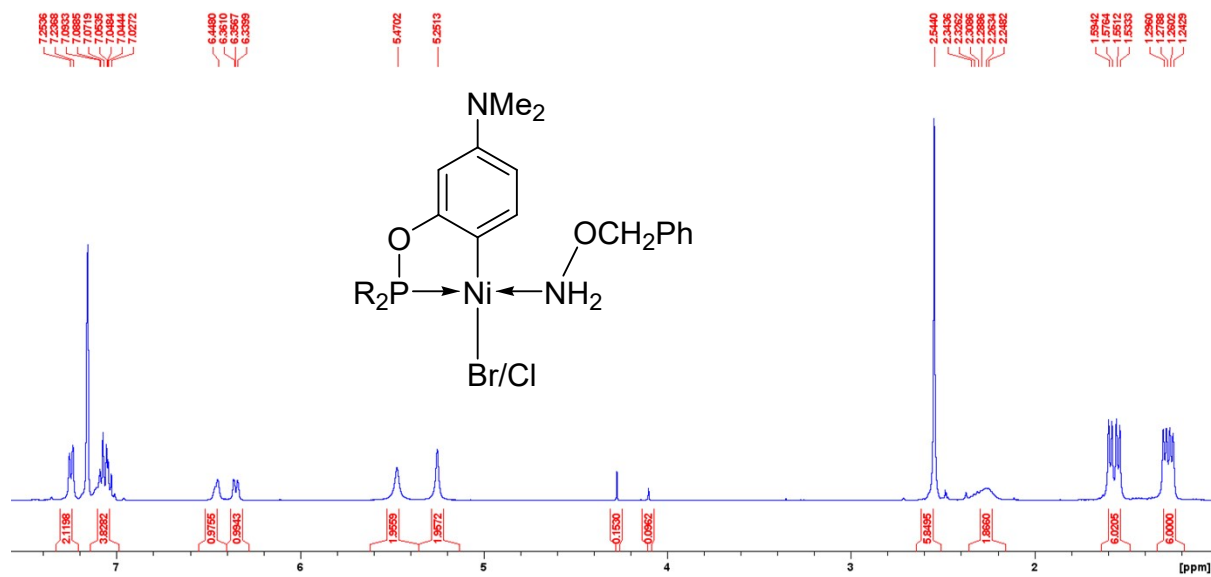


Figure S108. ¹H NMR spectrum of **8a** in C₆D₆.

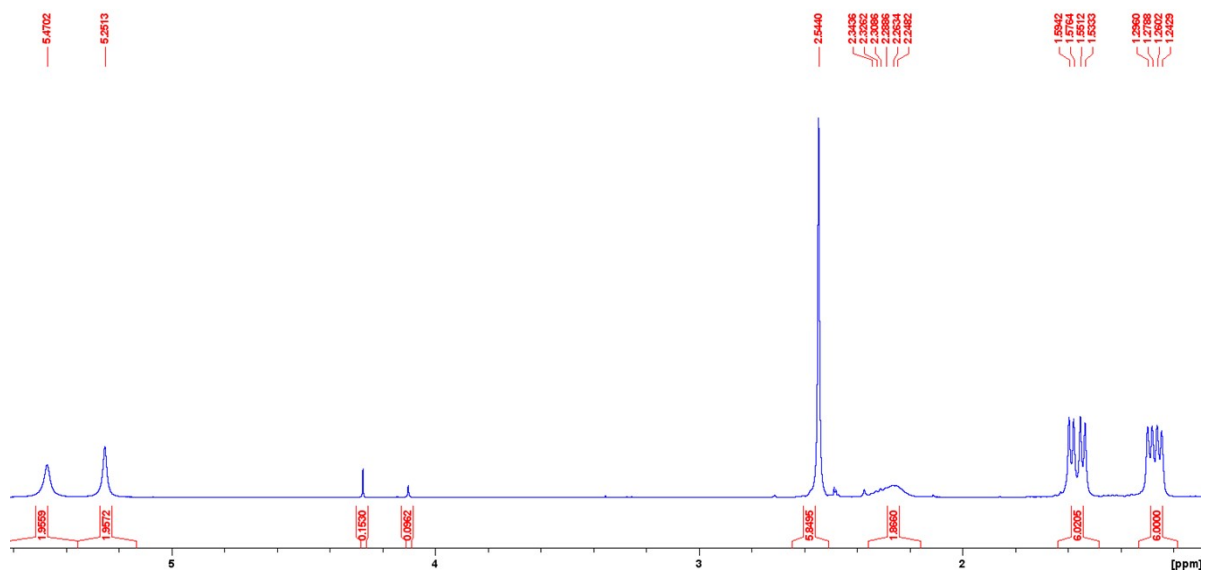


Figure S109. The aliphatic region of the ¹H NMR spectrum of **8a** in C₆D₆.

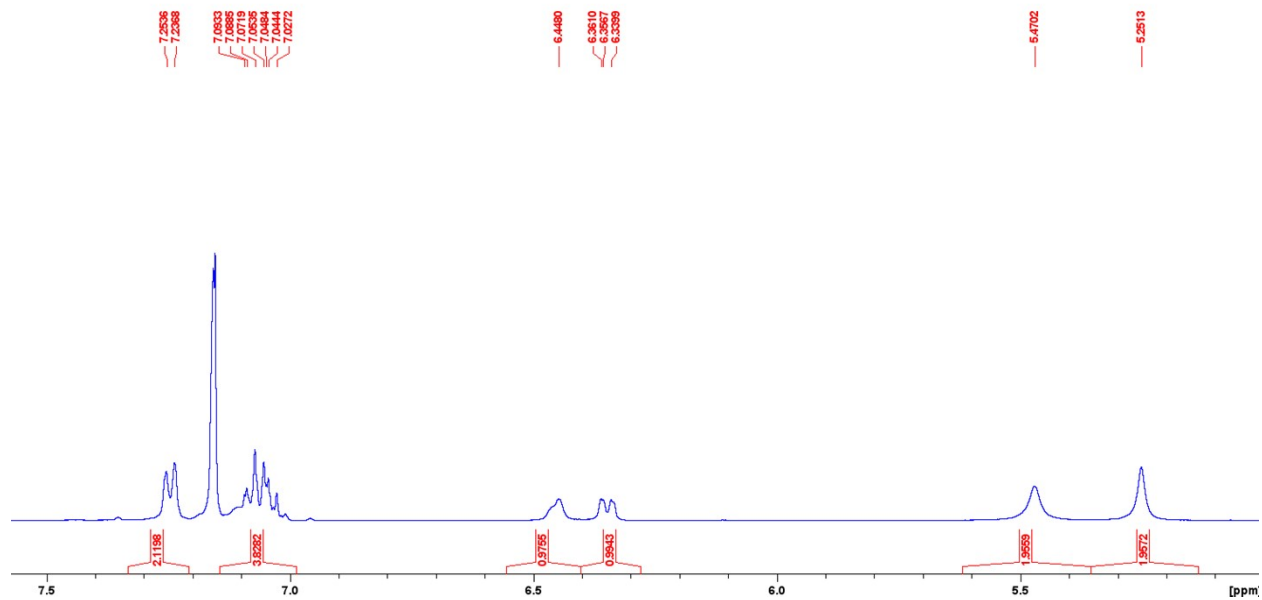


Figure S110. The aromatic region of the ^1H NMR spectrum of **8a** in C_6D_6 .

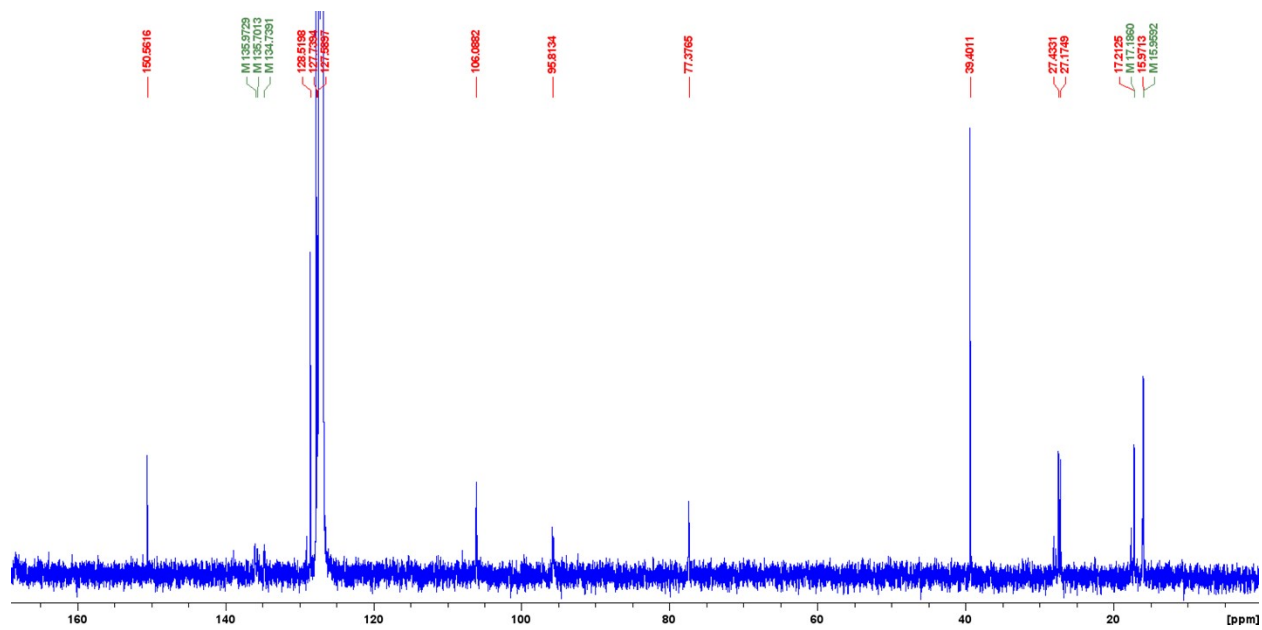


Figure S111. Full ^{13}C NMR spectrum of **8a** in C_6D_6 .

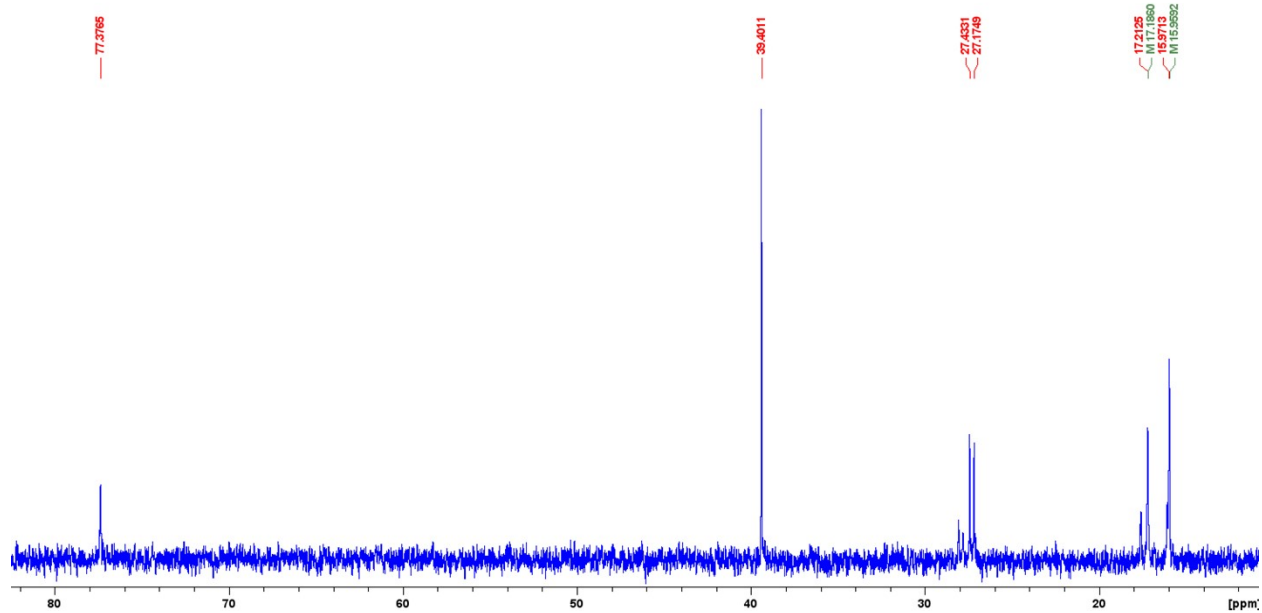


Figure S112. The aliphatic region of the ^{13}C NMR spectrum of **8a** in C_6D_6 .

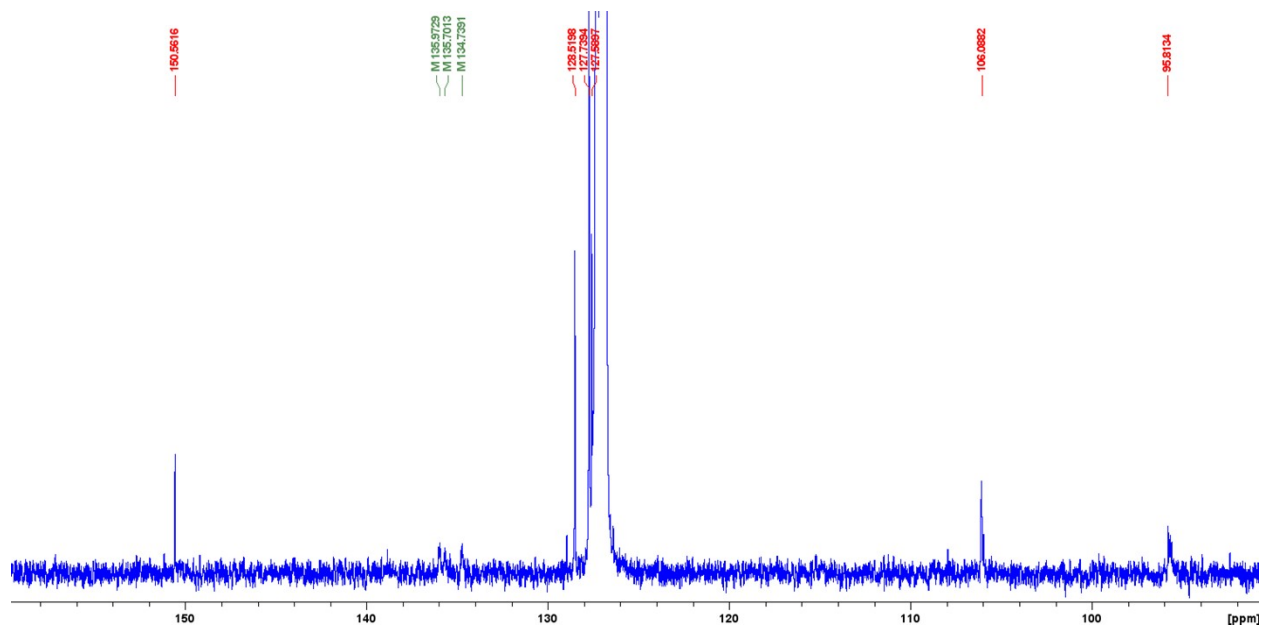


Figure S113. The aromatic region of the ^{13}C NMR spectrum of **8a** in C_6D_6 .

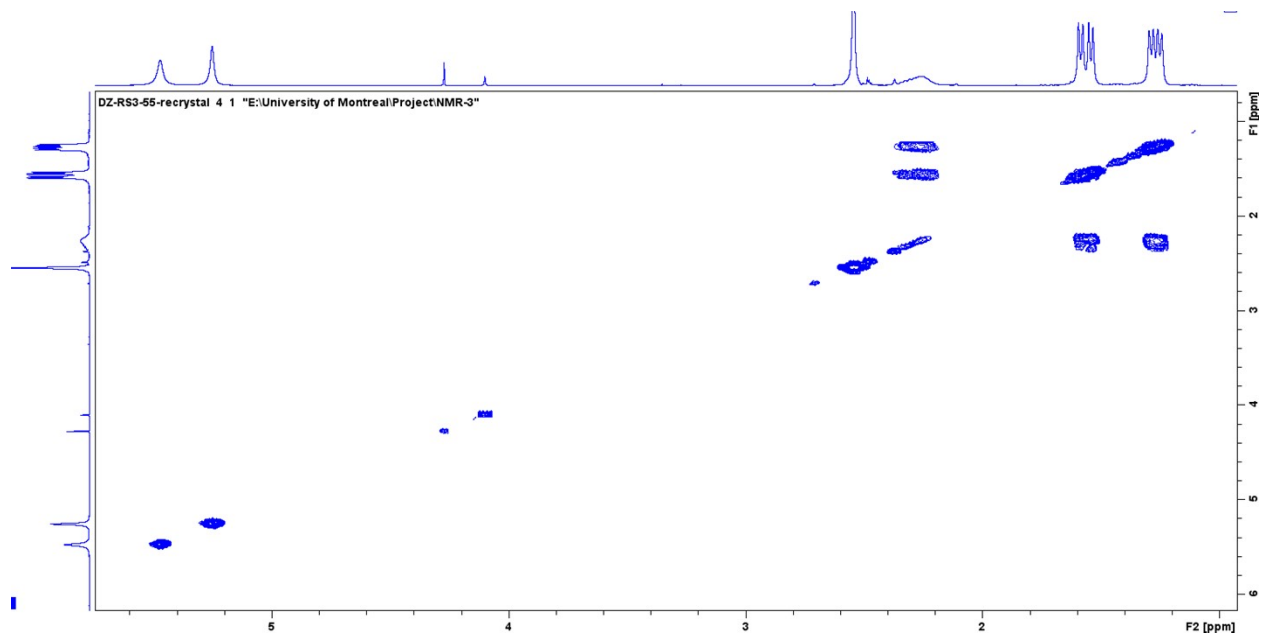


Figure S114. The aliphatic region of the COSY NMR spectrum of **8a** in C₆D₆.

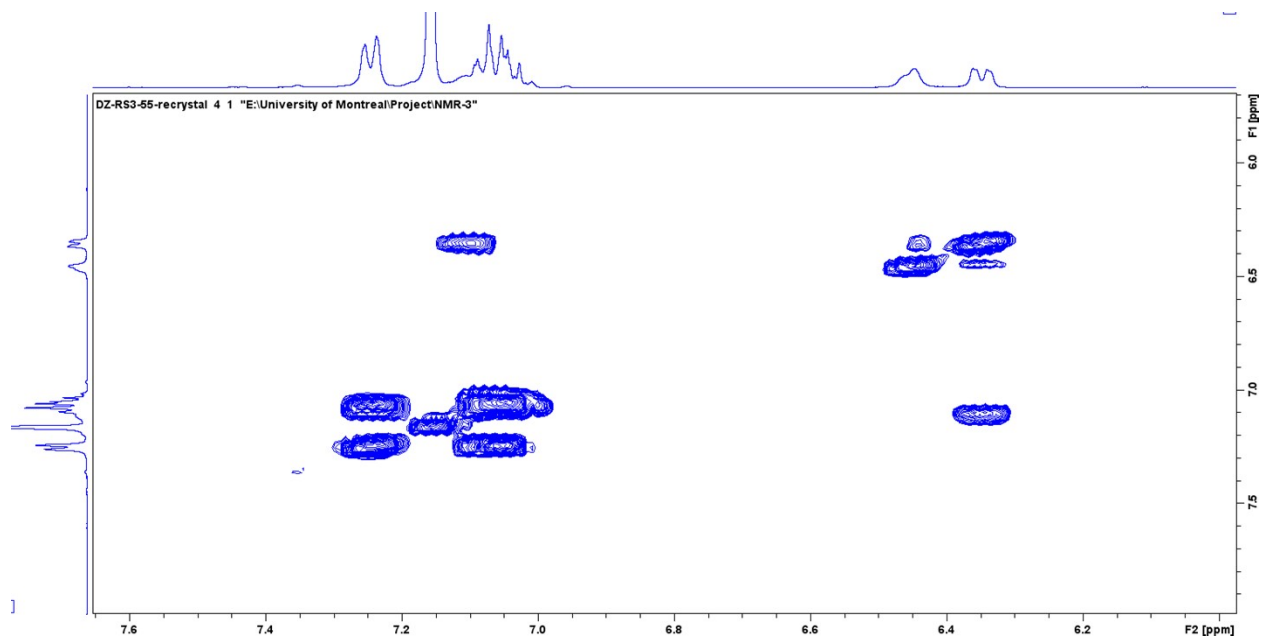


Figure S115. The aromatic region of the COSY NMR spectrum of **8a** in C₆D₆.

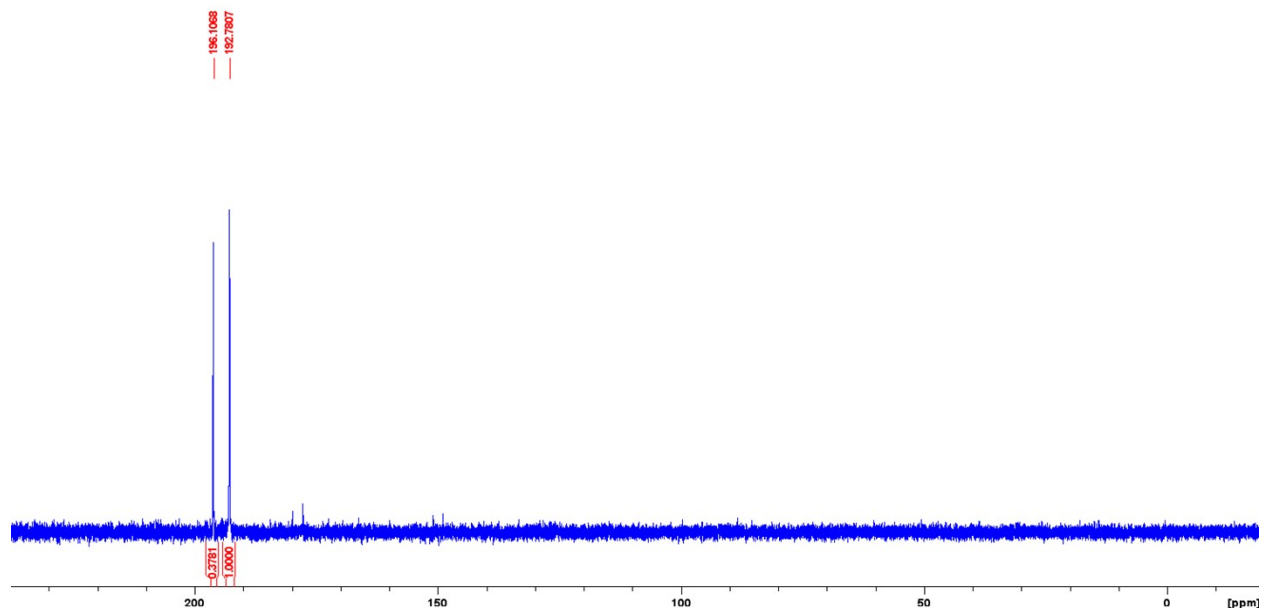


Figure S116. $^{31}\text{P}\{^1\text{H}\}$ NMR spectrum of **8a** in C_6D_6 .

NMR spectra of complexes **8b**

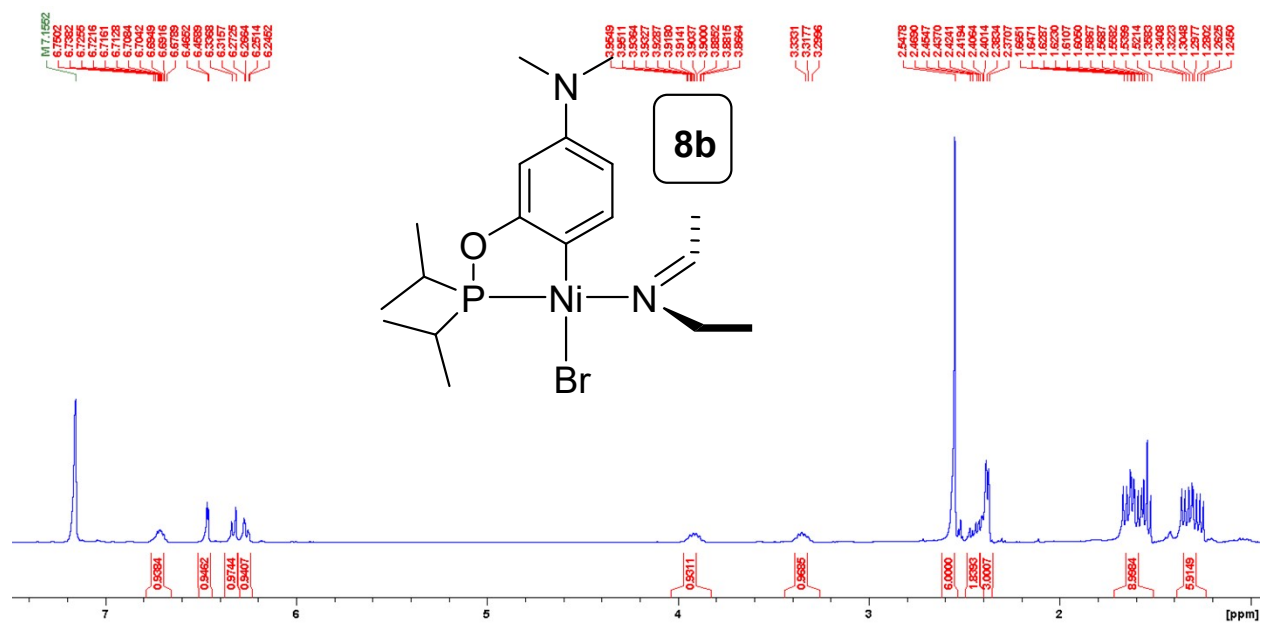


Figure S117. Full ^1H NMR spectrum of **8b** in C_6D_6 .

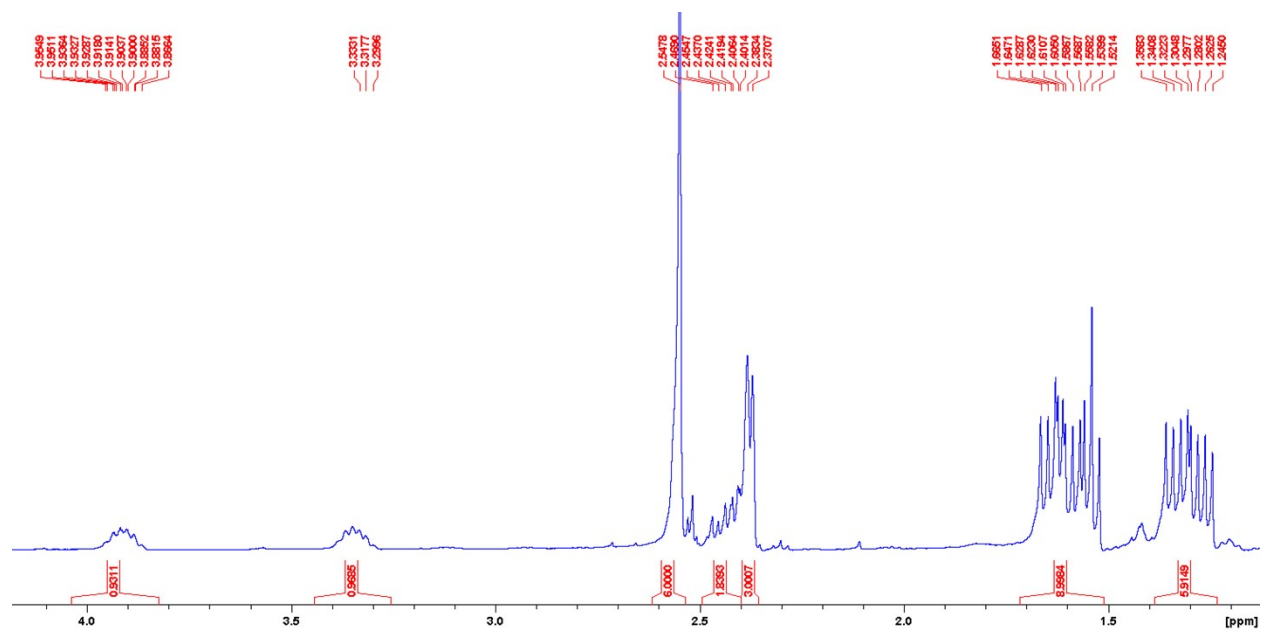


Figure S118. The aliphatic region of the ^1H NMR spectrum of **8b** in C_6D_6 .

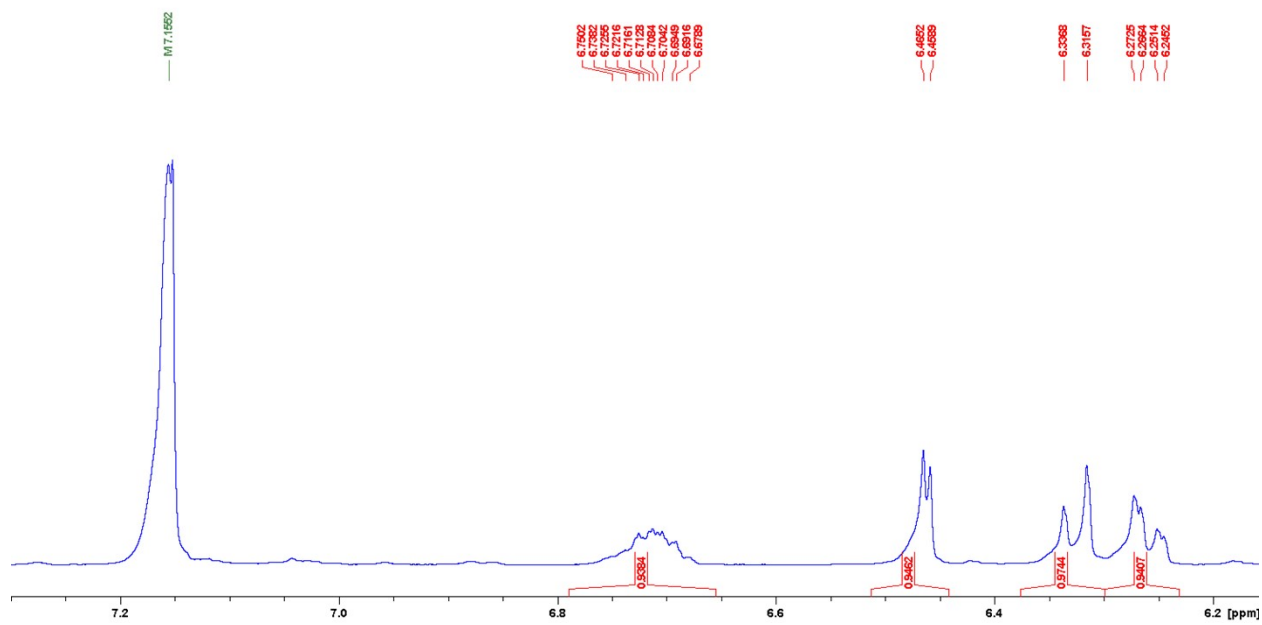


Figure S119. The aromatic region of the ^1H NMR spectrum of **8b** in C_6D_6 .

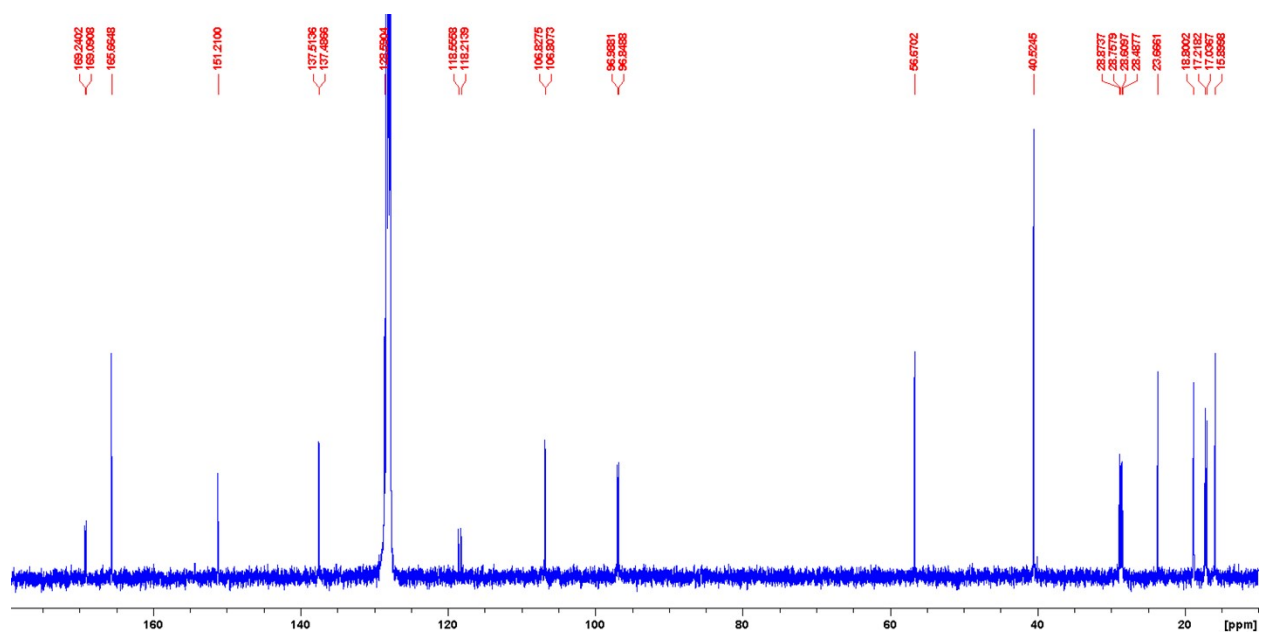


Figure S120. Full ^{13}C NMR spectrum of **8b** in C_6D_6 .

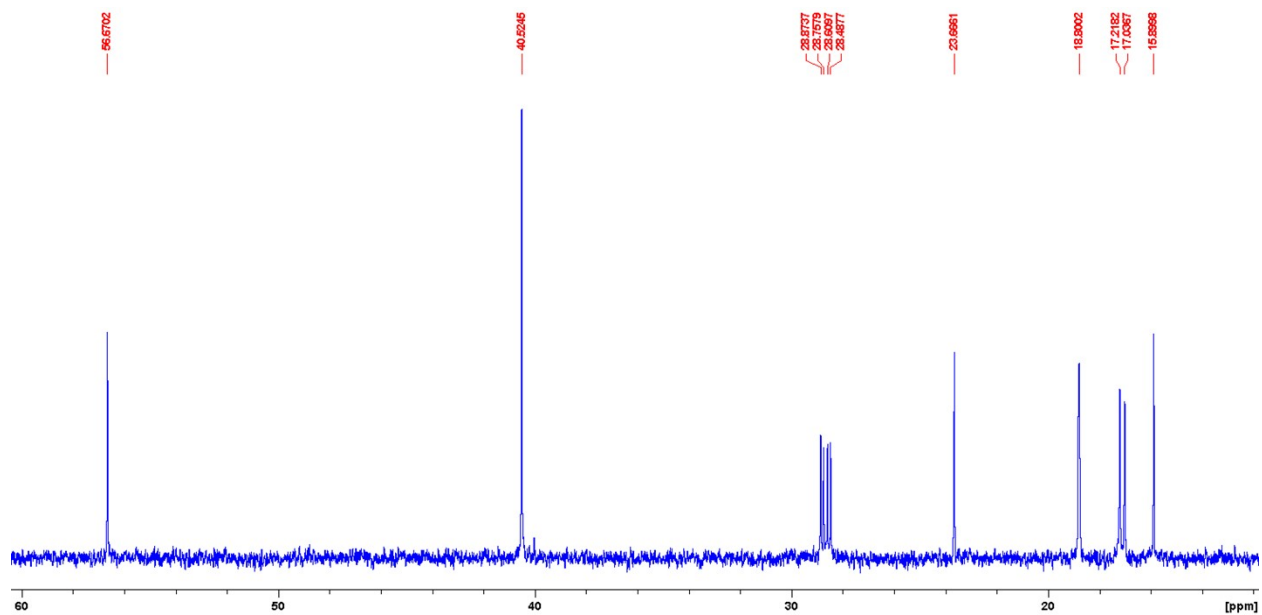


Figure S121. The aliphatic region of the ^{13}C NMR spectrum of **8b** in C_6D_6 .

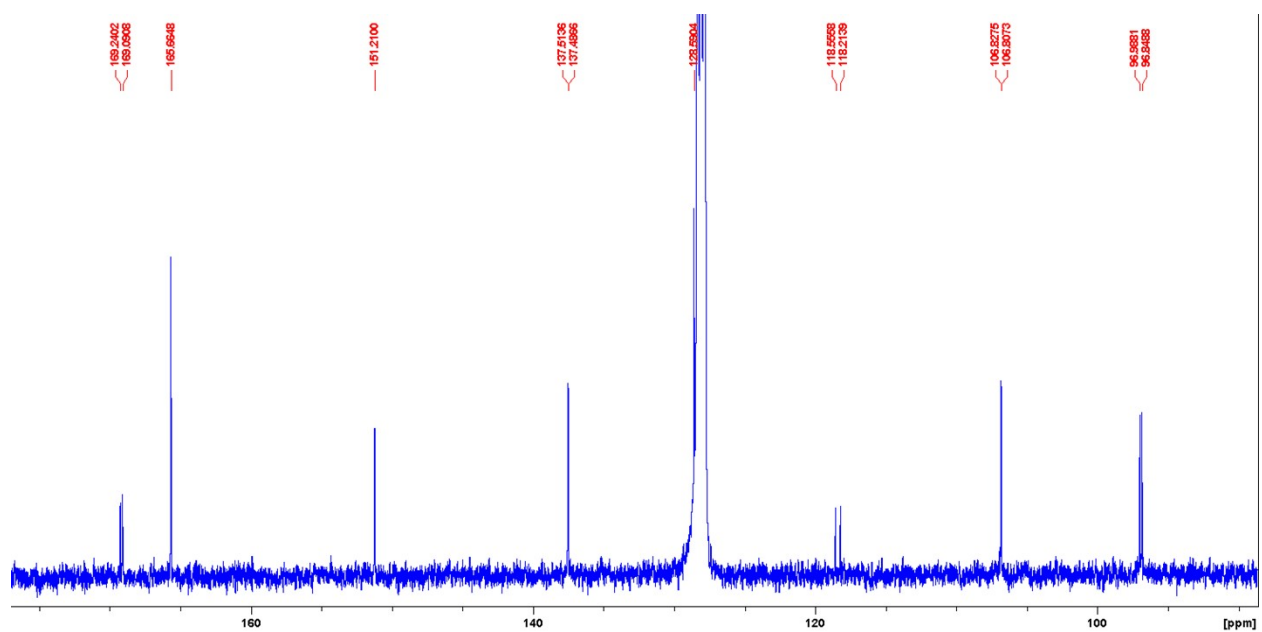


Figure S122. The aromatic region of the ^{13}C NMR spectrum of **8b** in C_6D_6 .

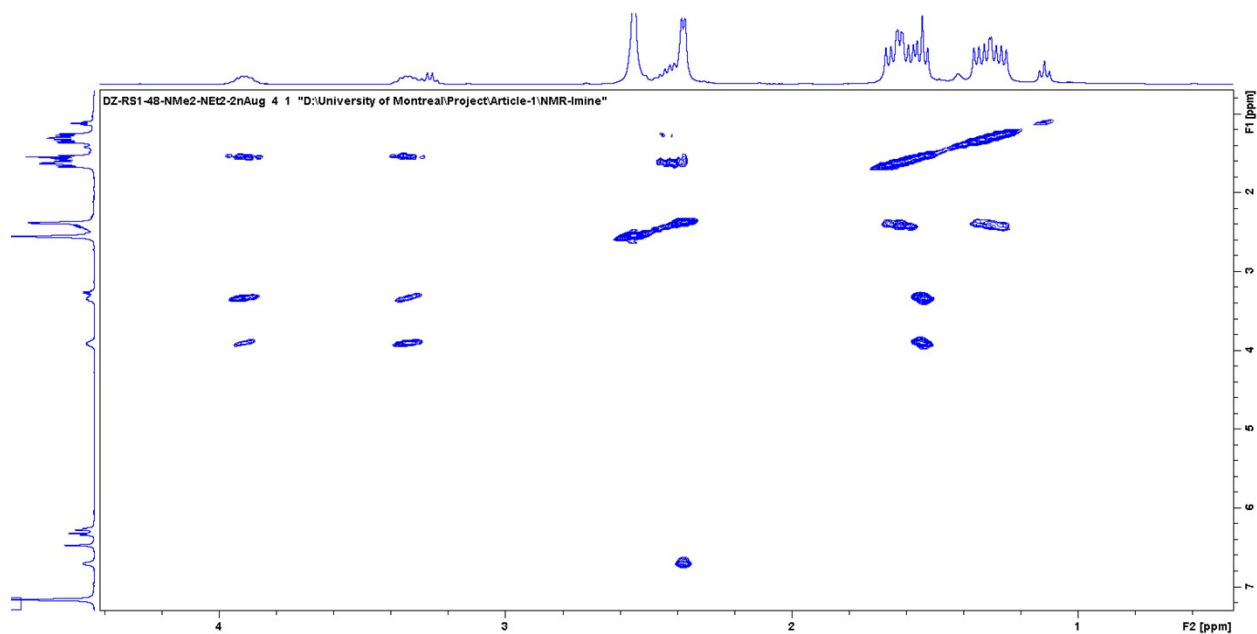


Figure S123. The aliphatic region of the COSY NMR spectrum of **8b** in C_6D_6 .

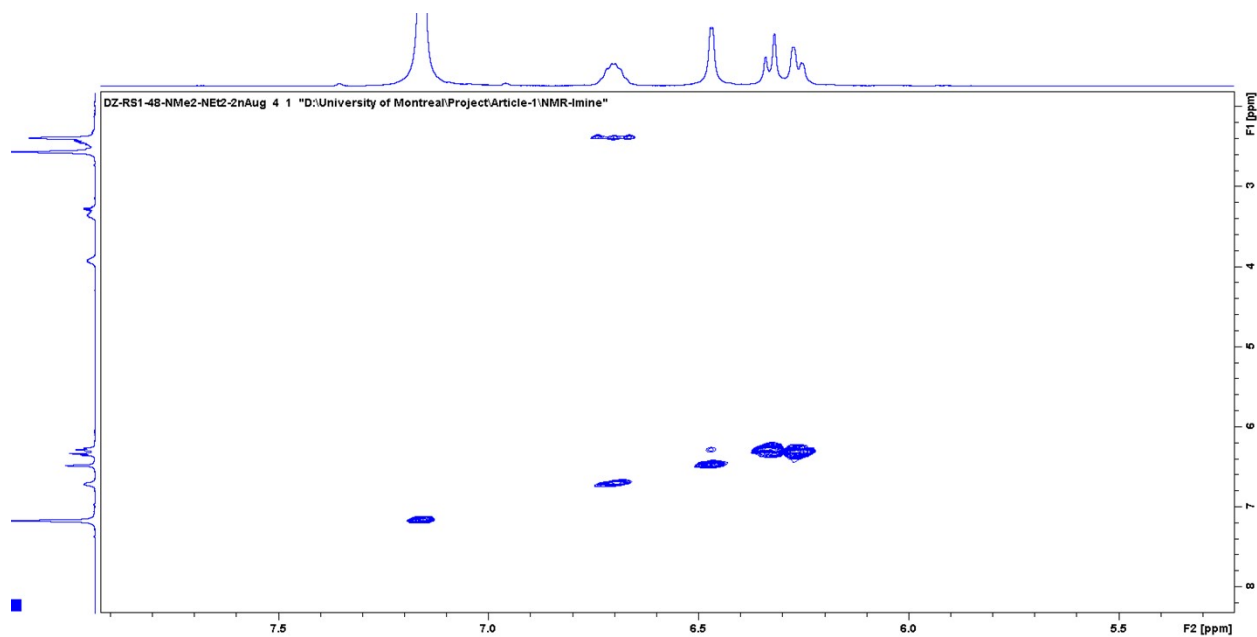


Figure S124. The aromatic region of the COSY NMR spectrum of **8b** in C_6D_6 .

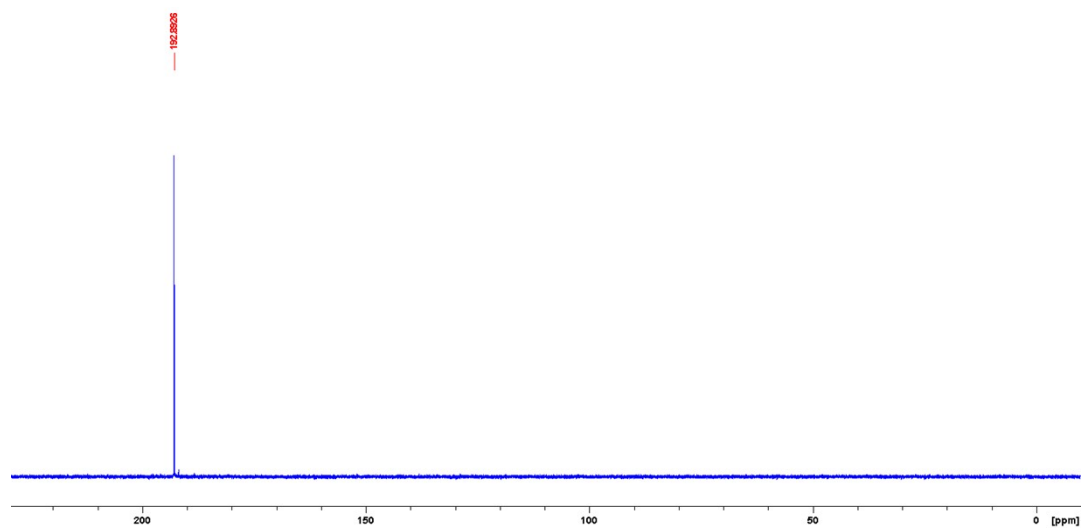


Figure S125. $^{31}\text{P}\{^1\text{H}\}$ NMR spectrum of **8b** in C_6D_6 .

4. ^{31}P NMR spectra of some crude reaction mixtures

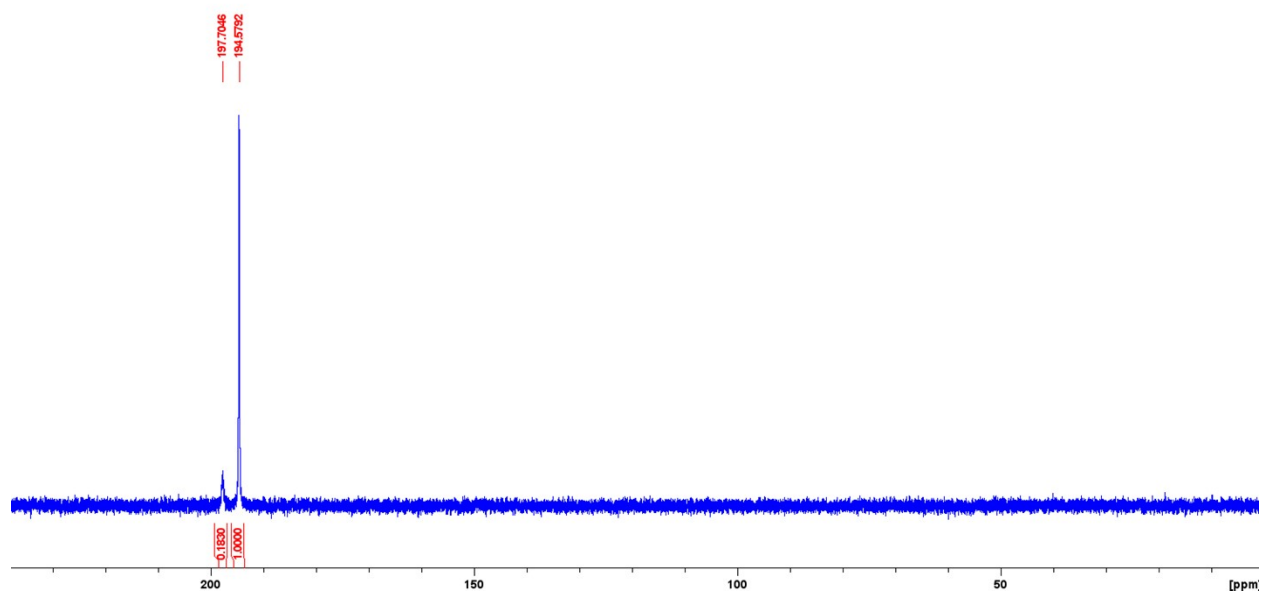


Figure S126. $^{31}\text{P}\{^1\text{H}\}$ NMR spectrum of the crude mixture for the reaction **1** + BnONH₂ in CH₂Cl₂.

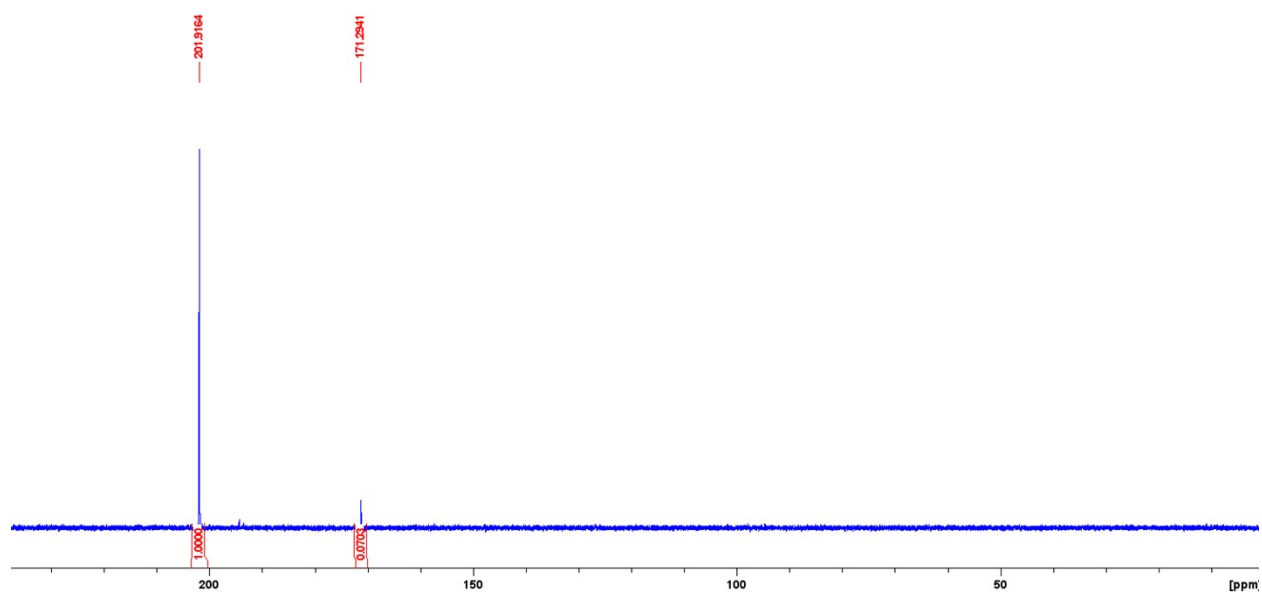


Figure S127. $^{31}\text{P}\{^1\text{H}\}$ NMR spectrum of the crude mixture for the reaction **1** + Et₂NOH in CH₂Cl₂.

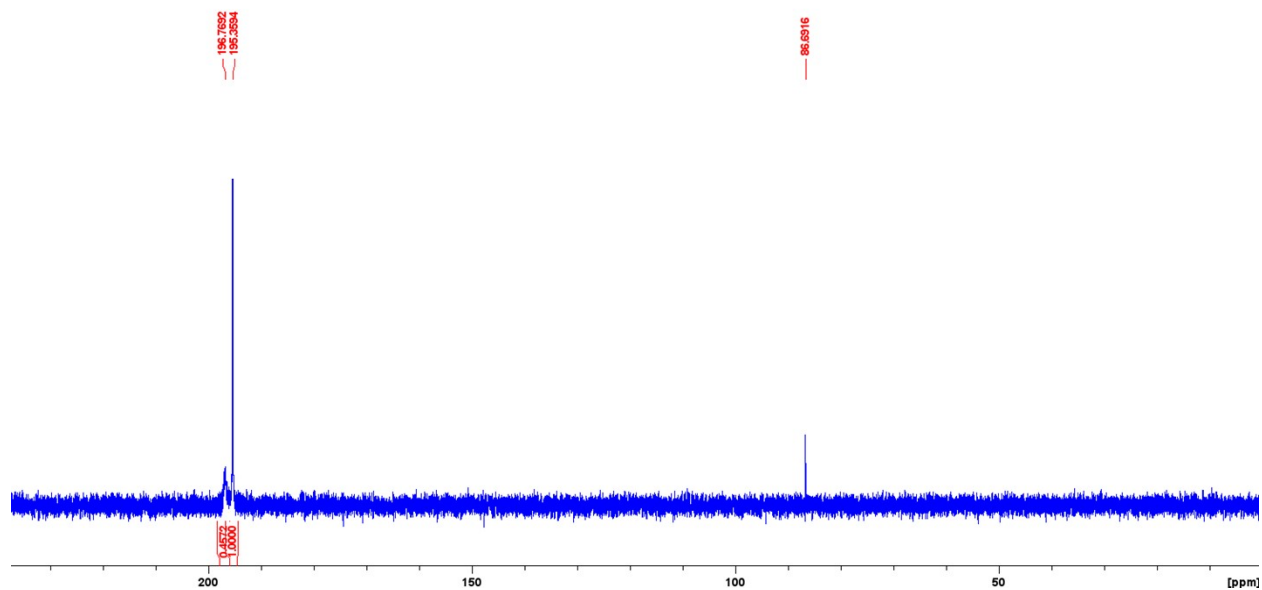


Figure S128. $^{31}\text{P}\{^1\text{H}\}$ NMR spectrum of the crude mixture for the reaction **1-NCMe** + Et_2NOH in acetonitrile.

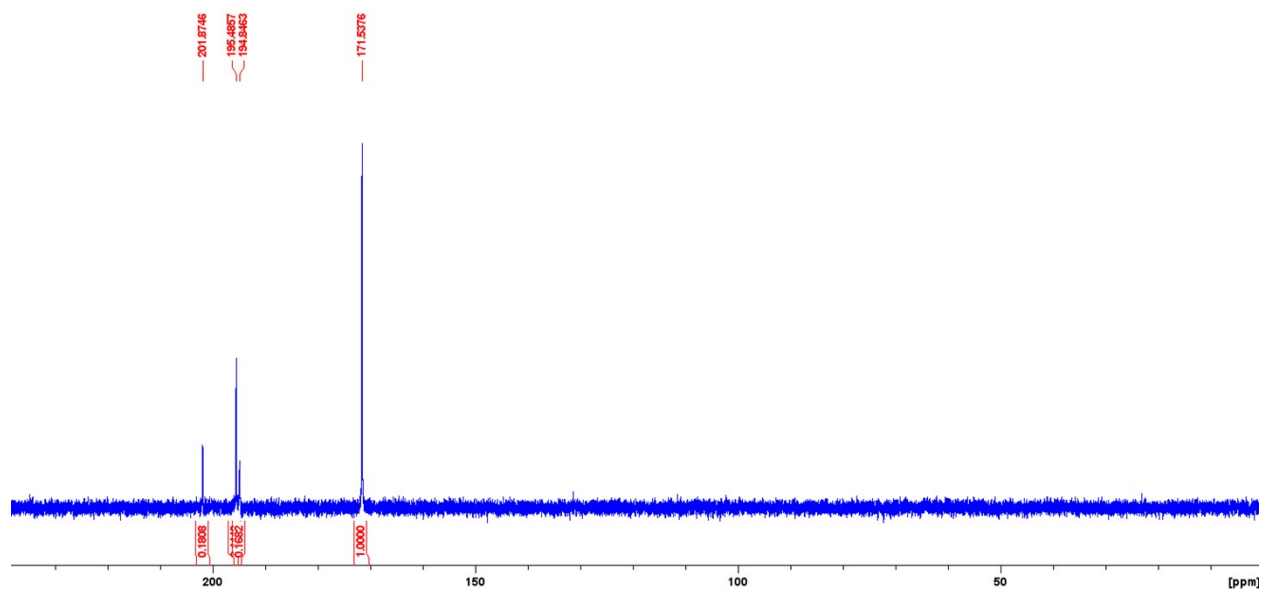


Figure S129. $^{31}\text{P}\{^1\text{H}\}$ NMR spectrum of the crude mixture for the reaction **1** + Bn_2NOH in CH_2Cl_2 .

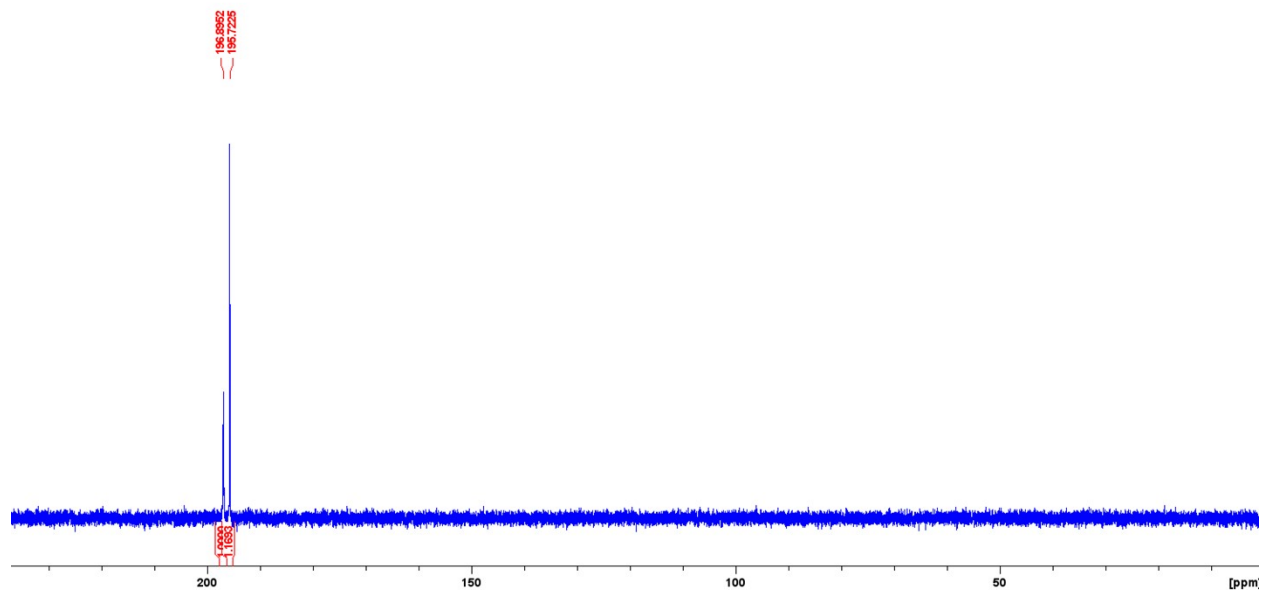


Figure S130. $^{31}\text{P}\{^1\text{H}\}$ NMR spectrum of the crude mixture for the reaction **1** + Bn_2NOH in acetonitrile.

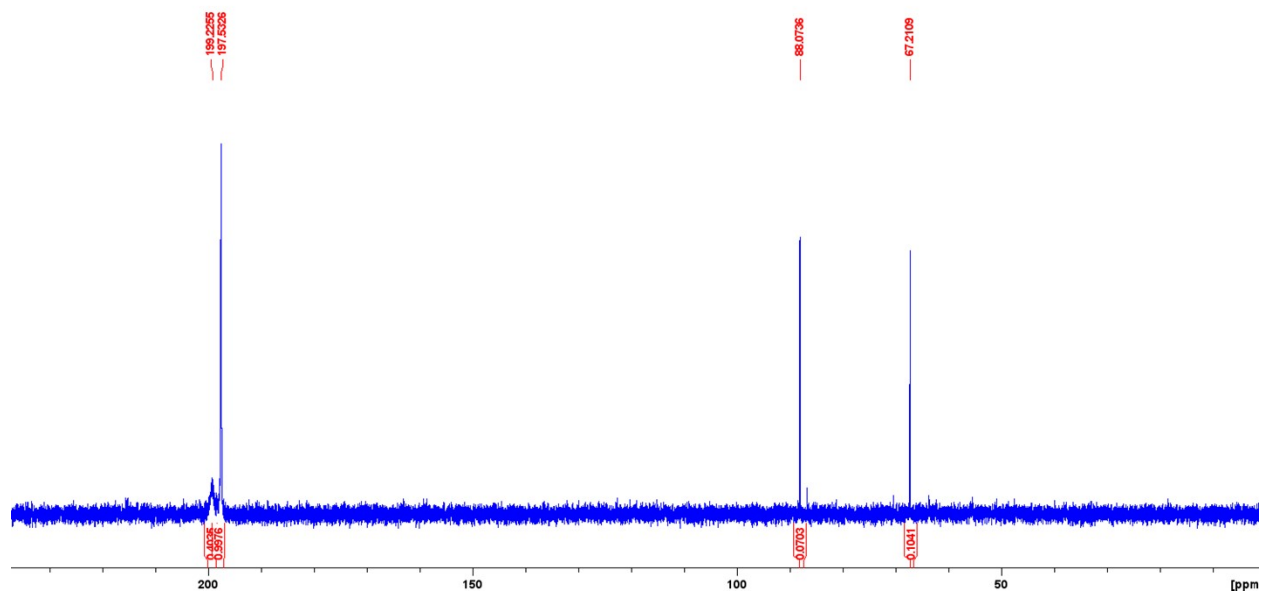


Figure 131. $^{31}\text{P}\{^1\text{H}\}$ NMR spectrum of the crude mixture for the reaction **2** + Et_2NOH in acetonitrile.

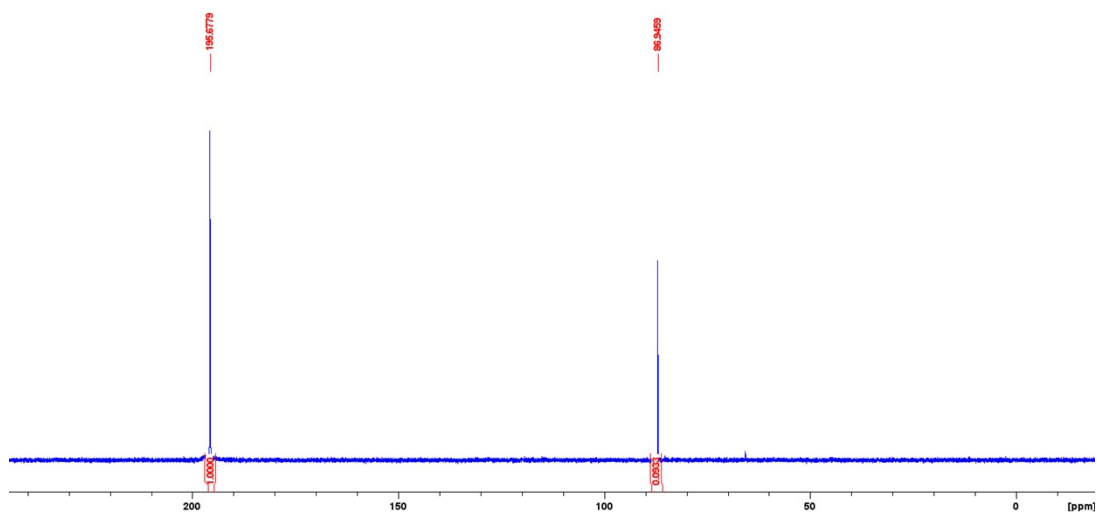


Figure S132. $^{31}\text{P}\{^1\text{H}\}$ NMR spectrum of the crude mixture for the reaction **3** + Et_2NOH in acetonitrile.

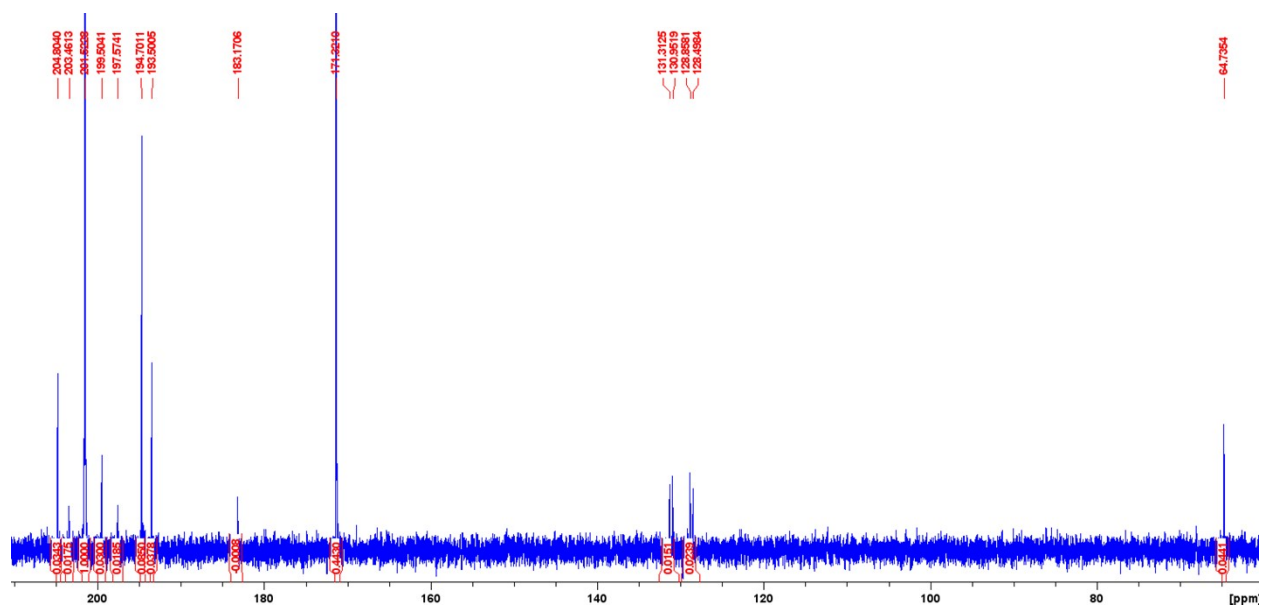


Figure S133. $^{31}\text{P}\{^1\text{H}\}$ NMR spectrum of the crude mixture for the reaction **3** + Et_2NOH in CH_2Cl_2 .

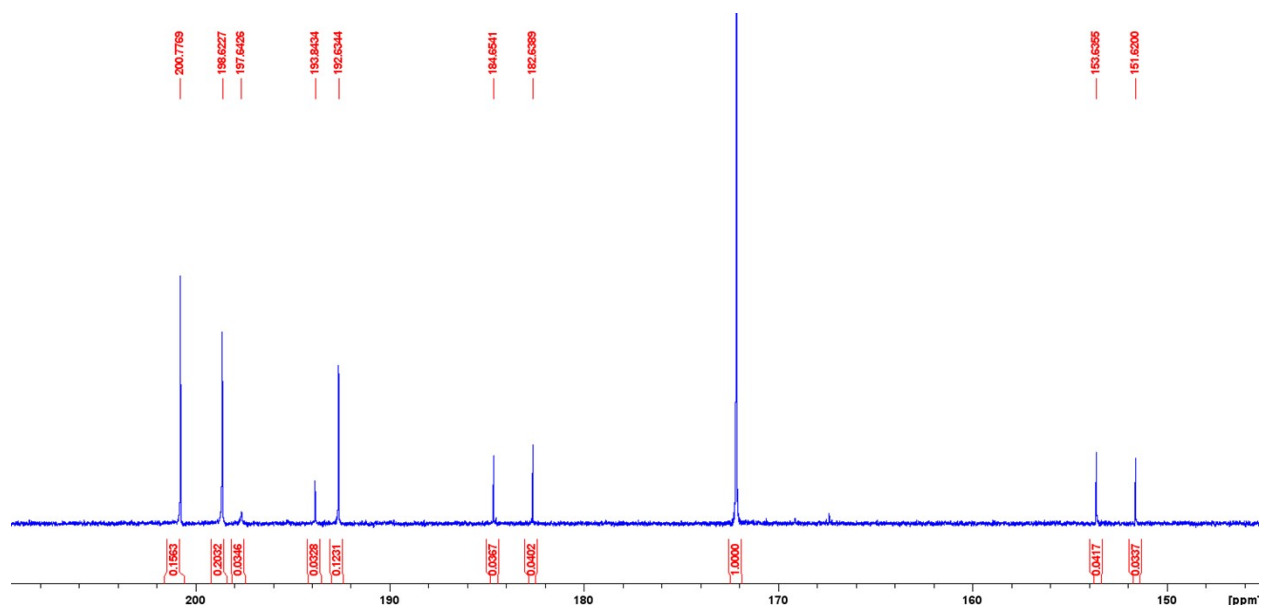


Figure S134. $^{31}\text{P}\{^1\text{H}\}$ NMR spectrum of the crude mixture for the reaction **3** + Et_2NOH in toluene.

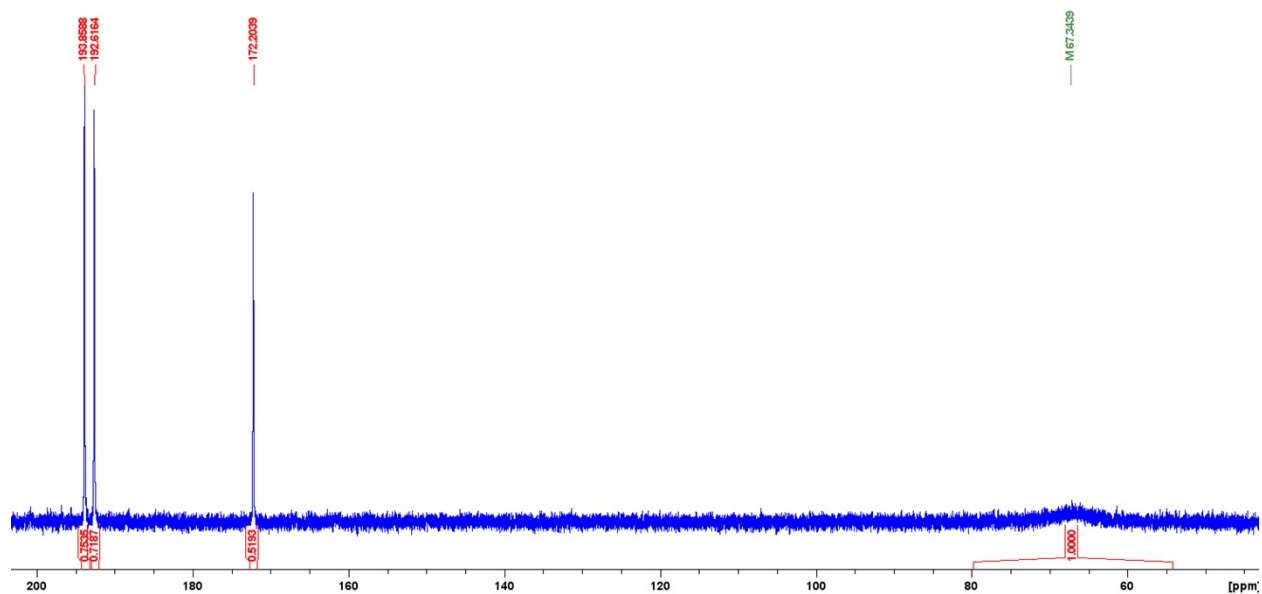


Figure S135. $^{31}\text{P}\{^1\text{H}\}$ NMR spectrum of the crude mixture for the reaction **3** + Et_2NOH in C_6D_6 .

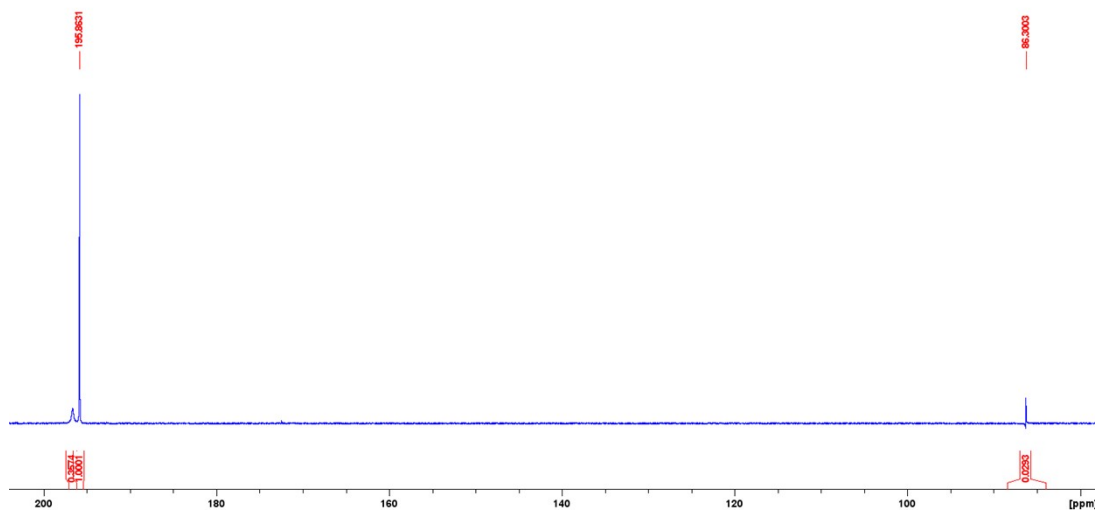


Figure S136. $^{31}\text{P}\{^1\text{H}\}$ NMR spectrum of the crude mixture for the reaction **3** + Bn_2NOH in acetonitrile.

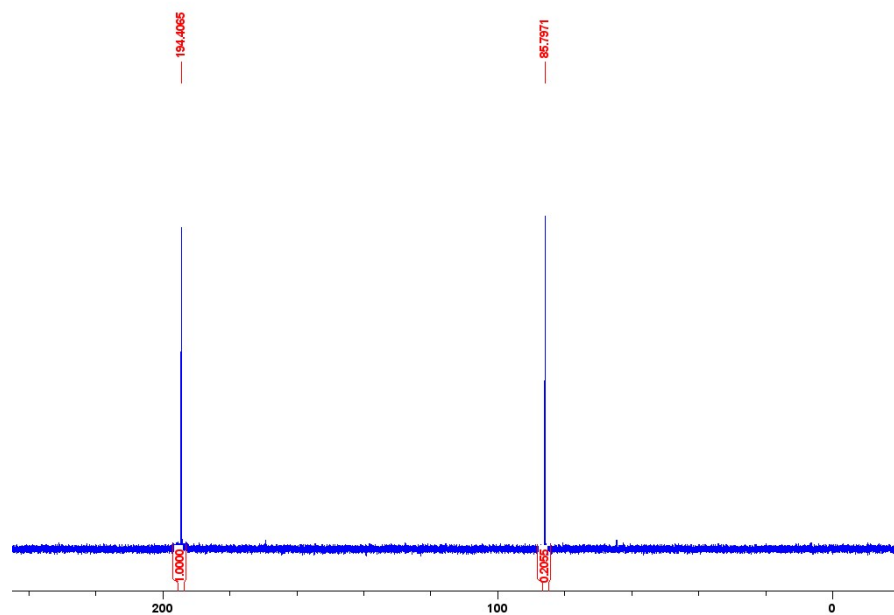


Figure S137. $^{31}\text{P}\{^1\text{H}\}$ NMR spectrum of the crude mixture for the reaction **4-NCMe** + Et_2NOH in acetonitrile.

5. Procedure and ^{31}P NMR spectra of the time profile experiments.

A stock solution was prepared by dissolving 30 mg of dimer **3**, [$\{\kappa^P, \kappa^C-(i\text{-Pr})_2\text{PO}-(5\text{-OMe-C}_6\text{H}_3)\}\text{Ni}(\mu\text{-Br})_2$], (0.040 mmol) and 7 mg of Et_2NOH (0.079 mmol) in 6 mL MeCN or C_6D_6 . This was stirred at room temperature and under inert atmosphere for about 1-2 min to ensure homogeneity, and then a small portion of it ($\approx 1\text{ mL}$) was withdrawn to prepare an NMR sample to be used for recording the ^{31}P NMR spectra of the reaction mixture over the reaction time interval (20 h for the acetonitrile reaction, 48 h for the C_6D_6 reaction). The concentrations of the major products/intermediates detected in this reaction were estimated from the integration values for the 4 most intense signals appearing in the chemical shift region 210-170 ppm. These were plotted as % of the combined integration values against elapsed time to generate the time profile for this reaction.

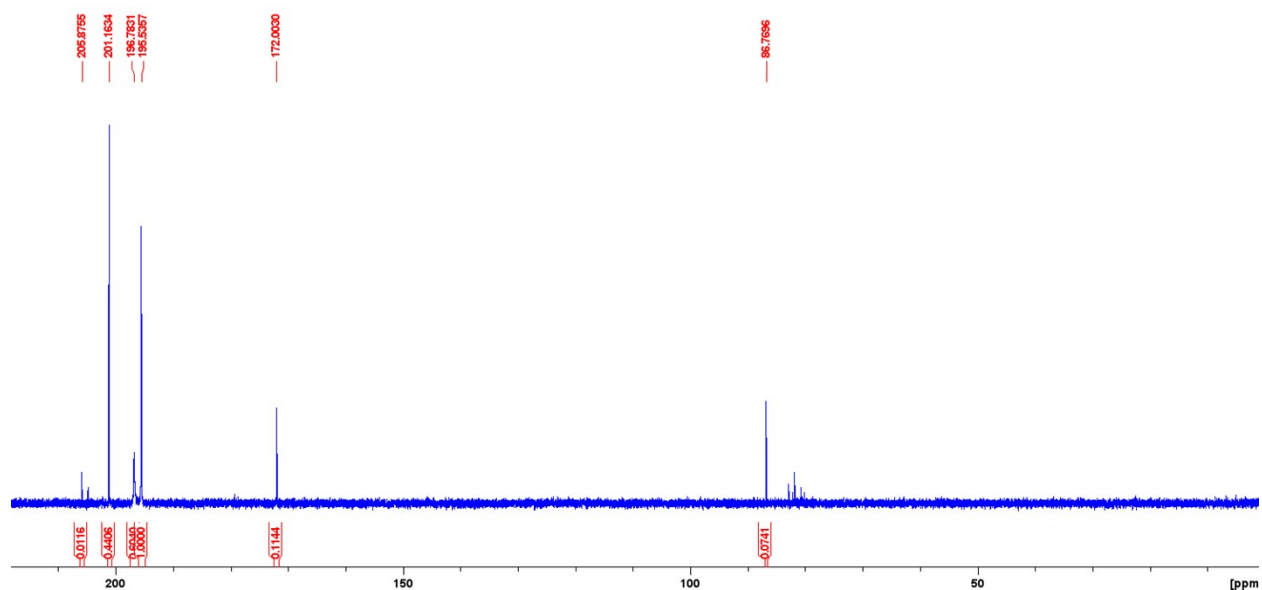


Figure S138. $^{31}\text{P}\{^1\text{H}\}$ NMR spectrum of the crude mixture for the reaction **3** + Et_2NOH in acetonitrile ($t=10$ min).

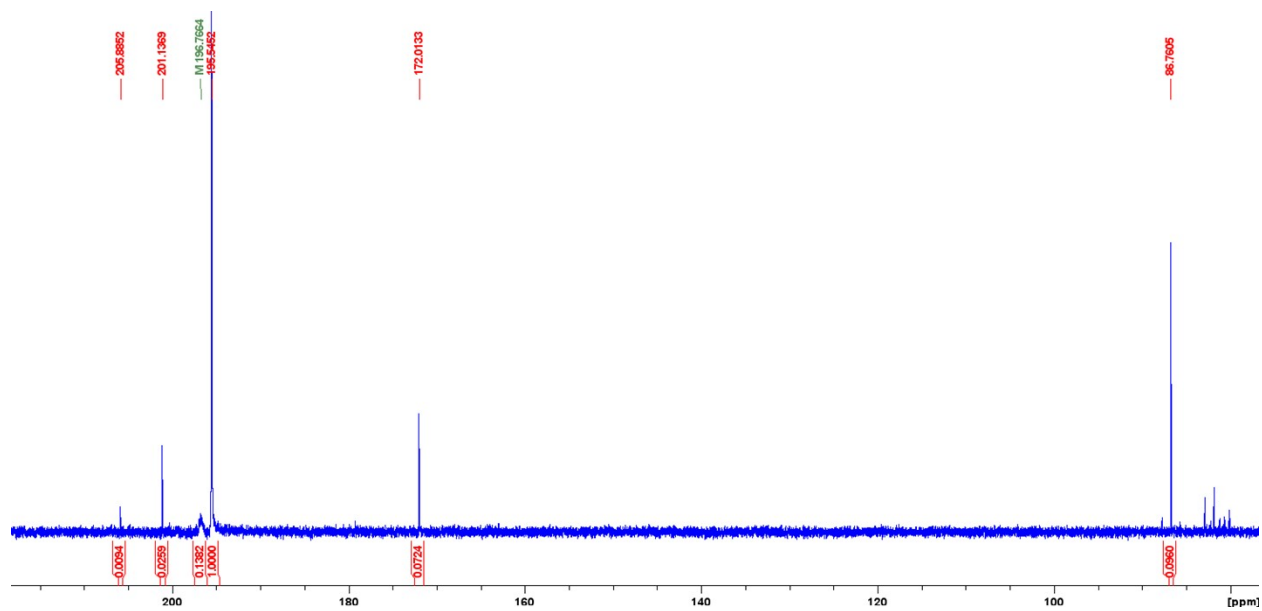


Figure S139. $^{31}\text{P}\{^1\text{H}\}$ NMR spectrum of the crude mixture for the reaction **3** + Et_2NOH in acetonitrile ($t=20$ min).

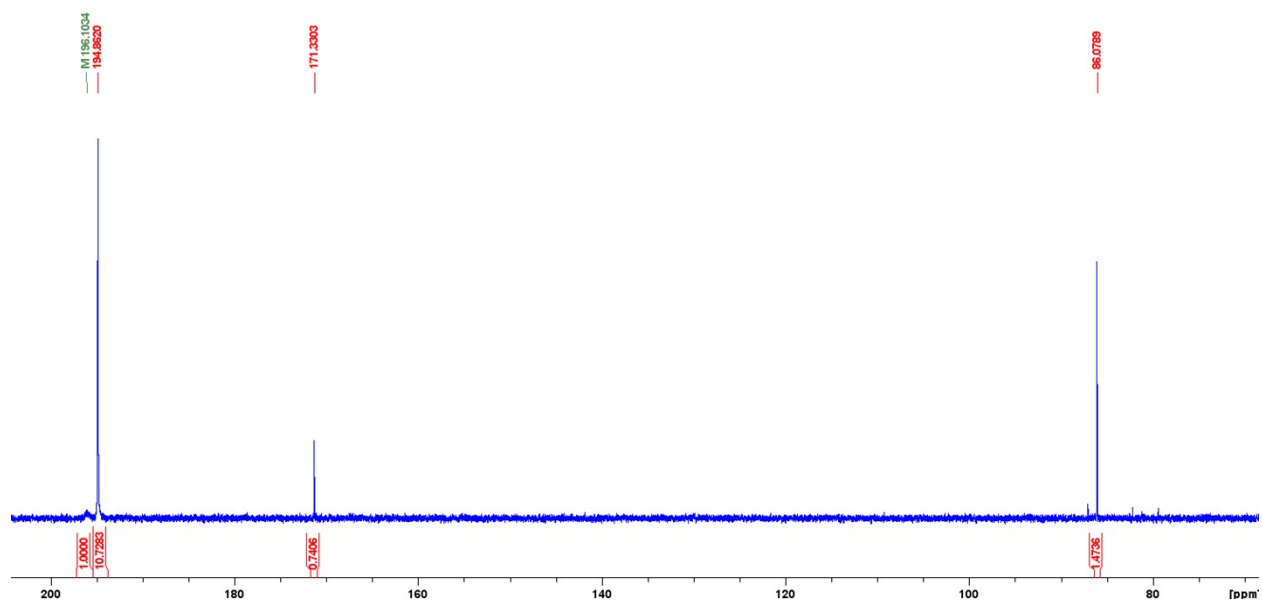


Figure S140. $^{31}\text{P}\{^1\text{H}\}$ NMR spectrum of the crude mixture for the reaction **3** + Et_2NOH in acetonitrile ($t=90$ min).

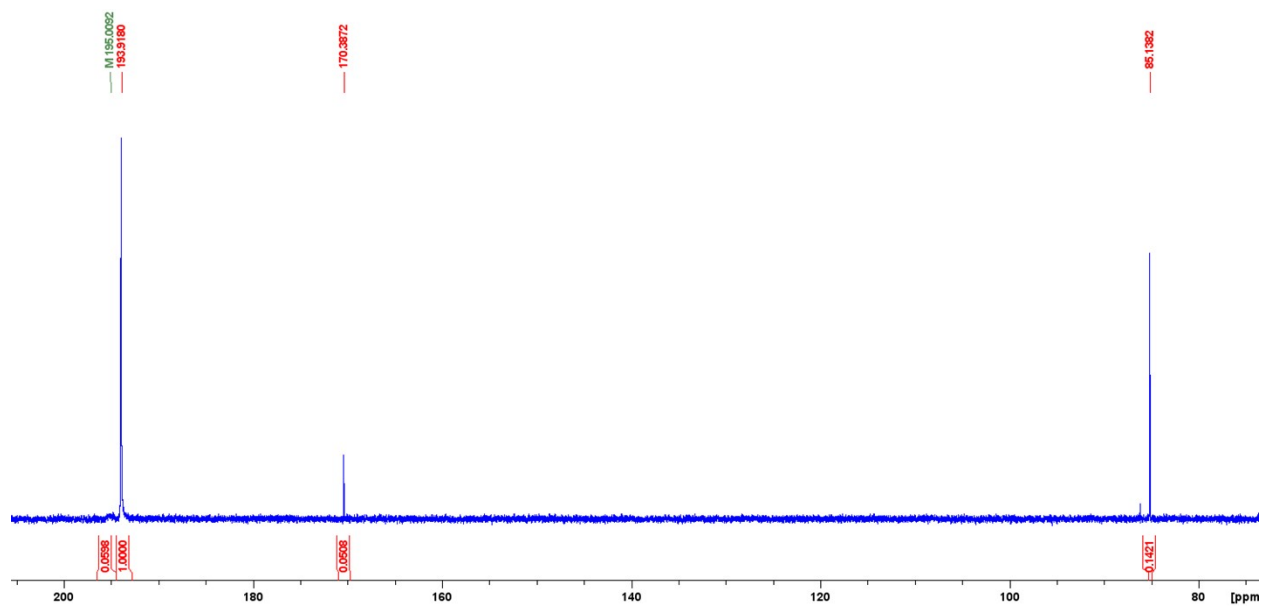


Figure S141. $^{31}\text{P}\{^1\text{H}\}$ NMR spectrum of the crude mixture for the reaction **3** + Et_2NOH in acetonitrile ($t=7$ h).

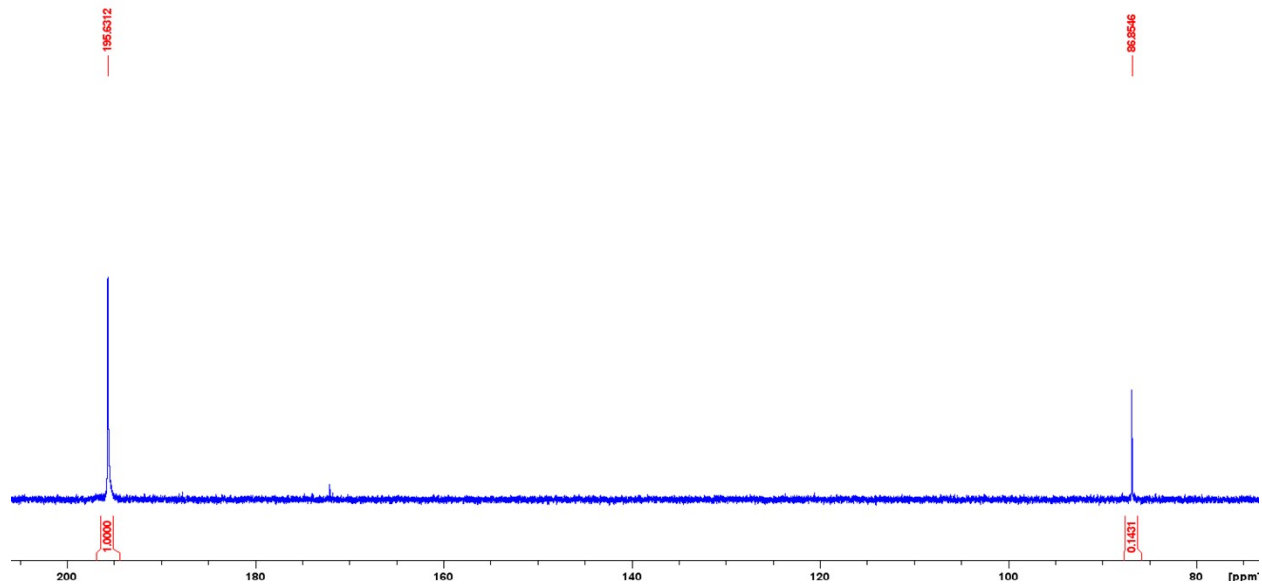


Figure S142. $^{31}\text{P}\{^1\text{H}\}$ NMR spectrum of the crude mixture for the reaction **3** + Et_2NOH in acetonitrile ($t=20$ h).

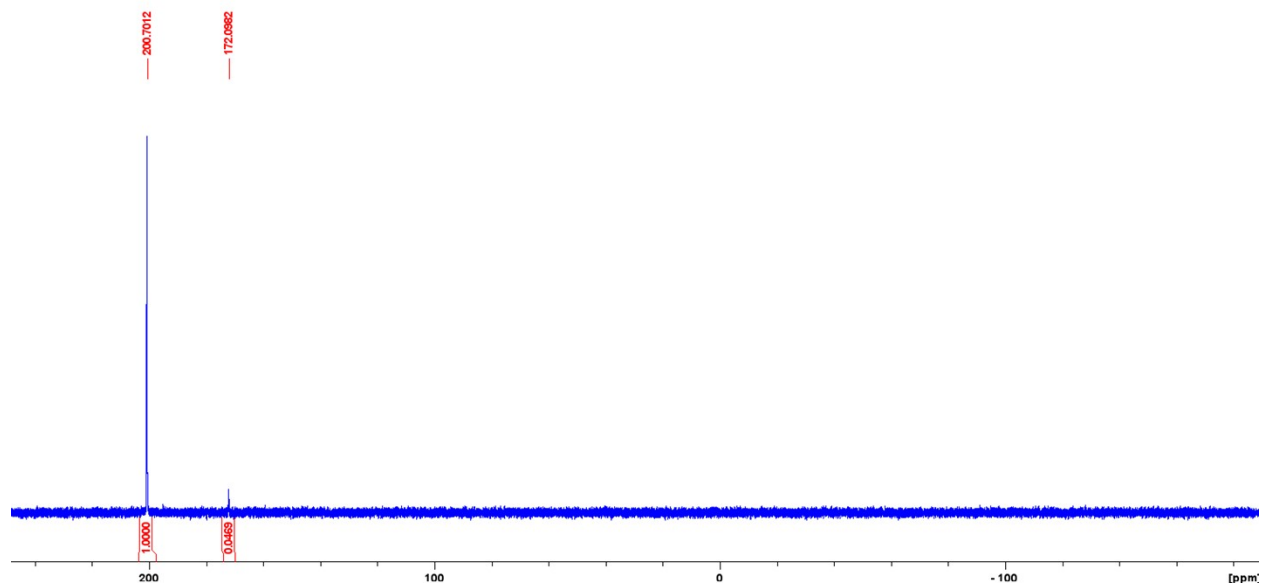


Figure S143. $^{31}\text{P}\{^1\text{H}\}$ NMR spectrum of the crude mixture for the reaction **3** + Et_2NOH in C_6D_6 ($t = 10$ min).

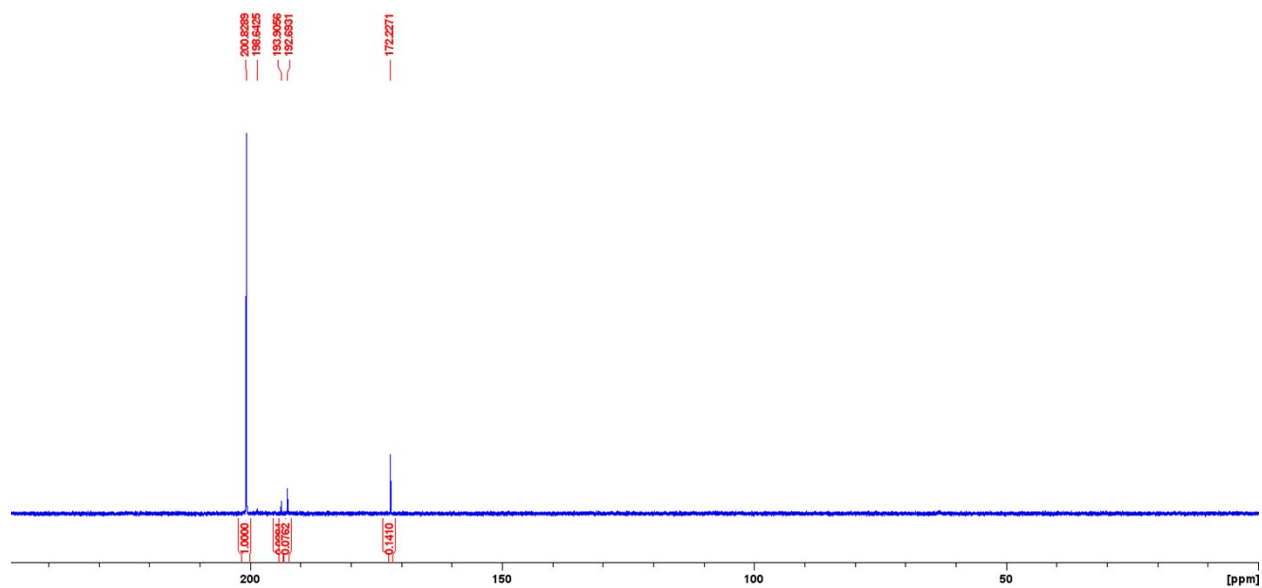


Figure S144. $^{31}\text{P}\{^1\text{H}\}$ NMR spectrum of the crude mixture for the reaction **3** + Et_2NOH in C_6D_6 ($t = 24$ h).

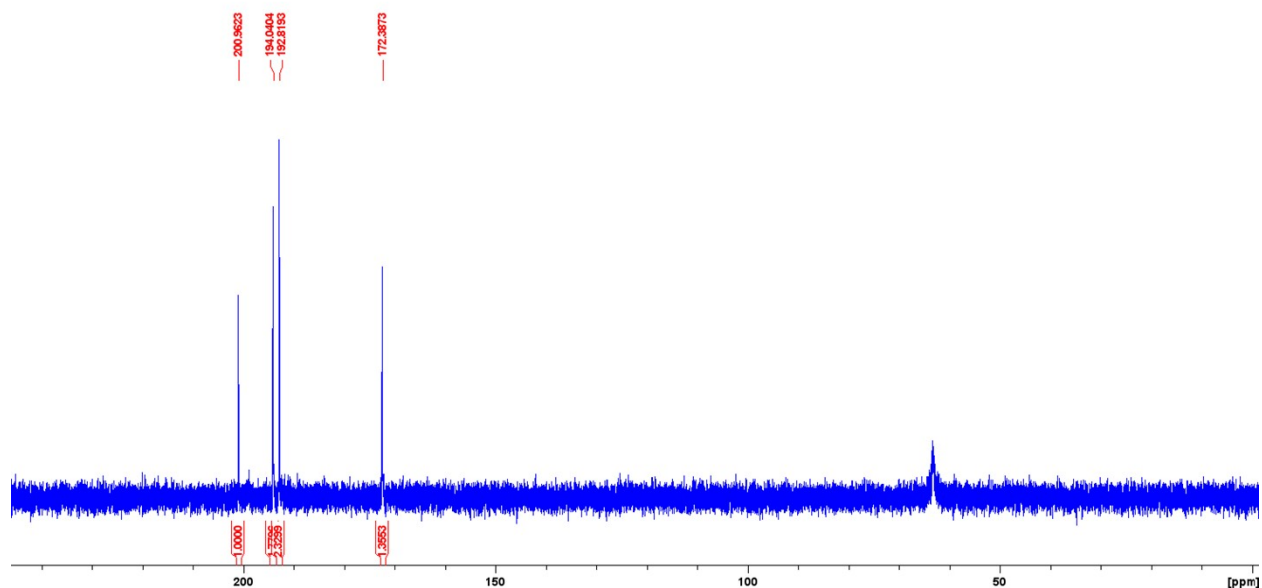


Figure S145. $^{31}\text{P}\{^1\text{H}\}$ NMR spectrum of the crude mixture for the reaction **3** + Et_2NOH in C_6D_6 ($t= 48$ h).

6. PXRD spectra of selected complexes

Powder X-ray diffraction data were collected for 10 powder samples to establish bulk purity. The data collection mode and instrumental details are given below, and the diffraction patterns and the Rietveld fits are shown in the following pages.

Mode organic standard 10 min"

Instrument: Malvern PanAlytical Empyrean 3

Geometry: Bragg Brentano $\theta - \theta$

Radiation: $\text{CuK}\alpha$, $\lambda = 1.54178 \text{ \AA}$ (45 kV, 40 mA)

Detector: PIXcel^{3D}

mode 1D continuous scan (255 channels)

Pulse height distribution (PHD): 25%-70%

Optics Incident side: iCore module:

Bragg-Brentano HD Cu X-ray mirror;

automatic divergence slit set to irradiated length of 10 mm;

0.03 rad Soller slit;

14 mm primary mask, 6 mm secondary mask.

Optics diffracted side: dCore module:

automatic anti-scatter slit set to irradiated length of 10 mm;

0.04 rad Soller slit.

Scan: 2θ range: 4 to 40° ;

Step size: 0.0131° ;

Counting time 45.6 s;

Total time: 10 min.

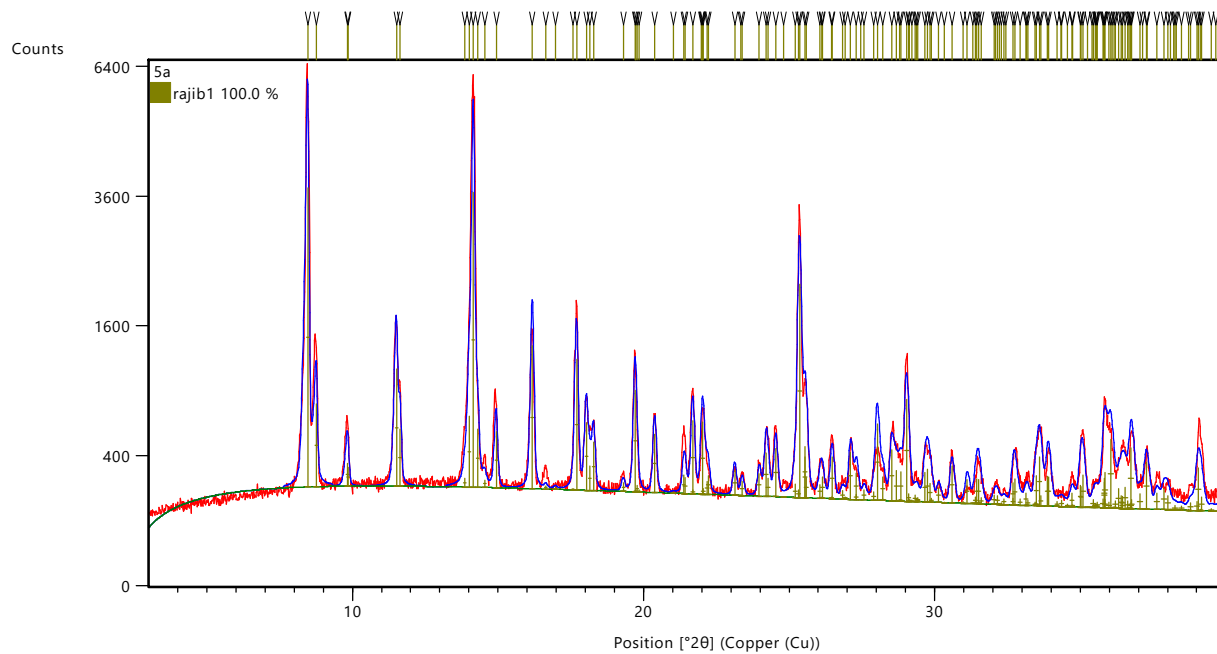


Figure S146. PXRD pattern obtained experimentally for complex **5a** (red trace) and the simulated pattern (blue trace) obtained by a Rietveld fit based on the unit cell parameters of complex **5a**.

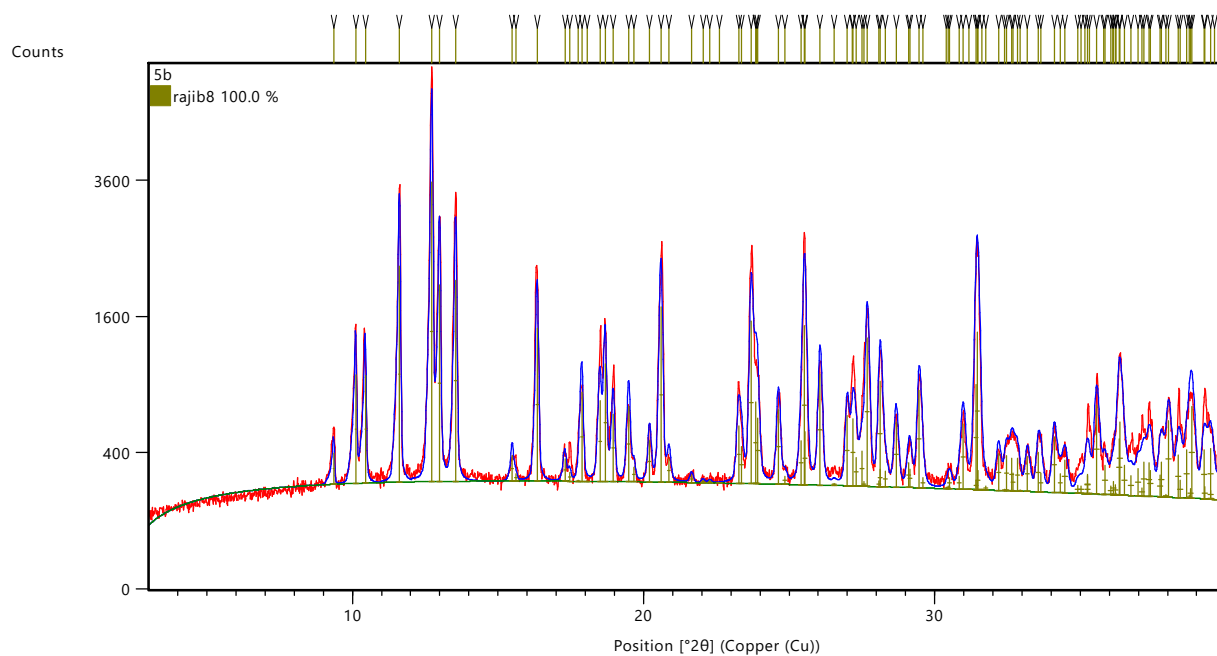


Figure S147. PXRD pattern obtained experimentally for complex **5b** (red trace) and the simulated pattern (blue trace) obtained by a Rietveld fit based on the unit cell parameters of complex **5b**.

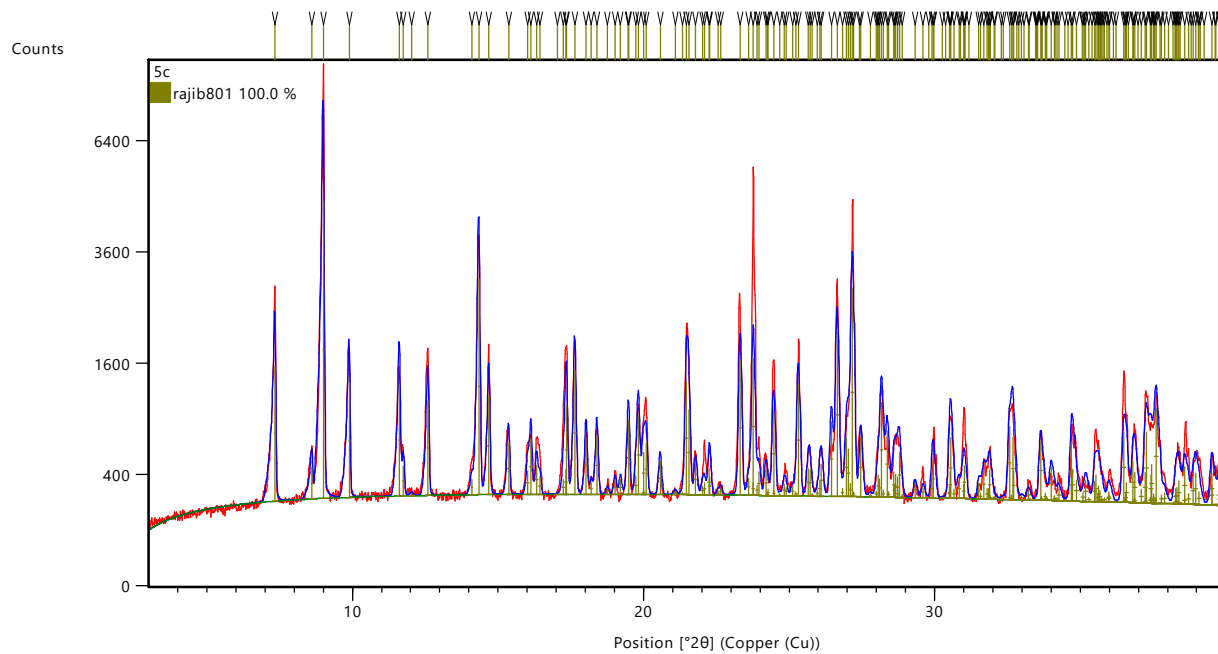


Figure S148. PXRD pattern obtained experimentally for complex **5c** (red trace) and the simulated pattern (blue trace) obtained by on a Rietveld fit based on the unit cell parameters of complex **5c**.

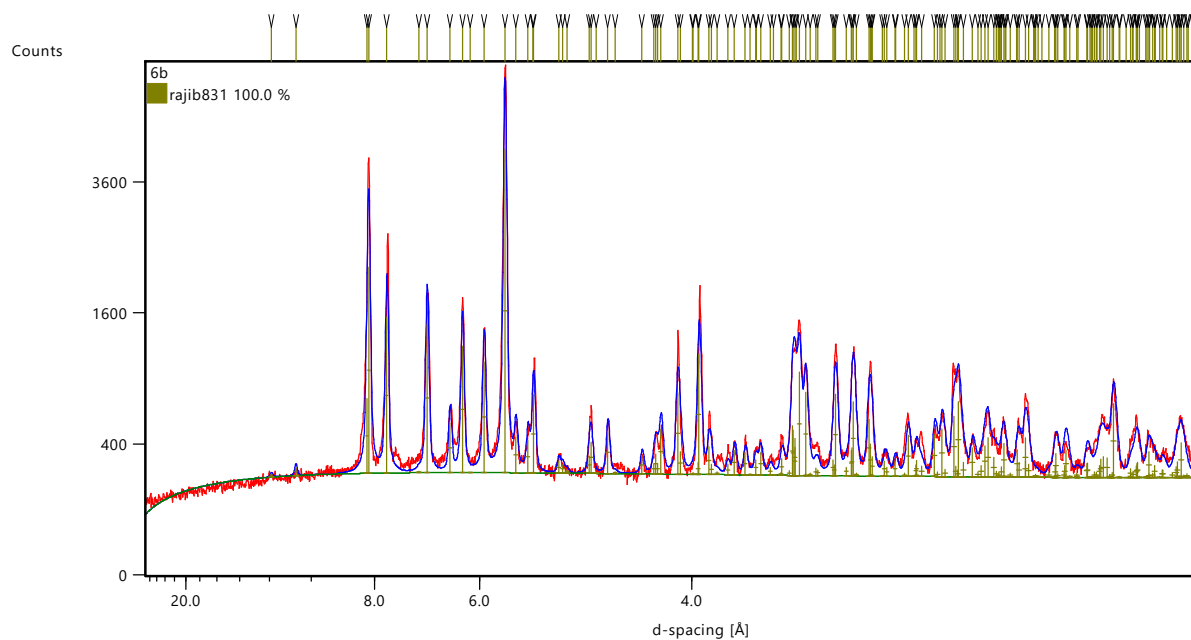


Figure S149. PXRD pattern obtained experimentally for complex **6b** (red trace) and the simulated pattern (blue trace) obtained by a Rietveld fit based on the unit cell parameters of complex **6b**.

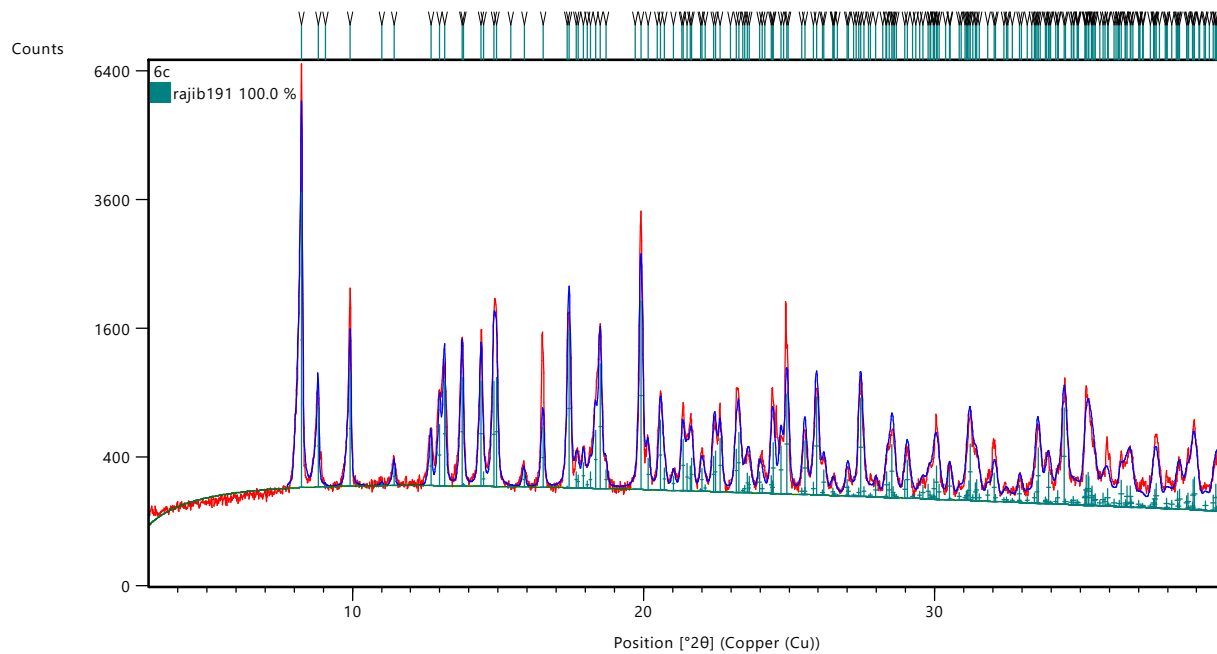


Figure S150. PXRD pattern obtained experimentally for complex **6c** (red trace) and the simulated pattern (blue trace) obtained by a Rietveld fit based on the unit cell parameters of complex **6c**.

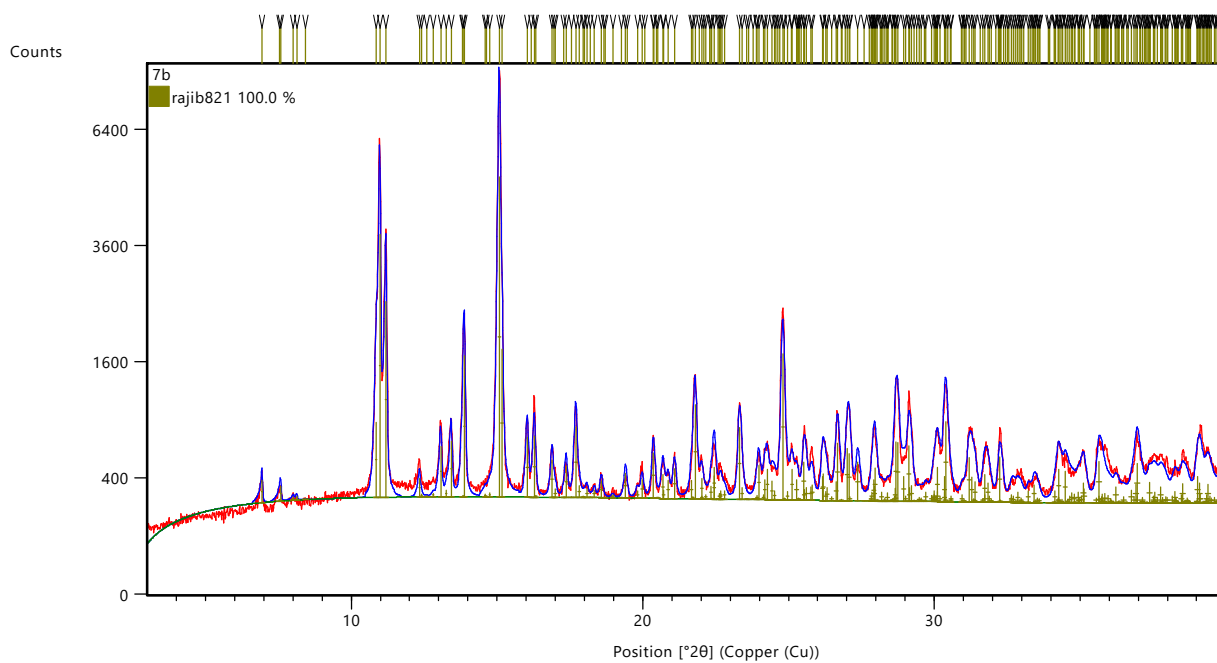


Figure S151. PXRD pattern obtained experimentally for complex **7b** (red trace) and the simulated pattern (blue trace) obtained by a Rietveld fit based on the unit cell parameters of complex **7b**.

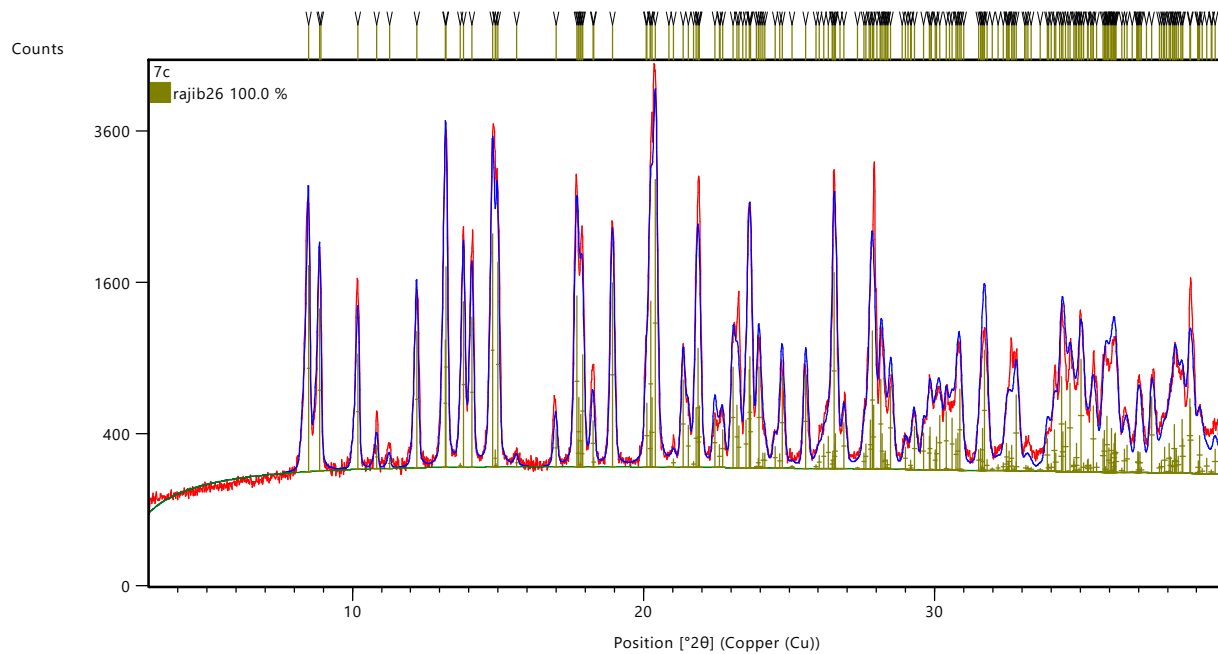


Figure S152. PXRD pattern obtained experimentally for complex **7c** (red trace) and the simulated pattern (blue trace) obtained by a Rietveld fit based on the unit cell parameters of complex **7c**.

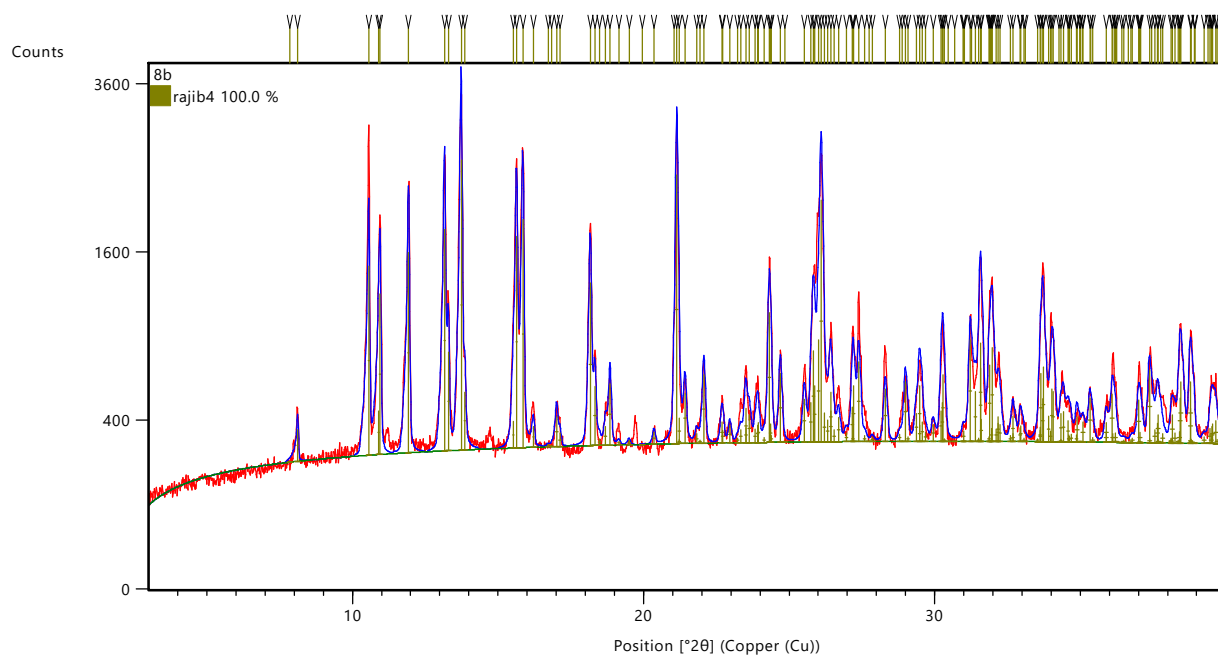


Figure S153. PXRD pattern obtained experimentally for complex **8b** (red trace) and the simulated pattern (blue trace) obtained by a Rietveld fit based on the unit cell parameters of complex **8b**.

7. Crystallographic data tables

Table S1: Crystal description and refinement indicators for complex **4'**

	4'
chemical formula	C ₂₈ H ₄₇ BrN ₂ NiO ₂ P ₂
crystal colour	orange
crystal size (mm)	0.07 × 0.08 × 0.065
index ranges	-11 ≤ h ≤ 11 -14 ≤ k ≤ 14 -21 ≤ l ≤ 21
<i>F</i>w; <i>F</i>(000)	644.23; 676.0
<i>T</i> (K)	150
wavelength (Å)	1.34139
space group	P-1
<i>a</i> (Å)	8.6766(3)
<i>b</i> (Å)	10.8198(4)
<i>c</i> (Å)	16.2208(6)
<i>α</i> (deg)	91.2360(10)
<i>β</i> (deg)	93.385(2)
<i>γ</i> (deg)	90.311(2)
<i>Z</i>	2
<i>V</i> (Å³)	1519.75(10)
<i>ρ</i>_{calcd} (g·cm⁻³)	1.408
<i>μ</i> (mm⁻¹)	5.295
<i>θ</i> range (deg); completeness	4.748 - 121.456; 0.998
collected reflections; <i>R</i>_σ	36465; 0.0250
unique reflections; <i>R</i>_{int}	6953; 0.0363
<i>R</i>₁^a; <i>wR</i>₂^b [<i>I</i> > 2σ(<i>I</i>)]	0.0255; 0.0695
<i>R</i>₁; <i>wR</i>₂ [all data]	0.0269; 0.0706
GOOF	1.046
largest diff peak and hole	0.75 and -0.47

$$^a R_1 = \frac{\sum(|F_o| - |F_c|)}{\sum|F_o|}$$

$$^b wR_2 = \left\{ \frac{\sum[w(F_o^2 - F_c^2)^2]}{\sum[w(F_o^2)^2]} \right\}^{1/2}$$

Table S2: Crystal description and refinement indicators for compounds **5a-5c**

	5a	5b	5c
chemical formula	C ₁₉ H ₂₇ Br _{0.3} Cl _{0.7} NNiO ₂ P	C ₁₆ H ₂₉ BrNNiO ₂ P	C ₂₆ H ₃₃ BrNNiO ₂ P
crystal colour	yellow	brown	red
crystal size (mm)	0.1 × 0.224 × 0.065	0.101 × 0.129 × 0.130	0.075 × 0.145 × 0.200
index ranges	-10 ≤ h ≤ 11	-12 ≤ h ≤ 12	-39 ≤ h ≤ 39
	-13 ≤ k ≤ 13	-13 ≤ k ≤ 12	-11 ≤ k ≤ 11
	-13 ≤ l ≤ 13	-20 ≤ l ≤ 20	-26 ≤ l ≤ 26
<i>F</i>_w; <i>F</i>(000)	438.33; 458.0	436.99; 904	561.12; 2320.0
<i>T</i> (K)	100	100	100
wavelength (Å)	1.54178	1.54178	1.54178
space group	P-1	P2 ₁ 2 ₁ 2 ₁	C2/c
<i>a</i> (Å)	9.2167(3)	10.312(3)	32.2326(6)
<i>b</i> (Å)	10.7893(3)	11.182(3)	9.4013(2)
<i>c</i> (Å)	11.1469(3)	16.878(5)	21.8275(4)
<i>α</i> (deg)	108.3090(10)	90	90
<i>β</i> (deg)	99.2590(10)	90	128.5790(10)
<i>γ</i> (deg)	99.2440(10)	90	90
<i>Z</i>	2	4	8
<i>V</i> (Å³)	1011.92(5)	1946.1(9)	5170.76(18)
<i>ρ</i>_{calcd} (g·cm⁻³)	1.439	1.491	1.442
<i>μ</i> (mm⁻¹)	3.728	4.661	3.648
<i>θ</i> range (deg); completeness	4.977- 72.028; 0.974	4.744- 72.212; 0.995	3.508- 71.960; 1.000
collected reflections; <i>R</i>_σ	41853; 0.0089	40151; 0.0143	34847; 0.0156
unique reflections; <i>R</i>_{int}	3861; 0.0217	3813; 0.0293	5060; 0.0275
<i>R</i>₁^a; <i>wR</i>₂^b [<i>I</i> > 2σ(<i>I</i>)]	0.0237; 0.0640	0.0168; 0.0436	0.0267; 0.0711
<i>R</i>₁; <i>wR</i>₂ [all data]	0.0238; 0.0640	0.0168; 0.0436	0.0278; 0.0720
GOOF	1.063	1.094	1.047
largest diff peak and hole	0.39 and -0.20	0.57 and -0.26	0.86 and -0.55

$$^a R_1 = \frac{\sum(|F_o| - |F_c|)}{\sum|F_o|}$$

$$^b wR_2 = \left\{ \frac{\sum[w(F_o^2 - F_c^2)^2]}{\sum[w(F_o^2)^2]} \right\}^{1/2}$$

Table S3: Crystal description and refinement indicators for compounds **6b** and **6c**.

	6b	6c
chemical formula	C ₁₆ H ₂₆ BrCINNiOP	C ₂₆ H ₃₀ BrCINNiOP
crystal colour	brown	yellow
crystal size (mm)	0.09 × 0.09 × 0.14	0.07 × 0.07 × 0.17
index ranges	-9 ≤ h ≤ 10 -12 ≤ k ≤ 13 -0 ≤ l ≤ 14	-15 ≤ h ≤ 15 -19 ≤ k ≤ 19 -16 ≤ l ≤ 15
<i>F</i>w; <i>F</i>(000)	453.42, 464.0	577.55; 1184.0
<i>T</i> (K)	100	150
wavelength (Å)	1.54178	1.34139
space group	P-1	P2 ₁ /n
<i>a</i> (Å)	8.1691(4)	12.9011(5)
<i>b</i> (Å)	10.6197(5)	15.7816(6)
<i>c</i> (Å)	11.5954(5)	13.2557(5)
<i>α</i> (deg)	85.083(2)	90
<i>β</i> (deg)	83.391(3)	107.169(2)
<i>γ</i> (deg)	89.300(3)	90
<i>Z</i>	2	4
<i>V</i> (Å³)	995.58(8)	2578.93(17)
<i>ρ</i>_{calcd} (g·cm⁻³)	1.513	1.488
<i>μ</i> (mm⁻¹)	5.748	6.422
<i>θ</i> range (deg); completeness	3.851 – 72.221; 0.981	3.655 – 55.022; 1.000
collected reflections; <i>R</i>_σ	26093; 0.0348	34837; 0.0410
unique reflections; <i>R</i>_{int}	3767; 0.1273	4899; 0.0691
<i>R</i>1^a; <i>wR</i>2^b [<i>I</i> > 2σ(<i>I</i>)]	0.0535; 0.1480	0.0374; 0.0868
<i>R</i>1; <i>wR</i>2 [all data]	0.0578; 0.1519	0.0518; 0.0935
GOOF	1.132	1.050
largest diff peak and hole	1.33 and -0.56	0.35 and -0.50

$$^a R_1 = \frac{\sum(|F_o| - |F_c|)}{\sum|F_o|}$$

$$^b wR_2 = \left\{ \frac{\sum[w(F_o^2 - F_c^2)^2]}{\sum[w(F_o^2)^2]} \right\}^{1/2}$$

Table S4: Crystal description and refinement indicators for compounds **7b-7d**.

	7b	7c	7d
chemical formula	C ₁₇ H ₂₉ BrNNiO ₂ P	C ₂₇ H ₃₃ BrNNiO ₂ P	C ₁₇ H ₃₁ BrNNiO ₂ P
crystal colour	yellow	yellow	yellow
crystal size (mm)	0.08 × 0.11 × 0.13	0.15 × 0.16 × 0.26	0.07 × 0.13 × 0.15
index ranges	-11 ≤ h ≤ 11 -13 ≤ k ≤ 13 -29 ≤ l ≤ 29	-17 ≤ h ≤ 16 -20 ≤ k ≤ 20 -17 ≤ l ≤ 17	-14 ≤ h ≤ 14 -15 ≤ k ≤ 15 -20 ≤ l ≤ 20
<i>F</i>_w; <i>F</i>(000)	449; 928.0	573.13; 1184.0	451.02; 936.0
<i>T</i> (K)	150	150	150
wavelength (Å)	1.34139	1.34139	1.34139
space group	P-1	P2 ₁ /n	P2 ₁ /c
<i>a</i> (Å)	8.7051(4)	13.1430(3)	11.3886(4)
<i>b</i> (Å)	10.5840(5)	15.5918(4)	11.7955(4)
<i>c</i> (Å)	22.8298(11)	13.1678(3)	15.5240(5)
<i>α</i> (deg)	87.918(2)	90	90
<i>β</i> (deg)	86.659(2)	103.5710(10)	92.048(2)
<i>γ</i> (deg)	74.060(2)	90	90
<i>Z</i>	4	4	4
<i>V</i> (Å³)	2018.65(17)	2623.05(11)	2084.07(12)
<i>ρ</i>_{calcd} (g·cm⁻³)	1.477	1.451	1.437
<i>μ</i> (mm⁻¹)	7.316	5.718	7.087
<i>θ</i> range (deg); completeness	3.375 – 60.836; 0.994	3.892 – 60.656; 0.977	3.378 – 60.641; 0.993
collected reflections; <i>R</i>_σ	41903; 0.0593	38929; 0.0313	31567; 0.0372
unique reflections; <i>R</i>_{int}	9162; 0.0701	5913; 0.0435	4759; 0.0533
<i>R</i>1^a; <i>wR</i>2^b [<i>I</i> > 2σ(<i>I</i>)]	0.0733; 0.2153	0.0272; 0.0706	0.0516; 0.1664
<i>R</i>1; <i>wR</i>2 [all data]	0.0835; 0.2304	0.0276; 0.0709	0.0526; 0.1684
GOOF	1.067	1.102	1.115
largest diff peak and hole	1.60 and -1.43	0.30 and -0.37	0.95 and -1.19

$$^a R_1 = \frac{\sum(|F_o| - |F_c|)}{\sum|F_o|}$$

$$^b wR_2 = \left\{ \frac{\sum[w(F_o^2 - F_c^2)^2]}{\sum[w(F_o^2)^2]} \right\}^{1/2}$$

Table S5: Crystal description and refinement indicators for compounds **8a** and **8b**

	8a	8b
chemical formula	C ₂₁ H ₃₂ Br _{0.7} Cl _{0.3} N ₂ NiO ₂ P	C ₁₈ H ₃₂ BrN ₂ NiOP
crystal colour	yellow	brown
crystal size (mm)	0.065 × 0.081 × 0.143	0.08 × 0.10 × 0.13
index ranges	0 ≤ h ≤ 25 -12 ≤ k ≤ 0 -13 ≤ l ≤ 13	-36 ≤ h ≤ 36 -8 ≤ k ≤ 10 -26 ≤ l ≤ 26
<i>F</i>_w; <i>F</i>(000)	500.74; 1042.0	462.04; 1920.0
<i>T</i> (K)	100	100
wavelength (Å)	1.54178	1.54178
space group	Pc	C2/c
<i>a</i> (Å)	20.5518(11)	29.6233(12)
<i>b</i> (Å)	10.3023(5)	8.5715(4)
<i>c</i> (Å)	10.8188(7)	21.7605(15)
α (deg)	90	90
β (deg)	97.918(3)	130.3570(10)
γ (deg)	90	90
<i>Z</i>	4	8
<i>V</i> (Å³)	2268.8(2)	4210.4(4)
ρ_{calcd} (g·cm⁻³)	1.466	1.458
μ (mm⁻¹)	3.814	4.319
θ range (deg); completeness	2.170- 72.555; 0.983	3.916 – 70.098; 0.991
collected reflections; R_σ	14082; 0.0401	41086; 0.0232
unique reflections; R_{int}	4343; 0.0746	3962; 0.0450
R1^a; wR2^b [I > 2σ(I)]	0.0516; 0.1452	0.0299; 0.0841
R1; wR2 [all data]	0.0538; 0.1484	0.0301; 0.0843
GOOF	1.047	1.081
largest diff peak and hole	0.98 and -0.79	0.50 and -0.35

$$^a R_1 = \frac{\sum(|F_o| - |F_c|)}{\sum|F_o|}$$

$$^b wR_2 = \left\{ \frac{\sum[w(F_o^2 - F_c^2)^2]}{\sum[w(F_o^2)^2]} \right\}^{1/2}$$

6. Additional Thermal ellipsoid plots

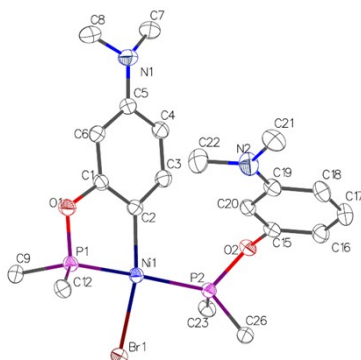


Figure S154. Side view of the molecular diagram of compound **4'**. Thermal ellipsoids are shown at the 50% probability level; hydrogen atoms are refined via riding model.

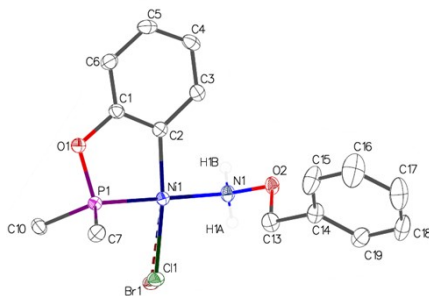


Figure S155. Side view of the molecular diagram of compound **5a**. Thermal ellipsoids are shown at the 50% probability level; hydrogen atoms are refined via riding model.

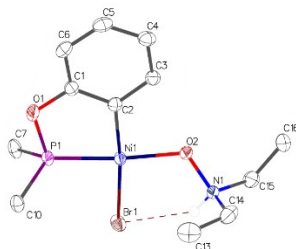


Figure S156. Side view of the molecular diagram of compound **5b**. Thermal ellipsoids are shown at the 50% probability level; hydrogen atoms are refined via riding model.

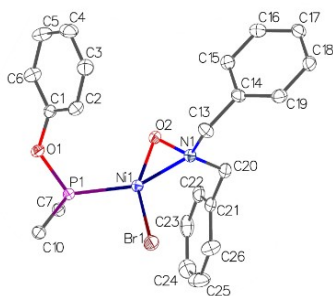


Figure S157. Side view of the molecular diagram of compound **5c**. Thermal ellipsoids are shown at the 50% probability level; hydrogen atoms are refined via riding model.

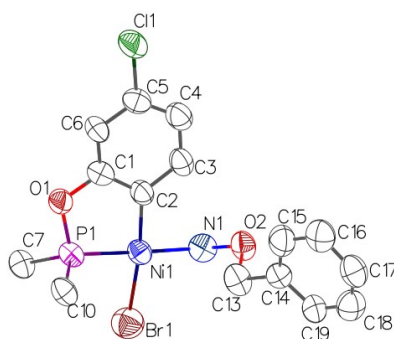


Figure S158. Side view of the molecular diagram of compound **6a**. Thermal ellipsoids are shown at the 50% probability level; hydrogen atoms are refined via riding model.

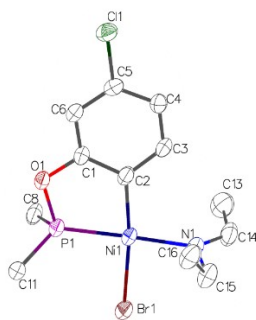


Figure S159. Side view of the molecular diagram of compound **6b**. Thermal ellipsoids are shown at the 50% probability level; hydrogen atoms are refined via riding model.

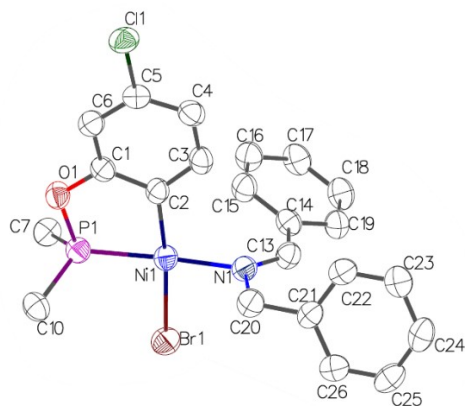


Figure S160. Side view of the molecular diagram of compound **6c**. Thermal ellipsoids are shown at the 50% probability level; hydrogen atoms are refined via riding model.

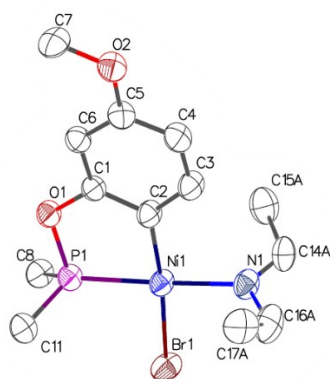


Figure S161. Side view of the molecular diagram of compound **7b**. Thermal ellipsoids are shown at the 50% probability level; hydrogen atoms are refined via riding model.

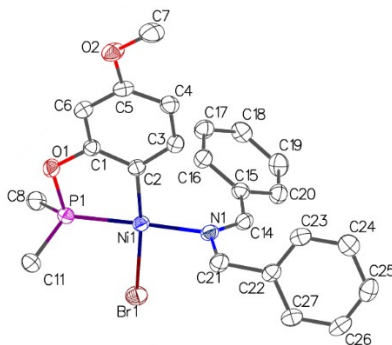


Figure S162. Side view of the molecular diagram of compound **7c**. Thermal ellipsoids are shown at the 50% probability level; hydrogen atoms are refined via riding model.

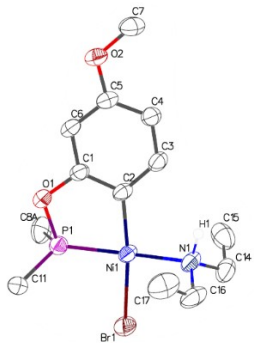


Figure S163. Side view of the molecular diagram of compound **7d**. Thermal ellipsoids are shown at the 50% probability level; hydrogen atoms are refined via riding model.

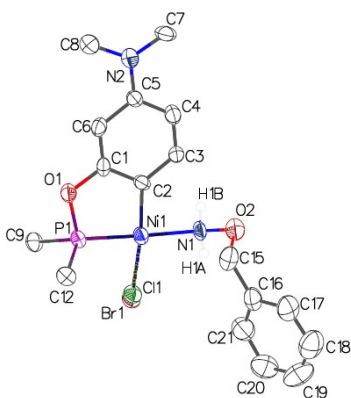


Figure S164. Side view of the molecular diagram of compound **8a**. Thermal ellipsoids are shown at the 50% probability level; hydrogen atoms are refined via riding model.

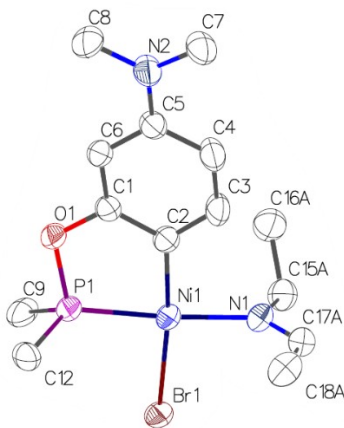


Figure S165. Side view of the molecular diagram of compound **8b**. Thermal ellipsoids are shown at the 50% probability level; hydrogen atoms are refined via riding model.

Table S6 Selected bond distances (Å) for all new complexes.

	Ni-C2	Ni-P1	Ni-Cl/Br	Ni-N/Ni-O	N-O	N-C _{sp2}	N-C _{sp3}
4'	1.9310(15)	2.1364(4)	2.3576(3)				
5a	1.9091(13)	2.1024(4)	2.250(8)/ 2.320(9)	1.9762(11)	1.4533(13)		
5b	1.911(2)	2.1007(8)	2.3749(6)	1.9173(17)	1.405(3)		
5c		2.1568(5)	2.3055(3)	1.8956(13)/ 1.8378(11)	1.3768(17)		
6b	1.909(4)	2.1058(11)	2.3506(8)	1.945(3)		1.289(6)	1.456(6)
6c	1.907(4)	2.1031(11)	2.3500(7)	1.934(3)		1.277(5)	1.505(5)
7b	1.916(4)	2.1047(11)	2.3664(7)	1.942(3)		1.265(18)	1.513(16)
7c	1.911(3)	2.1054(7)	2.3581(5)	1.943(2)		1.273(3)	1.489(3)
7d	1.918(2)	2.1041(7)	2.3699(4)	1.999(2)			1.492(4)
8a	1.911(14)	2.120(4)	2.12(2)/ 2.350(4)	1.973(11)	1.446(15)		
8b	1.912(2)	2.1047(7)	2.3711(4)	1.950(2)		1.295(4)	1.416(4)

Table S7 Selected bond angles (°) for all new complexes.

	C-Ni-Cl/Br	N/O-Ni-P1	C-Ni-P1	C-Ni-N/O	P1-Ni-Cl/Br	N/O-Ni-Cl/Br	Ni-N-C _{sp2}
4'	166.20(4)		81.95(4)		88.605(12)		
5a	173.5(2)/ 169.7(2)	177.93(3)	83.28(4)	95.96(5)	90.8(2)/ 88.0(3)	90.0(2)/ 93.0(3)	
5b	173.12(7)	172.97(6)	83.26(8)	89.79(9)	91.05(3)	95.96(5)	
5c							
6b	172.79(12)	176.25(11)	83.39(12)	96.57(16)	89.54(4)	90.58(10)	124.9(3)
6c	173.82(12)	172.75(10)	83.67(12)	94.64(15)	90.27(4)	91.22(10)	128.8(3)
7b	173.75(11)	177.53(11)	83.24(12)	94.33(15)	90.54(3)	91.88(11)	126.7(7)
7c	172.58(8)	175.00(7)	83.41(8)	95.06(10)	90.32(2)	90.85(7)	128.34(19)
7d	169.71(7)	171.84(8)	82.78(8)	95.2(1)	89.04(2)	93.75(7)	
8a	175.6(9)/ 171.2(4)	178.5(4)	83.2(4)	95.9(5)	92.5(7)/ 90.86(14)	88.4(8)/ 90.1(4)	
8b	173.74(4)	174.86(7)	82.43(7)	95.26(9)	91.52(2)	90.89(6)	124.4(2)

8. Regarding the unusually downfield signals in the ^1H NMR spectra of **6c and **7c**.** Recall that the ^1H NMR spectra for **6c** and **7c** displayed unusually downfield signals at δ 8.93 and 8.82, respectively, which were assigned to the ortho protons belonging to one of the Ph rings in the imine moiety $\text{PhCH}_2\text{NCHPh}$. In search of some rationale for these observations, we examined the solid-state structures of these complexes to see if any unexpected H---element close contacts might be present in the crystal lattice. Indeed, we found that one of the ortho protons in the PhC(H)N moiety of these complexes does lie fairly close to the Ni atom ($\text{Ni---H}_{\text{ortho}} \approx 2.44$ in **6c** and 2.49 \AA in **7c**). Assuming (a) that the orientation observed in the solid-state of these complexes is maintained in solution, and (b) that there is free and rapid rotation around the Ph-C(H)N bond, it seemed conceivable that the unusually downfield signals for the ortho protons in **6c** and **7c** might be related to such close contacts.

The question arises whether the observed $\text{Ni---H}_{\text{ortho}}$ distances reflect orbital interactions, or whether they are caused by the specific orientation of the Ph ring, which might, in turn, be dictated by some other factor. To be sure, agostic Ni---(H-C) interactions should not be favored in the 16-electron d^8 complexes under discussion here because they are perceived to be functionally saturated. Nevertheless, we examined the solid-state parameters for **6c** and **7c** in search of clues that might rationalize the particular orientation of the Ph ring in question. We found that the vinylic proton in the imine moiety NCHPh is orientated toward and fairly close to the Ph ring of the NCH_2Ph moiety ($\text{H---C}_{\text{ipso}} \approx 2.35$ and 2.34 \AA , respectively).

Therefore, it seemed plausible that the short $\text{Ni---H}_{\text{ortho}}$ distances in **6c** and **7c** might be due to secondary structural constraints such as this observed $\text{H---C}_{\text{ipso}}$ close contact. If it were true that the unusual Ni---H interactions are related to the particular orientation of Ph groups, then such interactions must not be present in those structures that lack Ph moieties in the imine ligand. Yet, when we inspected the solid-state structures of the analogous complexes **6b** and **7b** that feature a $\text{NCH(CH}_3)$ moiety but no Ph substituents, we found that both CH_3 groups in these complexes were pointing toward the Ni centre and the $\text{Ni---H}_{\text{CH}_3}$ distances were almost as short as for the *ortho* protons in **6c** and **7c** (ca. 2.55 - 2.87 \AA vs 2.44 and 2.49 \AA). In other words, the absence of Ph moieties in **6b** and **7b** does not appear to eliminate close Ni---H contacts. What is more, this phenomenon appears to be quite general as both CH_3 groups in the amine and imine adducts **7d** and **8b** also point toward the Ni centre, and the $\text{Ni---H}_{\text{CH}_3}$ contacts found in these complexes are almost as short: 2.75 - 2.80 \AA in **7d** and 2.70 - 2.86 \AA in **8b**.

To conclude from the above findings, the close Ni---H contacts in question appear to be a common feature of the imine and amine adducts discussed here, but the data at hand do not allow us to pinpoint a specific phenomenon that might rationalize our observations. We hope to probe this phenomenon in future investigations.

9. DFT Computational studies.

Experimental

All DFT calculations were performed using Gaussian 16 revision C01 package¹⁰ on Graham cluster, access to which was granted by CalculCanada/ComputeCanada . Geometry optimizations were carried out in standard conditions (namely equimolar amounts of the MeCN adduct and Et2NOH) using Pople's 6-311+g** basis set¹¹ for all light atoms (C, H, O, P, N) and Karlsruhe triple zeta def2TZVP basis set for Ni and Br.¹² The M06 functional¹³ was exploited in implicit acetonitrile solvent using the SMD model.¹⁴ Local minima were assessed by default convergence criteria and the absence of imaginary frequencies in the frequency calculations. Transition states were assessed by the existence of a single imaginary frequency along the expected reaction coordinate and have been linked to intermediates by the intrinsic reaction coordinates (irc) routine using the local quadratic approximation (lqa),¹⁵ followed by re-optimization. The energies displayed on the schemes and figures are ΔG_0 and the values in parenthesis are ΔH_0 , and include the solvation energies. For the transition state TS31, the thermal parameters induced a lower energy than its closely related intermediate int21, and so the local barrier of 0.6 kcal/mol was determined by their difference in electronic energies only (in other words, the same thermal correction was applied for both geometries). The transition states TS81 and TS82 for the OH radical transfer were found by a fragment guess (open shell singlet) followed by an SCF calculation and test of the wavefunction's stability. Further optimization of a transition state using the same guess generated broken symmetry transition states, for which the wavefunction was shown to be stable under the perturbations considered by Gaussian. Molecular diagrams of the relevant intermediates and transition states were generated by CYLview20.¹⁶ The geometry of all presented stationary points are available in the .xyz file provided with the ESI.

Discussion

The DFT studies summarized here were undertaken to shed light on the mechanism of hydroxylamines dehydration promoted by the cyclonickelated dimeric complexes $\kappa^C, \kappa^P\text{-}\{2\text{-OP}(i\text{-Pr})_2, 4\text{-X-C}_6\text{H}_4\}_2\text{Ni}_2(\mu\text{-Br})_2$ (X = H, Cl, OMe, NMe₂). The reaction energy profile was calculated at the M06/6-311+g**/def2TZVP(Ni,Br) level of theory in implicit MeCN solvent using the SMD model.¹⁷ The energies discussed and displayed on the figures are Gibbs free energies, and are referenced to the acetonitrile adduct int10-NCMe (**Figure S166**). It should also be noted that the monomeric acetonitrile adduct of the parent dimeric Ni complex (X = H) has been used as a realistic model for the precursor complex, because such adducts are known to form readily in MeCN solutions. Moreover, the *i*-Pr substituents of the phosphinite moiety in the title complexes were replaced with Me groups for simplicity and to avoid making the

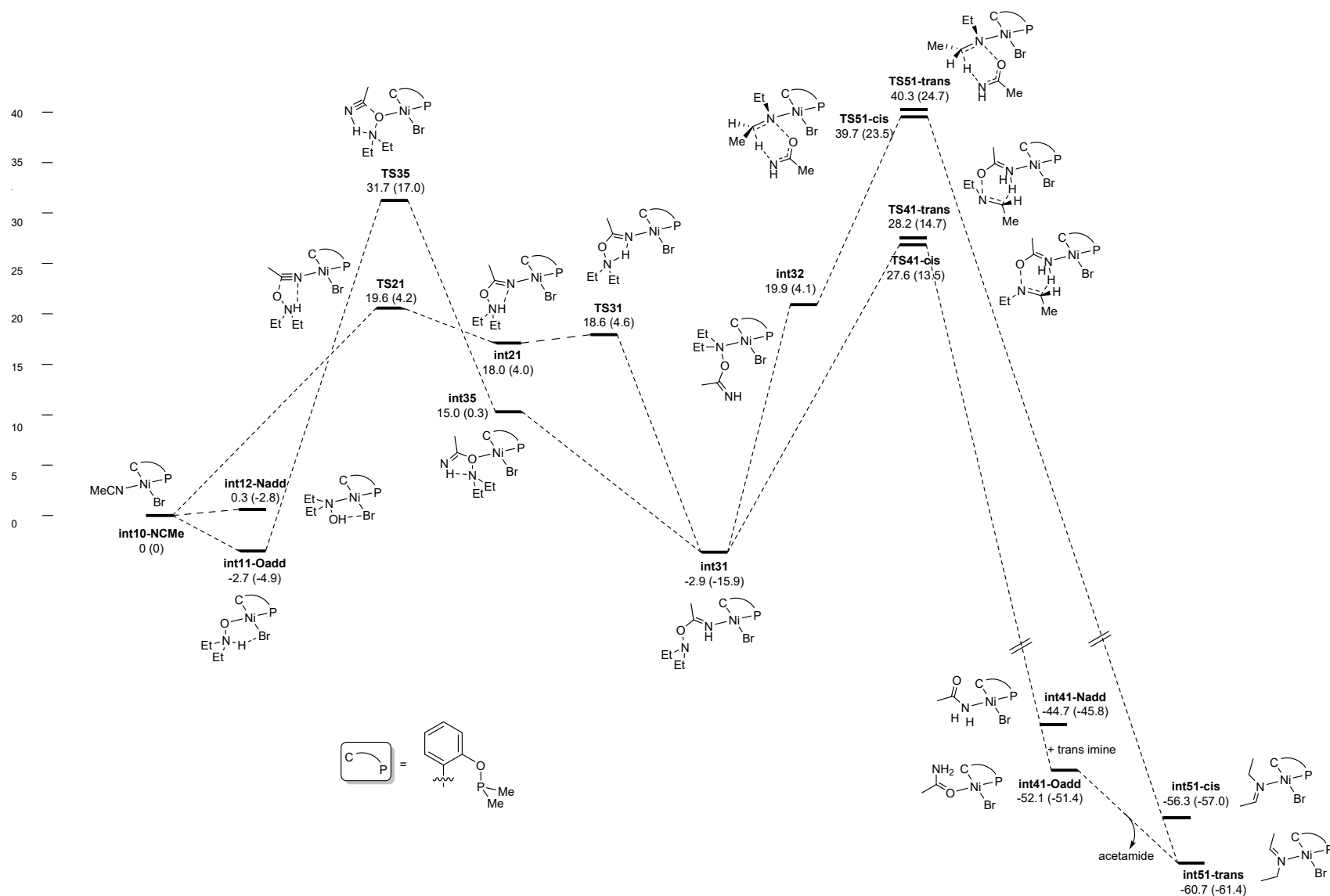


Figure S166. Proposed potential energy surface for the dehydration of hydroxylamines via a nucleophilic attack pathway at the M06/6-311+g**/def2TZVP level of theory. Energies presented are ΔG° (ΔH°) and are expressed in kcal/mol.

computational work more cumbersome due to the various possible conformations of the *i*-Pr groups. Thus, the model complex $\kappa^C, \kappa^P\text{-}\{2\text{-OPMe}_2\text{-C}_6\text{H}_4\}\text{Ni}(\text{Br})(\text{NCMe})$ has served as the starting point of our calculations.

As a first step, we studied the thermodynamics of substrate coordination to the nickel center. It was found that the replacement of MeCN by the canonical form of the hydroxylamine substrate, Et₂NOH, was not favored. In contrast, the substitution reaction becomes nearly thermoneutral (+0.3 kcal/mol) when the OH group in the substrate is allowed to form a hydrogen-bond with the Br ligand (**int12-Nadd**), whereas using the zwitterionic form Et₂N(H)⁺O⁻ made the substitution fully exergonic (by 2.7 kcal/mol). The latter reaction leads to **int11-Oadd**. This observation is in accordance with the following experimental observations: (1) the closely related adduct **5b** was isolated from the reaction of dimer **1** with Et₂NOH in CH₂Cl₂, and (2) re-dissolving crystals of **5b** in MeCN led to partial reformation of the acetonitrile adduct, implying the viability of the proposed equilibrium $\kappa^C, \kappa^P\text{-}\{2\text{-OPMe}_2\text{-C}_6\text{H}_4\}\text{Ni}(\text{Br})(\text{NCMe}) \rightleftharpoons \text{int11-Oadd}$.

The second step on the postulated pathway for dehydration of hydroxylamine (i.e., a closed shell nucleophilic addition by the hydroxylamine substrate on Ni-coordinated MeCN) is the attack of the substrate on the nitrile carbon. The lower transition state for this step (**Figure S167**) was found to be the addition of the zwitterionic hydroxylamine, the process being aided by hydrogen bonding between the NH moiety of the substrate and the N atom of the MeCN ligand. The barrier for this process is 19.6 kcal/mol (**TS21**), and leads to an intermediate containing the zwitterionic ligand Et₂N⁺(H)-O-C(Me)=(N⁻), **int21**, with only a slightly lower energy of 18.0 kcal/mol.

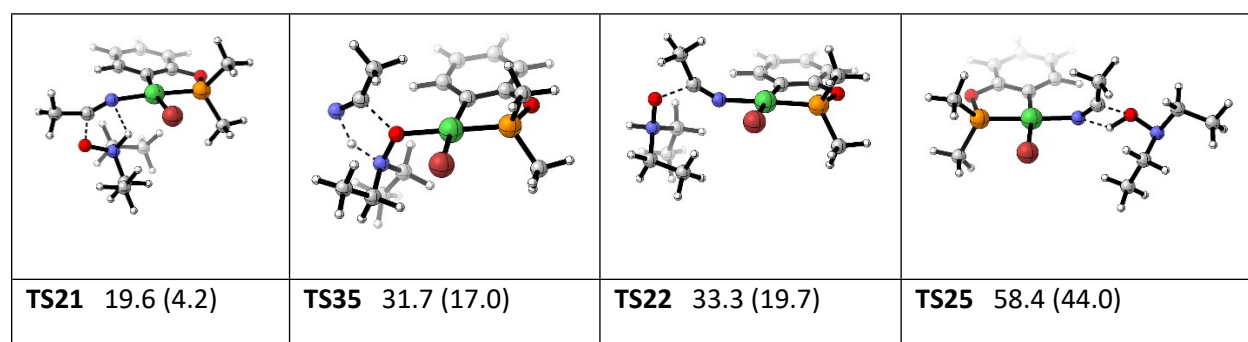


Figure S167. Molecular diagrams of various transition states for the nucleophilic attack of the zwitterionic hydroxylamine on MeCN

It is worth emphasizing that the nucleophilic attack is significantly less favorable without the assistance of a hydrogen bonding (**TS22**, 33.3 kcal/mol) or via a concerted O-H addition on the nitrile involving the canonical form of the hydroxylamine (**TS25**, 58.4 kcal/mol). In addition, the attack from the Ni-bound zwitterionic hydroxylamine adduct **int11-Oadd** to an external MeCN molecule (**TS35**) also has

a higher barrier of 31.7 kcal/mol; this approach leads to the more energetic **int35**, which, although being stabilized by internal H-bonding, should quickly convert to **int31**. Subsequent to the nucleophilic attack described above, the N—H proton is then transferred in a somewhat barrierless manner to generate the much more stable tautomer **int31** (by -2.9 kcal/mol). We speculate that the course of this reaction can probably be observed. Indeed, the ^{31}P monitoring of the reaction of dimer **3** with Et_2NOH in acetonitrile revealed a number of unidentified peaks that might well represent such intermediates.

The dehydration products must form from this key intermediate **int31** through a cyclic proton transfer whereby H^+ jumps from the α -carbon of the $\text{N}(\underline{\text{C}}\text{H}_2\text{CH}_3)_2$ moiety to the imine nitrogen atom coordinated to Ni. This process, that leads to either a trans- or a cis-imine, can pass through four possible transition states, all in a very narrow range of energies. In addition, the two lower energy transition states leading to the cis imine (**TS41-cis**) or the trans-imine (**TS41-trans**) showed very similar ΔG^\ddagger values, 27.6 and 28.2 kcal/mol, respectively (**Figure S168**). These transition states lead to a free imine and a Ni-acetamide complex, which is first bound via the NH_2 (**int41-Nadd**) but later converts to the O-bound isomer (**int41-Oadd**). With these two products being as low as -44.7 and -52.1 kcal/mol, respectively, this is the most exergonic step of the process, and the one that renders the overall transformation irreversible. The acetamide is then exchanged by the free imine, where the trans-imine complex **int51-trans** (-60.7 kcal/mol) is significantly lower in energy than its cis counterpart **int51-cis** (-56.3 kcal/mol). This implies that, although there is little or no kinetic E/Z selectivity in the system, the Ni center must promote the isomerization to the more stable trans-imine Ni-complex since this is the only isolated product (as observed in the crystal structures). Further substitution of the Ni-bound imine by a MeCN ligand is disfavored by 7.6 kcal/mol, consistent with the observed isolation of the imine adducts. It should be noted that the (unobserved) re-formation of the acetonitrile adduct would increase the overall barrier in the event of a Ni-catalyzed dehydration of hydroxylamines coupled to nitrile hydration.

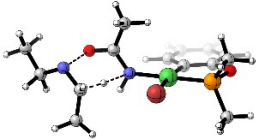
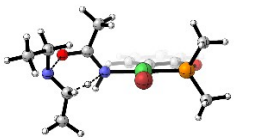
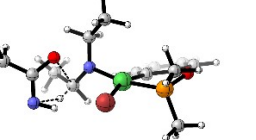
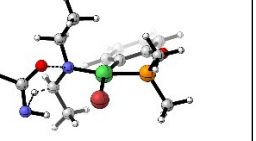
			
TS41-cis 27.6 (13.5)	TS41-trans 28.2 (14.7)	TS51-cis 39.7 (23.5)	TS51-trans 40.3 (24.7)

Figure S168. Molecular diagrams of transition states for the cyclic intramolecular proton transfer leading to breakage of the N-O bond.

Another pathway starts from **int35**, a coordination isomer of the more stable **int31** wherein the N α to the O is bound to the nickel center during the cyclic proton transfer, and leads directly to free acetamide and **int51-cis/trans**. Again, the four possible transition states were found in a very narrow range, with little to no cis/trans selectivity, but these transition states (**TS51-cis** and **TS51-trans**) were found as high as 39.7 and 40.3 respectively. Finally, another pathway from the zwitterionic intermediate **int21**, which was confirmed to be a local minimum, leads to a Ni-bound deprotonated acetamide and cis/trans iminium (**Figure S169**). Although this step is also found to be largely exergonic (-33.2 and -36.9 kcal/mol), the located barriers are much higher: **TS45-cis** with ΔG^\ddagger of 57.2 kcal/mol and **TS45-trans**, with 57.0 kcal/mol.

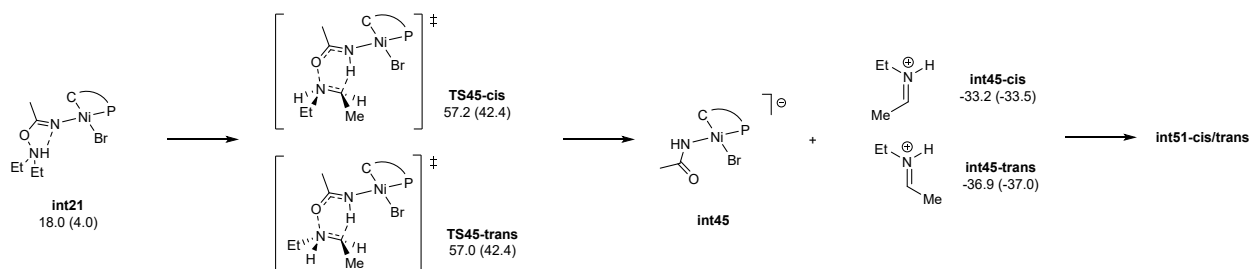


Figure S169. Proposed energy profile for the direct proton transfer from **int21**. Energies presented are ΔG^0 (ΔH^0) and are expressed in kcal/mol.

Finally, two additional pathways were probed: one going through Ni(IV) intermediates, and one going through radical species (**Figure S170**). The first one implies the N-O oxidative addition from the canonical hydroxylamine bound to the metal center (either through the O atom, **int12-Oadd** at 7.5 kcal/mol, or the N atom, **int12-Nadd** at 0.3 kcal/mol) and leading to 5-coordinate Ni(IV) intermediates featuring apical positions occupied by the NEt_2 fragment (**int71** at 29.5 kcal/mol) or the OH fragment (**int72** at 32.3 kcal/mol). However, the transition states to access these intermediates, **TS71** and **TS72**, are > 10 kcal/mol higher in energy than the more favored Ni(II) pathway, with ΔG^\ddagger of 39.8 and 43.8 kcal/mol. In addition, coordination of MeCN, which we believe is necessary to form acetamide, gives 6-coordinate intermediates as high as 37.5 and 36.5 kcal/mol for **int71-NCMe** and **int72-NCMe**, respectively, making this pathway improbable.

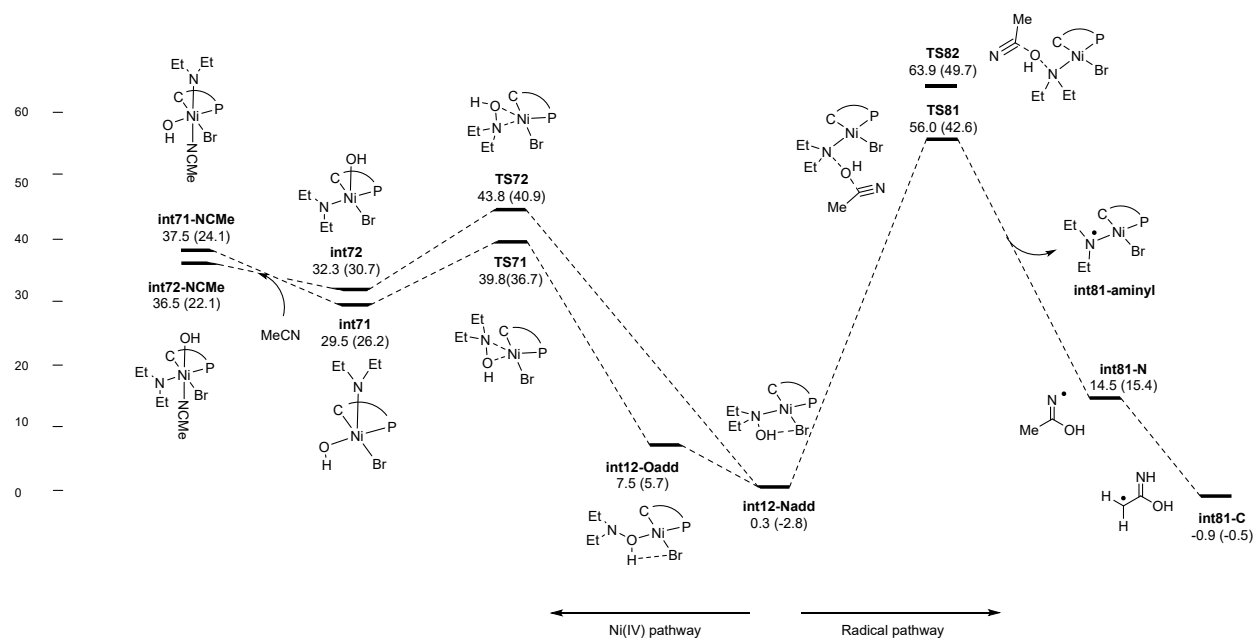


Figure S170. Proposed potential energy surface for the Ni(IV) and radical pathways at the M06/6-311+g**/def2TZVP level of theory. Energies presented are ΔG^0 (ΔH^0) and are expressed in kcal/mol.

The second additional pathway involves a formal OH·-radical transfer from the N-bound canonical hydroxylamine to an external molecule of MeCN, leading to the acetamide radical, primarily centered on the nitrogen (**int81-N** at 14.5 kcal/mol) which should tautomerize to its more stable form with the radical centered on the carbon atom (**int81-C** at -0.9 kcal/mol, **Figure S171**). This step also generates a radical Ni-NEt₂ complex, **int81**, which has been shown to be a Ni(II) species bearing an aminyl ligand, with most of the spin density located on the nitrogen. Although this step is nearly thermoneutral, the transition states located for this radical transfer, **TS81** and **TS82**, were found highly energetic with ΔG^\ddagger of 56.0 and 63.9 kcal/mol, indicating that this pathway is the least probable.

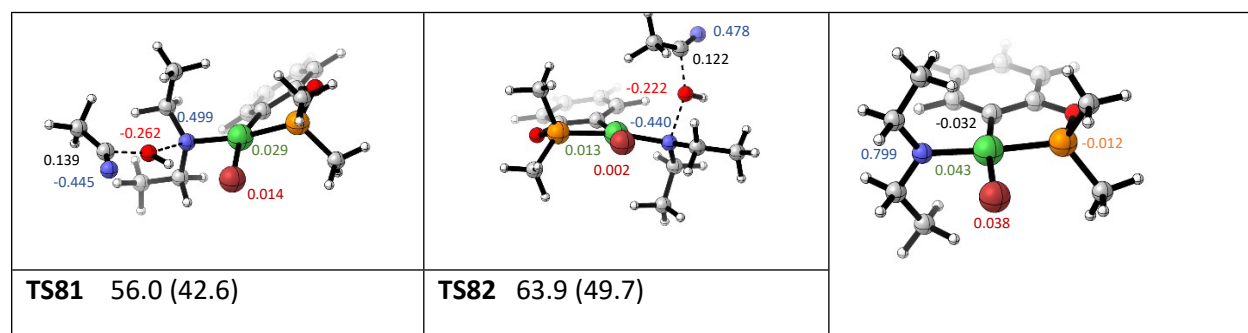


Figure S171. Molecular diagrams for the transition states and the Ni-aminyl intermediate on the radical transfer pathway. The numbers on the diagram represent Mulliken spin populations at the M06/6-311+g**/def2TZVP level of theory.

The above results allow us to conclude that, overall, the most probable pathway involves the attack of the zwitterionic hydroxylamine on the C≡N bond of a Ni-coordinated acetonitrile ligand, in an asynchronous manner, to give the stable ligand (Et₂NO)(Me)C=NH bound to Ni. The latter breaks apart into an imine and a molecule of acetamide through a concerted cyclic proton transfer/O-N bond breaking, on a closed shell surface. Although at this level of theory the overall barrier (from **int11-Oadd**) of 30.3 kcal/mol is too high to compare with the actual observed rate of reaction, this seems to us the most probable pathway and is in accordance with the mechanistic experiments described in the main manuscript. Adding a correction for the huge excess of MeCN in the actual reaction conditions only lowers the overall barrier by 4.3 kcal/mol only. In addition, the results of DFT calculations conducted on a Ni-free reaction show that the thermodynamics are similar (-53.0 kcal/mol). However, the barriers on the potential energy surface are higher, and indicate that the nickel complex facilitates the nucleophilic attack (this time in a synchronous fashion) by 7.7 kcal/mol, and the formation of the products by 8.5 kcal/mol.

References

- ¹(a) B. Vabre, D. M. Spasyuk, D. Zargarian, *Organometallics*, 2012, **31**, 8561-8570. (b) B. Vabre, F. Lindeperg, D. Zargarian, *Green Chemistry*, 2013, **15**, 3188-3194.
- ²L. P. Mangin, D. Zargarian, *Dalton Trans.*, 2017, **46**, 16159-16170.
- ³Bruker (2012). APEX2 / Bruker (2016) APEX3, Bruker AXS Inc., Madison, WI, USA.
- ⁴Bruker (2012). "SAINT Integration Software for Single Crystal Data", Bruker AXS Inc., Madison, WI, USA.
- ⁵(a) G. M. Sheldrick (1996). *SADABS/TWINABS*. University of Göttingen, Germany. (b) Bruker (2001). *SADABS/TWINABS*. Bruker AXS Inc., Madison, Wisconsin, USA.
- ⁶Bruker (2012). Data Preparation and Reciprocal Space Exploration Program, Bruker AXS Inc., Madison, WI, USA.
- ⁷A. O. V. Dolomanov, L. J. Bourhis, R. J. Gildea, J. A. K. Howard and H. Puschmann. "OLEX2: a complete structure solution, refinement and analysis program". *J. Appl. Cryst.*, 2009, **42**, 339-341.

-
- ⁸ G. M. Sheldrick, "SHELXT - Integrated space-group and crystal structure determination", *Acta Cryst.*, 2015, **A71**, 3-8.
- ⁹ G. M. Sheldrick, Crystal structure refinement with SHELXL, *Acta Cryst.*, 2015, **C71**, 3-8.
- ¹⁰ Gaussian 16, Revision C.01, M. J. Frisch, G. W. Trucks, H. B. Schlegel, G. E. Scuseria, M. A. Robb, J. R. Cheeseman, G. Scalmani, V. Barone, G. A. Petersson, H. Nakatsuji, X. Li, M. Caricato, A. V. Marenich, J. Bloino, B. G. Janesko, R. Gomperts, B. Mennucci, H. P. Hratchian, J. V. Ortiz, A. F. Izmaylov, J. L. Sonnenberg, D. Williams-Young, F. Ding, F. Lipparini, F. Egidi, J. Goings, B. Peng, A. Petrone, T. Henderson, D. Ranasinghe, V. G. Zakrzewski, J. Gao, N. Rega, G. Zheng, W. Liang, M. Hada, M. Ehara, K. Toyota, R. Fukuda, J. Hasegawa, M. Ishida, T. Nakajima, Y. Honda, O. Kitao, H. Nakai, T. Vreven, K. Throssell, J. A. Montgomery, Jr., J. E. Peralta, F. Ogliaro, M. J. Bearpark, J. J. Heyd, E. N. Brothers, K. N. Kudin, V. N. Staroverov, T. A. Keith, R. Kobayashi, J. Normand, K. Raghavachari, A. P. Rendell, J. C. Burant, S. S. Iyengar, J. Tomasi, M. Cossi, J. M. Millam, M. Klene, C. Adamo, R. Cammi, J. W. Ochterski, R. L. Martin, K. Morokuma, O. Farkas, J. B. Foresman, and D. J. Fox, Gaussian, Inc., Wallingford CT, 2019.
- ¹¹ (a) R. Krishnan, J. S. Binkley, R. Seeger, J. A. Pople, *J. Chem. Phys.*, 1980, **72**, 650-654. (b) T. Clark, J. Chandrasekhar, G. W. Spitznagel, P. Von R. Schleyer, *J. Comput. Chem.* 1983, **4**, 294-301. (c) A. D. McLean, G. S. Chandler, *J. Chem. Phys.* 1980, **72**, 5639-5648. (d) M. M. Francl, W. J. Pietro, W. J. Hehre, J. S. Binkley, M. S. Gordon, D. J. DeFrees, J. A. Pople, *J. Chem. Phys.*, 1982, **77**, 3654-3665. (e) G. W. Spitznagel, T. Clark, P. Von R. Schleyer, W. J. Hehre, *J. Comput. Chem.*, 1987, **8**, 1109-1116.
- ¹² F. Weigend, R. Ahlrichs, *Phys. Chem. Chem. Phys.*, 2005, **7**, 3297.
- ¹³ Y. Zhao, D. G. Truhlar, *Theor Chem Account* 2008, **120**, 215-241.
- ¹⁴ A. V. Marenich, C. J. Cramer, D. G. Truhlar, *J. Phys. Chem. B*, 2009, **113**, 6378-6396.
- ¹⁵ (a) M. Page, J. W. McIver Jr., *J. Chem. Phys.*, 1988, **88**, 922-935. (b) Page, M.; Doubleday Jr., C. ; McIver Jr., J. *W. J. Chem. Phys.*, 1990, **93**, 5634-5642.
- ¹⁶ CYLview20; Legault, C. Y. Université de Sherbrooke, 2020 (<http://www.cylview.org>).
- ¹⁷ Note that the cyclonickelation reaction leading to the title complexes has been modelled using the same computational procedures used in the present study. We have shown that this approach generated data that were very close to the experimentally obtained results: L. P. Mangin, D. Zargarian, *Organometallics*, 2019, **38**, *Organometallics* 2019, **38**, 1479-1492.